UNIVERSITY OF SOUTHAMPTON

FACULTY OF ENGINEERING AND THE ENVIRONMENT

On the search to reduce a swimmer's resistance

Surface-piercing bluff bodies over the critical *Re*-*Fr* range

by

Marion C. James

Thesis for the degree of Doctor of Philosophy

July 2016

Ph.D. thesis

Marion C. James, 2016.
[redacted]
Boldrewood Innovation Campus,
Faculty of Engineering and the Environment,
University of Southampton,
Southampton, SO16 7QF.
United Kingdom.

Typeset in LaTeX. Page, figure, table and bibliographic references use hypertext. *DOI*s are also hyperlinked.

UNIVERSITY OF SOUTHAMPTON

ABSTRACT

FACULTY OF ENGINEERING AND THE ENVIRONMENT
Fluid Structure Interactions

Thesis for the degree of Doctor of Philosophy

ON THE SEARCH TO REDUCE A SWIMMER'S RESISTANCE

Surface-piercing bluff bodies over the critical *Re-Fr* range

by Marion Carole James

Swimming as an Olympic sport is getting ever more competitive. Since the ban of the full-body length suits in 2009, research in swimming has had the aim of re-establishing new world records. This research investigates the likely dominance of the flow regime around the swimmer's head on their overall drag resistance. Both pool testing of swimmers and numerical simulations were initially undertaken to provide an insight into the measurement challenges at stake when evaluating a swimmer's resistance. Due to the inherent variability of a swimmer's performance, limited access to elite swimmers and excessive computational requirements the work concentrates on the use of rigid models for testing in a towing tank. A methodology aimed at breaking down the complexity of the flow physics around a swimmer's body is developed through the study of three models arrangements: a sphere, a head and a mannequin. A surface-piercing sphere is drag-tested over the critical Re-Fr range ($1\text{x}10^5 \leq Re \leq 7\text{x}10^5$, and $0.4 \leq Fr \leq 1.5$). Using a combination of above-water still photographs/videos and drag/vertical force measurements, a flow taxonomy is established. The existence of a drag crisis over the laminar to turbulent boundary layer transition is highlighted as a key feature that influences a swimmer's resistance. It is coupled with a sharp change of free surface deformation, from a large breaking wave to a thin sheet of fluid that passes cleanly over the sphere. A similar flow taxonomy is observed in the case of a head and visual observations of a flow regime change over the head are noticed when part of the mannequin. Various caps/goggles and head positions/shapes are tested on either the head only or with the mannequin's body. These studies indicate that equipment can have a large influence on a swimmer's resistance. Although a pre-selection process in a towing tank environment proved to be useful for manufacturers, an elite athlete still needs to be drag-tested to determine the best equipment for their head shape and body morphology. An initial protocol to select the best equipment (goggles, cap and suit) for each individual athlete is therefore suggested.

Contents

List of Figures

List of Tables

Academic Thesis: Declaration of Authorship

I, Marion Carole James, declare that the thesis entitled 'On the search to reduce a swimmer's resistance, surface-piercing bluff bodies over the critical *Re-Fr* range' and the work presented in the thesis are both my own, and have been generated by me as a result of my own original research. I confirm that:

1. This work was done wholly or mainly while in candidature for a research degree at this University;
2. Where any part of this thesis has previously been submitted for a degree or any other qualification at this University or any other institution, this has been clearly stated;
3. Where I have consulted the published work of others, this is always clearly attributed;
4. Where I have quoted the work of others, the source is always given. With the exception of such quotations, this thesis is entirely my own work;
5. I have acknowledged all main sources of help;
6. Where the thesis is based on work done by myself jointly with others, I have made it clear what was done by others and what I have contributed myself :
7. Either none of this work has been published before submission, or parts of this work have been published as:

   Banks, J., James, M., Hudson, D., Taunton, D. and Turnock, S. (2014), An analysis of a swimmer' s passive wave resistance using experimental data and CFD simulations, in 'Biomechanics and Medicine in Swimming XII', Canberra.

   James, M. C., Forester, A., Hudson, D. A., Taunton, D. J. and Stephen, R. (2015), Experimental study of the transitional flow of a sphere located at the free surface, in 'Proceedings of the 9th International Workshop on Ship and Marine Hydrodynamics', Glasgow.

Signed:.....

Date:.....

Statement of Ethics

When undertaking a research project involving humans, ethics approval is required. For this research project, all testing sessions were approved by the University of Southampton ethics committee (Ethics and Research Governance Online - ERGO). The ethics reference # is listed against each individual testing session in Appendix A.

Signed:.....

Date:.....

Acknowledgements

I would like to acknowledge the following people:

The project supervisors, Professor Stephen Turnock, Professor Dominic Hudson, Doctor Dominic Taunton and Doctor Alex Forrester for their continued help, advice and support;

The PhD sponsors: British Swimming, English Institute of Sport, EPSRC, Speedo and UK Sport;

The other team members of the SwimSIM project, Scott Michaels, Doctor Joe Banks, Doctor Chris Phillips and Doctor Angus Webb for their great collaboration in this project. In particular, I am thankful with the work they put in the design and build of the mannequin model and rig, as well as their support during the testing sessions.

PhD students part of the Fluid-Structure Interactions group for their support and great share of knowledge;

The Wolfson Unit for their valuable input in the tank testing work and CFD post-processing;

Aparna Subaiah-Varma, Jasmine Bencheley-Gordon and Pavittar Bassi for facilitating the finance work for the swimSIM project;

All my amazing friends, and in particular Egis Jankevicius and Jake Genauer for their incredible support despite the distance;

My dad for helping me with the build of the first prototype sphere, and my great uncle, Marcel Lavache, for building the two wooden spheres, both contributing to a large part of my research, and finally,

My parents and my sister for their continuous support and love.

Nomenclature

Symbols are defined in the text when used for the first time. Symbols used in several sections are included in this nomenclature. The co-ordinate system is Cartesian, where $x_i = (x_1, x_2, x_3) = (x, y, z)$ represent the streamwise, wall-normal (or vertical) and spanwise directions.

Latin symbols

symbol	description	units
A_p	projected area	$[m^2]$
$C_{()}$	cap	
d	immersion depth	$[m]$
D	diametre	$[m^2]$
F_D	drag force	$[N]$
g	gravitational constant	$[m^3.kg^{-1}.s^{-2}]$
$G_{()}$	goggles	
h	air draught	$[m]$
H	height	$[m]$
l	characteristic length	$[m]$
m	swimmer's added mass	$[kg]$
M	swimmer's mass	$[kg]$
p	p-value	
P	pressure	$[N.m^{-2}]$
t	time	$[s]$
U	free stream velocity	$[m.s^{-1}]$
W	weight	$[kg]$

Greek symbols

μ	dynamic viscosity	$[kg.m^{-1}.s^{-1}]$
∇	displacement volume	$[m^3]$

ν	kinematic viscosity	$[m^2.s^{-1}]$
ϕ_S	boundary layer separation angle	$[degrees]$
ρ	density	$[kg.m^3]$
$\theta_{()}$	spray angle	$[degrees]$

Dimensionless groups

$C_{()}$	force coefficient	$2()/\rho A_p U^2$
Fr	Froude number	$U/\sqrt{lg}$
Re	Reynolds number	Ul/ν
St	Strouhal number	fl/U

Abbreviations and acronyms

COV	Coefficient of Variance	
$ERGO$	Ethics and Research Governance Online	
$FINA$	Federation International de Natation	
FR	Flow Regime	
$LVDT$	Linear Varying Displacement Transformer	
MAD	Measure Active Drag	
$PISO$	Pressure Implicit Splitting of Operators	
PSD	Power Spectral Density	
$T°$	Temperature	$[degrees]$
UoS	University of Southampton	
$URANS$	Unsteady Reynolds Averaged Navier Stokes	
WSA	Wetted Surface Area	$[m^2]$

Dedicated to my beloved family.

"Look deep into nature, and then you will understand everything better."

by Albert Einstein

"Water is the driving force of all nature."

by Leonardo da Vinci

"Les poissons, les nageurs, les bateaux
Transforment l'eau.
L'eau est douce et ne bouge
Que pour ce qui la touche.

Le poisson avance
Comme un doigt dans un gant,
Le nageur danse lentement
Et la voile respire.

Mais l'eau douce bouge
Pour ce qui la touche,
Pour le poisson, pour le nageur, pour le bateau
Qu'elle porte
Et qu'elle emporte."

Poisson de Paul Eluard.

Part A

MOTIVATION

1 Introduction

In this chapter, the background and motivation for this Ph.D thesis are first presented. To carry out this thesis, the researcher is supported by both university and industry partners, whose relationships are explained. The basic rules of swimming as an Olympic sport are then introduced.

A major part of this chapter is devoted to the development of this research project with initial thoughts and observations shared. The associated challenges are exposed to define key research questions. The aims and objectives for this Ph.D. thesis are subsequently defined. Finally, the report layout is presented through a mind map and described to facilitate the reader's experience.

1.1 Background

In his paper entitled 'The need for speed: how high-technology swimsuits changed the sport of swimming', Meyer (2013) describes competitive swimming as follows:

> From the outside looking in, you can't understand it; from the inside looking out, you can't explain it. For most people, competitive swimming is a novelty sport, usually watched only during the summer Olympics. However, for competitive swimmers, the year-round sport is best characterized as a 'love-hate' relationship.

Swimming, as a world-class and Olympic sport, is indeed a complex sport which requires lots of training and winning a race depends on a fraction of a second. Swimming racing times are typically measured to the nearest 0.01s, and in a final race, the top eight swimmers have swimming times within 0.5 s (male 50-m freestyle, Olympic Games 2012). Hence, any small performance gains can make a difference between a Gold medal and a 4th place.

In 2008, Speedo launched the LZR Racer suit (Figure 1.1). This full-body length suit provided better oxygen flow to the muscles and a more hydrodynamic position of the body. With the use of ultrasonically bonded seams, skin friction was reduced by 24% compared to the previous Fastskin Speedo suit (Jones, 2011). As of the 2009 World Aquatics Championships, 93 world records had been broken by swimmers wearing the LZR Racer suit (Thurow and Rhoads, 2008).

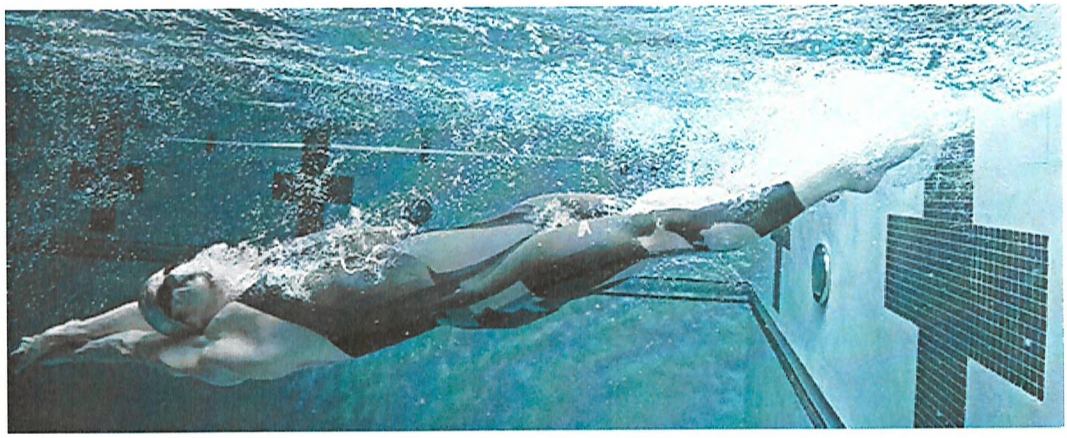

FIGURE 1.1: Speedo LZR Racer suit worn by Olympic swimmer Michael Phelps who supported the development of this swimsuit. Credit: Speedo.

After the 13^{th} World Championships, the Federation Internationale de Natation (FINA) recalled *'the main and core principle that swimming is a sport essentially based on the physical performance of the athlete.'* Following this declaration, FINA decided to ban the LZR Racer suit and restricted suit length from waist to knee for men and shoulders to knee excluding the neck for women. Since then, scientific research in swimming has been more active than ever with the aim of setting up new world records.

Over the 2008-2012 period, UK Sport, British swimming and Speedo partnered with the Performance Sports Engineering Laboratory at the University of Southampton in preparation to the London Olympic Games. The program entitled *SwimSIM* was aimed at improving the performances of British Swimming elite swimmers. Three PhD students, now Dr. Joe Banks, Dr. Chris Philipps and Dr. Angus Webb, worked as a team under the supervision of Prof. Stephen Turnock, Prof. Dominic Hudson, Dr. Dominic Taunton and Dr. Alex Forrester, to develop specific testing systems. These were designed to measure a wide range of measurements such as force, speed and body

kinematics, all synchronised with video footage. These tools provided detailed feedback to the elite athletes and their coaches to make decisions on stroke technique alterations and swimming equipment selection. Furthermore, fundamental research was undertaken with the use of computational fluid dynamics, musculo-skeletal models and race time simulations.

This research program identified the need to better understand the flow physics around a swimmer. A new cycle of research and innovation was initiated for the run-up to the Rio 2016 Olympic Games. Innovative ways to improve elite swimmers' technique and equipment, using experimental tests, numerical models and data analyses, were considered due to fierce worldwide competition.

1.2 PhD partners, from engineers to swimmers

Following the success of the 2008-2012 *SwimSIM* program, two PhD students, Marion James and Scott Michaels, started in October 2012 to further develop the swimming research towards Rio 2016 Olympic Games. The same supervisory team was kept and the first three PhD students on the *SwimSIM* program carried on with part-time post-doc positions with the English Institute of Sport. The researcher for this PhD project thus benefited from a large support team at the University of Southampton. The support included:

- Assistance with running pool and tank testing sessions (i.e. a minimum of 3 or 4 people is required to run all the equipment and to take care of the athlete. Also for safety reason, the researcher cannot be by herself in the testing facilities.);
- A CFD test case to simulate the flow past a swimmer located at the free surface;
- The design and build of the mannequin and its dynamometer frame.

In addition, assistance was provided to make the two sphere models.

The research is sponsored by the Engineering and Physical Sciences Research Council (EPSRC), the English Institute of Sport and Speedo. The researcher is working closely with the other university researchers in the Performance Sport Engineering Laboratory, British Swimming athletes with their coaching team, and Speedo Aqualab. In addition, since 2015, the researcher started working with Dr. Carl Payton from Manchester Metropolitan University to support Para-Swimming athletes.

Acknowledging the help stated above, the author certifies being the only contributor to all the analyses run throughout this thesis.

1.3 Swimming, an Olympic sport

1.3.1 Swimming races

Swimming is a water-based sport practised individually or as a team and revolves around four main strokes: freestyle, backstroke, breaststroke, and butterfly. Figure 1.2 illustrate the key position for each stroke (Olympic Committee, 2016). An in-depth description of the different swimming styles is provided in Maglischo (2003).

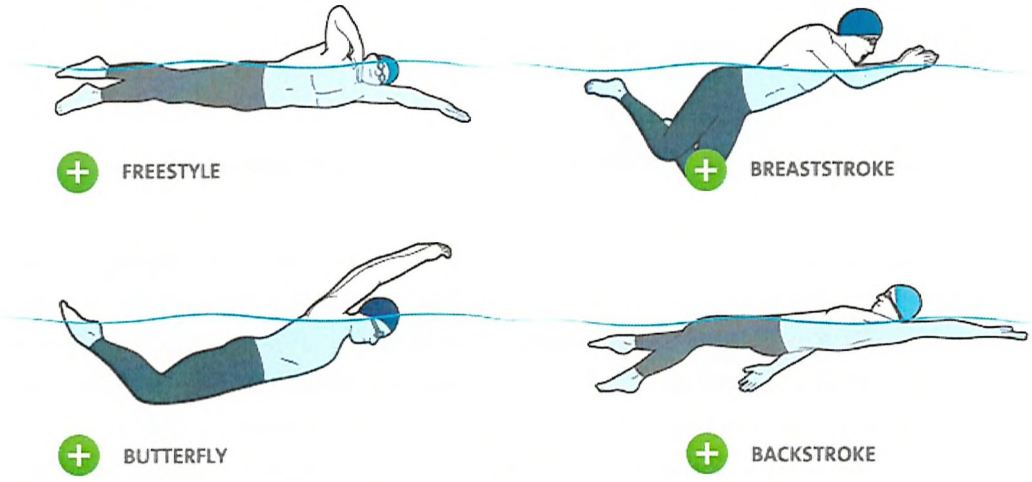

FIGURE 1.2: Ilustration of the four main swimming styles provided by the Olympic Committee (2016).

The Federation Internationale de Natation (FINA) was founded in 1908 to act as the international governing body for swimming competitions. They organise international-level swimming events both in pool and open-water environments (ocean, sea, lake, river, etc.).

In competitive pool swimming, there are two types of course: Short-Course (SC) in 25-m pool and Long-Course (LC) in 50-m pool. The Olympic Games are set in a 50-m pool, while other major international events such as the World and European Championships can be organised in both short-course and long-course. During a short-course event, the swimmer turns more often creating a different race dynamic compared to a long-course race, hence world records are always set with reference to the course type. The key phases in a swimming race are:

1. Start (dive-start or backstroke start)
2. Underwater swim (following the start and after each turn)
3. Surface swim

4. Turn
5. Finish

In addition to the two course types, swimming is also characterised by a large number of events ranging from 50 m sprint to 1500 m endurance races. Depending on the race distance, phases 2 - 4 are repeated.

1.3.2 Swimming equipment

Elite swimmers wear three main types of equipment during a race: a suit, a cap and goggles (Figure 1.3). The design and manufacture of these swimming equipment are governed by FINA (2014) where all the detailed rules may be found.

(a) For pool competitions (b) For open-water competitions

FIGURE 1.3: Typical equipment worn by elite male and female swimmers.

No swimmer shall be permitted to use or wear any device, which may be an aid to their speed, endurance or buoyancy. Only a nose clip and earplugs may be used in addition to the suit, cap and goggles.

In a pool environment, the key rules for suit design currently states that: 'Men's swimsuits shall not extend above the navel or below the knee. Women's swimsuits shall not cover the neck, extend past the shoulders, or below the knee.' In open-water competitions, both men and women 'shall not cover the neck, extend past the shoulder, or extend below the ankle'. Manufacturers are now offering the options to use opened- or closed- back suits for women. All suits are to be made out of textile fabrics, must be soft folding and are not allowed to provide additonal buoyancy greater than 0.5 N.

Caps and goggles must be two separate items. Elite swimmers typically wear two caps with the goggles placed after the first cap to secure the goggles and to avoid the goggles' strap flapping around. The maximum thickness of the cap must be lower or equal to 2 mm, and the material may have some rigidity but must still follow the natural shape of the head. Different materials and thicknesses may be used on the same cap as long as they do not create additional artificial shaping on the outer surface of the cap.

The goggles' prime function is to protect the swimmer's eyes from the water and to ensure good visibility. Any additional hydrodynamic shapes which do not fulfill these functions are not accepted.

1.4 Development of the research project

1.4.1 Initial observations and thoughts

As identified in the opening background (Section 1.1), there is a need to better understand the flow physics around a swimmer's body in order to improve technique and equipment. Since the head is the swimmer's leading edge, it is thought to potentially have a large impact on the total resistance of a swimmer.

Initial visual observations of the flow past swimmers' heads have emphasised different types of bow waves (Figure 1.4), revealing the existence of multiple flow regimes experienced by a swimmer as speed and body position fluctuate. The surface speed of a competitive freestyle swimmer is around 2.0 $m.s^{-1}$, while underwater speeds of up to 3.1 $m.s^{-1}$ were recorded (Zaidi, 2008). For a breaststroker, the swimming speed varies significantly depending on the stroke phase (limb recovery/propulsion), between 0.5 and 2.0 $m.s^{-1}$.

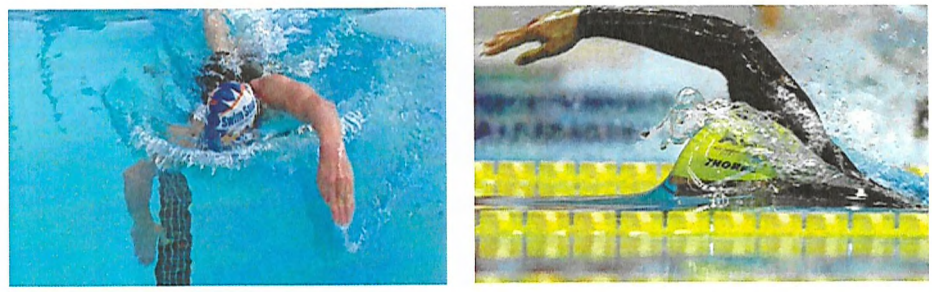

(a) Large breaking wave ahead (b) Smoother wave on head, breaking on top only

FIGURE 1.4: An initial observation of different flow regimes experienced by swimmers around their head.

The flow regime encountered by a swimmer can be characterised by two non-dimensional parameters, Reynold number, Re, and Froude number, Fr. They are both related to the

body speed, U, and characteristic length, l. Reynolds number corresponds to the ratio between the inertial and viscous forces, and thus characterises the development of the boundary layer flow in a single fluid (Equation 1.1). Froude number is the ratio of the inertial to gravity forces and therefore describes the free surface deformation (Equation 1.2).

$$Re = \frac{\rho U l}{\mu} = \frac{U l}{\nu} \tag{1.1}$$

$$Fr = \frac{U}{\sqrt{lg}} \tag{1.2}$$

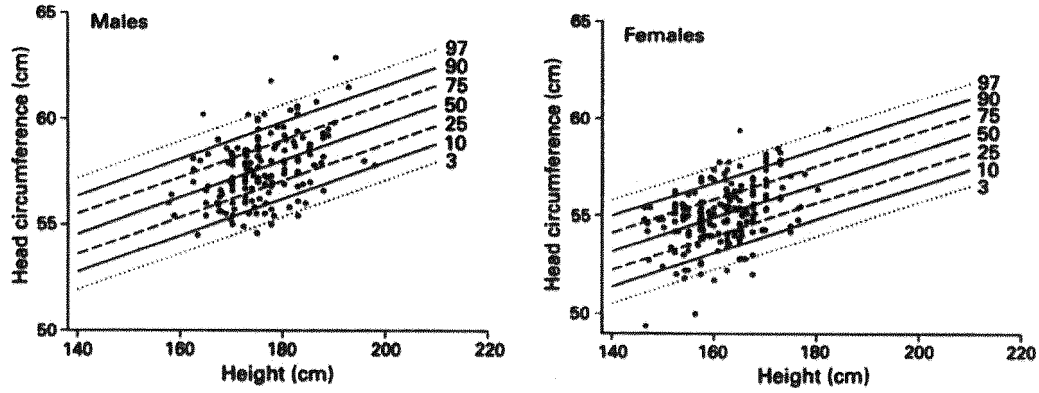

(a) Head circumference plotted against height in 159 adult males. The line describing the mean of the distribution is 42.4+0.08673xheight (Bushby et al., 1992)

(b) Head circumference plotted against height in 195 adult females. The line describing the mean of the distribution is 41.02+0.08673xheight (Bushby et al., 1992)

FIGURE 1.5: Empirical formulae derived by Bushby et al. (1992) to determine the head circumference of male and female as a function of their height.

Bushby et al. (1992) derived an empirical formula to determine the head circumference of both male and female based on their height as shown in Figure 1.5. Considering an average male height of 1.80 m and female height of 1.70 m, their average head diameters are 18.5 cm and 17.7 cm respectively. Assuming an average swimmer's head diameter of 18 cm and a fresh water kinematic viscosity, ν, of 0.84 $\times 10^{-6}$ $m^2.s^{-1}$ for a typical swimming pool water temperature of 28° (Newman, 1977), the local head Reynolds number and Froude number are derived for a range of speeds in Table 1.1. In addition, the non-dimensional parameters for a swimmer's height of 1.80 m are given.

TABLE 1.1: Froude number, Fr, and Reynolds number, Re, defined for the head only and for the total body length.

	Head D = 0.18 m		Swimmer L = 1.80 m	
Speed $[m.s^{-1}]$	Fr	Re	Fr	Re
0.5	0.4	1.1×10^5	0.1	1.2×10^6
2.0	1.5	4.3×10^5	0.5	4.8×10^6
3.1	-	6.6×10^5	-	7.4×10^6

When considering the local Reynolds and Froude numbers around a swimmer's head, it may be noticed that over a certain speed range, a swimmer's head undergoes two critical flow regimes. A swimmer's head can be associated to a sphere. Interestingly, Hoerner (1965) showed that, for a sphere, the laminar boundary layer undergoes a transition to become fully-turbulent for $10^5 \leq Re \leq 10^6$. On the other hand, the head of a swimmer also encounters a change of flow regime associated with the development of the bow wave as observed in Figure 1.4. This phenomenon may be linked to the critical Froude number of 1.0 in a similar manner to the classic hydraulic jump problem (Hervouet, 2007). Another limitation is associated to Froude number based on the swimmer's length. When $Fr \sim 0.5$, the swimmer reaches a maximum speed as his/her length is equal to the wave length created. The swimmer may not have the physical ability to overcome the bow wave he or she is sitting behind.

Mollendorf et al. (2004) modelled a swimmer by a sphere and circular cylinders. Since the boundary layers are assumed to be thin enough compared to the radii, he used the flat plate boundary layer theory to characterise the flow along the length of a swimmer. He stated that the critical Reynolds number was $\sim 5 \times 10^5$ and thus observed that the laminar-to-turbulent transition would occur near the maximal diameter of the head. He mentioned that the head is therefore an interesting area to reduce drag as the boundary layer could be tripped early to maintain the flow attached. However, he did not comment any further on what kind of drag reduction could be expected.

1.4.2 Challenges: from a swimmer's head to a sphere

The head of a swimmer is a bluff body with a complex geometry. Before studying the flow past a swimmer's head, it is thus best to simplify the problem to a sphere as suggested by Mollendorf et al. (2004). A literature review of the flow past a sphere was undertaken to gain a better understanding of the challenges involved for a bluff body in this Reynolds number range.

Drag crisis experienced by bluff bodies at the critical Re The flow past a submerged sphere has been studied since the early 20^{th} century in wind tunnels and water channels using both qualitative flow visualisation techniques and quantitative measurements. Research on the variation of the wake structure with diameter based Reynolds number indicates that below Reynolds number of 20, the flow is fully attached (Taneda, 1956). When $Re \simeq 24$, laminar flow separation occurs and stationary axi-symmetric rings are generated up to $Re \simeq 210$ (Taneda (1956), Achenbach (1974*a*)). The vortex rings begin to oscillate around $Re \simeq 270$ and horse-shoe shaped vortex loops are shed behind the sphere, leading to an unstable non-axi-symmetric wake (Achenbach, 1974*a*). The vortex loops diffuse rapidly and the wake flow becomes turbulent at $Re \simeq 800$.

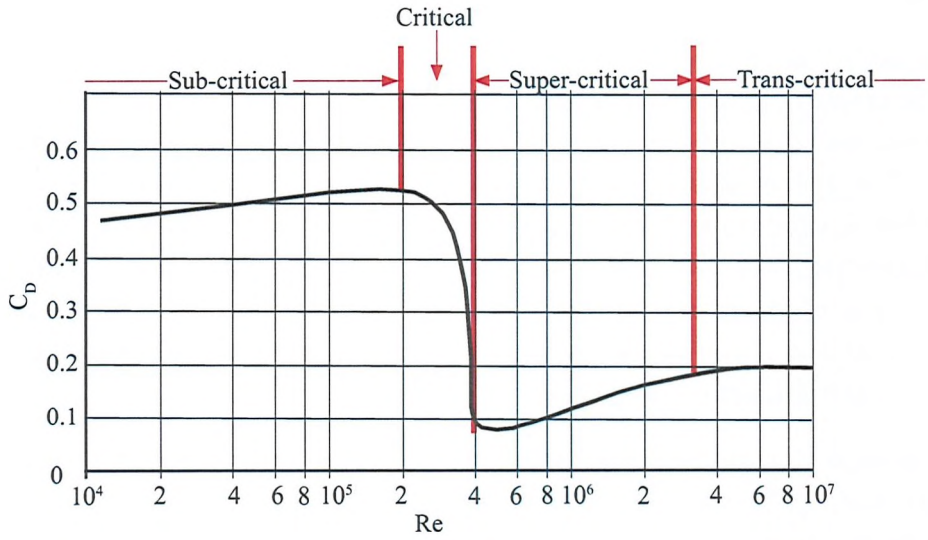

FIGURE 1.6: An observation of the four flow regimes. Figure modified from (Achenbach, 1972).

The turbulent region was studied by Achenbach (1972), who classified the different flow types observed into: sub-critical ($Re \leq 2 \times 10^5$), critical ($2 \times 10^5 \leq Re \leq 4 \times 10^5$), super-critical ($4 \times 10^5 \leq Re \leq 10^6$) and trans-critical ($Re \geq 10^6$). Using a surface oil flow visualisation technique, Taneda (1978) observed that the laminar boundary layer separates at an angle $\phi_S = 80°$ from the front stagnation point for $10^4 \leq Re \leq 3 \times 10^5$. Over the same experiment, Taneda (1978) used smoke to study the wake structure. At sub-critical Reynolds numbers, he characterised the near-wake as a large recirculating region with a progressive periodic motion of wave length $\lambda = 4.5D$ and velocity $\simeq 0.9U$ and a constant Strouhal number of about 0.2, emphasising the strong periodicity of the rolled-up vortices. In addition, he observed an irregular rotation of the separation point. This random process was later explained by Kim and Durbin (1988), Sakamoto and Haniu (1990), Bakic and Peric (2005), Bakic et al. (2006) and Ozgoren et al. (2011). Indeed, besides the low-frequency mode of Strouhal number due

to the large-scale instabilities of the turbulent wake behind the sphere, a co-existing high-frequency mode was identified due to periodic fluctuations of the shear layer.

As Reynolds number increases further ($Re \simeq 3.5 \times 10^5$), Taneda (1978) observed a sudden change in the skin friction distribution on the downstream half of the sphere. The laminar boundary layer separation point moved to $\phi_S = 100°$ on average. Moreover two other separation lines appeared further downstream indicating the presence of a separation bubble containing a vortex ring. The flow reattached at $\phi_S = 117°$ (re-attachment line) and separated again at $\phi_S = 135°$ (turbulent separation line). At the rear of the sphere, an Ω-shaped line was observed due to the re-attachment of all the streamlines. Hair-pin vortices are shed at the rear of the sphere in an asymmetric manner (Kiya et al., 2000).

Quantitative measurements gathered by Hoerner (1965) and Achenbach (1972) have shown that the drag coefficient has a fairly constant value of 0.47 at sub-critical Reynolds numbers, but undergoes a sharp decrease down to 0.1 in the critical Reynolds number range. This phenomenon is well known under the name of 'drag crisis'. Due to the high turbulent mixing, the turbulent boundary layer has a higher momentum near the wall and is therefore better able to withstand the adverse pressure gradient at the rear of the sphere. Hence, the separated region gets smaller with higher pressure levels in the near wall downstream of the sphere, leading to a decrease in the pressure differential between the front and the rear of the sphere.

As Reynolds number increases further, the turbulent structures in the mixing layer become finer. The separated shear layer loses momentum and thus separates earlier, resulting in an increase in drag coefficient (Bakic and Peric, 2005). In this super-critical Reynolds number region, the wake flow was found to be fully turbulent with an offset from the streamwise axis (Taneda, 1978).

Free surface deformation Although in-depth research was carried out for the flow past a sphere in a single-phase flow (air or water), reported results for experiments including a free surface remain rare. The influence of the free surface on a submerged sphere travelling at a speed equivalent to Reynolds number 5000 was studied both experimentally and numerically by Hassanzadeh et al. (2012), Ozgoren et al. (2012) and Ozgoren et al. (2013). For small immersion depths, Hassanzadeh et al. (2012) showed that the recirculating region in the half-lower side of the wake region is larger compared to the half-upper side. Furthermore, a strong interaction between the fluctuated streamwise and transverse velocities in the half-lower side of the wake region was observed leading to a higher mixing flow rate. At an immersed depth to diameter ratio of 0.25 (from the top side of the sphere), a strong interference between the sphere wake and the free surface was noticed by Ozgoren et al. (2013).

Despite the absence of published research on the effects of the free surface on the flow past a sphere, other bluff bodies located at the free surface such as cylinders have been studied. Yu et al. (2008) performed large-eddy simulations of the flow past a surface-piercing cylinder. The free surface was found to inhibit the vortex generation in the near wake. At $Fr \simeq 0.8$, the flow exhibits 2-D vortex structures in the deep wake, whereas nearer to the free surface 3-D vortex structures are observed. The intensity of the vortices shed decreases further as Froude number increases. At a higher Reynolds number $\simeq 1.0 \times 10^5$, the free surface effects on the vortex structures in the near wake become less significant and the wake features a flow similar to a 2-D flow without a free surface. The flow past bluff bodies located at the free surface is therefore strongly related to both Reynolds number and Froude number.

1.4.3 Research questions

The drag crisis identified by Hoerner (1965) in the case of a sphere in a single phase flow occurs over the range of the local Reynolds number for a swimmer's head, which is of great interest to swimmers. Important free gains (from a swimming effort point of view) might be achieved through the use of passive flow control techniques such as different cap surface roughness, various goggles designs, different hair management types under a cap or by adopting a different head position. However, there exists a strong interaction between the free surface and the wake behind the bluff body, which is likely to impact the drag crisis.

Several research questions have thus emerged:

- How can a better understanding of the flow physics around a swimmer be gained without the involvement of elite swimmers? Could numerical simulations or towing tank tests be used instead?
- Does a swimmer's head located at the free surface undergo a drag crisis over the elite swimmer speed range?
- Can elite swimmers benefit from swimming over this transitional flow regime to improve their performance?
- How should swimming equipment be selected to ensure best performance?

1.5 Aim and objectives

As a research group, the main goal of this project is to improve British Swimming elite swimmers' performances for the next Rio 2016 Olympic Games.

This Ph.D. thesis is primarily aimed at investigating the passive flow physics (no arm/no leg movements) around a swimmer's body at the free surface, with a particular focus on the head, in order to determine how to better select equipment for improved swimming performance. Passive swimming only is considered to reduce the complexity and eliminate the influence of technique on the equipment selection. This research project combines testing athletes in a swimming pool, numerical simulations and experimental work in a towing tank environment.

In order to achieve this aim, a set of objectives has been defined:

- To perform a series of testing sessions in a swimming pool environment to gain a better insight into the different resistance components of a swimmer and to evaluate the impact of equipment on a swimmer's resistance.
- To simulate the flow characteristics past a swimmer's body located at the free surface using two numerical methods: 2-D linear potential flow theory (Thinship) and 3-D Unsteady Reynolds-Averaged Navier-Stokes (URANS) computational fluid dynamics simulations to allow future parametric studies to be run without the involvement of elite swimmers.
- To develop a methodology in a controlled towing tank environment to study a swimmer's resistance and the influence of equipment and body position. A progressive approach is to be used by first towing a sphere, followed by a head and a mannequin, all at the free surface over the elite swimmer speed range.
- To research the influence of realistic flow control devices to reduce the swimmer's total resistance through the water.

Although several pool testing sessions were devoted to the assessment of technique and suit testing for both British Swimming and Speedo, focus is maintained on the flow past a swimmer's head in this Ph.D. thesis.

1.6 Novelty

In this research project, the novelty arose from:

1. The establishment of a flow taxonomy for a surface-piercing sphere undergoing a drag crisis over the critical *Re-Fr* range, $8 \times 10^4 \leq Re \leq 6 \times 10^5$ and $0.4 \leq Fr \leq 2.9$ (including the elite swimmer speed range);
2. The development of an experimental methodology in a towing tank environment decomposing the flow characteristics past a swimmer starting with a sphere, followed by a head and a mannequin, before going back to a real swimmer. This

build-up of complexity while increasing reality provides insight into how to best select swimming equipment;

3. The first developmental tests of a potential natural flow control device, using hair management into a bun-shape at the top of the head, to reduce a swimmer's resistance.

1.7 Publications

James, M. C., Turnock, S. R., Hudson, D. A. (2012) Design of retrofit devices using CFD, validated with wind tunnel tests, Numerical Towing Tank Symposium, Cortona, Italy.

James, M. C., Turnock, S. R., Hudson, D. A. (2013) Flow past a sphere at the free surface using URANS, Numerical Towing Tank Symposium, Germany, Mulheim.

James, M. C., Lloyd, T. P. (2013) Large eddy simulations of circular cylinders at a range of Reynolds numbers, Proceedings of ITTC Workshop on Wave Run-Up and Vortex Shedding, France, Nantes.

Banks, J., James, M., Hudson, D., Taunton, D. and Turnock, S. (2014), An analysis of a swimmer' s passive wave resistance using experimental data and CFD simulations, in 'Biomechanics and Medicine in Swimming XII', Canberra.

James, M. C., Forester, A., Hudson, D. A., Taunton, D.J. and Stephen, R. (2015), Experimental study of the transitional flow of a sphere located at the free surface, in 'Proceedings of the 9th International Workshop on Ship and Marine Hydrodynamics', Glasgow.

Lloyd, T. P. and James, M. (2015), Large eddy simulations of a circular cylinder at Reynolds numbers surrounding the drag crisis, Applied Ocean Research (November).

James, M. C., Hudson, D. A., Taunton, D. J. and Stephen, R. (2017), Flow taxonomy of a surface-piercing sphere over the transitional Fr-Re range (to be submitted - journal paper to be determined).

1.8 Report layout

This PhD thesis has been divided into four key parts as indicated in Figure 1.7. Part A introduces the motivation for this research project, followed by the methods in Part B, the studies in Part C and finally the epilogue in Part D.

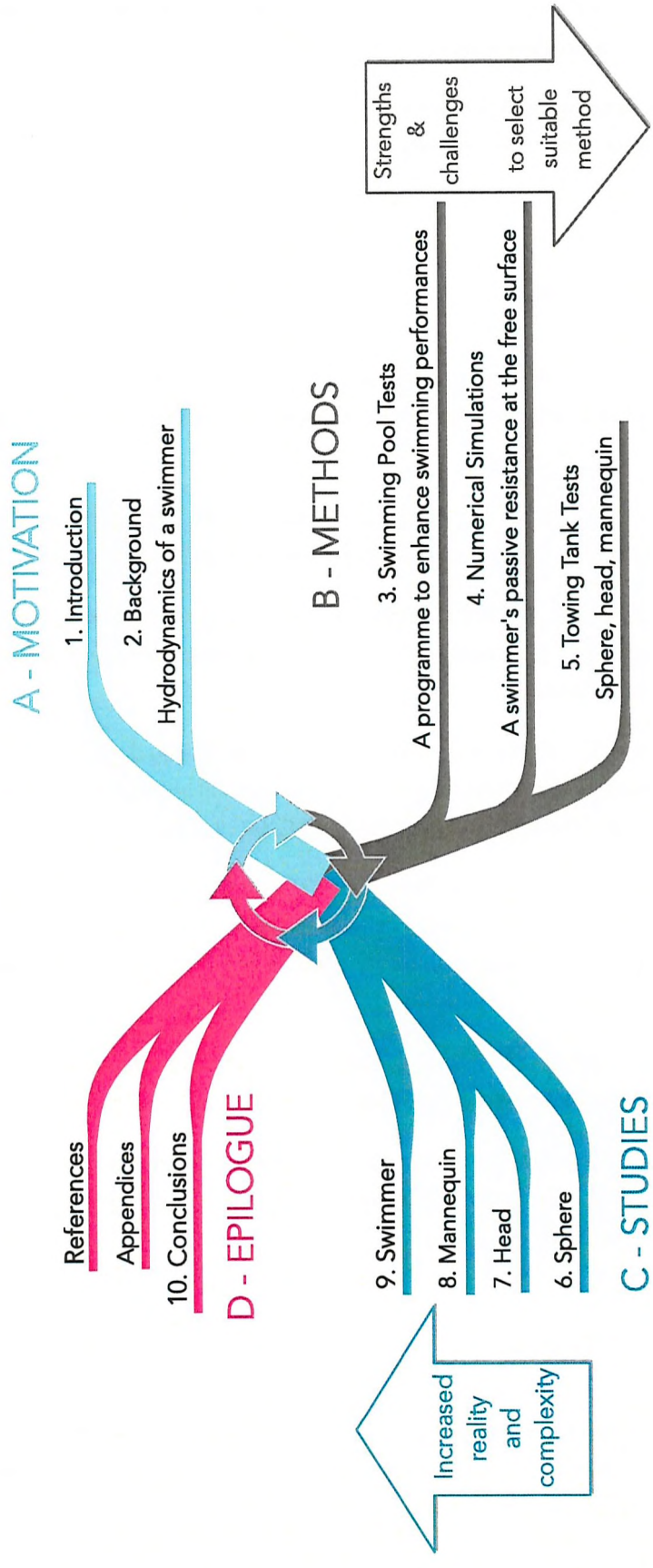

FIGURE 1.7: Ph.D. thesis mind map divided into four key parts : A - Motivation, B - Methods, C - Studies, D - Epilogue.

In Part A, the motivation is set through an introduction chapter which presented the recent background for this research project, the sport of swimming, the key research questions and the associated challenges leading to the aims and objectives. To better prepare the reader, the novel contributions that arose from this research project have been listed in addition to this report layout. In Chapter 2, background on the hydrodynamics of a swimmer and the research done-to-date on swimming equipment and head position are presented so that all partners, whether from the sport of swimming or from engineering, can understand the work developed through this thesis.

In Part B, the strength and challenges of the various methods that can be used to study the flow physics around a swimmer are explored. Details on the organisation and testing systems used to assess a swimmer's performance in a swimming pool environment are introduced in Chapter 3. A case study ends this chapter to highlight the swimmer's lack of consistency when assessing the drag difference between various equipment. In addition to being variable, swimmers are also difficult to take out of their intense training environment, hence the need to move to a more controlled environment. First, in Chapter 4, numerical simulations are considered with the case of a swimmer being passively towed at the free surface. A breakdown of the different forces is considered with the total resistance and skin friction drag extracted from 3-D URANS simulations, while wave resistance is obtained from a 2-D potential flow code. Simulations of the free surface with breaking waves remain too challenging considering the available computational power, hence the decision to go down the route of experimental tank testing. In Chapter 5, the models and testing apparatus are described.

The core of this research forms Part C, which includes four studies on the flow past: a sphere (Chapter 6), a head (Chapter 7), a mannequin (Chapter 8) and a swimmer (Chapter 9). They are presented in increasing order of complexity with the aim of breaking down the challenges associated with the flow physics around a swimmer. As the level of complexity increases, each study becomes closer to the real case of a human swimmer. Throughout these studies, the effect of head position, goggles, caps and hair styles on swimming performances are investigated.

In the epilogue, Part D, the outcome for each technique/equipment are summarised under separate sections alongside recommendations for further work (Chapter 10). Additional information to support Chapters 3 and 6 are found in the Appendices.

NB: Throughout this report, both terms *resistance* and *drag* have the same meaning.

2

Background
Hydrodynamics of a swimmer

This chapter is aimed at providing a review in the field of the hydrodynamics of a swimmer, with a particular focus on drag and swimming equipment.

In this background chapter, terminologies from both the sport of swimming and naval architecture principles are mixed to ensure that all partners benefit from a good comprehension of this Ph.D. thesis. After emphasising the analogy between a swimmer and a ship, this literature review introduces the various components of a swimmer's resistance based on the traditional naval architecture approach. First, experimental methodologies to measure a swimmer's passive resistance are explained and the more complex active swimming case follows. Initial numerical simulations performed to-date are then summarised although less insight into a swimmer's resistance has been provided through these due to computational power limitations. Finally, the research done into high-performance swimming equipment is highlighted in a stand-alone section, and ends with initial research done on the influence of head position.

2.1 General hydrodynamics of a swimmer

A plethora of sports science books, scientific papers and amateur's blog articles are available to explain the hydrodynamics of a swimmer. A general review shows a great

deal of controversy historically and still nowadays, which highlights how complex the subject is.

Starting from the basics, considering the direction of motion only, as a swimmer moves through the water, there are two key forces opposing each other, namely the propulsion force, $\vec{F_P}$, and the drag force, $\vec{F_D}$. Newton's second law therefore states that:

$$\vec{F_P} + \vec{F_D} = (M + m) * \vec{a} \tag{2.1}$$

where M and m are the swimmer's mass and added-mass respectively, and $\vec{a}$ his/her acceleration vector.

At constant speed, the propulsion force is equal to the drag force. The propulsion force comes from the arms and legs movement propelling the swimmer in the direction of motion, whereas the drag force impedes the swimmer's motion. Consequently, for the swimmer to accelerate, an increase in propulsion force or a decrease in drag is required.

In a review of the forces involved in competitive swimming, Rushall et al. (1994) concluded that although the production of force is important, it is also associated with a much greater increase in drag in comparison with the change in speed due to propulsive forces. It is thus recommended to focus on reducing drag in the first instance, and then develop a stronger propulsion force as long as positions for minimal resistance are maintained. Sanders et al. (2001) also suggested that swimming performance may be best enhanced by slightly adjusting a stroke technique to reduce drag, rather than by chasing improvement in the propulsive force.

The remaining part of this background chapter will thus be devoted to the drag force, also known as resistive force or resistance. For the interested reader, further information related to the propulsion force may be found in Toussaint et al. (2000).

2.2 The drag force breakdown

2.2.1 Analogy between a swimmer and a ship

A swimmer can in many ways be associated to a ship travelling through the water. Both resistance and propulsion components are to be taken into account when considering the speed at which a swimmer or a ship will travel through the water (Larsen, 1981).

A wave pattern is created from both solid bodies when going through the calm water free surface and typical features such as the bow wave can be identified from both a swimmer's head and a ship's bow (Vennell et al., 2006). Figure 2.1 highlights the similarities coming from the diverging wave system and the turbulent wake when a swimmer is being passively pulled at the free surface. The propulsion due to a swimmer's

arms can be modelled in a similar way as for a propeller when doing computational fluid dynamics simulations, as emphasised by Banks (2013). The set of skills developed by naval architects to improve ships' performance can therefore be utilised to get a better understanding of the flow around a swimmer's body and her/his propulsive efficiency.

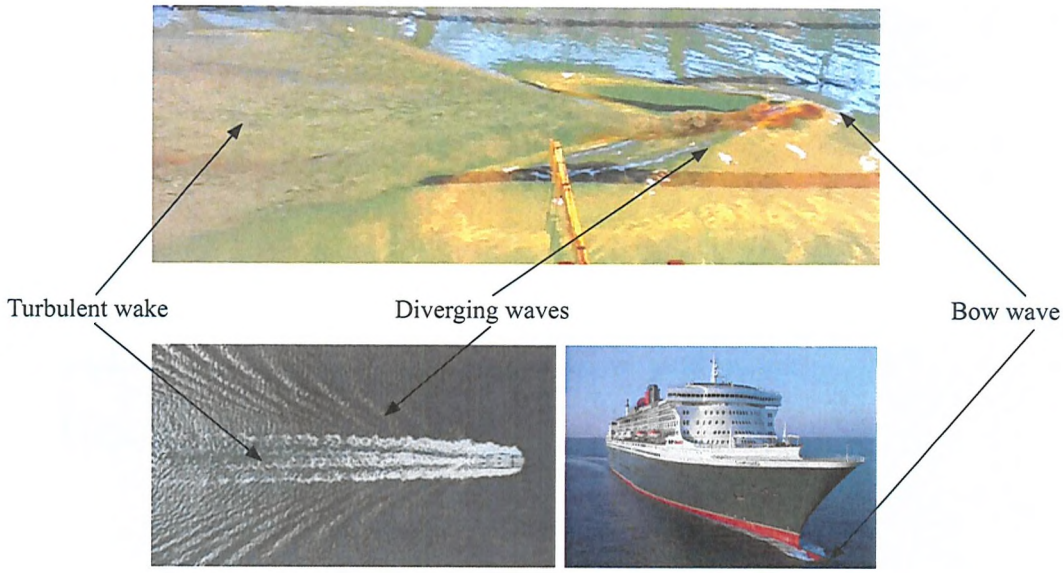

FIGURE 2.1: An observation of the wave pattern similarities between a swimmer and a ship. Top: swimmer being passively towed at the University of Southampton pool (28/01/2013). Bottom-left: aerial photograph of a powerboat's wave system (Newman, 1977). Bottom-right: Queen Mary II with surface-piercing bulbous bow, credit: Cunard.

The total resistance of a ship is typically measured at model scale in a towing tank and is then converted back to a full-scale resistance using Froude number scaling. In the case of a swimmer, resistance scaling is not necessary, so his or her total resistance can be directly evaluated using similar techniques as for model ships. Specific experimental methods to determine the total resistance of a swimmer are described in Section 2.3.

Molland et al. (2011) wrote a review of how naval architects consider the breakdown of the total resistance. Naval architects have long established that the total resistance of a ship's hull form could be either derived from an energy dissipation perspective (Figure B.3(a)) or by directly considering the forces acting on the hull (Figure B.3(b)). When travelling through the water, a ship creates a wave pattern which follows the hull form. In addition, a wake is generated behind the ship transom, resulting in energy losses. These two phenomena lead to the resistive force which can be analysed as the integration of the normal and tangential pressure forces over the hull's wetted surface area.

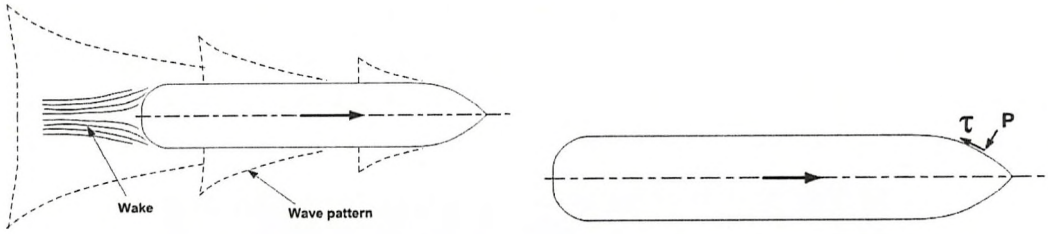

(a) Wave pattern and turbulent wake.

(b) Pressure and frictional forces.

FIGURE 2.2: Two approaches to explain the causes of a ship's resistance (Molland et al., 2011).

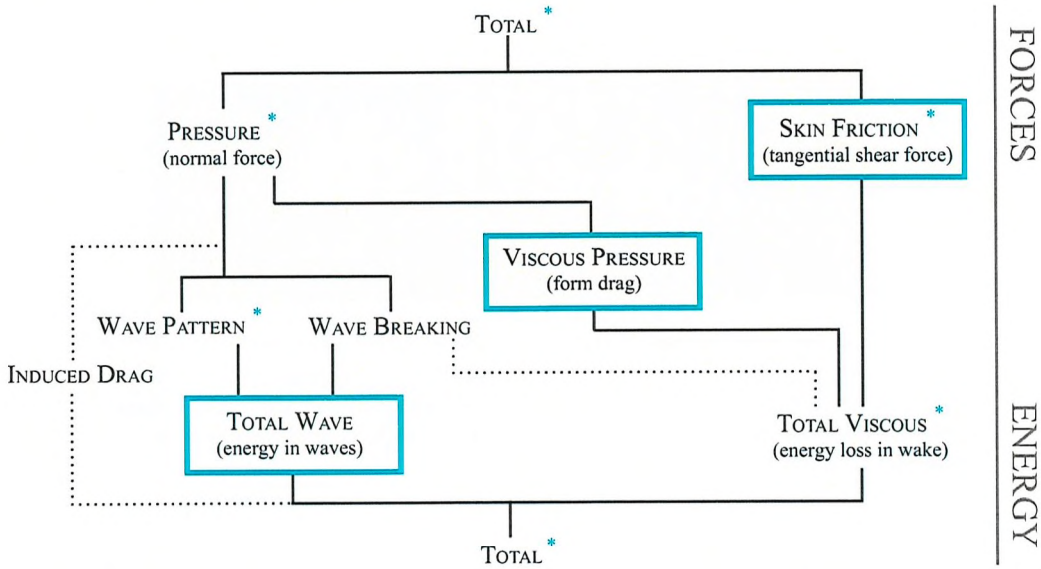

FIGURE 2.3: Detailed resistance components of a ship's hull form. The blue rectangular frames indicate the resistance components typically referred to when describing the resistance of a swimmer. * Resistance terms which can be determined experimentally. Adapted from Molland et al. (2011).

A detailed breakdown of the different resistance components of a ship's hull form is presented in Figure 2.3. The frictional resistance, also known as skin friction resistance or tangential shear force, arises from the fluid viscosity only, whereas the pressure force emerges from both viscous effects and hull wavemaking. In a viscous flow, the pressure differential between the bow and the aft of the ship forces the flow to separate. Since this component mainly depends on the variation of the cross-sectional area of a ship, it is also commonly referred to as form drag. Wave resistance comes from the required energy to create the transverse and dissipation wave systems as the ship breaks the undisturbed free surface. Induced drag is created from local geometrical changes, resulting in rapid pressure changes inducing vortices. It may be assumed that induced drag constitutes a less significant part of the total resistance. Consequently, naval architects often break down the total resistance of a ship as follows:

Total resistance = Frictional resistance
+ Viscous Pressure resistance
+ Wave resistance

Karpovich (1933) was the first one to use this breakdown when describing the resistance of a swimmer. However, for a long time, this delineation was not used much in the world of swimming. It was re-introduced by Sheehan and Laughrin (1992) who suggested to swimming coaches the direct implications of reducing each force component. Indeed coaches understand that frictional resistance can be reduced by shaving (Webb et al., 2014) or by wearing a suit that presents a low drag coefficient. Moreover, the form drag and wave drag can both be reduced by adopting a more streamline body position and by reducing any exagerated vertical or lateral movements.

A more detailed explanation of each term will be offered for the case of a swimmer in the following sections.

2.2.2 Frictional resistance

The frictional resistance or skin friction is due to the viscosity of the fluid. Friction effects were first investigated by Prandtl in 1904 during his experiments of a fluid past a flat plate (Vogel-Prandtl and Ram, 2004). The water particles in direct contact with the skin swirl violently in a tangle of microscopic eddy's and are reduced to zero velocity. This is the no-slip condition and thus there exists a boundary layer where the fluid velocity increases progressively to reach the free stream velocity (Figure 2.4).

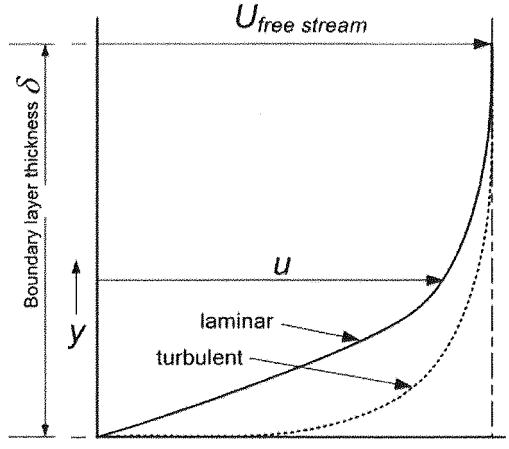

FIGURE 2.4: Boundary layer velocity profiles (Molland et al., 2011).

The velocity gradient between the boundary layer and the still water exerts a tangential shearing pressure on each surface of the swimmer's body and gives rise to the frictional resistance after integration over the entire surface of the swimmer (Clarys, 1979). The

wall shear stress can be evaluated with the use of a hot-film probe, a stanton tube or a preston tube and can thus be determined using Equation 2.2. These methods are not so practical for swimmers, thus the empirical ITTC 1957 formula (Equation 2.4, combined with Equation 2.5) is mostly used to determine the frictional in the world of swimming (Webb et al., 2011). The frictional drag varies linearly with speed and is a function of fluid viscosity, wetted surface area, flow regime and surface roughness (Rushall et al., 1994).

$$\tau_w = \mu * \frac{\partial u}{\partial y} \tag{2.2}$$

$$C_F = \frac{\tau_w}{\frac{1}{2}\rho U^2} \tag{2.3}$$

$$C_F = \frac{0.075}{(log_{10}(Re) - 2)^2} \tag{2.4}$$

$$R_{Frictional\ resistance} = \frac{1}{2}\rho * WSA * C_F \tag{2.5}$$

2.2.3 Viscous pressure resistance

Similarly to a ship, the viscous pressure resistance depends on the body shape, hence its other appellation: 'form drag'. Toussaint and Truijens (2005) explained how the inflow of a swimmer is generally ordered but it separates at a set point depending on the shape, size and speed of the swimmer. This so-called 'separation point' is due to the formation of an adverse pressure gradient in the boundary layer, resulting in vortices being shed away from the body. This results in a pressure differential between the front and rear of a swimmer. The form drag varies with speed as a quadratic relationship (Rushall et al., 1994). Moreover, he emphasised the necessity to minimise the body cross-sectional area by keeping the body streamlined at all times. Lyttle et al. (1998) mentioned that a swimmer's body shape is non-uniform. The complex geometry induces large pressure gradients and turbulent regions as the swimmer's body advances through the water. These pressure variations initiate vortices especially where the body shape changes suddenly (head, shoulder, elbow, hip, knee or feet).

No direct experimental techniques exist to determine the form drag. However, an empirical approach can be taken as suggested by Webb et al. (2011). The viscous pressure resistance can be assumed to be due to bluff body separation when considering a negligible boundary layer growth (Equation 2.6). The pressure drag coefficient, C_{D_p} can be chosen as 0.3 (equivalent as for an elliptical bluff body) and the projected area can be determined from a photograph of the swimmer.

$$R_{Viscous\ pressure\ resistance} = \frac{1}{2}\rho * A_p * C_{D_p} \tag{2.6}$$

2.2.4 Wave drag

Wave drag is due to the loss of energy from the kinetic energy created by the swimmer when changed into potential energy as waves are formed. Similarities between the wave pattern of a swimmer and a ship were observed in Figure 2.1. This type of wave pattern is often referred to as a 'Kelvin wave system', and is said to be formed due a travelling point disturbance on the water surface (Newman, 1977). This pattern may be observed for several objects (ship, swimmer, etc.). As long as the wave system is large enough compared to the object, then the object may be considered as a point source. Figure 2.5 shows the two primary types of waves which may be observed from an aerial point of view: diverging waves moving sidewards and transverse waves moving in the direction of motion (Larsson and Eliasson, 1994).

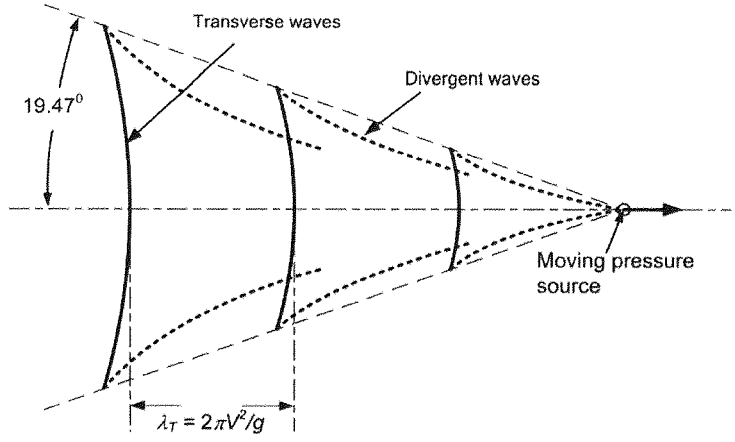

FIGURE 2.5: Kelvin wave pattern (Molland et al., 2011).

Although from far away all Kelvin wave patterns are similar, locally the wave pattern is strongly influenced by the object shape. Indeed, when taking the case of a ship, the bow and stern both represent high pressure regions, resulting in large disturbances of the calm free surface. These two wave systems interfere together as shown in Figure 2.6(a). There is indeed a strong relationship between wave length and hull speed. At a set speed, the bow wave will have its crest intersecting with the creation of the stern wave. Hence, larger waves are created, resulting in a hump in the drag curve (Figure 2.6(b)). On the other hand, when the bow wave trough intersects with the initiation of the stern wave, a lower amplitude wave is created; thus the observed hollow in the drag curve. Humps and hollows highly depend on both Froude number and the hull shape. The larger variation in curvature, the higher change in pressure along the hull. However,

Vennell et al. (2006) thought that it was unlikely that the complex body geometry of a swimmer would create such clear humps and hollows in its drag curve.

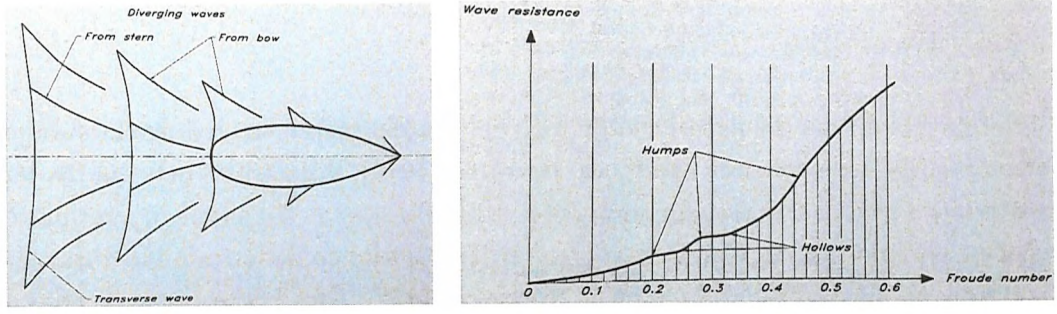

(a) Interference between bow and stern wave systems

(b) Wave resistance curve

FIGURE 2.6: As the bow and stern wave systems interfere, smaller or larger crests and trough appear resulting in humps and hollows in the wave resistance curve as speed increases (Larsson and Eliasson, 1994).

As the speed increases, the wave length increases until it reaches the swimmer's waterline-length (Newman, 1977) (Figure 2.7). This speed is commonly called the 'hull speed' in the naval architecture industry. Miller (1975) was the first to introduce this terminology into competitive swimming.

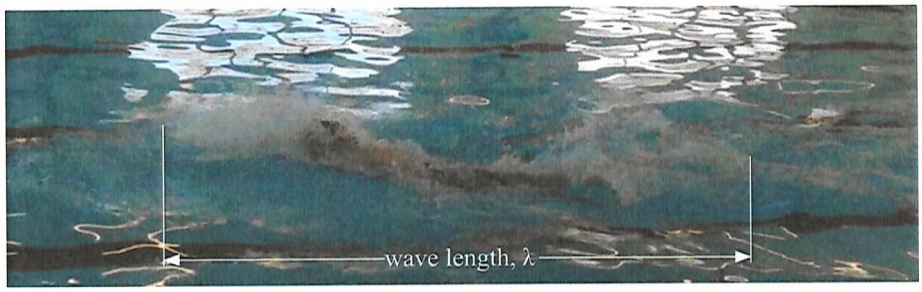

FIGURE 2.7: Wave length of a swimmer (Photo taken during a testing session in the Jubilee swimming pool at the University of Southampton).

Since the wave resistance of a swimmer was directly recorded during this project, a specific appendix detailing the background theory is included (Appendix B).

2.3 Experimental measurements in the world of swimming

An alternative way of decomposing the drag force is to consider passive and active drag. In passive mode, the resistance of a swimmer without any arm or leg movement is considered. According to Chatard et al. (1990), the passive resistance phase represents between 10 and 25% of the race course (starting glide and push-off turns) and up to

44% of the time when considering breaststroke. At a time where swimming races are being won by a fraction of a second, improvement in this passive swimming phase could change the race outcome.

In active mode, the arm/leg movements generating propulsion also create drag. Therefore, drag during locomotion is significantly higher than the drag measured by towing an object through the water (Pendergast et al., 2005).

Measurement techniques to assess both passive and active drag are introduced in the following sections.

2.3.1 With a mannequin

Only a few studies were found with the use of a mannequin to evaluate a swimmer's drag. Vennell et al. (2006) investigated the contribution of wave resistance to the total resistance by positioning a full-body mannequin in a flume both on the free surface and submerged. Bixler et al. (2007) studied the influence of wearing a suit with the same mannequin fully submerged. Chung and Nakashima (2013) developed a swimming humanoid robot with the objective of better understanding the flow physics associated with the propulsion phase for the different strokes, rather than to investigate the drag force of a swimmer.

2.3.2 Human passive swimming

Passive swimming has been investigated experimentally using towing systems such as the one developed by Lyttle et al. (1998) (Figure 2.8), Oh et al. (2013) and Webb (2013). The swimmer can be towed with arms by side with a belt under their arms or he/she can hold a handle with arms extended in front of the body.

Alternatively, passive swimming can be evaluated through the use of a velocimeter (also known as speed reel). During a push-off, the swimmer is attached around his/her waist with a belt and the swimmer's deceleration is recorded. A velocity-dependent drag coefficient can thus be obtained.

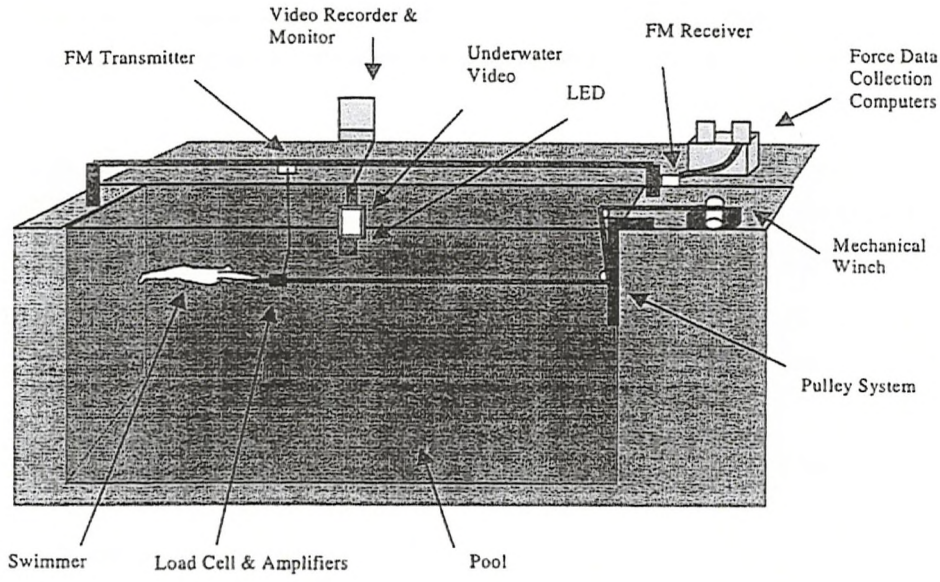

FIGURE 2.8: Set-up to measure passive drag (Lyttle et al., 1998).

2.3.3 Human active swimming

As the swimmer's arms and legs move through the water the place of the pressure points keep on changing resulting in an unsteady wave pattern. The Measure Active Drag (MAD) system was created by Hollander et al. (1986) to measure the force at each stroke cycle with the use of dynamo-metric blocs (Figure 2.9). This system has been actively used so far in the Netherlands ((Toussaint, Van den Berg and Beek, 2002), (Toussaint et al., 2004), (Toussaint and Truijens, 2005)).

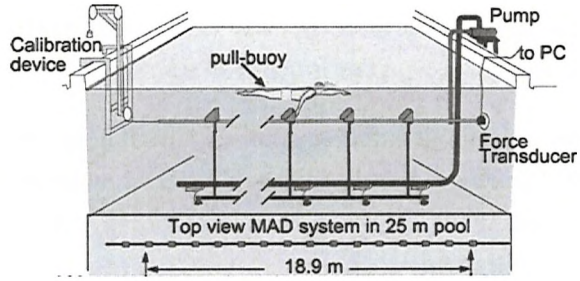

FIGURE 2.9: MAD system, measuring swimming active drag for each stroke cycle Toussaint and Truijens (2005).

Alternatively, swimmers can be towed on the free surface while actively swimming (Webb et al., 2011). Instead of holding a handle in the prone position, the swimmer is strapped with a belt around the torso so that the arm movements can be executed.

2.3.4 Review of specific studies

The use of such systems has allowed the swimming scientific community to investigate experimentally the various components of drag as previously identified for a ship. A few conclusions made from these experiments are now presented.

Friction drag Rushall et al. (1994) observed the flow past different types of swimmer's skin (Figure 2.10). Hairy skin or a rough suit creates large eddies absorbing energy, resulting in high frictional drag. Smooth skin with a hydrophobic surface repels the water away from the surface across a smaller shear-region, allowing for a decrease in frictional drag (Aljallis et al., 2013). Rushall et al. (1994) believes that by shaving and wearing a cap, the flow will stay laminar for longer around the body, allowing the swimmer to move through the water with less frictional drag. Indeed, by removing hair, the skin is smooth granulated allowing for a thin layer of water to adhere to the surface. The water is therefore not moving directly on the skin, but water on water, hence less friction. This was later confirmed by Webb (2013) who investigated the effect of shaving body hair on a male swimmer by doing both push-off glides and underwater passive tows. A 9.5% drag reduction was found in both cases, hence the importance of shaving hair for swimmers.

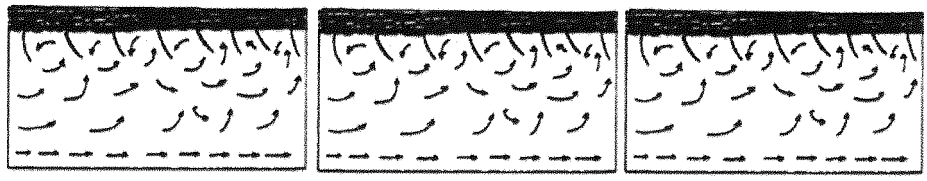

FIGURE 2.10: Observation of the flow between different surface smoothness (Rushall et al., 1994). From top to bottom: skin with hair, smooth skin but with hydrophobic surface, smooth granulated surface (i.e. shaved skin).

Form drag With the aim of reducing form drag, Clarys (1979), Lyttle et al. (1998) and Clothier (2004) investigated body position and body shape during a glide position. Clarys (1979) studied the difference between a usual glide position and a lateral glide. The drag was larger for the usual glide; however, for speeds over 1.8 $m.s^{-1}$, there was no influence in changing to a lateral glide. This was later confirmed by Lyttle et al. (1998).

Cortesi and Gatta (2015) measured a reduction of 17.6% in passive drag when towing swimmers underwater in the prone position with arms extended in front of the head in comparison with arms by side. The extension of the arms in front of the head increases the length of the body and offers a more streamline leading edge. Studies on the effect of suit compression on form drag will be later presented in Section 2.5.1.

Wave drag Wave drag increases as the swimmer is closer to the free surface and as speed increases. The influence of immersion depth on wave drag has been studied by Hertel (1966), Larsen (1981), Lyttle et al. (1998) and more recently by Vennell et al. (2006). All studies conducted were only considering changes in total drag with variation of the immersion depth. Maximum drag of a streamline object was observed by Hertel (1966) when the object was just under the free surface. The wave drag component goes to zero when the object is immersed by three diameters or more as shown in Figure 2.11.

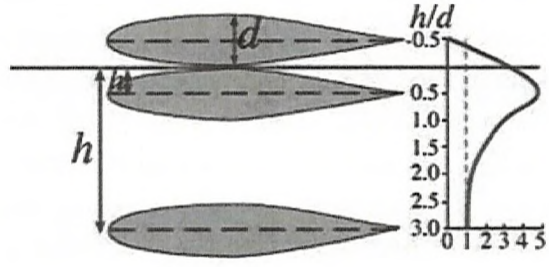

FIGURE 2.11: Influence of immersion depth with respect to object diameter (Hertel, 1966).

Vennell et al. (2006) recorded the drag on the mannequin at the free surface to be 2.4 times greater than when the mannequin was fully submerged. Passive wave drag contribution to the total drag was therefore considerably underestimated in the past, as Vennell et al. (2006) revealed a contribution between 50% and 60%. The influence of depth was also studied, concluding that, during the underwater phases, swimmers should stay streamlined at depths greater than 1.8 chest depths below the surface at Froude number of 0.2, and 2.8 chest depths at Froude number of 0.42. This corresponds to speeds of 0.9 and 2.0 $m.s^{-1}$, respectively, for a chest depth of 0.25 m and toe to finger length of 2.34 m.

Toussaint and Truijens (2005) considered the influence of active swimming on wave drag. He cited Hout (2003) unpublished work on the activity of the swimmer's legs which could possibly reduce the wave resistance by disrupting the pressure field at the rear of the swimmer (Figure 2.12).

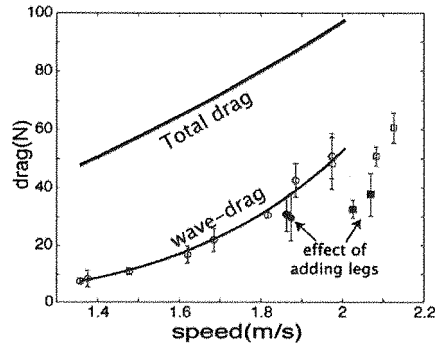

FIGURE 2.12: Wave drag curve compared with total drag. The wave drag swimming freely with arms only is no different from that swimming on the MAD system (filled dots). The addition of leg activity (swimming whole stroke; filled squares) seems to induce a lower wave drag for this swimmer as mentioned by Hout (2003) (Toussaint and Truijens, 2005).

Contribution of each drag component Clothier (2004) recalled the human morphology equivalent to fundamental hydrodynamics parameters as initially described by Clarys (1979) in Table 2.1. Although observations have been made, further experimental data would be required to establish a relationship between body shape and passive/active drag. As speed increases, the flow regime experienced by the swimmer will change and the proportion of the different resistance components towards the total resistance will be altered. Knowing the breakdown of forces allows the research to focus on a specific aspect of drag reduction, even if all components are still interlinked (Sanders et al., 2001).

TABLE 2.1: Human morphology equivalent to fundamental hydrodynamics parameters (Clothier (2004), adapted from Clarys (1979)).

Hydrodynamic parameters	Human morphology equivalents	Drag component
Body length	Body height	D_{wave}
Wetted area	Body surface area (wetted)	$D_{frictional}$
Midship section	Greatest body cross-section	D_{form}
Buoyancy	Hydrostatic weight, body volume/density	D_{form}
Length/Breadth ratio	Body height/Biacromial breadth	D_{form}
Length/Depth ratio	Body height/Thorax depth	$D_{frictional}$
Length/Thickness ratio	Body height/Greatest body cross-section	D_{form}
Length/Surface ratio	Body height^2/Body surface area	$D_{frictional}$
Slenderness degree	Body height/Body volume	D_{wave}
Breadth/Depth ratio	Biacromial breadth/Thorax depth	D_{form}

Since individual components of drag cannot be experimentally measured, theoretical methods in conjunction with experimental data have been used to get some insight.

A regression analysis was developed by Mollendorf et al. (2004), further used by Pendergast et al. (2005) and Pendergast et al. (2006) to study the effect of swimsuit. A passively towed swimmer could be approximately represented by a sphere (modelling the head) followed by elongated cylinders (modelling the body). Reynolds number for a swimmer is in the laminar-to-turbulent region. Using flat plate theory, an expression for the skin friction drag was established. The form drag formula is based on a linear variation with the second power of the speed, and related to the frontal surface area. Wave drag is said to be proportional to the fourth power of speed, whereas it was usually assumed to be to the third power of speed (Rushall et al., 1994). Pendergast et al. (2006) passively towed seven male and female swimmers at the free surface in an annular pool with velocities starting at 0.4 $m.s^{-1}$, up to 2.2 $m.s^{-1}$ with increments of 0.2 $m.s^{-1}$. A full drag curve over the entire swimming speed range was thus obtained for all tests performed. With such a detailed drag curve, curve fit and data regression were used to break down the experimental total drag into the various components.

At 1.4 $m.s^{-1}$, women and men respectively, the break down of forces were: 45% and 47% for skin friction, 51% and 50% for pressure drag, and only 4% and 3% for wave drag. As speed increased to 2.0 $m.s^{-1}$, the relative percentage of drag did not change for men. For women, the skin friction drag decreased to 42%, and wave drag increased to 8%, whereas form drag remained the same. These results are in contradiction with Vennell et al. (2006) who claimed 60% contribution of wave drag.

More recently, using naval architecture theory, Webb et al. (2011) estimated the drag break down to be closer to Vennell et al. (2006)'s claim with 59% wave drag, 33% form drag and 8% friction drag at 1.5 $m.s^{-1}$.

2.4 Advances in numerical simulations for swimming

Bixler and Schloder (1996) first investigated the viability of applying CFD to swimming. They performed a 2-D CFD analysis to understand the effects of accelerating a flat circular plate through the water. From these simulations, they concluded that a 3-D CFD analysis of an actual human would be able to provide valuable information to the sport. Hence, some years later Bixler and Riewald (2002) simulated the flow past a 3-D model of a hand and an arm. The results compared well with the experiments carried out by Schleihauf (1979) in a flume channel and Berger et al. (1995) in a towing tank. He identified a significant boundary layer separation from the arm and hand, confirming that idealised numerical formulations such as Bernoulli's equation cannot be used to describe the lift generated by a swimmer. Bixler et al. (2007) then investigated the passive drag of a 3-D model of a swimmer and validated the results with testing carried out in a flume. The simulation was still single phase, with the water surface modelled as a symmetry plane. The mannequin was positioned 0.75 m below the free surface. The drag values

obtained from CFD appeared to be within 4% of the experimental data, confirming the importance of developing CFD tools to better understand the flow around a swimmer's body. Bixler et al. (2007) recommended that further CFD simulations leading to the case of a swimmer actively swimming on the surface should be performed in the following order:

- Passive drag of swimmer on the water's surface (including wave drag)
- Evaluate underwater active drag while the swimmer is kicking
- Kicking on the surface
- Arm motion added
- Development of roughness parameters for human skin

All the above suggestions made by Bixler et al. (2007) would allow an optimisation process to be carried out on different techniques and body positions, as well as evaluating the performance of swimming equipment.

Marinho (2009) started a 3-D CFD investigation of the flow past the hand and arm of the swimmer. He found results agreeing with both past experimental and numerical studies ((Schleihauf, 1979), (Berger et al., 1995), (Bixler and Riewald, 2002), (Silva et al., 2005), (Rouboa et al., 2006)). Using his previous work, Marinho et al. (2010) investigated the effect of the fingers spacing. This study revealed that with a small finger spread, the propulsive force was increased thanks to an increased projection area.

Silva et al. (2008) investigated the effect of drafting using a 2-D single phase simulations including two swimmers. The drag coefficient of the back swimmer was found to be about 56% of the leading swimmer for the smallest inter-swimmer distance (0.5 m). The drag coefficient of both swimmers was similar when the drafting distance was 6.45 m at 2.0 $m.s^{-1}$ and 8.90 m at 1.8 $m.s^{-1}$.

Tokyo Institute of Technology has been actively involved with research in swimming with their numerical model SWimming Human Model (SWUM) ((Nakashima M., 2007), (Nakashima M., 2009)). The model computes the absolute motion of the swimmer's whole body as one rigid body, by solving the equations of motion for the rigid body with the given relative body motion as joint angles. Each body segment is represented as a truncated elliptic cone. The unsteady fluid force which consists of inertial force due to added mass of fluid, normal and tangential drag forces and buoyancy, is assumed to be computable, without solving the flow, from the local position, velocity, acceleration, direction, angular velocity, and angular acceleration at each part of the human body at each time step. The program output data such as swimming speed, roll, pitch and yaw motions, joint torques, etc. The program was validated with experiments and

showed 10% difference in the evaluation of the unsteady forces (Nakashima et al., 2007). It provides an approximation of thrust and drag of a swimmer during a stroke cycle. The corresponding forces in the muscles could then be determined using the software AnyBody, and were validated with electromyographic data. A diagram of the SWUM program is showed in Figure 2.13.

Analyses of several strokes were undertaken. In particular, the investigation of the six-beat front-crawl showed that most of the thrust comes from the hand stroke. The flutter kick produces almost no thrust, but helps maintaining the lower half of the body in a streamlined position. It was also showed that buoyancy is the main factor in the body roll motion.

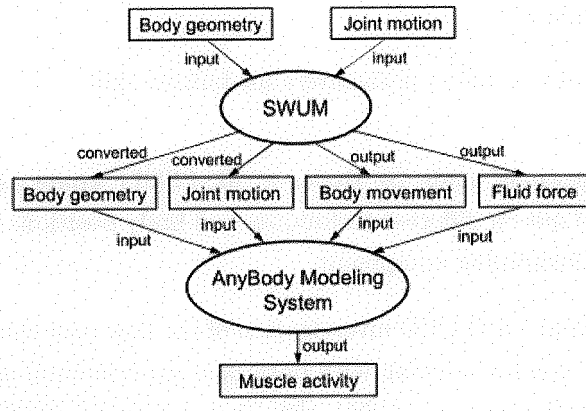

FIGURE 2.13: Schematic diagram of the SWUM program (Nakashima and Motegi, 2007).

So far the numerical methods presented were based on solving Newton's equation of motions or the Reynolds-Averaged Navier-Stokes equations using a grid-based technique. More recent studies have been using a Lagrangian mesh free method called Smoothed Particle Hydrodynamics (SPH) ((Cohen et al., 2009), (Cohen et al., 2011)). This method was initially developed by astrophysicist but was adapted to the hydrodynamic field by Monaghan (1994). The main advantage of using such a technique is that the particles already have a mass and the pressure is computed from weighted contributions of neighbouring particles, avoiding the need to solve a pressure-Poisson equation at each time step. Consequently, SPH methods are suitable to solve both complex deforming boundaries and splashing fluid free surfaces. Cohen et al. (2011) studied the underwater fly-kick of a swimmer with the presence of a free surface. The results showed that ankle flexibility had almost no effect; however the amount of thrust generated strongly depends on kick frequency. A powerful extension kick (downbeat) was advised to be worked on for improved propulsion during the underwater fly-kick phase.

Another novel CFD technique is the immersed boundary method, allowing the determination of unsteady forces on a moving body. von Loebbecke et al. (2009) used this method to study the underwater fly-kick with the presence of a free surface. Generation

and propagation of vortices from the swimmer's leg-kick were observed and compared with a typical Cetacean stroke. A mean propulsive efficiency of 21% was achieved for the swimmer, whereas the Cetacean showed an efficiency of 56%.

Not many 3-D CFD simulations including a free surface have been performed to date. Keys (2010) used the CFD package FLUENT with the inclusion of the free surface to study the influence of the freestyle flutter-kick. A user defined function based on video-recorded kinematics was written in FLUENT in order to define the movement of each node and surface mesh. The wave height created was of the order expected for a swimmer travelling at a set speed in a set water depth, which provided Keys (2010) with good confidence about his results. He concluded that, when the feet breached the free surface, a considerable amount of momentum was lost, resulting in a speed decrease of about 5%.

2.5 Research on swimming equipment

Most research on swimming equipment focused on the development of high-performance swimsuit and will thus be presented first. Research around the flow past a head, whether it is about cap/goggles design and head position was primarly published over the course of this PhD and remains scarce.

2.5.1 Suit

Swimsuit fabrics have progressed from wool to cotton, silk, Nylon, Lycra and finally polyurethane based products. Research on swimsuit started with wetsuits. Toussaint et al. (1989) used the MAD system to investigate the effect of wearing a wetsuit for triathlete. Reductions in active drag of 12% at 1.25 $m.s^{-1}$ and 14% at 1.50 $m.s^{-1}$ were observed across all 12 tested swimmers. This significant total drag reduction is a result of the increased buoyancy provided by the suit, thus reducing both the frontal and wetted surface area. The authors speculated on the arrival of full-body length suits with neoprene to increase buoyancy and thus reduce drag during pool competition.

Although FINA bans the use of buoyancy suits, the early 2000's fast suits presented an initial buoyancy effect. They provided reduced surface drag and helped male swimmers in particular to raise their legs allowing for a better streamline position (Kjendlie and Stallman, 2008). Since flotation enhancement is not allowed by FINA, swimwear manufacturers tried to optimise their products by focusing on the reduction of skin friction and by postponing flow separation which will reduce pressure drag (Toussaint, Van den Berg and Beek, 2002).

At the 2000 Olympic Games, Speedo released the 'Fastkin' suit, a full-body coverage suit with a surface area presenting shark-like properties to reduce drag (Sanders et al., 2001).

These suits were manufactured by superimposing vertical resin stripes. These stripes were aimed at generating vertical vortices to reduce the separation bubbles and thus form drag. These stripes are commonly known as 'ribblets' and for these to be effective they should be aligned with the fluid flow. Although the 'Fastskin' suits may perform better during passive drag test, they are unlikely to perform well during the active swimming phase since the limbs move and will thus present the riblets at a different angle to the flow direction. This is particularly true for breaststroke during the leg recovery phase. In this case, suits with riblets are more likley to hinder the swimmer's resistance as observed by Bergen (2001) during time-trials of the new suits on different strokes.

Suit compression was another factor of debate (Sanders et al., 2001). Some think that compression has a positive impact on performance since it removes the excessive skin movement due the subcuttaneous adipose tissue at higher speeds and also allows for a better blood flow. It is also thought that the compression may help restrict unwanted sideways movements of the hips which would otherwise increase form and wave drag. On the other hand, some swimmers reported that tightness hindered their performance due to limb movement restrictions during the stroke and loss of the feel for water on the arms. Hence, the preferred full-body length suit was not covering the arms.

To scientifically validate the manufacturers claims about this revolutionary suit, Toussaint, Truijens, Elzinga, van de Ven, de Best, Snabel and de Groot (2002) tested six male and seven female swimmers on his MAD system with the 'Fastskin' suit and with a conventional suit. A non-statistically significant drag reduction of about 2% over the speed range of 1.10 up to 2.0 $m.s^{-1}$ was found in contrary to the 7.5% drag reduction stated by Speedo. On one occasion a significant drag reduction of 11% was observed and was reported to be more due to a misplacement of the body position or an ill-fit of the conventional suit, rather than as a result of wearing the Fastskin suit.

Sanders et al. (2001) recalled that in order to measure drag differences between different suits, the swimmers must be able to repeat active swims with both the same technique and effort. In addition to drag measurements difficulties, the drag assessment of body suits for swimmers is a very complex problem due to the large number of factors involved (suit fitting, placebo effect, suit wetness, etc.). Few objective scientific studies are presented and manufacturers keep on stating drag reduction numbers without any information on the testing methodologies. The difficulty in assessing suit performance in a passive manner is pointed out since as the swimmer moves through the water the velocity of the fluid on the swimmer's body surface changes and this will impact all forms of drag. In particular, form drag will be largely dependent on the swimming velocity on the body as a result of the fluctuating flow separation point. Both Mollendorf et al. (2004) and Pendergast et al. (2006) investigated suit body coverage and the use of turbulators placed on the suit to delay the separation point.

Mollendorf et al. (2004) drag tested seven males wearing five different suits covering various body surface areas. Since the upper-body part is in a laminar-transitional flow regime, changes in a swimsuit on the upper-body makes the most of a difference on the overall drag. The upper-body suits increased the skin-friction force contribution but reduced both the form and wave drag due to a delayed boundary layer separation, resulting in a total drag reduction.

Pendergast et al. (2006) passively towed seven males and females at the surface in an annular pool. Turbulators were carefully positioned on the swimmers' back based on calculations of separation point. Configurations with either one (upper back) or three (across the upper back, the chest and across the buttocks) turbulators were compared with a similar full-body suit without turbulators. On average across all speeds the total drag was reduced by 11-12% by one turbulator and 13-16% by three turbulators. The presence of the turbulators did not significantly increase friction or wave drag; however, the flow was attached to the body as there was a significant reduction in pressure drag (19-41%).

Through the use of CFD simulations, Marinho et al. (2012) modelled the underwater glide prone position of a female swimmer wearing a full-body length suit, a conventional suit and no suit. Higher total drag values were reported when the swimmer had no suit (40% greater). This last generation of swimsuit presented less pressure drag than the conventional suit, due to less projected area as a result of compression. However, this study did not take in account the surface roughness of the skin and suit.

2.5.2 Cap

A brief introduction to the history of swimming caps is given by Epic Sports Swimming (2016). Caps in competitive swimming were introduced in 1883 after the invention of rubber. They were made out of latex, a thin extensible non-permeable material which allowed a better fit around the swimmer's head compared to the previous net-type caps. It is only in the 1960-70s that swimming caps lost their 'fashion statement' and new materials started being used such as lycra and silicon to improve swimming performance. Lycra caps are fabric-based. They are more comfortable to wear for the casual swimmer but the fit is not as good as for a latex cap. On the other hand, the arrival of the thicker silicon caps was welcomed by competitite swimmers as a good alternative to latex caps as they offered less wrinkles and also proved to be more durable. Improved manufacturing techniques now allow silicon swimming caps to be printed without seams providing even less wrinkles and potentially a better fit.

All major swimming brands claim to produce drag-reducing caps but no details on methodology to establish the performance gains made are provided. To-date, only Marinho

et al. (2011), Gatta et al. (2013) and Gatta et al. (2015) have published initial scientific studies on the influence of the cap model and surface roughness.

Marinho et al. (2011) assessed the influence of wearing a cap in the typical streamlined position (arms extended above head with one hand above the other). The passive drag was numerically evaluated for the scanned swimmer positioned 0.75 m below the free surface at speeds of 1.5, 2.0 and 2.5 $m.s^{-1}$. A 17% drag reduction at 2.0 $m.s^{-1}$ is obtained with the use of a cap, hence the author's recommendation to wear a swimming cap during the glide phase. These numerical simulations have not been validated with experimental data or through a rigorous verification and validation study. The magnitude of the passive drag force was just compared to other numerical simulations and was found to be of a similar order, between 44 and 87 N for the range of speeds tested. Little information is given on the types of simulation carried out except the fact that they are 3-D single phase simulations. This study lacks important information, though, to make any conclusions as to why a decrease in drag was measured with the use of a cap. The cap worn by the swimmer is not reported and the swimmer's geometry showing the hair position with and without the cap is not shown, making it difficult to assess by how much the head shape changed by applying a cap. Without this information, it remains difficult to establish whether the drag difference comes from a simple change in volume due to the additional cap thickness or if the general shape of the head was changed due to different positioning of the hair inside the cap.

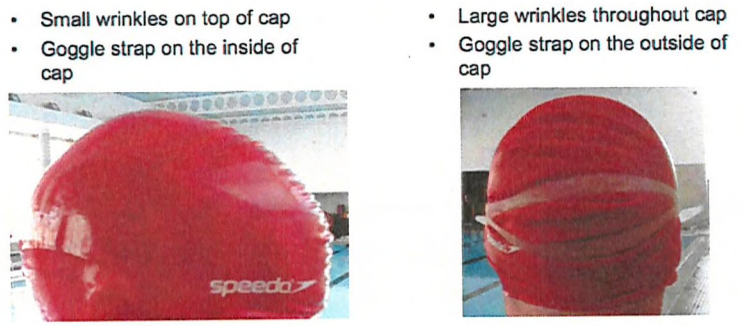

FIGURE 2.14: Cap and goggles arrangement assessed during passive and active swimming tow tests.

The effect of the cap/goggles arrangement between: a good cap (smooth cap with goggles' strap inside) and a bad cap (wrinkled cap with goggles' strap outside) was investigated by Webb (2013) (Figure 2.14). One swimmer was passively towed underwater five times for each condition at 2.0 $m.s^{-1}$. The good cap/goggles arrangement showed a 2% drag reduction but the results were not statistically significant based on permutation tests (p=0.11). When actively swimming freestyle on the surface, the drag reduction was just under 1%. This small discrepancy is more likely due to variations in the swimming technique rather than on the change in cap/goggles arrangement.

Using boundary layer theory for a flat plate, Mollendorf et al. (2004) and Pendergast et al. (2006) both identified that the swimmer's head is in laminar flow until the maximum circumference of the head, emphasing the importance of focusing on drag reduction techniques on the head. As a result, it is expected that tripping the boundary layer at the head should give the greatest reductions in drag. Gatta et al. (2013) passively towed 16 swimmers on the free surface at three speeds: 1.5, 1.7 and 1.9 $m.s^{-1}$. The effect of wearing three different caps (lycra, silicon and helmet silicon without seams) was assessed. The standard silicon cap showed reduced drag compared to the Lycra cap but was non-statistically significant. However, significant drag reductions, between 5.0 and 6.6% based on the tested speed, were found between the lycra cap and silicone cap with no seams. Statistically significant drag reduction was also found between the two silicon caps indicating that drag reduction for caps is due to both the material but also to the fit of the cap. Silicon caps provide a larger compliant surface to the head and will thus offer less wrinkles when fitted onto the head. Gatta et al. (2013) therefore recommend to wear a solid silicon cap (without seams) and to take great care during the fitting process to ensure that the leading edge of the swimmer presents a limited amount of wrinkles. Yet, these new silicon caps without seams are now typically worn by elite swimmers who still display large wrinkles on the starting block and if not then by the end of the race.

Gatta et al. (2015) also considered the influence of cap surface roughness on passive drag. A similar towing procedure was used for these tests, except the swimmer was towed 0.6 m below the free surface and in two different positions: arms extended in front of head as before and arms by the side. These changes were decided to improve the accuracy of the results and indeed the mean coefficient of variation decreased down from 3.5% to 2.1%. Three caps were tested over the same range of speed of 1.5, 1.7 and 1.9 $m.s^{-1}$. The baseline cap is the smooth seamless silicon cap tested by Gatta et al. (2013). The two other cap models have an increased surface roughness: one with bumps and one with dimples. No difference between the three caps was observed with the arms extended above the head. However, in the case where the arms were by the side of the swimmer, the cap with the bumps showed an increase in drag of 4.4%. This study reiterates the potential detriment on swimming performance of wearing a cap with wrinkles.

2.5.3 Goggles

Similarly to the caps, several manufacturers claimed significant drag-reduction when releasing a new goggles, but without any scientific evidence (Behm, 2014). Only a CFD company article was found on numerical research undertaken to reduce goggles' drag (Silvester, 2012). Speedo teamed up with Ansys Fluent to predict the fluid flows around a swimmer's body in the outstretched glide position, identifying areas where the slowing effects of drag were likely to occur. Using several head scans, the design of new goggles

was optimised for least-drag and best all-around fit. Both underwater and free surface simulations were performed but no other details on the type of simulations are provided.

2.6 Specific research on a swimmer's head position

In 1978, Miyashita and Tsunoda towed 12 male and 7 female swimmers in a flume and measured drag force with a load cell (as reported by Miyashita (1999)). A significantly greater drag force was generated with a higher head position.

Zaïdi et al. (2008) undertook a 2-D numerical analysis of the steady flow past a swimmer's body during the underwater swimming phase while changing the head position: up, down and aligned with the body. Her studies showed that at high swimming velocities, the position of the head is critical to minimise drag during the underwater phase as it considerably changes the wake around the swimmer's body. At low speeds small differences were observed, whereas at 3.1 $m.s^{-1}$, a 20% drag reduction was measured with the head aligned case compared to head down case. With the use of the turbulence model $k-\epsilon$, interesting flow structures such as recirculating vortices in the neck and chin regions were observed. However, these results are to be taken into account carefully since the effect of the free surface was neglected and the body position was kept fixed whereas changing the head position is likely to change the entire body position.

Popa et al. (2012) carried on the work initiated by Zaïdi et al. (2008) with a 3-D CFD code and the use of the $k-\omega$ turbulence model. A large influence of the head position on total drag was confirmed. Flow separation and reattachment areas have been clearly identified around the nape, chin and buttocks. In addition, large recirculation zones on both sides of the head, at the lower back level and on the back of buttocks were observed. The head aligned with the body offers the least resistance in comparison with positions where the head is lowered or lifted up, generating a reduction of 4% on the total drag compared to the other two positions.

Cortesi and Gatta (2015) used the same methodology as Gatta et al. (2015) to assess the impact of the head position on the underwater glide drag with arms above the swimmer's head and with arms by side. The same head positions as numerically studied by Zaïdi et al. (2008) were investigated (head up, aligned and down) over the range of speed of 1.5, 1.7 and 1.9 $m.s^{-1}$. The head aligned and down cases showed a reduction of 4.0-5.2% in passive drag across the entire speed range in the case where the swimmers had their arms by the side. With arms extended above the head, an even more significant decrease in drag of 10.4-10.9% was observed.

2.7 Chapter summary

In this chapter, general knowledge on the hydrodynamics of a swimmer have been introduced with a prime focus on the resistive force.

According to Zamparo et al. (2009), active drag measurements remain difficult. There exists a debate on how to best measure the actual drag of a swimmer during a full effort without altering the swimming technique. Measurements of passive drag are still useful and widely accepted by the scientific community ((Chatard et al., 1990), (Mollendorf et al., 2004), (Pendergast et al., 2006), (Wilson and Thorp, 2003), (Zamparo et al., 2009)). This method appears to be better suited to studying the effects of drag reducing technologies. Since small drag differences are expected, the elimination of the potential noise in the swimming technique is key.

Numerical simulations are under constant evolution and might be the key to better understand active drag. The inclusion of the free surface when performing numerical simulations is vital to gain a better understanding of the wave resistance component and the interaction with form drag and friction drag.

A large amount of attention has been devoted to swimsuit research to reduce drag as the rules evolved. This highlighted the challenges in the assessment of equipment performance for a swimmer. Detailed flow characteristics around the head and the upper-body of the swimmer have not been investigated yet in much depth. There appears to be little research on cap and goggles designs that has been reported to-date. It is only over the course of this PhD project that cap studies have been published (Marinho et al. (2011), Gatta et al. (2013) and Gatta et al. (2015)).

Similarly, although the influence of head position has long been known to have an impact on a swimmer's drag, both experiments and numerical simulations on this topic have been carried out underwater, ignoring the effect of the head piercing the free surface.

Part B

METHODS
Strengths & Challenges of:
Swimming pool tests
Numerical simulations
Towing tank tests

3

Swimming Pool Tests
A programme to enhance swimming performance

The SwimSIM project originated from the Performance Sports Engineering Laboratory for the run-up to the London 2012 Olympic Games. Testing systems and protocols have been designed to assess and improve the performances of British Swimming elite athletes.

In this chapter, the systems in use for this PhD research project are first introduced. Initial results highlighting the strengths and challenges of assessing swimmers' resistance in a swimming pool environment are then presented through detailed calibration procedures of each system and a case study on equipment selection with elite swimmers.

3.1 SwimSIM: 2008 - 2012 London Olympics cycle

As mentioned in Chapter 1, Dr. Banks, Dr. Philipps and Dr. Webb, designed, built and tested a range of testing systems which allowed elite swimmers' performances to be improved for London 2012 Olympic Games.

These testing systems include force, speed and wave elevation measurements. They are used in conjunction with above- and under-water video footage, all synchronised with the measurement traces. Detailed feedback can thus be provided to British Swimming elite athletes and their coaches so that they can make appropriate changes to their technique.

Although most of the measurement systems developed for this testing program have their origins in systems used to test ship models, they have been designed specifically for use with swimmers.

All the systems used for this specific PhD project are presented in Subsections 3.1.1 - 3.1.4.

3.1.1 Force measurements - 'tow rig'

The tow rig system was designed to measure the resistance of a swimmer. As shown in Figure 3.1, the system contains a towing winch on one end of the pool to tow a swimmer from the other end of the pool in either a glide position (on the free surface or underwater) or while actively swimming. In the glide position, the swimmer is towed along by a tow line, which is connected to their hands using a handle. During an active stroke, the swimmer is attached to the tow line via a strap around their waist (Figure 3.2(b)), and towed at a speed 5% higher than their maximum speed at a prescribed stroke rate.

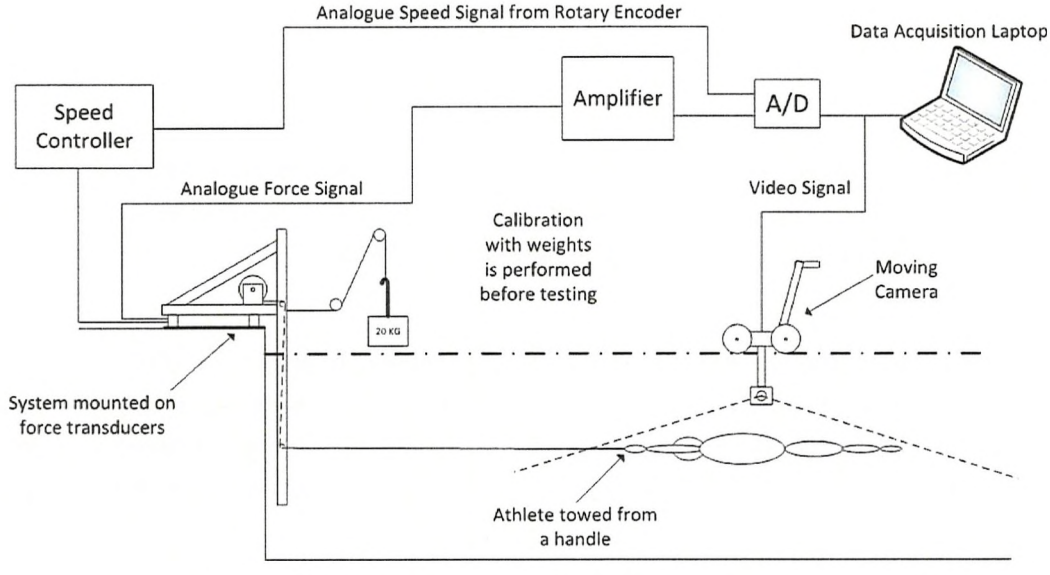

FIGURE 3.1: Schematic of tow rig system, displaying the mechanical and electrical components (Webb, 2013).

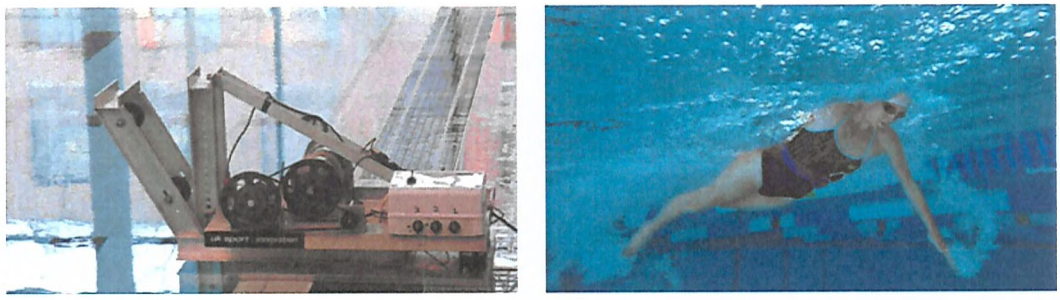

(a) Tow rig system (b) Athlete on an active swimming tow

FIGURE 3.2: Tow rig systems by pool side and while in use.

The swimmer's resistance is measured via three electrical force transducers mounted on the tow-rig platform. A Linear Varying Displacement Transformer (LVDT) is positioned onto a flexure, which can move in one direction only. The electrical data are sampled at a frequency of 250 Hz. Through a systematic linear calibration process between 0 and 20 kg, the force applied onto the line during a run can be determined by averaging the forces obtained from each force block.

The tow rig measures the force required to maintain a set speed throughout a run (Figure 3.3). When the athlete generates a large amount of propulsion this force goes down. In between propulsion phases or when the athlete adopts a bad position, this force goes up to indicate less propulsion or more drag.

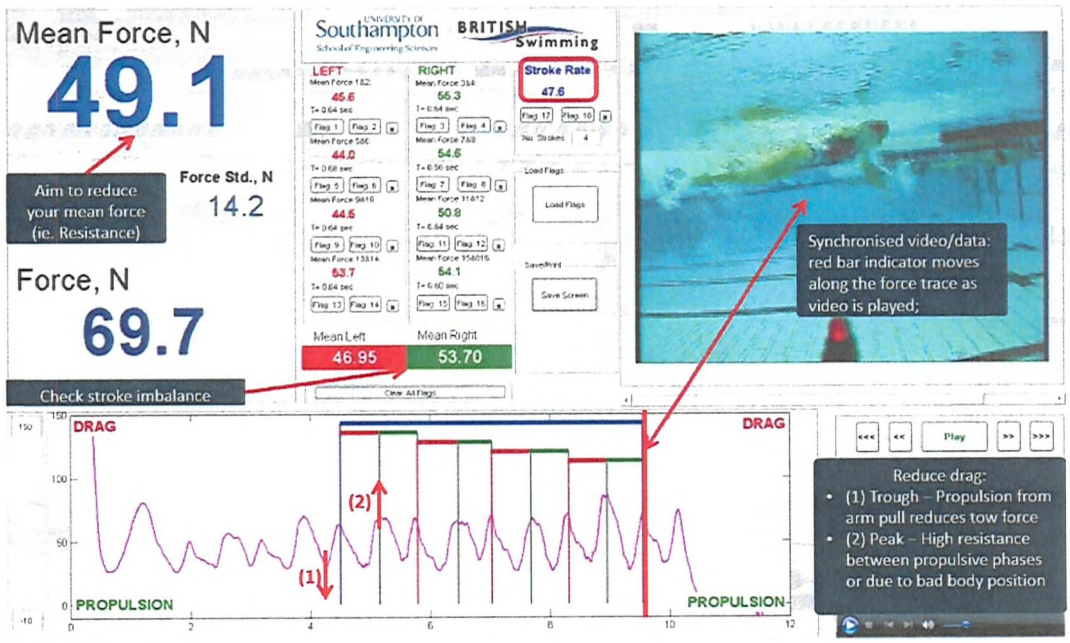

FIGURE 3.3: Feedback screen - Force trace for freestyle.

The tow rig is tailored to strokes where speed changes throughout the stroke are negligible, such as freestyle and backstroke. The tow rig cannot be used for stroke with high velocity changes such as breaststroke and butterfly, since the water load on the swimmer would be too high during the low speed section of the stroke. In this case, a different system measuring speed is used to assess swimmers' performance.

3.1.2 Speed measurements - 'speed reel'

The speed reel system was designed to measure a swimmer's speed and is primarily used to assess swimmers' performance in the push-off position (start or turn) and with swimming strokes which introduce a large variation in speed (breaststroke or butterfly).

The device is positioned on one end of the pool, and in opposite to the tow rig the swimmer starts from the same end and pushes-off the wall (Figure 3.4). The athlete is attached to a strap around their waist linked to a thin line. Depending on the swimming phase to be analysed (under-water pull-down or free surface swim), the depth at which the swimmer pulls out the line can be adjusted. In the active swimming case, the athlete swims with a prescribed stroke rate at maximum power while pulling out the thin line. The speed is recorded via a rotatory encoder at a sampling frequency of 250 Hz, whilst a small amount of resistance is applied. The speed trace is then displayed with a synchronised video, as shown in Figure 3.5.

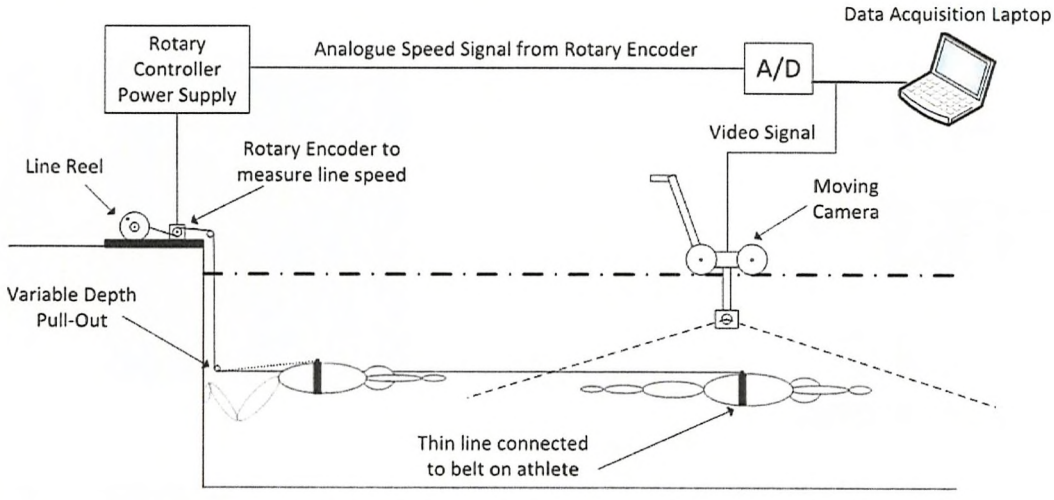

FIGURE 3.4: Schematic of speed reel system, displaying the mechanical and electrical components (Webb, 2013).

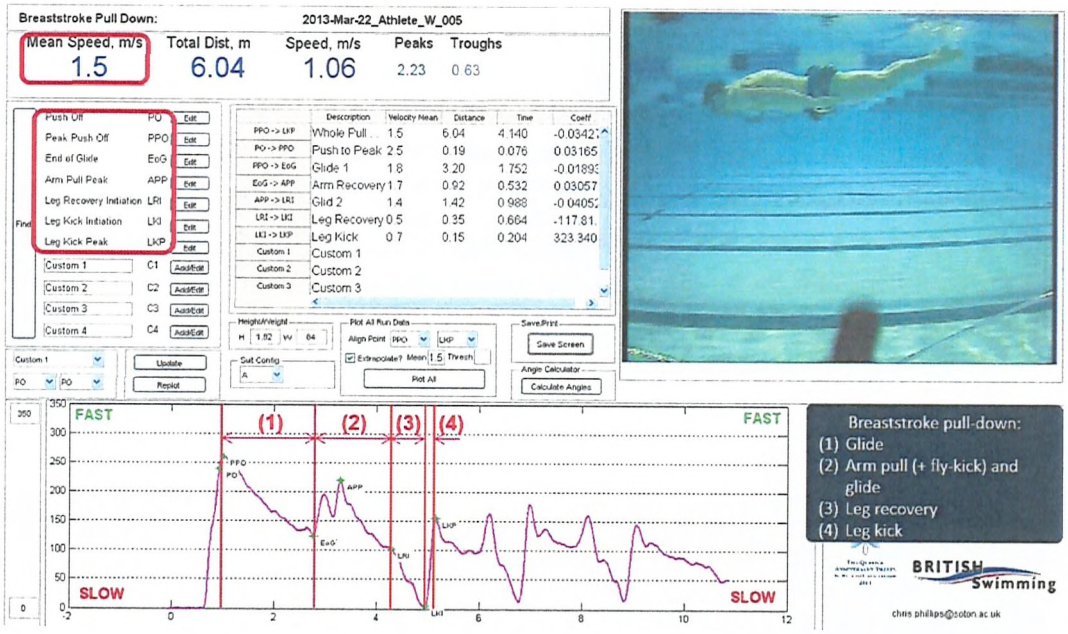

FIGURE 3.5: Feedback screen - Velocity trace for breaststroke.

3.1.3 Above- and under-water videos and photographs

Combined above- and under-water video footage are recorded from the side and synchronised with the force (or speed) trace to provide more insight to the coaches about what affects the performance of their swimmers (body position or specific stroke technique). Moreover, a camera is placed in front of the swimmer on the tow line to obtain further details about the stroke technique (Figure 3.6).

FIGURE 3.6: Detailed freestyle technique obtained from front-view video footage.

3.1.4 Wave elevation measurements - 'wave probes'

The equipment used to capture the wave pattern consists in an array of resistance wave probes penetrating the free surface as shown in Figure 3.7. The wave probes are professionally made by HR Wallingford with two stainless steel wires located 12 mm apart. The wave probes are mounted on a light beam extending from a tripod placed on the pool floor and accessible by pool side for calibration. The conductivity between air and water is significant enough that a change in voltage output can be measured as the free surface deforms. By measuring the wave height at specific known locations, the wave pattern and thus the wave resistance of the swimmer can be determined (Eggers, 1955).

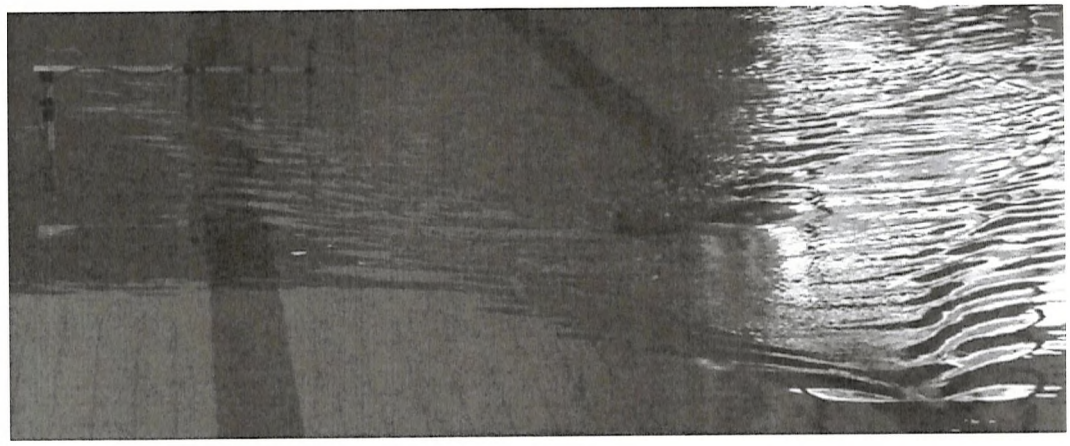

FIGURE 3.7: Wave probes arrangement mounted on a beam extending from a tripod to measure the wave resistance of a drag chute being towed under-water.

There exists two different experimental wave cut methods, transverse and longitudinal. Although the transverse cut method is theoretically more efficient since it is a finite cut, it is not a practical method due to the presence of the swimmer on the centreline of the cut. On the other hand, the longitudinal wave cut method has long been used in towing tank testing. Eggers et al. (1967) noted that the measurements must be made in the region where the effects of the boundary layer and the wake are negligibly small, since the derivation of the wave resistance equation is based on the assumption that the fluid is inviscid and the flow is irrotational. The swimmer is thus positioned at least 1.5 m away from the first wave probes. More details on this methodology may be found in Appendix B.

3.2 SwimSIM: 2012 - 2016 Rio Olympics cycle

3.2.1 List of pool testing sessions

The pool testing sessions undertaken over the 2012-2016 Olympic cycle are listed in a chronological order in Appendix A. In this report, each session will be referred to via its ID number (i.e. Session # i).

The testing sessions which took place in Manchester with the paralympic swimmers have been undertaken on systems designed and built by Dr. Carl Payton from Manchester City University. Both the tow rig and speed reel are based on the same underlying principle and use the same protocol as described in Section 3.1.

3.2.2 Testing plan, risk assessment and ethics approval

Towards London 2012, the SwimSIM team tested a large number of athletes under a single ethics approval (*ID 7207*) in conjunction with a risk assessment. Since 2013, the Ethics and Research Governance Online (ERGO) requested a specific application for each testing session involving a swimmer who is not part of the research team. This requirement improved the overall process of pool testing planning. Prior to a test being conducted, a form is sent to the sport scientist to provide the athlete's basic details such as height, weight, swimming technique strengths and weaknesses, as well as current injuries if any. The aim of the testing session is identified, allowing the apparatus to be selected, and a testing plan is devised.

From this information, an ethics form can be prepared. Key questions include the aim and objectives of the study, the background, the key research questions and the testing plan. This procedure allows each testing session to be considered from a research point of view, even when the testing session is initially undertaken to support British Swimming needs rather than research needs. In addition, the ethics form contains information related to the test subject, the testing protocols and the data management.

Once approval from ERGO is received, the swimmers are sent a participant information sheet. By pool side, the experimenter provides the swimmer with a briefing, explaining the protocol, the risks and measures to be aware of. The swimmer is then asked to sign a consent form. At the end of a testing session, the swimmer fills in a feedback questionnaire to monitor the impact of the systems on the swimmer (e.g. swimming technique, muscle fatigue, body temperature). This information allows the experimenter to improve the testing protocols over the course of the SwimSIM project. A feedback form with the results is finally sent to the sport scientist and/or the swimmer's coach.

3.2.3 Systems calibration

The researcher's toolbox for testing swimmers in the pool was introduced in Section 3.1. A comprehensive calibration procedure was undertaken for each system to better understand the uncertainty associated with each system.

'Tow rig' The tow rig is based on the electrical force transducer principle. A Linear Varying Displacement Transducer (LVDT), with a 1-mm range is positioned onto a flexure, which can move in one direction only with a displacement range of 2 mm. The response band in the data acquisition system is across 20 V [-10 V, +10 V] discretised in 2^{16} bit. The drag force was measured from three force blocks, each suitable to loads up to 500 N, resulting in a bias of the order of 10^{-3} N/bit, which is suitable.

Providing that a calibration procedure is applied before testing, the resistive force applied on the swimmer can be evaluated. A calibration process consists in applying several known weights and recording the corresponding amplified output voltages. A linear curve is fitted through the data points in order to get the rate to apply to the electrical response.

The tow rig was calibrated with weights ranging from 0 N up to 200 N, covering the range of the recorded drag forces. Several calibration data points were obtained for weights of [0, 50, 70, 100, 120, 150, 170, 200] N, which were applied in a random order. The 0 N response was established with a calibration hanger of 5 N to avoid any slack or misalignment of the calibration line. The calibration process is typically done at the start and end of each testing session to allow for potential changes in the system. Drifts in the electrical zero are not so important, since the zero is always acquired before each run.

For Session # 30, measurements were taken over two days, thus a calibration procedure was applied at the start of the first day (Cal 1), at the end of the first day (Cal 2) and at the end of the second day (Cal 3). Figure 3.8 emphasises the linearity of the calibration process. In addition to the calibration procedure, weights of 100 N were hanged through out the testing session to check that the system remained unchanged. Over the two testing days, this check procedure was undertaken 15 times. The mean force over two days was 100.7 N $\pm$ 1 N, and thus shows that the system has a coefficient of variation of about 1% around the standard amount of force measured. The output voltage for the 15 sets of 100 N weights was calibrated with both the lowest (Cal 1) and highest (Cal 2) rates, and the equivalent force was the same.

This end-to-end calibration includes the uncertainty relating to both electrical and mechanical components, and therefore provides the user with the total uncertainty in the data acquisition process.

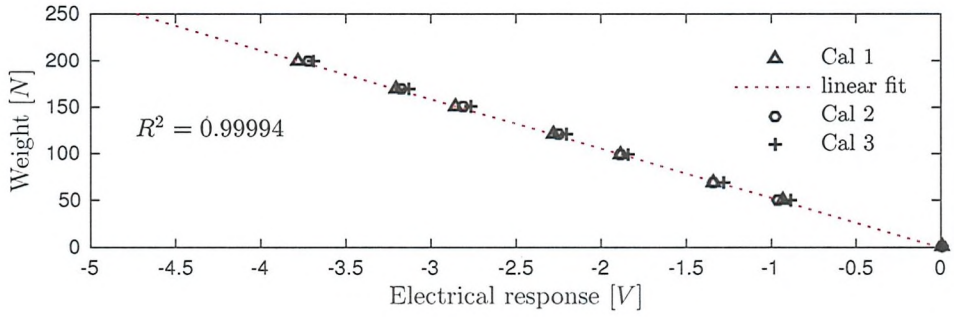

FIGURE 3.8: Calibration data points for the total output force over a two-day testing session, with a least-square fit applied to the calibration line of 'Day 1 start' - $R^2 = 1$.

'Speed reel' Dry calibration tests of the speed reel were undertaken to evaluate the system's accuracy and repeatability. The speed reel is based on a rotary encoder, with 100 pulses per rotation. The distance per one pulse can thus be obtained as $d_p = \frac{2*\pi r}{pulses/rev}$. The number of pulses, n_p, is acquired at a sampling frequency of 250 Hz. The accumulative distance is thus $D = n_p * d_p$, and the speed is directly evaluated by dividing the accumulative distance by the time.

The line was pulled out over set distances of 5, 10, 15, 20 and 25 m. The predicted distance was recorded and all tests were repeated five times. The predicted distance exhibits a linear relationship with the actual distance ($R^2 = 1$). The repeatability of the system is excellent, with the maximum coefficient of variation being 0.25% over the shortest distance, and decreasing down to 0.05% over 25 m.

The rotary encoder presents a resistance setting determined at the beginning of a test. The resistance must be large enough to ensure that the line does not become slack while the swimmer pushes away from the wall, but the resistance must remain low enough to not resist the swimmer's natural forward motion. The effect of the applied resistance on the predicted distance over 15 m was undertaken. The standard resistance used to do the previous repeatibility tests was increased and decreased by a similar amount (although not quantifiable). A null change was observed in the predicted distance between all the degrees of resistance. The speed reel measurements are thus reliable to do comparative studies.

'Wave probes' The four wave probes used during this research project were calibrated for wave elevations between -50 and +50 mm (Figure 3.9). The wave elevation signals were acquired at a frequency of 100 Hz through a monitor box which has an in-built 20 Hz filter. The excellent linear response of the wave probes makes them suitable to evaluate wave elevations of a swimmer.

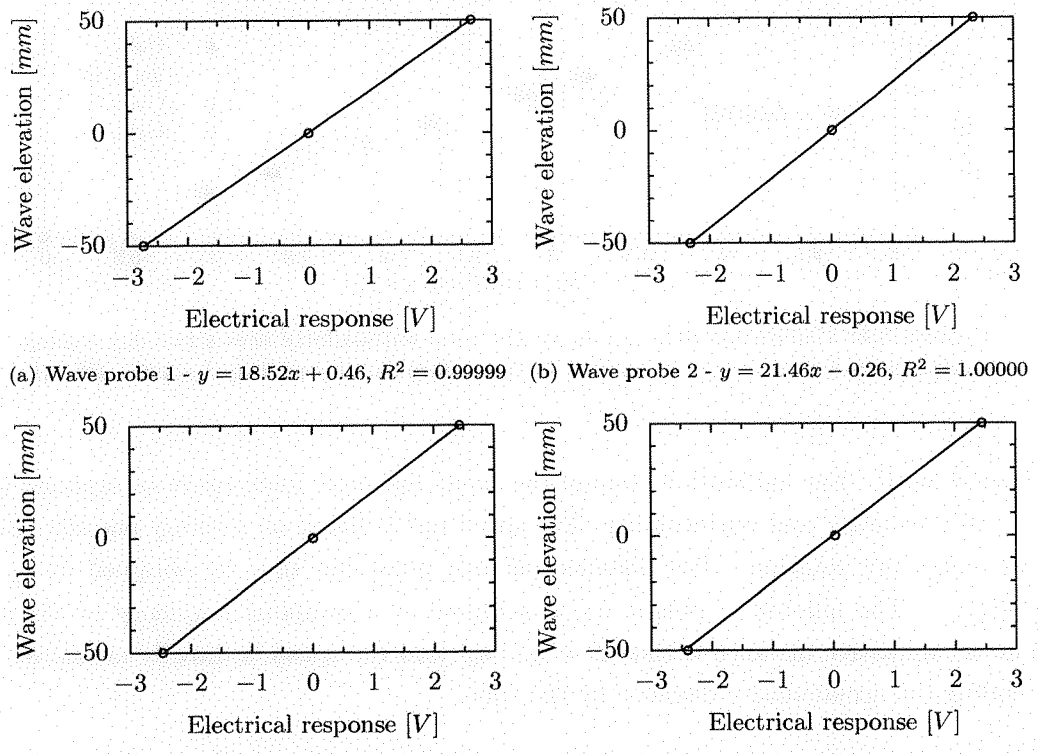

(a) Wave probe 1 - $y = 18.52x + 0.46$, $R^2 = 0.99999$ (b) Wave probe 2 - $y = 21.46x - 0.26$, $R^2 = 1.00000$

(c) Wave probe 3 - $y = 20.45x + 0.15$, $R^2 = 0.99997$ (d) Wave probe 4 - $y = 20.62x + -0.55$, $R^2 = 1.00000$

FIGURE 3.9: Linearity check of the four wave probes for wave elevations between -50 and 50 mm.

3.3 Case study: evaluation of equipment performance

In this section, the challenges of assessing swimmer's resistance in a pool environment will be highlighted through a case study on equipment selection for both British Swimming elite athletes and Speedo commercial products under development. Passive resistance only is used for the evaluation of equipment performance to remove the influence of the swimmer's technique skills.

3.3.1 British Swimming - Equipment selection on the 'speed reel'

Purpose The purpose of this study is to provide advice to British Swimming elite athletes as to which racing equipment gives the lowest drag and hence the fastest race time. Equipment configuration is defined as: cap, goggles and suit. Two configurations were tested for each swimmer: (A) New equipment versus (B) Current equipment. Two open-water swimmers decided to test the influence of jammers (waist to knee)/full-body suit, all currently approved by FINA, the international swimming federation.

Participants Testing was done at British Swimming intensive training centres in Bath and Loughborough (Testing sessions # 20 and # 21). In total, seven females and five males, including two open-water swimmers, were tested (Table 3.1).

TABLE 3.1: Summary of main particulars of tested swimmers - Format: Mean (min, max) expressed from mean, WSA = wetted surface area, ∇ = displacement volume.

	#	Height [cm]	Weight [kg]	WSA $[m^2]$	∇ $[m^3]$
Female	7	172 (-3,+3)	64.4 (-3.9,+7.1)	1.76 (-0.06,+0.06)	0.066 (-0.004,+0.007)
Male	5	186 (-7,+3)	81.7 (-8.2,+6.3)	2.06 (-0.12,+0.09)	0.083 (-0.008,+0.006)

Experimental procedure Each athlete was tested on the speed reel. They were first asked to push-off the wall to check the depth at which their waist was during push-off. The depth of the speed reel line coming off the wall was then adjusted accordingly.

The swimmers were asked to push-off the wall in a streamlined glide position until they surfaced due to buoyancy only. Each run takes between two and three minutes to allow for testing time, data acquisition and time for the athlete to recover before starting the next run. Between the swimmer's availability and a required minimum number of five runs as advised by Webb (2013), a 20-minute testing slot per athlete was allocated. A minimum of eight runs were recorded each time and up to ten runs when time permitted to ensure as large as a sample as possible for the statistical analysis comparing the two different equipment configurations. The swimmers were asked to push-off the wall with maximum effort, as they would in a race, to ensure as much consistency as possible. They were also reminded to put their cap back in place, had it slipped during the glide so that each run was as repeatable as possible. To control these aspects, the experimenter checked the yaw of the swimmer (movement of the leg sideways from the body centreline) and an underwater camera was positioned by pool-side parallel to the swimmer to ensure that a consistent body depth was adopted. In case of an abnormal position, a note was made in the data log and the run was taken out of the analysis.

Data processing The swimmer's motion is governed by Equation 3.1. The swimmer's resistance during the glide phase is defined by the deceleration rate of the swimmer from peak push-off speed (between 3.0 and 1.5 $m.s^{-1}$) down to a speed of 1.0 $m.s^{-1}$. The signal obtained is $1/U$ (or U/U^2). A second-order polynomial fit (Matlab, polyfit) is applied to the speed trace (Figure 3.10). The trace is then discretised into 1000 elements. Each element is differentiated with respect to time to obtain the local slope $\frac{dV}{dt}/V^2$ and the mean value of these local slopes gives the deceleration rate.

$$R(U) - (M + m)\frac{dU}{dt} = 0 \tag{3.1}$$

where:

- $R(U)$ $[N]$ Velocity dependent resistance of the swimmer
- M $[kg]$ Mass of the swimmer
- m $[kg]$ Added-mass of the swimmer (unknown, thus set as 0)
- dU/dt $[m.s^{-2}]$ Deceleration rate

The velocity dependent resistance was non-dimensionalised as:

$$C_T = M\frac{dU}{dt} / \left(\frac{1}{2}\rho WSA_{athlete}U^2\right) \tag{3.2}$$

The wetted surface area of each athlete is calculated based on DuBois and DuBois (1916) empirical formula ($WSA = 0.007184H^{0.725}W^{0.425}$ - H [cm], W [kg]). The pool water temperature was 27° Celsius in Bath and 28° Celsius in Loughborough. Since the water density, ρ, does not vary much with temperature, it was rounded up to 1000 $kg.m^{-3}$.

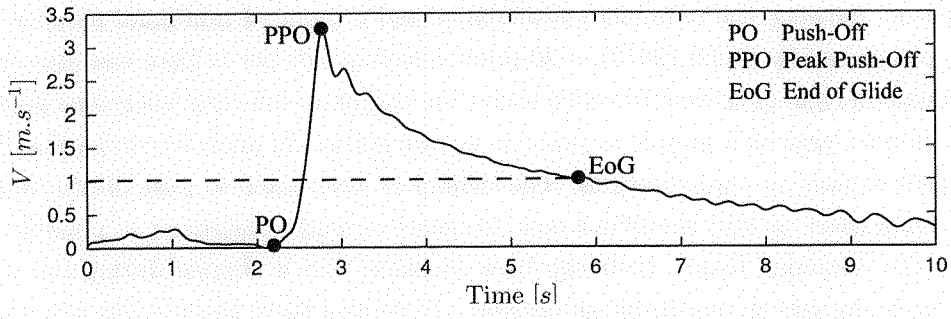

FIGURE 3.10: Typical push-off speed trace.

3.3.2 Speedo - Equipment development on the 'tow rig'

Purpose The aim of this study is to assess the performance of a new suit for the 2016 Olympic Games at a set speed (around 2.0 $m.s^{-1}$) using the tow rig system adjusted to tow the swimmer 1.0 m below the free surface. The new suit (C) is to be compared with two other suits, the previous racing suit (B) and a training suit (A), for two males and two females.

Participants Testing was done in Shaftesbury at St Mary's school (Testing session # 22). Two females and two males, swimming at an elite level, were tested (Table 3.1).

TABLE 3.2: Summary of main particulars of tested swimmers - WSA = wetted surface area, ∇ = displacement volume.

	ID	Height [cm]	Weight [kg]	WSA [m^2]	∇ [m^3]
Female 1	DR	170	63	1.73	0.0643
Female 2	DS	175	62	1.76	0.0633
Male 1	DT	196	90	2.23	0.0918
Male 2	DU	184	78	2.01	0.0796

Experimental procedure Each swimmer was towed 1.0 m below the free surface. The swimmer was attached to the tow-line via a handle with hands centred to replicate a standard glide position. From previous bootstrap statistical analyses (Webb, 2013), five repeat runs showed reasonable accuracy for the resistance of a swimmer towed under the water. In this study, between seven and twelve repeats were retained depending on time allocated and swimmer's consistency as mentioned in the speed reel study.

3.3.3 Results and discussion

Results from the British Swimming tests are presented in Figures 3.11 and 3.12. Speedo tests' results are displayed in Figure 3.13. The results highlight the mean of the measured data (drag coefficient for speed reel and drag for tow rig) and the relative standard deviation (a.k.a. coefficient of variance) for each configuration tested. The equipment worn is detailed with the brand, type and size. The percentage difference in measured data between the different configurations is given, alongside an estimated time savings for a 100-m freestyle race based on Webb (2013) race simulator (simulator set to: combined surface and fully submerged conditions). Further details on the simulator developped by Webb (2013) are given in Section 5.4. A colour code was applied to the configurations based on the permutation test results (see Section 3.3.3):

- If $p \leq 0.05$, the configuration with less drag is coloured green (statistically favourable) and the configuration with higher drag is coloured red (statistically unfavourable).
- If $p \geq 0.05$, the configuration with less drag is coloured orange (favourable but not statistically significant).

Athlete ID	Configuration	Cap	Goggles	Suit	Cd	STDEV	Rel. STDEV	% Cd difference between configurations A, B, C (A-B)/A	(A-C)/A	(B-C)/B	Race time saved on 100 m freestyle [s]
BO	A	Speedo silicon standard size	Speedo Speedsocket	Arena Full Body revo + open-water s28	0.01691	0.00039	2%	-1.6%	-0.3%	1.2%	0.16
	B	Speedo silicon standard size	Speedo Speedsocket	Adidas jammers S26	0.01717	0.00046	3%				
	C	Speedo Silicon Standard Size	Speedo Speedsocket	Adidas Leg S28	0.01696	0.00060	4%				
DO	A	Arena 3D race L Loughborough Club (under)	Speedo Speedsocket	Arena Full body revo + open-water S28 (M)	0.01729	0.00030	2%	-2.0%	-7.3%	-5.2%	0.20
	B	Arena 3D race L Loughborough Club (under)	Speedo Speedsocket	Arena Leg revo + open-water S28	0.01763	0.00067	4%				
	C	Arena 3D race L Loughborough Club (under)	Speedo Speedsocket	Speedo LZR 1 S28	0.01855	0.00037	2%				
DL	A	Arena moulded standard size	Arena Cobra	Arena Carbon-Flex S28	0.01368	0.00057	4%	0.6%	-	-	0.06
	B	Speedo bullet cap L	Speedo Swedish	Speedo LZR S26	0.01360	0.00063	5%				
W	A	Arena 3D Ultra Cap L	Arena Cobra	Arena Carbon-Flex S28	0.01435	0.00057	4%	-1.8%	-	-	0.18
	B	Speedo Fastskin bullet L	Speedo Aquasocket	Adidas GB Team S28	0.01462	0.00046	3%				
BJ	A	Arena ultra-cap L	Arena Cobra	Arena Carbon-flex S28	0.01369	0.00046	3%	-1.3%	-	-	0.13
	B	Speedo Fastskin bullet L	Speedo Speedsocket	Speedo LZR old S26	0.01386	0.00044	3%				

FIGURE 3.11: British Swimming male results - equipment testing on speed reel.

Athlete ID	Configuration	Cap	Goggles	Suit	Speed [m/s]	Rt [ll]	STDEV	Rel. STDEV	% Drag difference between configurations A, B, C (C-A)/C	(C-B)/C	(B-A)/B	Race time saved on 100 m freestyle [s]
Male												
DT	A	Speedo Fastskin bullet cap M	Speedo Elite	Speedo Training - 6 cm brief	2.16	155	3.97	3%	-4%	3%	-7%	0.69
	B	Speedo Fastskin bullet cap M	Speedo Elite	Speedo Fastskin LZR 2	2.16	145	6.96	5%				
	C	Speedo Fastskin bullet cap M	Speedo Elite	Speedo New	2.16	149	3.74	3%				
DU	A	Speedo Fastskin bullet cap M	Speedo Elite	Speedo Training - 6 cm brief	2.15	132	5.94	5%	-4%	-1%	-3%	0.41
	B	Speedo Fastskin bullet cap M	Speedo Elite	Speedo Fastskin LZR 2	2.18	128	5.31	4%				
	C	Speedo Fastskin bullet cap M	Speedo Elite	Speedo New	2.19	126	3.41	3%				
Female												
DR	A	Speedo Fastskin bullet cap M	Speedo Elite	Speedo 711 powerback	2.05	102	4.59	5%	-17%	3%	-21%	2.12
	B	Speedo Fastskin bullet cap M	Speedo Elite	Speedo Fastskin LZR 2	2.06	84	3.43	4%				
	C	Speedo Fastskin bullet cap M	Speedo Elite	Speedo New	2.06	87	3.09	4%				
DS	A	Speedo Fastskin bullet cap M	Speedo Elite	Speedo 712 powerback	2.05	96	1.62	2%	-6%	1%	-7%	0.73
	B	Speedo Fastskin bullet cap M	Speedo Elite	Speedo Fastskin LZR 2	2.05	90	3.68	4%				
	C	Speedo Fastskin bullet cap M	Speedo Elite	Speedo New	2.05	91	1.98	2%				

FIGURE 3.13: Speedo results - suit testing on tow winch.

Athlete ID	Configuration	Cap	Goggles	Suit	Cd	STDEV	Rel. STDEV	% Cd difference (A-B)/A	Race time saved on 100 m
BE	A	Speedo Aqua-V Race Cap L	Arena Cobra	Arena Carbon Flex S28	0.01936	0.00078	4%	-5.4%	0.54
	B	Loughborough Club (under) Speedo Aqua-V Race Cap L Loughborough Club (under)	Speedo Speedsocket	Speedo LZR S24	0.02041	0.00060	3%		
AL	A	Arena 3D ultra L Arena Silicon standard size (under)	Arena X-Vision	Arena Carbon Flex S26	0.02093	0.00040	2%	2.4%	0.24
	B	Speedo Aqua V Race Cap L Leicester penguins Club (under)	Speedo Speedsocket	Speedo LZR Elite S25	0.02042	0.00042	2%		
AJ	A	Speedo Fast Skin cap Arena Loughborough Club (under)	Speedo Speedsocket	Arena Carbon Flex 28	0.01839	0.00106	6%	-10.8%	1.08
	B	Speedo FastSkin Cap Arena Loughborough club (under)	Speedo Speedsocket	Speedo LZR 24	0.02037	0.00088	4%		
DM	A	Arena Loughborough Club (under) Speedo Aqua V race cap L	Arena X-Vision	Arena Carbon-Flex 28	0.01896	0.00073	4%	-2.6%	0.26
	B	Arena Loughborough Club (under) Speedo Aqua V race cap L	Arena X-Vision	Jaked 24	0.01945	0.00053	3%		
AH	A	Arena Ultra-Cap L	Arena Cobra	Arena Carbon flex S30	0.02346	0.00060	3%	4.4%	0.44
	B	Speedo Aqua-V Race cap L	Speedo Speedsocket	Speedo LZR old S24	0.02244	0.00054	2%		
G	A	Arena Ultra Cap L (bath team cap under)	Arena Cobra	Arena Carbon-Flex S32	0.01968	0.00034	2%	-1.3%	0.13
	B	Speedo Fastskin Bullet M (bath team cap under)	Speedo Speedsocket	Speedo Fastskin 2 S23	0.01993	0.00032	2%		
BG	A	Speedo Aqua V race cap L (Bath team cap under)	Arena X-vision	Arena Carbon-Flex S32	0.02135	0.00058	3%	2.2%	0.22
	B	Speedo Aqua V race cap L (Bath team cap under)	Arena X-vision	Speedo LZR 2 S24	0.02088	0.00048	2%		

FIGURE 3.12: British Swimming female results - equipment testing on speed reel.

Sources of variance The relative standard deviation across the number of runs performed is on average 3%. Although there may be some uncertainty in the data acquisition system, variance is likely to be mainly due to the swimmer.

On the speed reel, it is thought that the force applied by the swimmer on the wall during the push-off can vary. The drag coefficient is plotted against the peak push-off speed for two males and two females (Figure 3.14). Although it was thought as being an important factor, no trend can be seen between the peak push-off speed and the drag coefficient for one athlete.

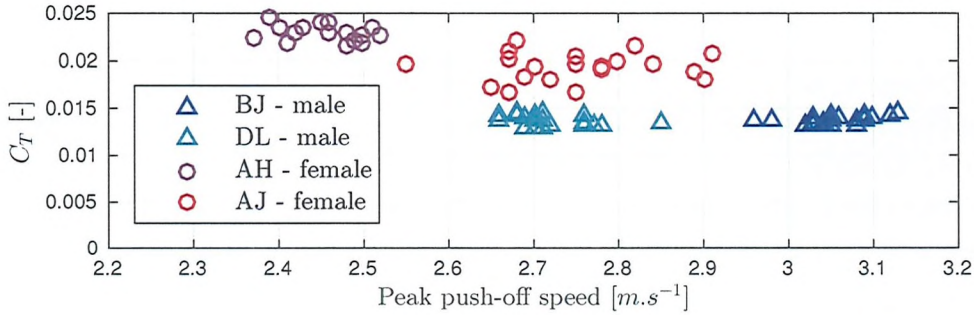

FIGURE 3.14: Influence of peak push-off speed on drag coefficient.

Similarly the effect of fatigue over time as the runs were performed for one male and one female was assessed but no influence on the drag coefficient is to be pointed out (Figures 3.15 and 3.16). The variance is more likely coming from changes in the swimmer's body position (immersion depth/leg yaw), resulting in frontal area changes. Although this is not quantifiable with the current experimental set-up, frontal area is known to have a significant influence on drag (Hoerner, 1965).

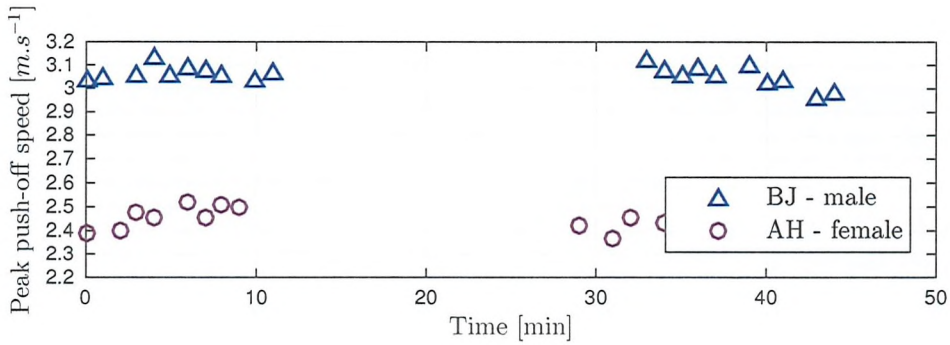

FIGURE 3.15: Effect of fatigue on peak push-off speed.

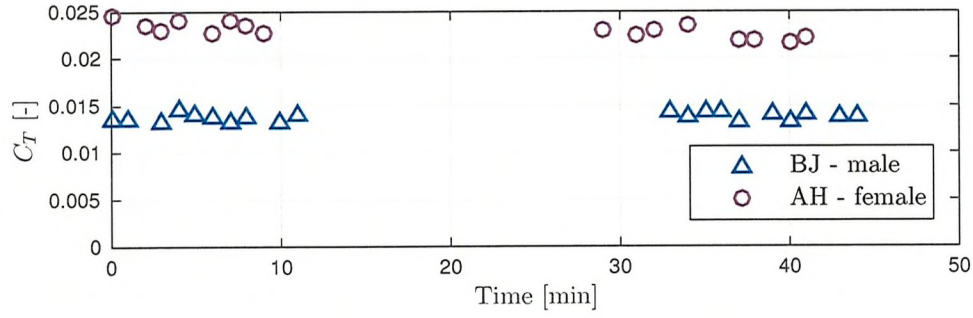

FIGURE 3.16: Effect of fatigue on drag coefficient.

On the tow rig, it can be difficult for the swimmer to keep the same position over the runs (immersion depth/pitch). Due to this unsteady body position, the swimmer experiences varying dynamic forces as shown in Figure 3.17. Consequently, even when averaging the force over the steady speed portion of the tow, the drag force may vary from an experiment to another.

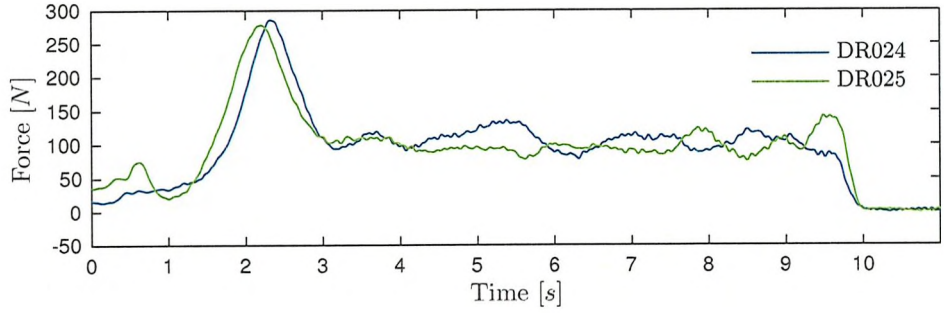

FIGURE 3.17: Comparison of two resistance time traces for the same athlete with the same equipment, showing the influence of body position. (DR024, $R_T = 108N$ and DR025, $R_T = 94N$).

A relative standard deviation of 3% could be considered as small. However, the percentage difference in drag or drag coefficient between two configurations is sometimes less than the relative standard deviation, which makes it difficult to make a judgement on the reliability of the data. Therefore, statistical methods must be used to determine if the difference in mean is statistically significant.

Statistical analyses In order to do this, the null hypothesis is assumed. It claims that the two sets of data come from the same population. In other words, the different configurations have no influence on the variable (drag or drag coefficient).

A small amount of samples (max. n = 10) was collected since the swimmers get tired and cold over time. To test the null hypothesis, a normal distribution is assumed and either a two-sample independent t-test (Lowry, 1998) or a permutation test (Hesterberg et al., 2003) can be applied.

A two-sample t-test assumes equal variance between the two populations. This assumption appears reasonable considering that the same acquisition system and the same athlete with the same likelihood of adopting a different position is tested with both configurations. The t-test calculates a pooled variance (Equation 3.3) from which the t-value can be established (Equation 3.4). The t-value is not a particularly useful value, thus t-tables exist to convert a t-value into a p-value based on the degree of freedom (Equation 3.5), using linear interpolation. This p-value is the probability of the difference between the means to be due to sampling errors. A difference in means is determined to be statistically significant if $p \leq 0.05$ (i.e. level of confidence = 95%). An extract from a t-table is presented in Figure 3.18 (MedCalc, 1993).

$$S_p = \sqrt{\frac{(n_A - 1) * S_A^2 + (n_B - 1) * S_B^2}{n_A + n_B - 2}} \tag{3.3}$$

where for i = A or B, the sample variance is: $S_i^2 = \frac{1}{n_i - 1} \sum_{j=1}^{n_i} (y_j - \bar{y_j})^2$

$$t = \frac{\bar{A} - \bar{B}}{S_p \sqrt{\frac{1}{n_A} + \frac{1}{n_B}}} \tag{3.4}$$

$$df = n_A + n_B - 2 \tag{3.5}$$

where: S_p is the pooled variance. n_A is the number of runs in sample A, with mean $\bar{A}$; and n_B is the number of runs in sample B, with mean $\bar{B}$. t is the t-value with its associated degree of freedom df.

As an example, let us consider, in Table 3.3, the drag coefficients recorded for athlete AH tested on the speed reel (Testing session # 20).

TABLE 3.3: Data sets of drag coefficients for athlete AH in suits A and B with a t-test statistical analysis (Testing session # 20).

		Suit A		Suit B
Drag	AH002	0.02069	AH010	0.01939
coefficients	AH003	0.01982	AH011	0.01901
	AH004	0.01926	AH012	0.01927
	AH005	0.02037	AH013	0.01983
	AH006	0.01911	AH014	0.01851
	AH007	0.02024	AH015	0.01848
	AH008	0.01973	AH016	0.01826
	AH009	0.01913	AH017	0.01869
Mean	$\bar{A}$	0.01979	$\bar{B}$	0.01893
Sample size	n_A	0.01979	n_B	0.01893
Sample variance	S_A	3.62×10^{-7}	S_B	2.90×10^{-7}
% diff. (B-A)/A		-4.4%		
Pooled variance		5.71×10^{-4}		
t-value		3.027		
Degree of freedom		14		
p-value		0.009		

The t-test was applied to all athletes tested and it was noticed that when the difference in means was below the relative standard deviations of both samples, the difference in means was not statistically significant. In other words, the different configurations have no effect on the measured data (drag or drag coefficient).

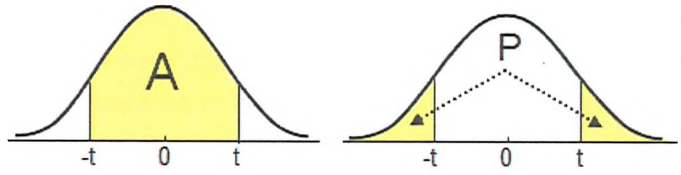

DF	A P	0.80 0.20	0.90 0.10	0.95 0.05	0.98 0.02	0.99 0.01	0.995 0.005	0.998 0.002	0.999 0.001
1		3.078	6.314	12.706	31.820	63.657	127.321	318.309	636.619
2		1.886	2.920	4.303	6.965	9.925	14.089	22.327	31.599
3		1.638	2.353	3.182	4.541	5.841	7.453	10.215	12.924
4		1.533	2.132	2.776	3.747	4.604	5.598	7.173	8.610
5		1.476	2.015	2.571	3.365	4.032	4.773	5.893	6.869
6		1.440	1.943	2.447	3.143	3.707	4.317	5.208	5.959
7		1.415	1.895	2.365	2.998	3.499	4.029	4.785	5.408
8		1.397	1.860	2.306	2.897	3.355	3.833	4.501	5.041
9		1.383	1.833	2.262	2.821	3.250	3.690	4.297	4.781
10		1.372	1.812	2.228	2.764	3.169	3.581	4.144	4.587
11		1.363	1.796	2.201	2.718	3.106	3.497	4.025	4.437
12		1.356	1.782	2.179	2.681	3.055	3.428	3.930	4.318
13		1.350	1.771	2.160	2.650	3.012	3.372	3.852	4.221
14		1.345	1.761	2.145	2.625	2.977	3.326	3.787	4.140
15		1.341	1.753	2.131	2.602	2.947	3.286	3.733	4.073
16		1.337	1.746	2.120	2.584	2.921	3.252	3.686	4.015
17		1.333	1.740	2.110	2.567	2.898	3.222	3.646	3.965
18		1.330	1.734	2.101	2.552	2.878	3.197	3.610	3.922
19		1.328	1.729	2.093	2.539	2.861	3.174	3.579	3.883
20		1.325	1.725	2.086	2.528	2.845	3.153	3.552	3.850

FIGURE 3.18: Extract from a t-table to convert a t-value into a p-value (MedCalc, 1993). Using linear interpolation, the p-value for the suits A and B for athlete AH can be determined by looking at the row degree of freedom = 14 and looking for the p-value range corresponding to the t-value, as framed in blue.

Another statistical method, permutation tests, was applied to see if more insight in the data could be obtained. The permutation tests also assess the null hypothesis by randomly re-sampling the data from either sample A or B to create 10000 sets of sample 1 and 2. In this case, the p-value is defined by Equation 3.6.

$$p = \frac{\#[(C_{T1} - C_{T2}) > (C_{TA} - C_{TB})]}{n+1} \tag{3.6}$$

where: n is the number of permutations.

The permutation test results are plotted in Appendix C for each athlete. An example for a female athlete is provided in Figure 3.19. The bootstrap distribution of each configuration is plotted with lines for the confidence interval set at a 95% confidence level.

The bootstrap distribution is obtained by re-sampling the data. This provides a visual indication of the likely variance of the population from which the data were sampled. The difference in means is statistically significant if the p-value is below 0.05. In the results' tables (Figures 3.11, 3.12 and 3.13), a colour code was applied to the configurations based on the permutation test results. If $p \leq 0.05$, the configuration with less drag is coloured green (statistically favourable) and the configuration with higher drag is coloured red. If $p \geq 0.05$, the configuration with less drag is coloured orange (favourable but not statistically significant). The permutation tests allow the experimenter to favour a configuration compared to another one with statistical significance ($p \leq 0.05$) even if the relative standard deviation is greater than the difference in means.

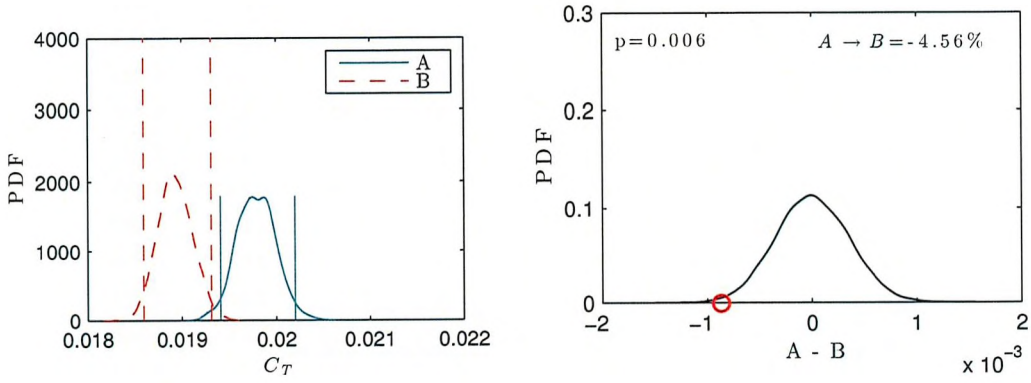

FIGURE 3.19: Statistical analysis for Athlete AH - Bootstrap distribution with 95% confidence interval (left) and permutation test (right). o: True mean.

Based on these statistical results, recommendations were made to each individual British Swimming athlete as to which configuration he/she should be wearing for minimum resistance through the water. No swimmers changed just goggles or caps between the two configurations, thus no conclusions on the impact of these devices on the drag can be made. However, in some cases, only the suit was changed. Sometimes the Arena Carbon Flex suit was better, sometimes the Speedo LZR was better. It therefore appears that the selection of a suit for an elite swimmer is morphology-dependent rather than a set choice, hence the need to drag-test all British Swimming athletes. Since females benefit from a larger suit surface area, the drag difference between two suits can be significant (up to 11% between two elite suits).

It is important to note that feel of the equipment may be as important during a race and should therefore be taken into account when selecting equipment for a specific athlete. From this study, it is thought that there is a definite competitive advantage for an elite athlete to swim in a race knowing that he/she has the best equipment configuration amongst pre-selected equipment choices.

The Speedo suit testing session was aimed at answering a different question. Are the new suits (male/female) better than the previous elite suits? This is a difficult question

since it was previously shown with the British Swimming athletes testing that suit performance was dependent on the athlete. To avoid bias due to athlete morphology, the tests were performed for two males and two females. The old suit proved to be statistically better for only one male and one female. The other male had less resistance with the new suit and the other female had better performance with the old suit, but the results were not statistically significant. This testing session demonstrates the need to test several athletes with varying morphologies to draw conclusions on the overall performance of a suit compared to another one.

Combined suit testing results A large range of elite swimmers were drag-tested with two different methodologies. With the speed reel, a velocity-dependent resistance is measured over a decelerating phase which leads to a drag coefficient; whereas on the tow rig, the resistance of the swimmer is directly recorded. In order to learn about the effect of morphology (height/weight) on a swimmer's resistance, all the resistance data obtained from the speed reel or the tow rig should be combined. To do so, the drag coefficient relationship defined in Equation 3.2 was used and the speed was set as the towing speed. Figure 3.20 presents the total resistance and its non-dimensional form versus weight of the least resistance configuration for each athlete.

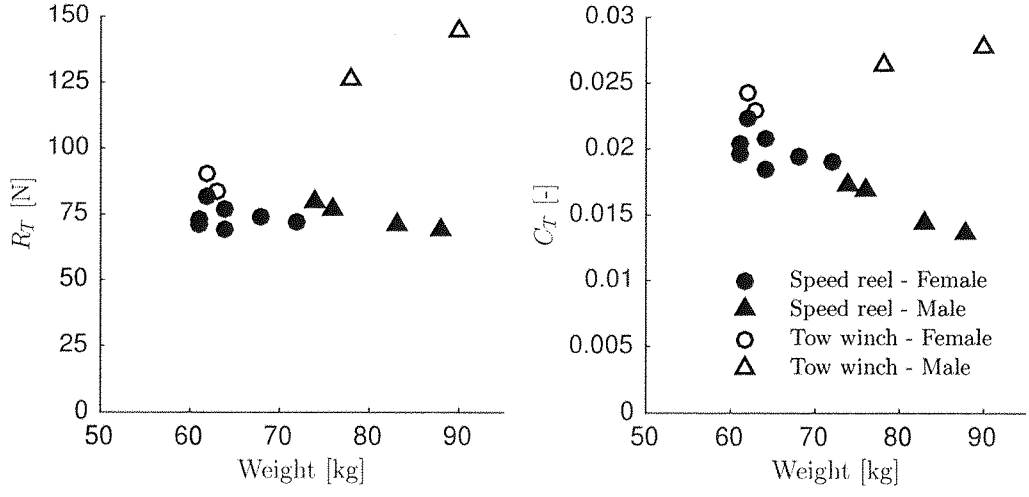

(a) Total resistance

(b) Total resistance coefficient

FIGURE 3.20: Comparison of speed reel and tow rig resistance data versus weight.

The resistance data obtained from the speed reel method appear to be under-estimated compared to the tow rig data, especially as the weight of the swimmer increases. In both cases, the swimmer is fully submerged and there is no wave resistance. Consequently, the total resistance reduces to the viscous resistance (Equation 3.7) and is expressed as a function of the frictional resistance, which can be estimated using the ITTC 1957 formula (Equation 3.8). The frictional resistance only varies by about 0.001 across the

deceleration phase when pushing-off the wall (Figure 3.21). The difference between the speed reel and tow rig data is more likely due to the difference in the adopted body position as shown in Figure 3.22.

$$C_T = C_V + C_W = (1 + k)C_F + 0 \tag{3.7}$$

$$C_F = \frac{0.075}{(log_{10}(Re) - 2)^2} \tag{3.8}$$

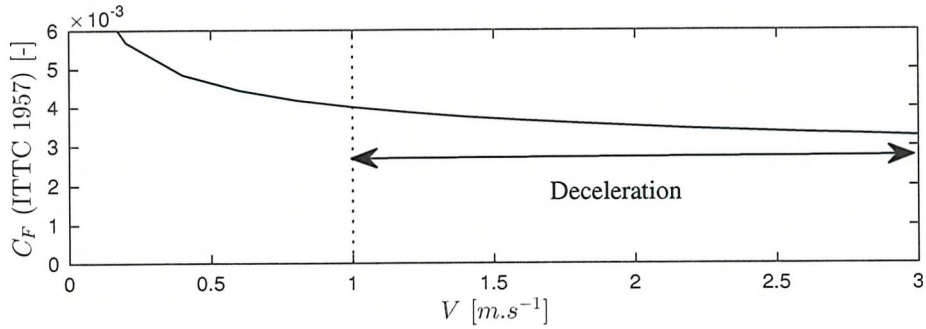

FIGURE 3.21: ITTC 1957 skin friction coefficient, C_F.

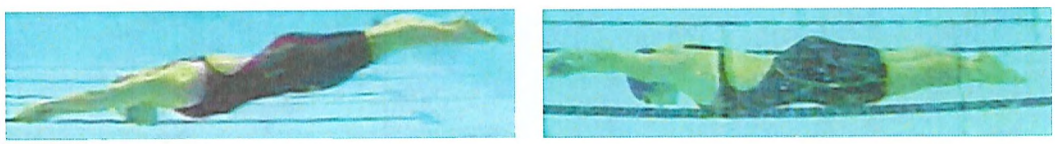

(a) Speed reel (Swimmer AH) (b) Tow rig (Swimmer DR)

FIGURE 3.22: Different body position during suit testing on speed reel and tow rig.

Another source of discrepancy is the absence of the added-mass in the determination of the drag coefficient for the speed reel runs. Indeed, with the body deceleration, an unknown amount of added-mass proportional to the body mass should be included. The drag coefficient obtained from the speed reel would thus increase and a better match with the tow rig data would be reached. The added-mass of a swimmer, in a set position, could be determined by accelerating the swimmer at a constant rate across the swimming pool using the tow rig. This is left as further work due to time constraint.

3.4 Chapter summary

In this chapter, the systems used to measure swimmers' resistance have been presented, alongside detailed calibration procedures emphasing the reliability of the systems in place.

Equipment were drag-tested with elite athletes with two different methodologies. With the speed reel, a velocity dependent resistance is measured over a decelerating phase which leads to a drag coefficient; whereas on the tow rig, the resistance of the swimmer is directly recorded. The relative standard deviation across the number of runs performed is on average 3%. Although this could be considered as small, the percentage difference in drag or drag coefficient between two configurations is sometimes less than the relative standard deviation, which makes it difficult to make a judgement on the reliability of the data. Consequently, the permutation test statistical method was used to determine if the difference in means was statistically significant.

No swimmers changed just goggles or caps between the two configurations, thus no conclusions on the impact of these devices on the drag could be made. However, in some cases, only the suit was changed. Across all the athletes tested, results indicate that the performance of a suit is morphology-dependent. Further studies on suit testing on a swimmer should be performed.

Although the pool testing systems allow swimmers to select their best equipment in some cases, there still exist some issues with the swimmers' variability. In addition, it remains difficult to take elite swimmers out of their training environment. To remedy to both the swimmers' variability and their lack of availability, it was thought that a numerical pool could be implemented (Chapter 4).

4

Numerical Simulations
A swimmer's passive resistance at the free surface

As highlighted in Chapter 3, even at an elite level, human variability in swimming technique is inevitable. In order to reduce the impact of swimmers' variability on the performance measured, the swimmers would be required to be tested over a longer period of time. However, this is not feasible due to the athletes becoming cold and fatigued, and thus further increasing their natural variability. In addition, swimming is a sport which requires a large amount of training time and it is thus difficult to take swimmers out of their training programme.

Numerical simulations thus appear to be a natural choice to answer research questions on swimming performance. By replicating a pool environment in a computer, the elite swimmers' involvement in research can be limited. In this chapter, an experimental test case of a swimmer passively towed at the free surface is simulated using a 2-D linear potential flow theory (thinship) and 3-D URANS method (Banks, 2013). This test case is aimed at determining whether numerical simulations could be used to study the passive resistance of a swimmer located at the free surface.

4.1 Experimental test case

During testing session #7, a male swimmer was passively towed at the free surface of a 25-m swimming pool with arms by his sides, with a tow-belt fixed around his waist.

The total resistance of the swimmer was measured by the tow rig system and wave elevations were recorded by the wave probes located at distances y =1.50, 1.75 and 2.00 m away from the track of the swimmer. The schematic of the pool experimental set-up is provided in Figure 4.1.

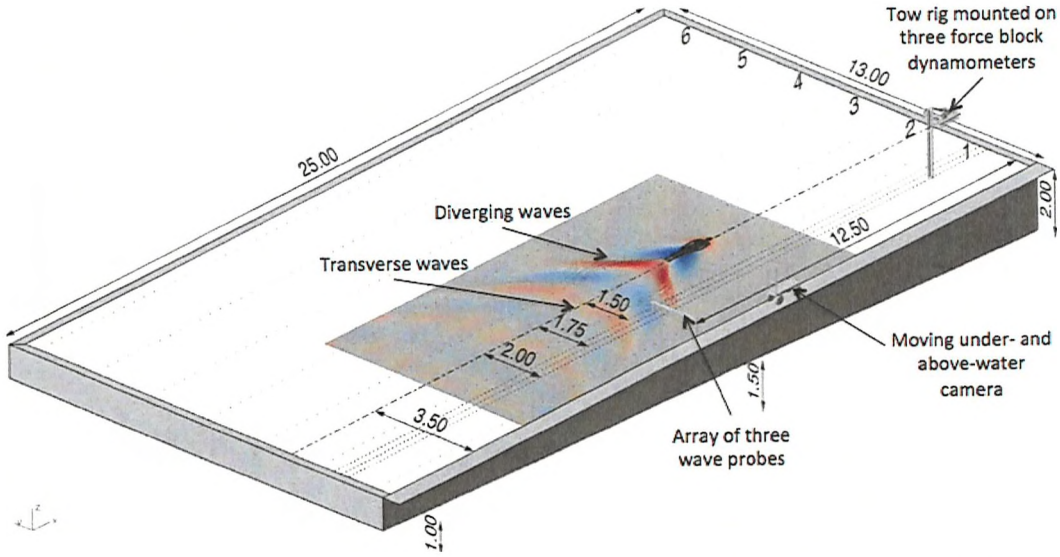

FIGURE 4.1: Schematic of the University of Southampton Jubilee swimming pool with infinity edges.

The swimmer was towed at two typical elite swimming speeds: 1.7 $m.s^{-1}$ (Case 1) and 2.1 $m.s^{-1}$ (Case 2), and three repeat runs were performed at each speed. This experimental case was simulated using a 2-D linear potential flow theory (Thinship) and a 3-D URANS method.

4.2 Geometry

A generic body scan of a human with his arms by his sides was used as a basis athlete geometry. This body scan was modified with an in-house meshing tool, Adaptflexi (Turnock (2004)), so as to match the different case conditions. This software has the capability to take a STereoLithography geometry (.STL file) and deform it in a number of different ways. First, variable scale factors are applied along the body to match a specific athlete's body shape. Secondly, joint rotations are performed to match the athlete's attitude and posture from the video footage acquired during the experiment (Figure 4.2). The total length of the swimmer with extended feet is 1.91 m.

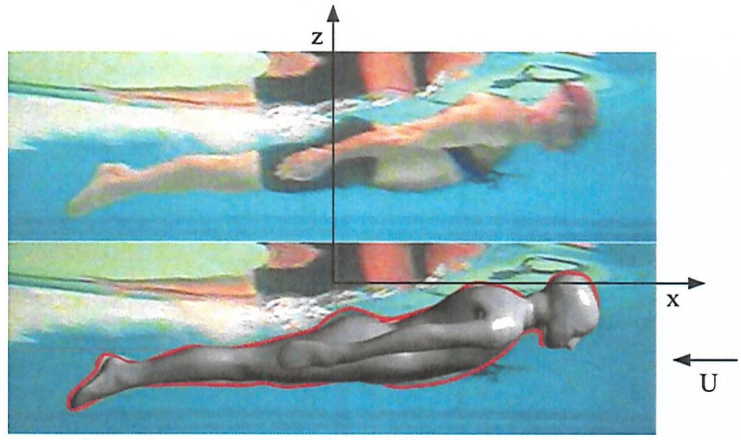

FIGURE 4.2: Swimmer's position from the under-water camera view used to modify a generic scanned body, at 2.1 $m.s^{-1}$. The axis system corresponds to the one used for both simulations (Thinship and CFD). The swimmer's body is located on the centreline (i.e. $y = 0$). The plane $z = 0$ corresponds to the calm free surface.

4.3 2-D linear potential flow theory - Thinship

An early linear potential flow method was pioneered by Michell (1898) and Eggers (1955), and further developed by Insel (1990) in order to determine the wave pattern of slender bodies and their associated wave resistance through a homogeneous, inviscid, incompressible fluid and an irrotational flow. The implementation undertaken by Taunton (2012) was chosen.

The domain width was set as 7 m to match the pool experimental set-up. The swimming pool has a varying pool depth, starting at 1 m from one end to 2 m on the other end. A study on the effect of water depth on wave resistance was first carried out. The wave cuts at 2.1 $m.s^{-1}$ are plotted in Figure 4.3 at depths of 1 m and 2 m. A different wave pattern is observed at the probe located furthest away from the swimmer. This indicates that there is a change in wave resistance when towing the swimmer along the length of the pool with varying depth. Indeed, the wave resistance of the swimmer changes with the water depth (Figure 4.4); the wave resistance in a water depth of 2 m shows a percentage decrease of 1% at 1.7 $m.s^{-1}$ and down to 8% at 2.5 $m.s^{-1}$, compared to when the domain depth is set to 1.0 m. Based on this study, a constant water depth of 1.5 m is to be used when performing a wave resistance analysis of wave cuts obtained in the Jubilee pool at the University of Southampton. The critical depth based Froude number ($Fr_D = 1$) occurs at a speed of 3.1 $m.s^{-1}$ at 1 m depth and 4.4 $m.s^{-1}$ at 2 m depth. Consequently, the swimmer is always in the sub-critical Froude number regime when towed on the free surface in the Jubilee pool at typical free surface swimming speeds (i.e. up to 2.2 $m.s^{-1}$).

For the boundary conditions, the inlet and outlet boundary field types are defined as a fixed velocity inlet/outlet respectively. The free stream velocity range chosen is based on the elite swimmer speed range of 1.0 to 2.5 $m.s^{-1}$. The upper, bottom and side walls are given a slip condition as the effects of shear stress are considered negligible.

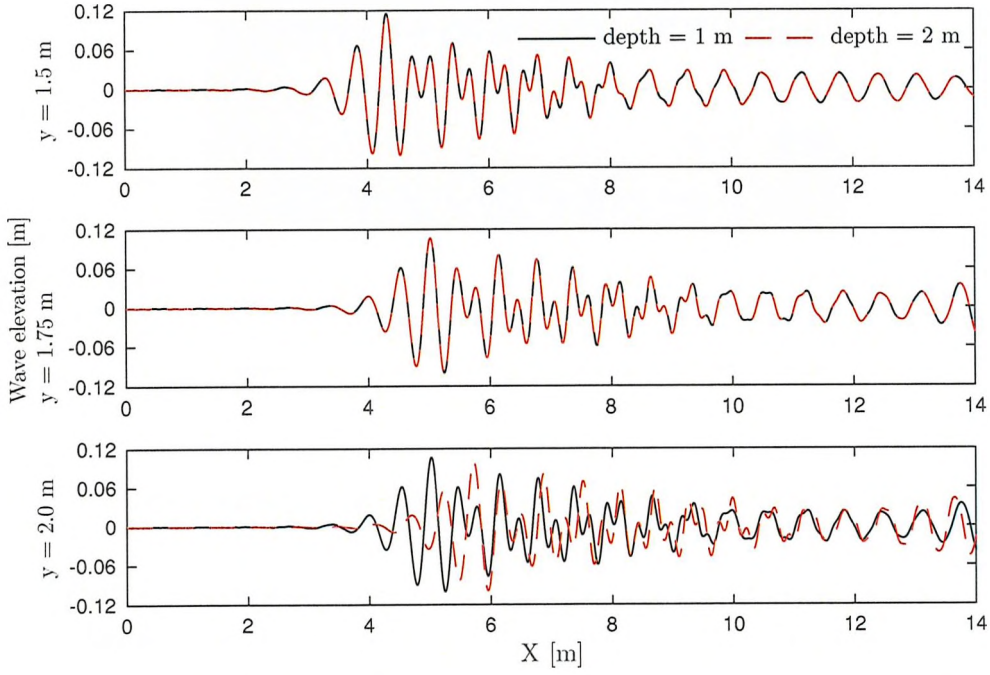

FIGURE 4.3: Wave elevation obtained from thinship theory at 2.1 $m.s^{-1}$ at two different tank depths, 1 m and 2 m.

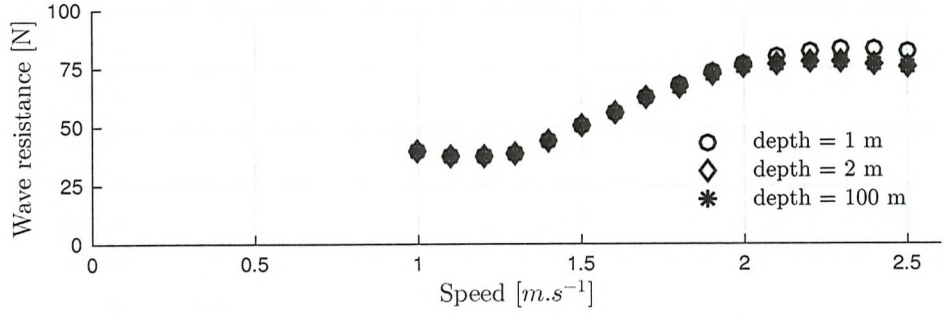

FIGURE 4.4: Influence of pool depth on wave resistance across the swimmer's speed range 1.0 - 2.5 $m.s^{-1}$.

The swimmer's geometry, presented in Figure 4.2, was discretised with 1.8 $\times 10^4$ panels. The disturbance velocity potential of the discretised body is assumed to be generated by a planar distribution of Havelock sources over the centreline of the body (y = 0 - Figure 4.5). These sources have a strength, σ, proportional to the panel area (Equation 4.1) (Couser et al., 1998).

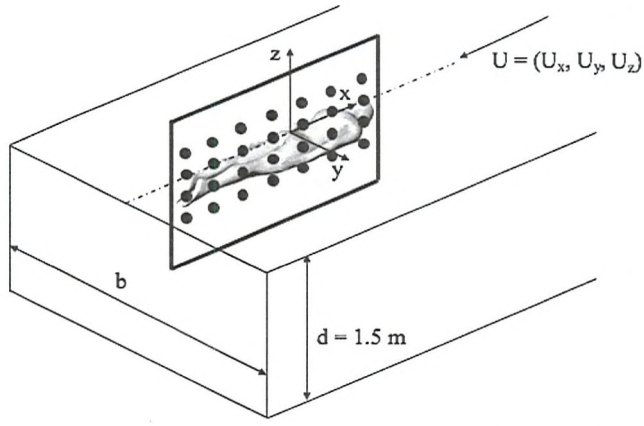

FIGURE 4.5: Thinship domain illustrating the principle of a planar distribution of Havelock sources.

$$\sigma = \frac{-1}{2\pi}\vec{n}\cdot\vec{U} \times panel\ area \tag{4.1}$$

where, $\vec{n}$ is the outward unit normal vector of the panel and $\vec{U} = (U_x, U_y, U_z)$ is the free stream velocity.

The wave pattern generated from these sources can be numerically described using the 'Eggers series' (Equation 4.2). The associated wave resistance is evaluated with Equation 4.4 (in deep water conditions). A full derivation of these equations is provided in Appendix B.

$$\zeta(x,y) = \sum_n \xi_n cos(x\gamma_n cos\theta_n) + \eta_n sin(x\gamma_n cos\theta_n) cos\left(\frac{2\pi n}{b}y\right) \tag{4.2}$$

For a source at $(x_\sigma,\ y_\sigma,\ z_\sigma)$, the Eggers coefficients, ξ_n and η_n, are :

$$\begin{aligned}\begin{bmatrix}\xi_n\\ \eta_n\end{bmatrix} =& \frac{16\pi U}{bg}\frac{\bar{\omega}+\omega_n\cos^2\theta_n}{1+\sin^2\theta_n-\omega_n-\bar{\omega}h\,sech^2(\omega_n h)}\\ &\times\sum_\sigma\left[\sigma_\sigma e^{-\omega_n h}\cosh[\omega_n(h+z_\sigma)]\begin{bmatrix}\cos(\omega_n x_\sigma cos\theta_n)\\ \sin(\omega_n x_\sigma\cos\theta_n)\end{bmatrix}\begin{matrix}\cos\frac{n\pi y_\sigma}{b}\\ \sin\frac{n\pi y_\sigma}{b}\end{matrix}\right]\end{aligned} \tag{4.3}$$

$$R_w = \frac{1}{4}\rho g b\left[\left(\xi_0^2+\eta_0^2\right)+\sum_{n=1}^{M}\left(\xi_n^2+\eta_n^2\right)\left(1-\frac{1}{2}cos^2\theta_n\right)\right] \tag{4.4}$$

4.4 3-D non-linear computational fluid dynamics

For naval architects, Thinship, as a 2-D potential flow method, is a well known tool to quickly evaluate the wave pattern of a slender object and thus its wave resistance (Molland et al., 2002). However, since the fluid is treated as inviscid, the influence of the boundary layer cannot be easily modelled, leading to unrealistic values of the total resistance. In order to numerically evaluate the total resistance of a swimmer, 3-D non-linear CFD methods taking into account the viscosity of the fluid are required.

4.4.1 Navier-Stokes equations

The fluid properties around the swimmer were solved with the Unsteady Reynolds-Averaged Navier-Stokes (URANS) equations. This set of equations is governed by three laws of conservation: mass, momentum and energy. Nevertheless, water is treated as an incompressible Newtonian fluid allowing the elimination of the energy conservation law.

The principle of conservation of mass states that the rate of change of mass in an infinitesimally small control volume is equal to the rate of mass flux through its bounding surface. Using the Cartesian tensor form, this principle is characterised by the continuity equation (Equation 4.5):

$$\frac{\partial u_i}{\partial x_i} = 0 \tag{4.5}$$

The principle of conservation of momentum states that the rate of change of momentum for the infinitesimally small control volume is equal to the rate at which momentum is entering or leaving through the surface of the control volume, plus the sum of the forces acting on the volume itself (Equation 4.6).

$$\rho\frac{\partial u_i}{\partial t} + \rho\frac{\partial}{\partial x_j}(u_j u_i) = -\frac{\partial p}{\partial x_i} + \mu\frac{\partial}{\partial x_j}\left(\frac{\partial u_i}{\partial x_j} + \frac{\partial u_j}{\partial x_i}\right) \tag{4.6}$$

Combining Equations 4.5 and 4.6 leads to the equations of motion of the incompressible Navier-Stokes equations :

$$\rho\frac{\partial u_i}{\partial t} + \rho u_j\frac{\partial u_i}{\partial x_j} = -\frac{\partial p}{\partial x_i} + \mu\frac{\partial^2 u_i}{\partial x_i \partial x_j} \tag{4.7}$$

As discussed in the introductory chapter (Section 1.4), an elite swimmer races in a turbulent flow regime with $1.2 \times 10^6 \leq Re \leq 7.4 \times 10^6$, and with a local Re for the head being in the transitional boundary layer flow regime, $1.1 \times 10^5 \leq Re \leq 6.6 \times 10^5$.

To solve the unsteady Navier-Stokes equations in such a turbulent flow regime, a very fine mesh and time step would be required to ensure all turbulent eddies could be captured. These types of simulations are known as Direct Numerical Simulations (DNS). They involve a very large amount of computational power and thus at the present time, it is not a viable option for most engineering fields dealing with high Reynolds numbers.

4.4.2 Turbulence modelling

Due to the highly turbulent character of the flow around a swimmer, the field properties (velocities and pressures) become random functions of time and space. In order to solve those properties, they are expressed as the sum of mean and fluctuating properties, also known as the Reynolds decomposition (Equations 4.8 and 4.9).

$$u_i = U_i + u_i^{'} = \frac{1}{\Delta t}\int_0^{\Delta t} u_i(t)\mathrm{d}t + u_i^{'} \tag{4.8}$$

$$p = P + p^{'} = \frac{1}{\Delta t}\int_0^{\Delta t} P(t)\mathrm{d}t + p^{'} \tag{4.9}$$

where $u_i^{'}$ and $p^{'}$ represent the fluctuating velocities and pressure around their respective means U_i and P. When dealing with unsteady simulations, the averaging period Δt corresponds to the simulation time step. The definition of the time step is critical for unsteady flows as it determines the precision at which turbulence effects are captured.

The non-linear Navier-Stokes equations may then be simplified by introducing the concept of time-averaging. Substituting Equations 4.8 and 4.9 into Equation 4.7 and time-averaging gives rise to the Reynolds-Averaged Navier-Stokes (RANS) equations.

$$\frac{\partial U_i}{\partial t} + U_j\frac{\partial U_i}{\partial x_j} = -\frac{1}{\rho}\frac{\partial p}{\partial x_i} + \nu\frac{\partial^2 U_i}{\partial x_i \partial x_j} - \frac{1}{\rho}\frac{\tau_{ij}}{\partial x_j} \tag{4.10}$$

where i and j represent the spatial dimensions 1, 2 and 3.

The last term in the above equation includes the so-called Reynolds Stresses $\tau_{ij} = \overline{u_i^{'}u_j^{'}}$. These terms are responsible for the non-closure of the RANS system of equations. As a result, the introduction of a set of equations known as a 'turbulence model' is required to solve the fluid properties.

The most common approach is the Boussinesq hypothesis (Boussinesq, 1877) which relates the Reynolds stresses to the mean velocity gradients as defined in Equation 4.12.

$$-\tau_{ij} = -\overline{u_i^{'}u_j^{'}} = \nu_T\left(\frac{\partial U_i}{\partial x_j} + \frac{\partial U_j}{\partial x_i}\right) - \frac{2}{3}k\delta_{ij} \tag{4.11}$$

where k is the turbulent kinetic energy; $k = \frac{1}{2}\overline{u_i'u_j'}$ (KE per unit mass) and, ν_T is the kinetic eddy viscosity $[Ns.m^{-2}]$.

The local eddy viscosity, τ_{ij}, is thus linked to the local velocity- and length-scales, both defining turbulences. Consequently, to close the system of equation, this model requires two transport equations for the intensity (velocity-scale) and dissipation rate (length-scale) of the turbulent kinetic energy. These equations are typically referred to as a two-equation model and the most common types are $k-\epsilon$ and $k-\omega$ turbulence models.

On one hand, the $k-\epsilon$ equation model is known to provide a good prediction of the behaviour of the viscous wake (Launder, B. and Sharma, 1974), but stability problems through the viscous sub-layer have been reported (Menter, 1994). On the other hand, Wilcox (1988) defined the $k-\omega$ turbulence model which takes into account the near-wall mesh spacing but it cannot cope with solving the turbulent transport energy in the viscous wake.

Nevertheless, for simulating the flow past a swimmer, both the near-field (separation) and far-field (viscous wake) turbulent energy transport need to be accurately modelled. Menter et al. (2003) applied a blending function to switch between the two models, creating the now-widely used turbulence model $k-\omega$ Shear Stress Transport. This model provides a reasonable representation of a boundary layer under adverse pressure gradients, separation and recirculation, and is consequently chosen as the turbulence model of preference for this study. The turbulent kinetic energy k, the turbulent dissipation rate ω and the turbulent viscosity ν_T are respectively defined as follows:

$$k = \frac{3}{2}(UI)^2\omega = C_\mu^{-\frac{1}{4}} * \frac{\sqrt{k}}{l}\nu_T = \frac{3}{2}(UIl) \tag{4.12}$$

A turbulence intensity, I, of 1% was selected, although an investigation on the influence of the turbulence intensity level on the results should be performed. The turbulent length scale,l, was based on 0.07D and the usual turbulent constant, C_μ of 0.09 was used. The turbulence model entry fields (k, ω, ν_T) have fixed inlet values and zero gradient outlet boundary conditions.

4.4.3 Numerical scheme

A second order Pressure Implicit Splitting of Operators (PISO) finite volume method was chosen to discretise the URANS equations derived above. This algorithm allows the time step to be adjusted during the simulation to meet a pre-defined Courant number limit.

4.4.4 Multi-phase model

A Volume Of Fluid (VOF) approach was used for the free surface with the volume fraction transport equation defined as:

$$\partial\phi\partial t + \frac{(\partial\phi U_j)}{\partial x_j} = 0 \tag{4.13}$$

where ϕ is the volume fraction calculated as the volume ratio of water to air in a given cell (Peric and Ferziger (2002)).

The fluid density, ρ, and viscosity, μ, can then be respectively calculated as:

$$\rho = \rho_{air}(1-\phi) + \rho_{water}\phi \tag{4.14}$$

$$\mu = \mu_{air}(1-\phi) + \mu_{water}\phi \tag{4.15}$$

4.4.5 Mesh

A hybrid mesh around the swimmer was created using the snappyHexMesh utility within the open source CFD package OpenFOAM-2.2.0 (OpenFOAM (2013)). The domain dimensions, 14.0 x 7.5 x 3.0 [m^3], were set to match the pool experimental set-up (Figure 4.6). The domain length allows for one body length before the swimmer and five body lengths behind, for the wave pattern to develop, as typically used according to best practices (Banks, 2013). A fixed depth of 2.0 m was set for the water phase, although in the experiment there is a varying bottom depth. An air draught of 1.0 m was chosen; it is thought not to have much influence since the air resistance is negligible.

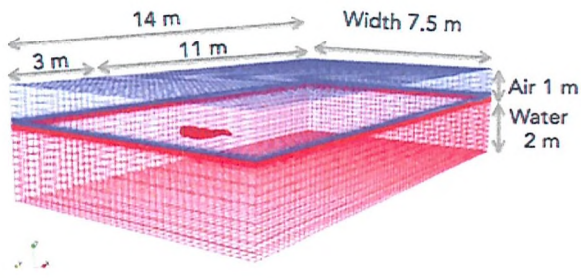

FIGURE 4.6: CFD domain dimensions matching the experiment.

Boundary conditions were chosen to closely represent the experimental pool conditions. The velocity and pressure fields inlet and outlet boundary conditions are fixedValue/outletInlet and zeroGradient/fixedValue respectively. The swimmer is modelled as a non-slip wall and the sides are considered as slip to reduce the computational time.

First, a coarse unstructured hexahedral block mesh was created with cells of 0.2 m in each direction of the entire domain. Regions were defined with up to six levels of isotropic refinement (recursively halving in all three local cell dimensions six times), gradually increasing the mesh density near the body, whilst maintaining a cell aspect ratio of approximately one. A structured boundary layer was added with elements growing out from the body surface mesh to provide a y^+ around 1. This places approximately 10 cells within an estimated y^+ of 40 allowing the viscous boundary layer to be captured (WS Atkins Consultants (2003)). These different levels of refinement allow high-pressure gradients just upstream of the swimmer, around it and in the wake, to be effectively captured.

In addition, uni-directional refinement was applied perpendicular to the free surface to provide good wave pattern resolution, whilst minimising mesh size. Moreover, with the use of a smooth growth rate throughout the domain, a numerical beach was created to damp any waves which may be reflected. The developed mesh structure contains approximately eight million elements and is shown in side elevation and plan view (Figure 4.7).

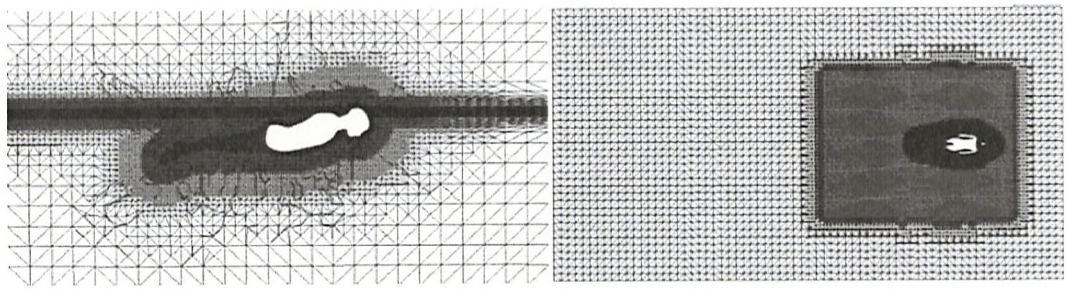

FIGURE 4.7: Mesh at plan y = 0 m (left) and plane z = -0.2 m (right).

4.4.6 Simulation

Two numerical cases were run at speeds of 1.7 $m.s^{-1}$ (Case 1) and 2.1 $m.s^{-1}$ (Case 2) with the same mesh (optimised for the higher speed). The fluid temperature was set to 25° Celsius with a density of 997 $kg.m^{-3}$ and a kinematic viscosity of 0.89 $\times 10^{-6}$ $m^2.s^{-1}$.

Due to the inclusion of a free surface, the solver interFoam from OpenFOAM-2.2.0 (OpenFOAM (2013)) was selected and a maximum Courant number set to 0.4. With only two cases to run, convergence criteria were chosen for best accuracy compared to a fast-run time : 10^{-7} for P and 10^{-8} for U, k and ω.

These multi-phase simulations were computed in parallel runs on the high performance computing facility available at the University of Southampton Iridis 4 (10×16 core nodes each with 4GB RAM/core). At the lowest speed, seven hours were required to simulate one second of real time and the simulations were run for 25 seconds in order to capture three flows through the domain.

4.4.7 Mesh sensitivity study

A mesh sensitivity study using the same solver settings was undertaken by Banks (2013). Three different mesh were built in addition to the baseline (5.7 M cells) : (i) a very coarse mesh, (ii) a coarser mesh and (iv) a finer mesh. The total force and its decomposition into pressure and viscous forces are presented in Table 4.1. In Figure 4.8, the evolution of the ratios of the force versus the force from the fine mesh (total, pressure and viscous) is considered based in the number of cells, $n^{1/3}$.

TABLE 4.1: Mean forces on the body with varying mesh densities (Banks, 2013).

	Mesh	n, # cells ($\times 10^6$)	Total force	Pressure force	Viscous force
(i)	Very coarse	0.7	109	97	12
(ii)	Coarse	1.9	112	99	14
(iii)	Baseline	5.7	116	106	10
(iv)	Fine	14.6	118	108	10

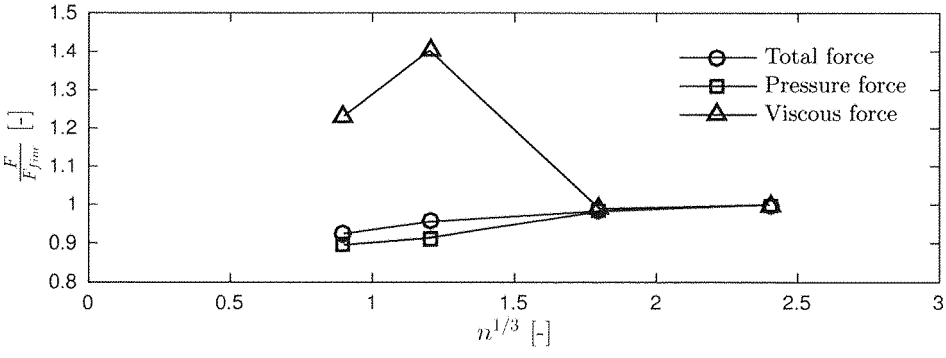

FIGURE 4.8: Grid sensitivity study undertaken by Banks (2013).

A good convergence of the dominant pressure force and thus the total force is to be noticed. However, the viscous force appears to be oscillating in the case of the two coarser mesh (i and ii). This phenomenon is due to the boundary layer mesh construction. The cell size closer to the body surface might be too large to capture smaller changes in curvature and thus cannot capture the changes in skin friction pressure. For Case 2, a mesh with 8 M elements was built for to ensure a good convergence of the total force without compromising on a much longer run time.

4.4.8 Summary of the numerical pool settings

TABLE 4.2: Summary of the numerical pool settings for Case 1 and Case 2.

	Pre-processing
Geometry	3-D swimmer geometry adapted from a generic scanned model to adopt a similar position as during the towed experiment. Model placed on the centreline and at the free surface (Figure 4.2).
Domain	14 x 7.5 x 3 $[m^3]$ - matching the experimental set-up with 2-m water depth and 1-m air draft (Figure 4.6).
Mesh	snappyHexMesh 2.2.0 - Hybrid hexahedral mesh (8 M cells): structured boundary layer mesh ($y^+ \sim 1$) and unstructured domain mesh with refinement levels increasing the mesh density near the body. Uni-directional refinement perpendicular to the free surface (Figure 4.7).
	Boundary conditions
Body	Non-slip wall, P: buoyant pressure, automatic kqRWallFunction and omegaWallFunction
Inlet	U: free stream velocity, P: buoyant pressure, k, ω: fixed values
Outlet	U: zero gradient, P: static pressure, k, ω: zero gradient
Top	Opening
Sides/bottom	Slip wall
	Solver settings (interFOAM 2.2.0)
Flow model	URANS with PISO pressure velocity coupling
Turbulence model	k-ω Shear Stress Transport (Menter et al., 2003)
Multi-phase model	Volume of fluid method (VOF)
Transient scheme	1^{st} order Euler
Grad(U) scheme	cellLimited Gauss linear 1
Div(U) scheme	Gauss linearUpwind grad(U)
Time marching	$Co_{MAX} = 0.4$, $Co_{MAX,VolumeFraction} = 0.4$, $\#\alpha$ sub-cycles = 1
Convergence criteria	P: 10^{-7} and U, k, ω: 10^{-8}
	Processing parameters
Computing system	IRIDIS 4 high performance computing facility (UoS)
Run type	Parallel (10×16 core nodes each with 4GB RAM/core)
Wall clock time	At 1.7 $m.s^{-1}$: 7 hrs of simulation for 1 s of real time. Total run time = 25 s (i.e. 3 flows through the domain)

4.5 Comparison of results from the numerical methods with the experiment

4.5.1 Direct comparison

The wave fields observed around the swimmer during the experimental tests and as obtained from the numerical simulations (both CFD and Thinship) are presented in Figures 4.9, 4.10 and 4.11. At the higher speed (Case 2 - U = 2.1 $m.s^{-1}$), more energy is transferred to the wave system resulting in a larger-amplitude wave pattern (Figure 4.9).

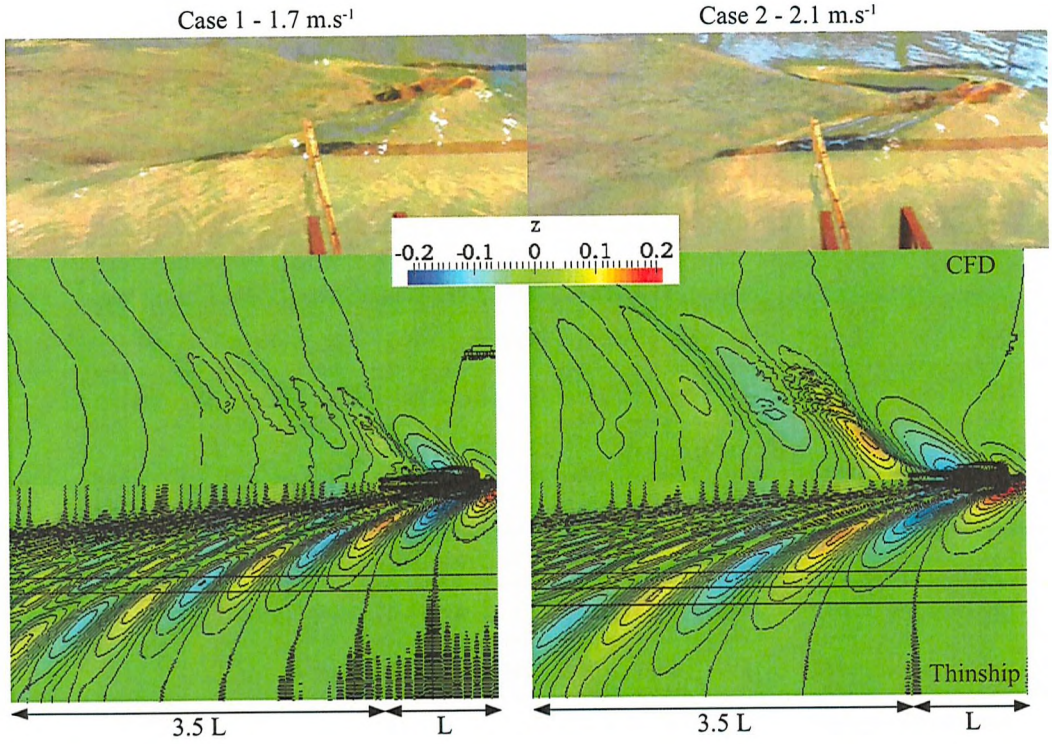

FIGURE 4.9: Comparison of the wave pattern observed around the swimmer during the experimental tests with the numerical solutions of the free surface. Free surface deformation displayed with contours ± 0.02 m and longitudinal wave cuts positioned at y = 1.50, 1.75 and 2.00 m away from the swimmer.

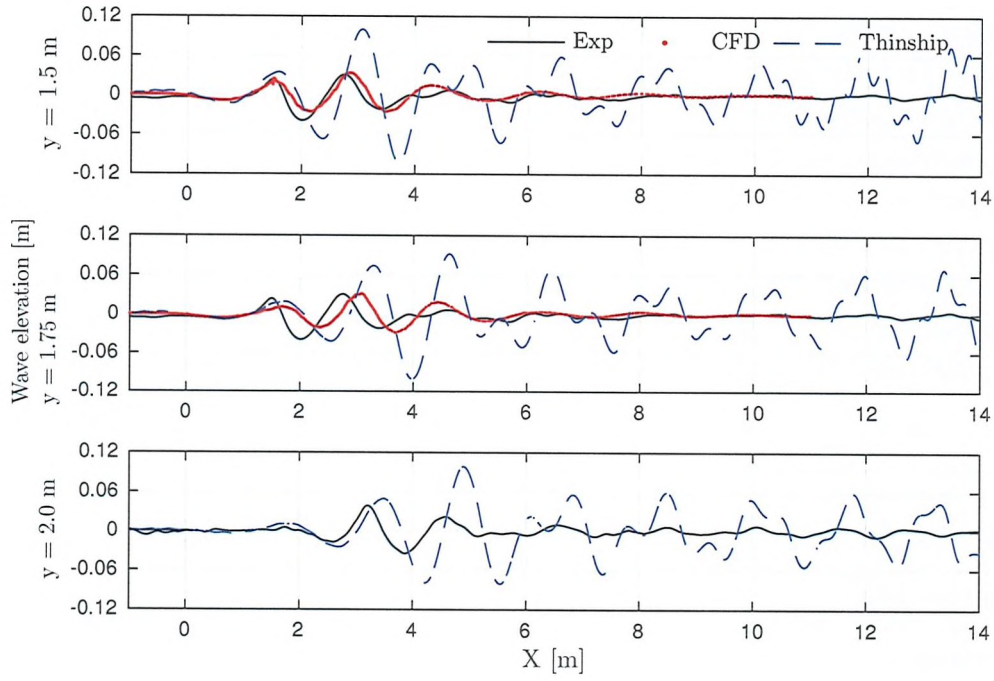

FIGURE 4.10: Case 1 (U = 1.7 $m.s^{-1}$) - A comparison of the experimental and numerical longitudinal wave cuts at different offset distances (y) from the centerline.

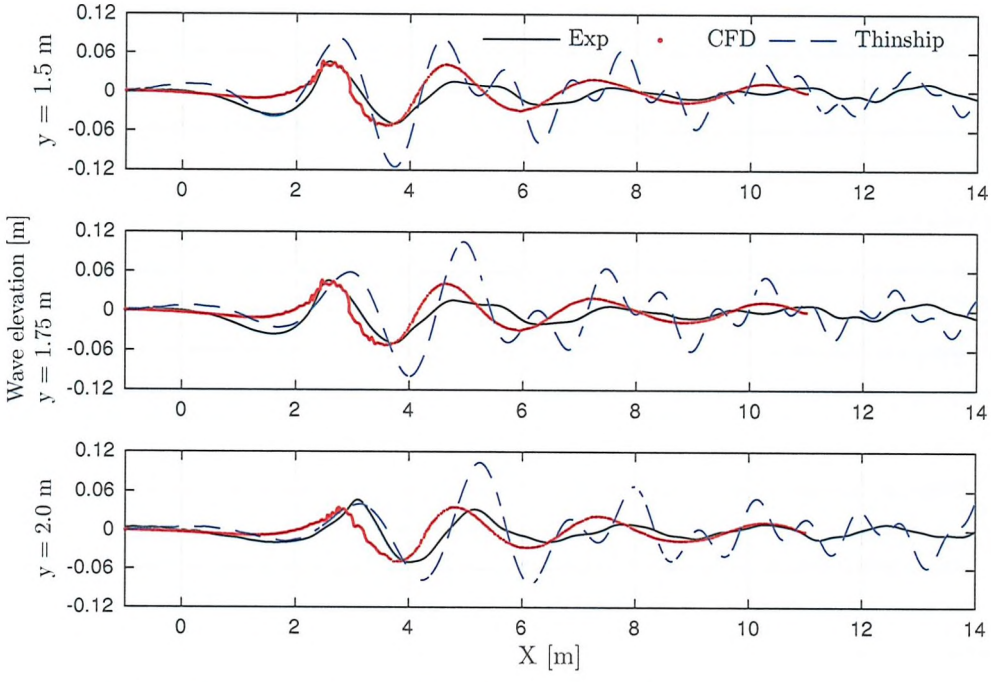

FIGURE 4.11: Case 2 (U = 2.1 $m.s^{-1}$) - A comparison of the experimental and numerical longitudinal wave cuts at different offset distances (y) from the centerline.

The CFD simulations effectively captured the wave system developed by the swimmer in a comparable manner to the experiment. Overall, there is a better agreement with the wave probe located closer to the swimmer and for the near-wake. On the other hand,

Thinship theory cannot simulate the flow separation and breaking waves around the swimmer's body and thus overestimates the wave elevation. The discrepancy between the numerically simulated free surface elevation and the measured longitudinal wave cuts comes from several factors. In a pool, there is only a partial wall reflection, whereas in the numerical tank a solid boundary is simulated. Furthermore, during the experiment, the free surface was never perfectly calm, despite time being allowed for the pool water surface to settle. This may have caused small wave interactions resulting in different wave resistances over the experimental set of runs (Tables 4.3 and 4.4). Numerical diffusion will also cause the simulated wave pattern to dissipate away from the swimmer.

TABLE 4.3: Case 1 (Speed = 1.7 $m.s^{-1}$) - ***Measured and simulated values.***

Resistance [N]	ITTC'57	Experiment	CFD Force [N]	CFD % R_T	CFD Coeff. [-]
Skin friction	3.61×10^{-3}		***10***	11%	3.78×10^{-3}
Pressure:					
P-viscous (form)					
P-wave		***13, 15, 19***			
P-total (P-v + P-w)			***87***	89%	3.14×10^{-2}
Total, R_T		***120, 120, 118***	97	100%	3.51×10^{-2}

TABLE 4.4: Case 2 (Speed = 2.1 $m.s^{-1}$) - ***Measured and simulated values.***

Resistance [N]	ITTC'57	Experiment	CFD Force [N]	CFD % R_T	CFD Coeff. [-]
Skin friction	3.45×10^{-3}		***17***	11%	3.71×10^{-3}
Pressure					
P-viscous (form)					
P-wave		***17, 25, 23***			
P-total (P-v + P-w)			***133***	89%	2.93×10^{-2}
Total, R_T		***183, 195, 193***	150	100%	3.30×10^{-2}

As presented in Tables 4.3 and 4.4, the total swimmer's passive resistance breaks down to the sum of the skin friction and pressure force. This last term can be further expressed in terms of the viscous pressure form and the wave resistance. The CFD skin friction and total pressure force were obtained by averaging the instantaneous values over two steady flows through.

The CFD simulations underestimate the total resistance by 23% at 1.7 $m.s^{-1}$ and 27% at 2.1 $m.s^{-1}$. Despite differences in the wave pattern generation, another source of

error comes from the variability in the swimmer's position during a run. Indeed, in the CFD simulations, the swimmer's geometry is fixed and changes in attitude are thus not accounted for.

The wave resistance from the CFD wave cuts could not be evaluated at this stage since the wave cuts are not long enough. Future CFD analyses should be run with a longer domain.

Since the wave pattern was overestimated from Thinship theory, investigations on various parameters were carried out in order to validate this methodology which could compute a fast answer to wave resistance studies.

4.5.2 Improvement of the 'Thinship' method

This section is aimed at researching ways to improve the use of the thinship methodology to replace the more complex and time-consuming 3-D URANS methodology to model the wave pattern of a swimmer. The effect of domain width and vertical body position of the swimmer with respect to the free surface are considered.

Effect of domain width In the swimming pool, there is an infinity edge with a partial wall reflection. The effect of the domain width on the 2-D potential flow simulations was thus first studied.

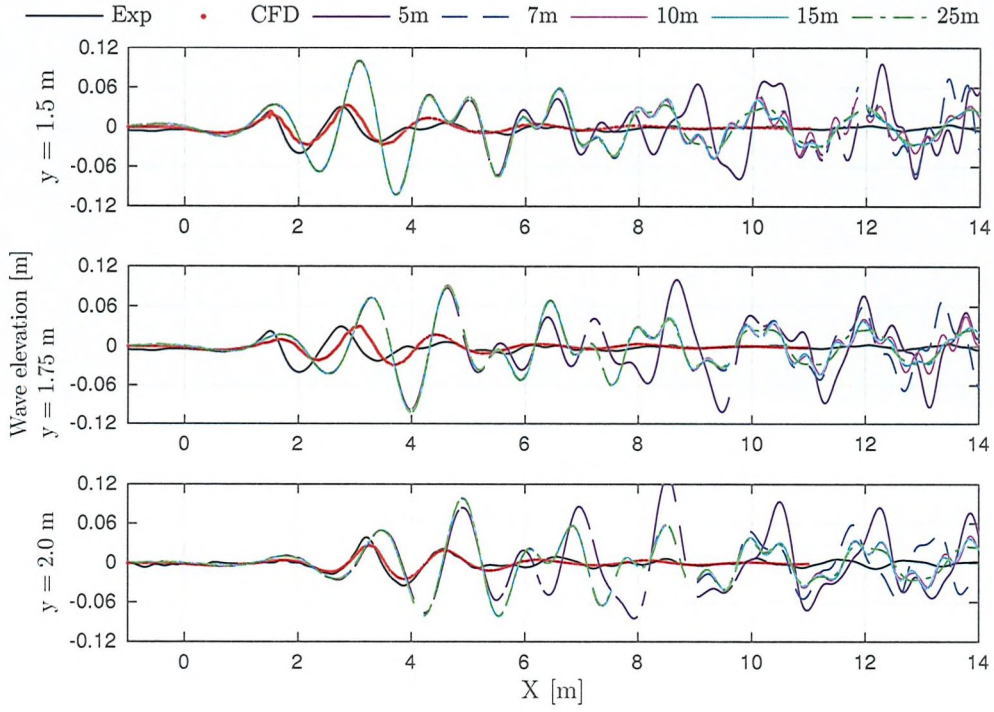

FIGURE 4.12: Case 1 (U = 1.7 $m.s^{-1}$) - Wave cuts for several Thinship domain widths, compared with experimental and CFD data.

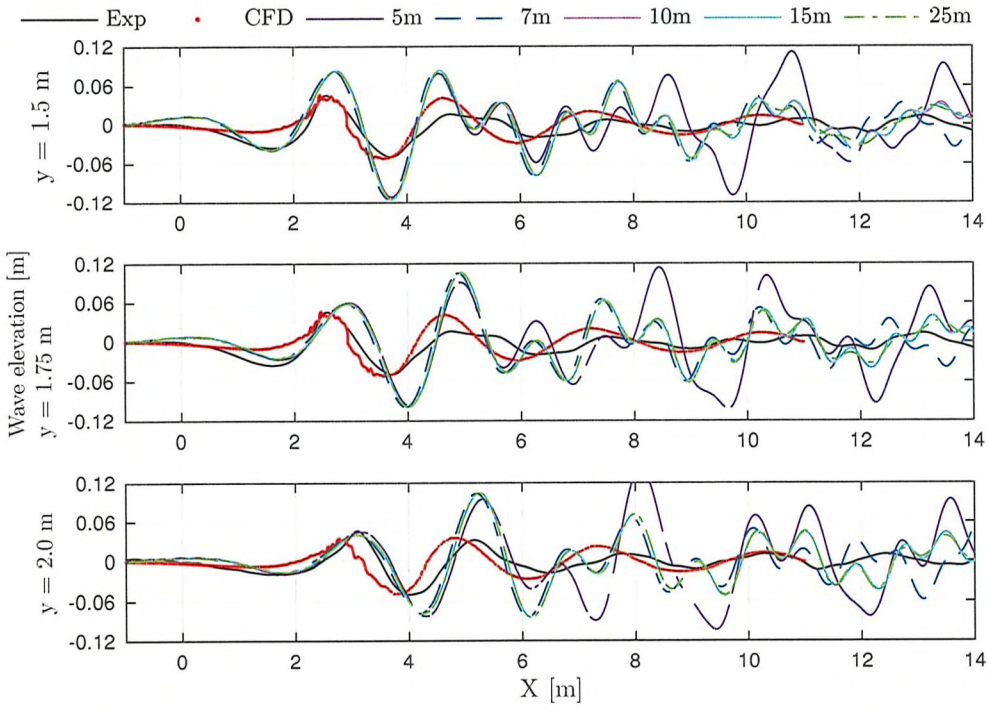

FIGURE 4.13: Case 2 (U = 2.1 $m.s^{-1}$) - Wave cuts for several Thinship domain widths, compared with experimental and CFD data.

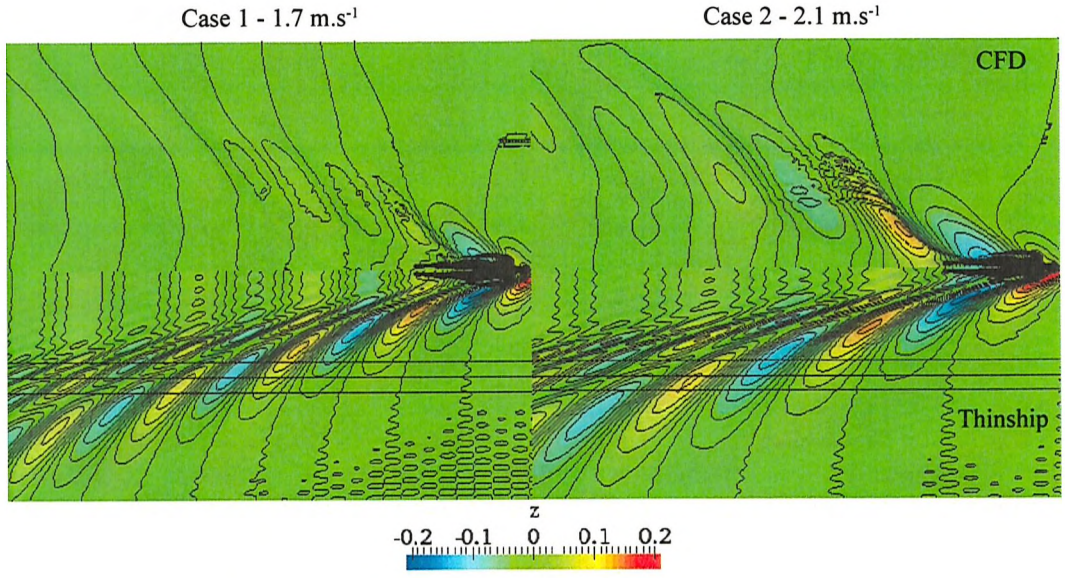

FIGURE 4.14: Comparison of CFD (top) and Thinship (bottom) wave patterns. Thinship domain width, W = 25 m. U = 1.7 $m.s^{-1}$ (left) and U = 2.1 $m.s^{-1}$ (right).

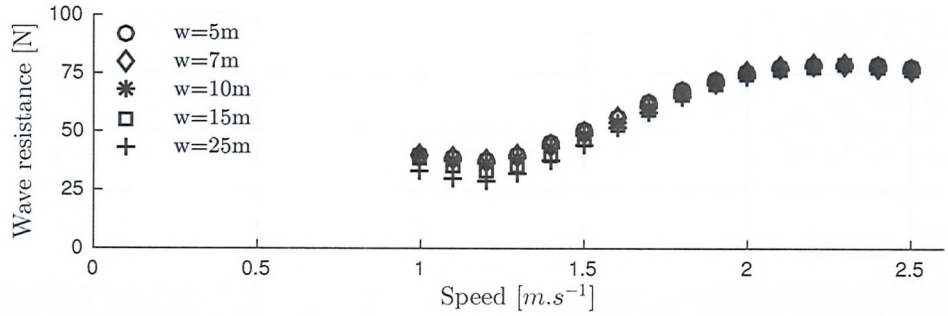

FIGURE 4.15: Influence of pool width on wave resistance across the swimmer's speed range 1.0 - 2.5 $m.s^{-1}$.

Figures 4.12 and 4.13 show that, with an increase in domain width in Thinship theory from 5, 7, 10, 15 and 25 m, a closer solution to the experimental wave cuts is obtained. The wave patterns of the different domain widths (Thinship) were generated. The best match to the CFD wave pattern was obtained with a domain width of 25 m and is presented in Figure 4.14. Less wave components are created with a domain width of 25 m compared to Figure 4.9, where a domain width of 7 m only was applied.

The wave resistance was calculated from the Thinship wave cuts for different domain widths (Figure 4.15). At speeds lower than 1.7 $m.s^{-1}$, the increase in domain width decreases the wave resistance by up to 23%.

Effect of body vertical position By observing the wave elevation at the centreline in CFD (Figure 4.16), it was noticed that the bow wave was running smoothly over the top of the swimmer's head. In reference to the calm free surface, the swimmer's head was not above the free surface anymore but submerged by about 0.10 m (Figures 4.17 and 4.18). It was thus decided to model this configuration with Thinship theory. The geometry was thus moved down to 0.10 m and 0.15 m from its original position.

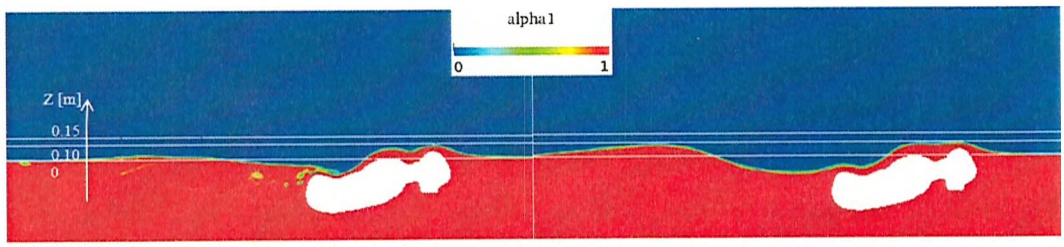

FIGURE 4.16: Side-view of the CFD free surface elevation at y = 0. U = 1.7 $m.s^{-1}$ (left) and U = 2.1 $m.s^{-1}$ (right).

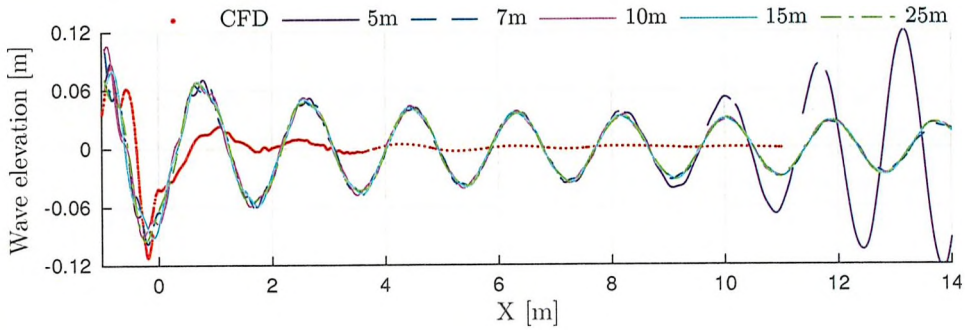

FIGURE 4.17: Case 1 (U = 1.7 $m.s^{-1}$) - Wave cut on the domain centerline y= 0 m, for several thinship domain widths, compared to CFD data.

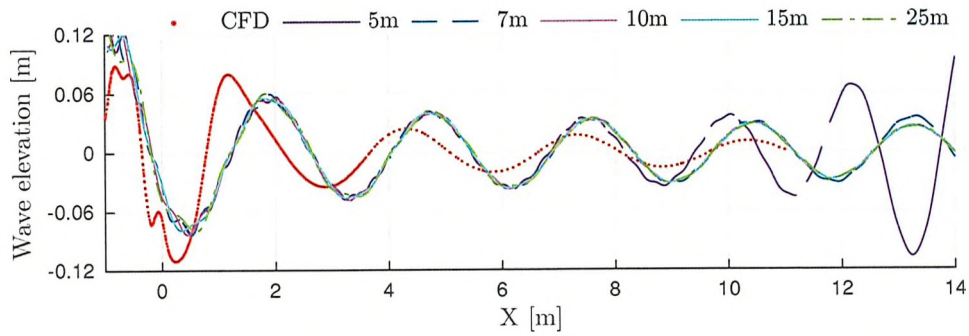

FIGURE 4.18: Case 2 (U = 2.1 $m.s^{-1}$) - Wave cut on the domain centerline y= 0 m, for several thinship domain widths, compared to CFD data.

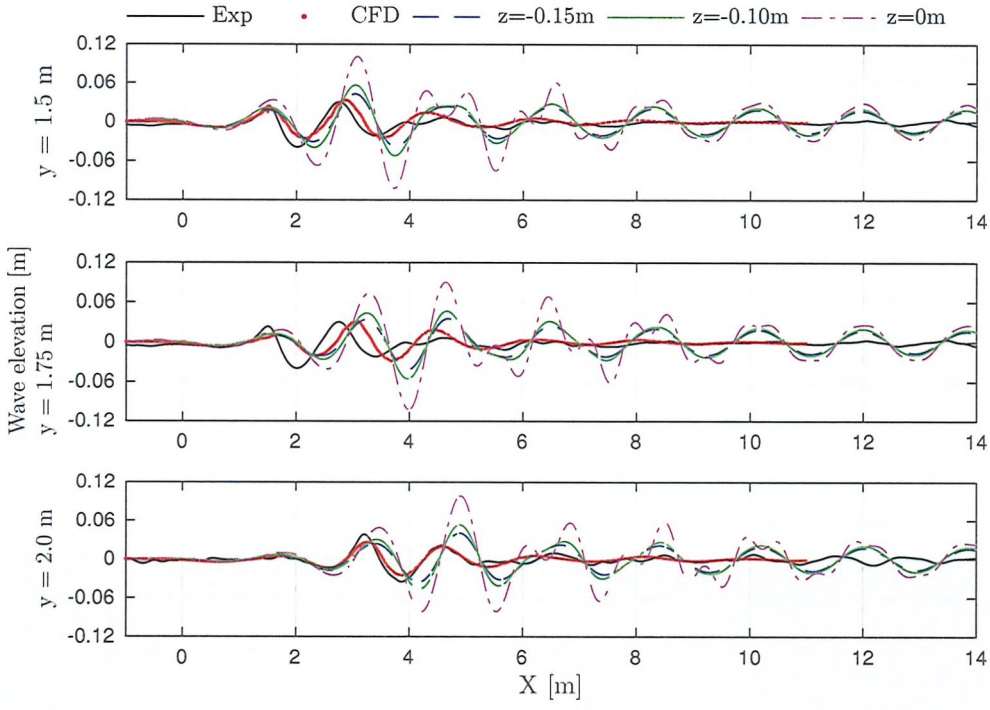

FIGURE 4.19: Case 1 (U = 1.7 $m.s^{-1}$) - Wave cuts for several body vertical positions, compared with experimental and CFD data.

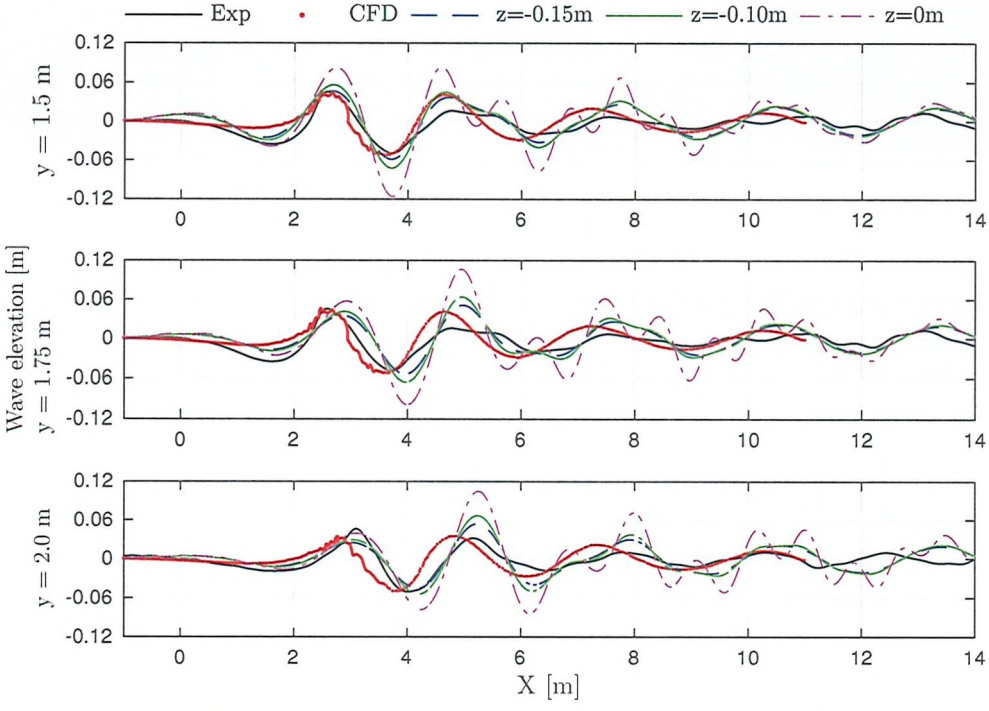

FIGURE 4.20: Case 2 (U = 2.1 $m.s^{-1}$) - Wave cuts for several body vertical positions, compared with experimental and CFD data.

The wave cuts generated from Thinship, with the body vertical position moved down

by 0.15 m and a domain width of 25 m, are in better agreement with the experimental and CFD data (Figures 4.19 and 4.20). The wave patterns from CFD and Thinship are compared with each other in Figure 4.21. Although with the Thinship methodology the wave breaking cannot be captured, the general wave pattern (elevation of troughs and crests) compare well with the CFD.

The wave resistance was calculated for the different body vertical positions and plotted against the experimental data. Figure 4.22 emphasises the large influence of the body position with respect to the free surface in Thinship theory. At the lower speed, a better match is obtained with the body positioned at z = -0.10 m; whereas at the higher speed, the wave resistance from Thinship with the body located at z = -0.15 m agrees better with the experimental data.

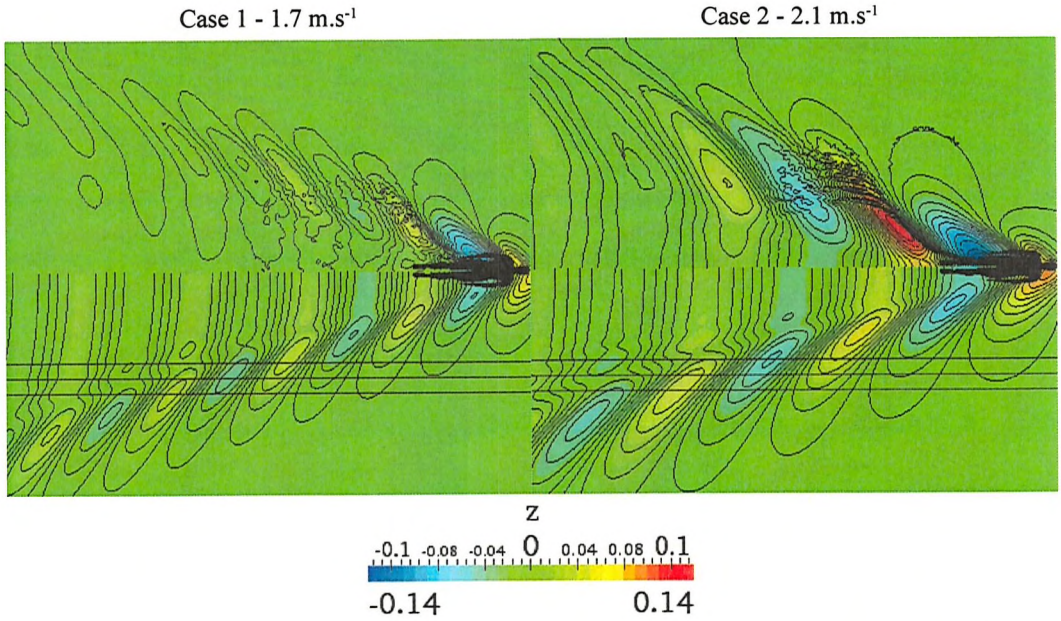

FIGURE 4.21: Comparison of CFD (top) and Thinship (bottom) wave patterns. Thinship domain width, W = 25 m - Body vertical position z = -0.15 m. U = 1.7 $m.s^{-1}$ (left) and U = 2.1 $m.s^{-1}$ (right).

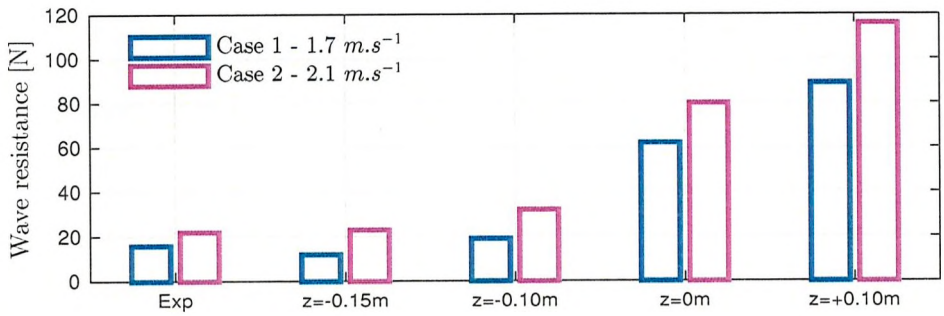

FIGURE 4.22: Comparison of wave resistance from experiment and Thinship with the body located at different vertical locations (z).

4.6 Chapter summary

Since it remains difficult to test a swimmer in a pool environment for research purposes, numerical simulations of a swimmer passively towed at the free surface were undertaken and compared with experimental data.

Compared to the experimental test case, the CFD simulations underestimate the total resistance by 23% at 1.7 $m.s^{-1}$ and 27% at 2.1 $m.s^{-1}$. These discrepancies partly come from the variability in the swimmer's position during the experimental tests. Indeed, in the CFD simulations, the swimmer's geometry is fixed and changes in attitude are thus not accounted for. Unfortunately, the wave resistance from the CFD wave cuts cannot be evaluated at this stage since the wave cuts are not long enough. Future CFD analyses should be run with a longer domain so that a complete breakdown of the resistance force can be obtained.

Since the wave pattern was initially overestimated from Thinship theory, investigations on various parameters were carried out in order to validate this methodology which could compute a fast answer to wave resistance studies. The domain width was extended to avoid an abnormally large number of wave components to be created. The study showed that the influence of the vertical body position with respect to the real wave amplitude at the body centreline is essential to predict the wave resistance.

Swimmers generate a large amount of breaking flow which cannot be modelled in Thinship theory. In addition, the boundary layer development is not taken into account with the assumption of a non-viscous flow. Consequently, Thinship is not a suitable tool to assess the influence of small resistance changes on caps and goggles.

An alternative numerical simulation would be Large Eddy Simulations (LES) in order to get a more detailed representation of the flow features around the head and the rest of the body. A test case for a 3-D circular cylinder in a single phase flow surrounding the drag crisis was simulated using LES (Lloyd and James, 2015). Due to the fine mesh required and the challenges associated with the choice of turbulence model and numerical scheme, this method appears to be not cost-effective for swimming.

Many more Olympic cycles would be required to improve these methodologies as computer power increases. It was thus decided to not pursue CFD techniques and to instead move to a more controlled experimental environment that is a towing tank with solid models. The experimental methodologies used for the towing tank will be explained in the upcoming chapter.

5

Towing Tank Tests
Sphere, head, mannequin

The previous two chapters detailing the methodologies to assess a swimmer's resistance in both a real and numerical pool environment have emphasised the need to reduce the level of complexity to first better understand the fundamental flow physics occuring around a swimmer. The use of a towing tank as a more controlled environment than a swimming pool was thus chosen to study the flow past a sphere (Chapter 6), a head (Chapter 7) and a mannequin (Chapter 8) across the typical swimming speed range. The complexity of the tested objects will thus progressively increase to eventually consider again the case of a real swimmer in the pool (Chapter 9).

The challenges involved in the tank testing methodologies arise from the different model sizes requiring the use of different towing tanks with different dynamometer rigs. In this chapter, the models tested are presented, as well as the goggles and caps tested on the head and mannequin, followed by a description of the experimental apparatus used. Finally, a method to relate drag differences between different equipment on the head only to an actual swimmer's performance is described.

5.1 Tested models

Both the sphere and head models started with initial prototypes which could be made at a reasonable cost and under a short timeline. After the first studies were undertaken,

professional models with additional features were built to support the development of the project.

5.1.1 Sphere

Due to time and cost constraints, a first sphere prototype (S1) was manually constructed based on a youth-size basketball covered with fibreglass and an epoxy resin. The resulting sphere diameter is 225 mm. This is 20% higher than the average head diameter, but it allowed to have a prototype done quickly to get a first estimate of the drag curve for a sphere located at the free surface across the desired range of Reynolds numbers. This sphere weighs 1.38 kg and was ballasted with 1.7 litres of fresh water in order to obtain neutral buoyancy. A vent was specifically placed at the rear of the sphere for this purpose, as can later be seen in Figure 5.9(a). A 5% margin was allocated in the neutral buoyancy calculation to ensure that no force would be acting upwards, protecting the mounting system on the dynamometer post.

Later on, two geosim sphere models (S2) of respective diameters $D_1 = 225$ mm and $D_2 = 125$ mm were professionally built out of iroko wood ($\rho = 0.66$) on a lathe with a tolerance of $\pm$ 0.1 mm on the diameter. A void was left in the middle of each sphere to ensure neutral buoyancy when the sphere has an immersion depth equal to 50% of its diameter.

5.1.2 Head

A geometry file obtained from the scan of a female swimmer's head wearing a cap (i.e. no ears extruding from the model) was provided by Speedo. Based on Speedo Fastskin cap size guide (Figure 5.1), the head model dimensions are: A $\sim$ 550 mm / B $\sim$ 340 mm. The head volume is 0.004 m^3, which is equivalent to a 0.2m-diameter sphere.

A first head model (H1) was manufactured out of Polylactic Acid (PLA) on an available 3-D printer at the University of Southampton. PLA has the advantage to not require a high-bed temperature allowing for a good finish quality. Although PLA is a strong material, it is extremely brittle.

A second head model (H2) was designed with a removable scalp to allow for different hair style shapes to be added. The parts were all 3-D printed out of Nylon, a much stronger and durable material than PLA. This head model is thus better suited for repeating testing in a towing tank environment.

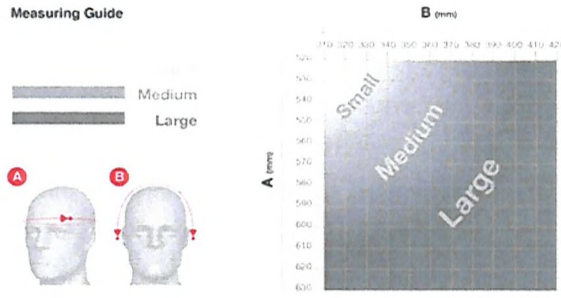

FIGURE 5.1: Speedo Fastskin cap size guide used as a standard to measure head size.

5.1.3 Mannequin

A mannequin geometry for a female swimmer was provided by Speedo. The mannequin does not have arms and the legs are cut just below the knees (Figure 5.12). The mannequin was manufactured out of high-density foam with Computer Numerical Control (CNC) machining, providing a smooth surface finish. It was built to be neutrally buoyant in order to ease the installation process on its mounting rig. The head model described above was fitted on the mannequin body and a soft foam neck was added to bridge the gap between the body and the head while still being able to adjust the head angle.

5.2 Tested swimming equipment

5.2.1 Goggles

When testing goggles, the head was equipped with a Speedo Fastskin cap at all times and no under cap was used. Based on the Speedo Fastskin cap size guide (Figure 5.1), a cap size M was selected. Five different goggles were tested, ranging from racing goggles to bottom range goggles (Figure 5.2).

(a) G1 - Speedo Elite

(b) G2 - Speedo Super-Elite

(c) G3 - Mizuno Cutters

(d) G4 - Speedo (bottom range)

(e) G5 - Speedo Aquasocket

FIGURE 5.2: Different goggles designs tested.

5.2.2 Caps

Seven caps were tested on the head only or on the mannequin's head, including both racing caps and caps displaying specific hydrodynamic features like studs or riblets (Figure 5.3). No under cap was used during tank testing, the caps were always fitted directly on the bare head. Goggles G1 or G5 were used when comparing the caps' drag performance, but the goggles were not changed during a specific cap testing session so that only the effect of the cap on drag could be determined.

(a) C1 - Speedo Fastskin Elite

(b) C2 - Arena Race Cap

(c) C3 - Adidas Adizero

(d) C4 - Speedo with studs

(e) C5 - Speedo LZR suit fabric

(f) C6 - Speedo leisure

(g) C7 - Speedo with riblets

FIGURE 5.3: Photographs of the different caps tested emphasising key features.

5.3 Towing tank facilities and apparatus

5.3.1 Towing tanks

Two towing tanks are available for testing in Southampton at present: the Lamont tank and the Solent tank. The Lamont tank, located on Highfield Campus at the University of Southampton, has dimensions 30.0 x 2.4 x 1.2 $[m^3]$. The maximum speed attainable in this tank is 2.2 $m.s^{-1}$, corresponding to the maximum swimming speed observed on the free surface. The equivalent depth-based Froude number for the entire tested speed range (1.0 - 2.2 $m.s^{-1}$) is between 0.3 and 0.7 (i.e. within the sub-critical flow range).

Also, with a projected area of 0.02 m^2 for the sphere when immersed at 50%D, the maximum blockage encountered in the tank is 0.7%. This is close to the 0.5% limit recommended by Molland et al. (2011); therefore, no correction for blockage is required and the Lamont tank is judged to be suitable to test small models like a sphere or a head. Due to the lack of thermal insulation of the tank building, the water temperature varied between 6 and 15° Celcius, depending on the time of the year.

Solent University towing tank is 60.0 m long, 3.7 m wide and 1.8 m deep and its carriage top speed reaches 4.0 $m.s^{-1}$. This larger tank accommodates the testing of the mannequin and provides a longer data acquisition time. Since this tank is well insulated, a constant temperature of 18° Celcius is maintained.

Figure 5.4 shows an overview of the experimental set-up in the Lamont tank. A similar overall set-up was used in the Solent tank with the same range of measurements taken. The model was mounted onto a dynamometer recording both drag and side forces and an above-water camera was placed on the carriage in order to observe the development of the bow wave across the tested speed range. In addition, an array of three wave probes was positioned on the side of the tank to obtain the wave elevations. The dynamometer rigs for the different tested models and the visualisation tools are subsequently presented in further details.

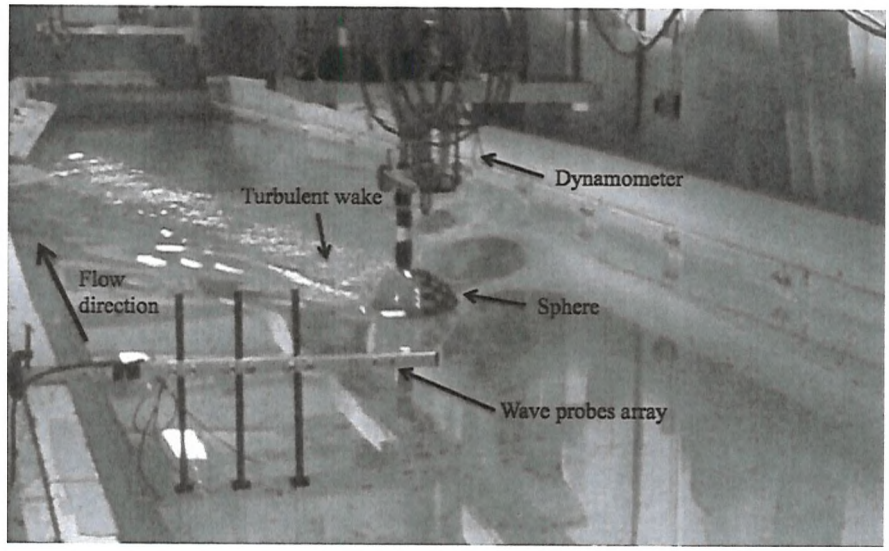

FIGURE 5.4: Overview of the experimental set-up in the Lamont tank.

5.3.2 Dynamometer rigs

Over the course of this PhD, several tank testing sessions have been undertaken to test the models introduced in Section 5.1. A chronological list of these tests is presented in Table 5.1. Due to the different model sizes and tank availability, various bespoke dynamometer rigs and mounting systems were designed and built.

TABLE 5.1: List of tank testing sessions with tank, models and dynamometry used.

Test #	Date	Tank, T° C	Models	Dynamometry
1	Mar 2013	Lamont, 6° C	Sphere (S1)	Drag and side forces: Lamont tank built-in dynamometer
2	Jul-Sep 2013	Solent, 18° C	Head (H1) / Mannequin with H1	Drag: Average of 3 x 500 N force block
3	Apr 2014	Lamont, 10° C	Sphere (S1)/Head (H1)	Drag: 1 x 50 N force block, Side force: 1 x 500 N force block
4	Sep 2014	Solent, 18° C	Mannequin with H1	Drag: Average of 3 x 100 N force block
5	Dec 2014	Solent, 18° C	Mannequin with H2	Drag: Average of 3 x 100 N force block
6	Jun 2015	Solent, 18° C	Sphere (S2)/Head (H2)	Drag: 1 x 100 N force block, Side force: 1 x 100 N force block
7	Nov 2015	Lamont, 15° C	Sphere (S2)/Head (H2)	Drag: 1 x 100 N force block, Side force: 1 x 100 N force block

Dynamometry The same underlying principle of the electrical force transducer positioned onto a flexure was used for all tests to measure the forces acting onto the tested model. A Linear Varying Displacement Transducer (LVDT), with a 1-mm range is positioned onto a flexure, which can move in one direction only with a displacement range of 2 mm. The response band in the data acquisition system is across 20 V [-10 V, +10 V] discretised in 2^{16} bit. Flexures which could take loads between 50 N and 500 N were used depending on the available dynamometry. The force measurements thus resulted in a bias of the order of 10^{-4} to 10^{-3} N/bit, which is suitable.

Providing that a calibration procedure is applied before testing, the force applied onto the model (head, sphere or mannequin) can be evaluated. A calibration process consists in applying several known weights and recording the corresponding amplified output voltages. A linear curve is fitted through the data points in order to get the rate to apply to the electrical response (Figure 5.8). Figure 5.5 highlights the bespoke calibration system used in the towing tank.

FIGURE 5.5: Dynamometer with two force blocks rotated by 90° measuring drag and side forces, system of pulley in place to calibrate the drag force.

The forces were measured at a sample rate of 100 Hz. A 2-Hz low-pass filter is first applied to the output voltage signal recorded to cut-off the large amount of high-frequency noise induced by the carriage vibrations and other electrical noises (Figure 5.6). Drifts in the electrical zero are not so important, since the zero is always acquired before each run.

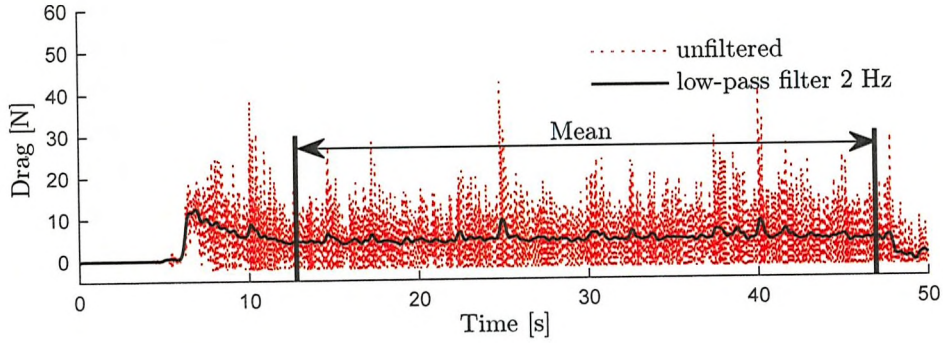

FIGURE 5.6: Effect of 2-Hz low-pass filter on acquired drag trace at 100 Hz frequency and selection of mean drag force.

The drag force is then obtained by averaging the drag signal over the constant-speed portion of the trace, between the acceleration and deceleration phases of the carriage, as identified in Figure 5.6.

With the exception of the initial sphere tests undertaken with the Lamont Tank dynamometer, all other tests performed in a towing tank used the same bespoke dynamometry designed by the Wolfson Unit (Wumtia, n.d.). The linear response of these force blocks was demonstrated for the 'tow rig' which measures the resistance of a towed swimmer in a swimming pool (Chapter 3). The Lamont tank dynamometer used for the initial sphere tests has been widely used over the years and is known to provide a linear response for a large range of forces tested (Figure 5.8). Figure 5.7 compares the key features of both dynamometers.

Following up damage encountered on the Lamont tank dynamometer, a new bespoke dynamometer was built with the Wolfson Unit force blocks. Two force blocks were positioned on top of each other, with a rotation of 90° in the X-Y plane to measure both drag and side forces (Figure 5.5). This set-up was used to test the sphere and the head models. On the other hand, the resistance applied onto the mannequin was measured by averaging the drag force from three force blocks, in a similar manner as previously presented for the 'tow rig'.

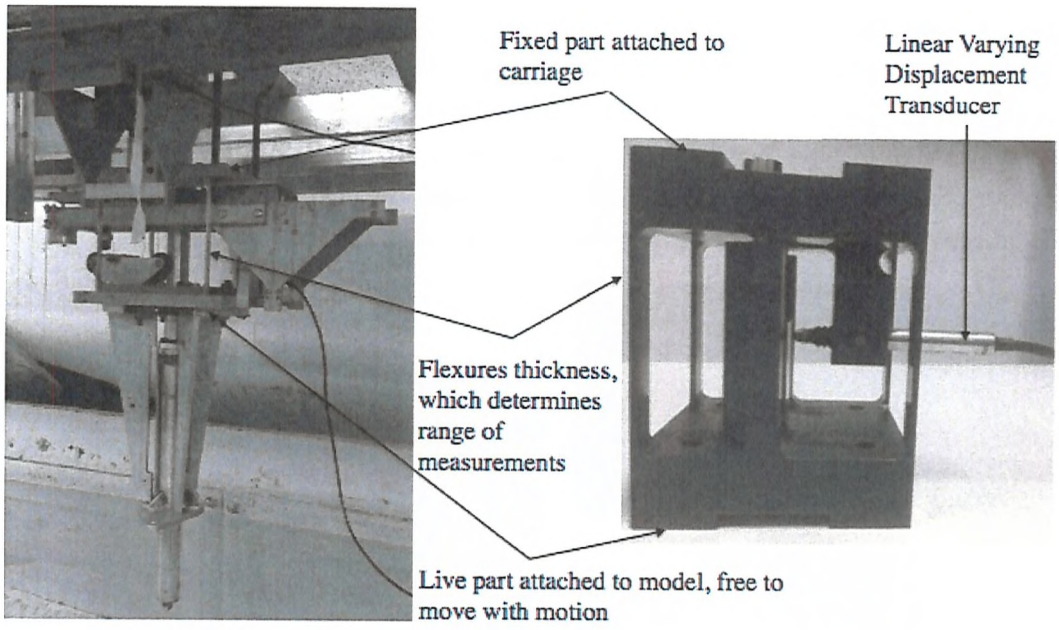

FIGURE 5.7: Lamont tank original dynamometer (left) and force blocks used for the bespoke dynamometer (right).

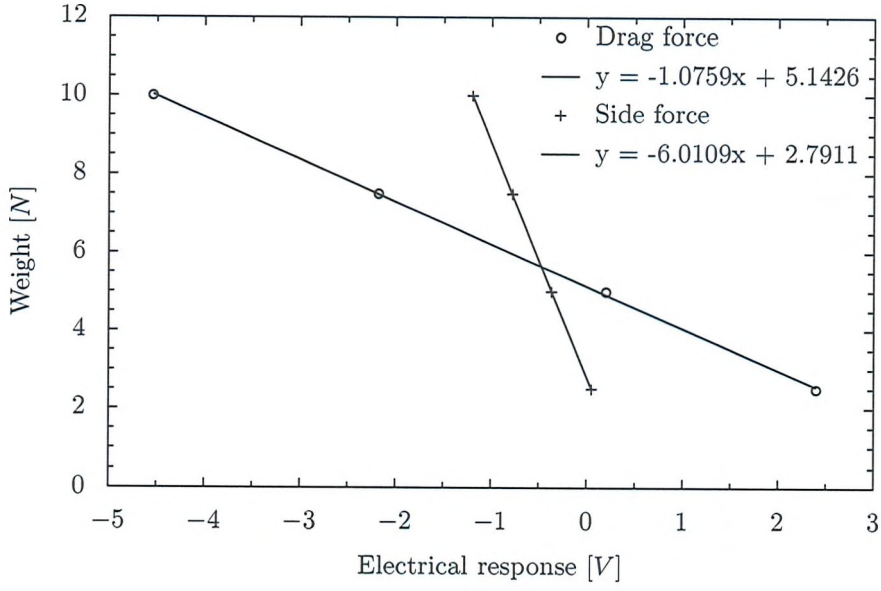

FIGURE 5.8: Lamont tank dynamometer calibration plot for drag and side force with a least-square fit.

Mounting rigs The sphere and the head models were both attached to their dynamometer via an L-bracket, whereas the mannequin had its own mounting rig.

The sphere was first mounted via a 16-mm diameter pipe extending at the rear of the sphere, and then replaced by a stronger 25-mm pipe (2-mm thickness) and going back up to the carriage with an L-bracket (Figure 5.9). Hoerner (1965) indicates that with a

rear spindle diameter less than D/4, the flow should not be significantly altered. This was more recently confirmed by Reynolds et al. (1997) who compared drag data for a sphere in a circulated water channel for both a strut and a sting mounting arrangement. The attachment pipe goes back up vertically at a distance $D_1/2$ from the rear of the sphere (S1). In a second arrangement (S2), a larger distance of D_1 was left. The same L-bracket was used for both sphere diameters, D_1 and D_2.

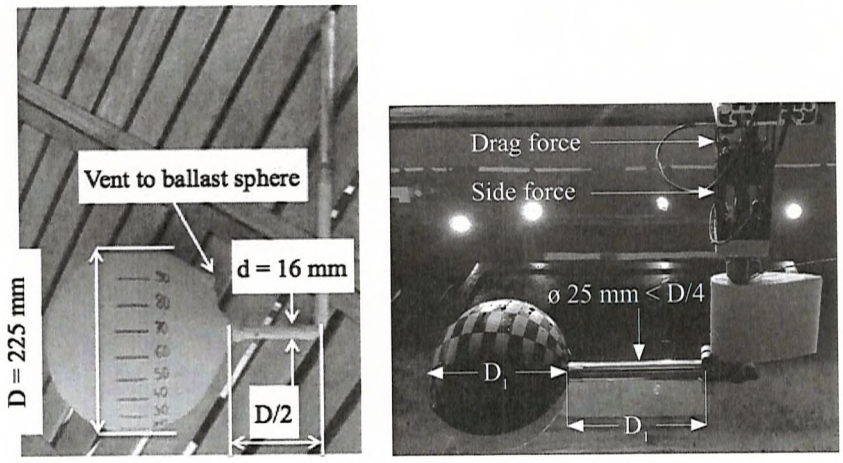

(a) Sphere S1 (Tests # 1 & 3) (b) Sphere S2 (Tests # 6 & 7)

FIGURE 5.9: Sphere L-brackets for S1 and S2.

When the Lamont tank dynamometer was used, an adapter was positioned at the end of the sphere rig to attach the model onto the dynamometer tow post typically used to tow ship models. With the use of the bespoke dynamometer, the sphere model was further apart from the dynamometer. In order to reinforce the support rig, the sphere tube had to be clamped on all its length to the long 25-mm-tube coming down from the dynamometer. The support rigs used for Test #1 and Test #3 only differ above the free surface and will thus have an insignificant impact on the flow regime around the sphere (Figure 5.10).

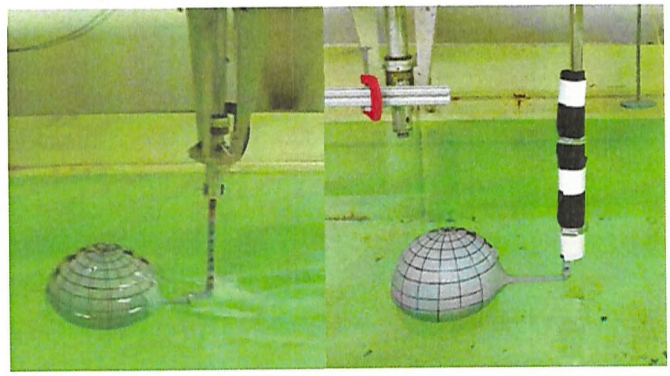

FIGURE 5.10: Sphere mounting system for Test #1 (left) and Test #3 (right). The mounting support differs slightly at the rear of the sphere. Since this difference is above the free surface, the effect on the flow past the sphere is assumed to be negligible.

The head was mounted onto the various bespoke dynamometers via a similar L-bracket as shown in Figure 5.11.

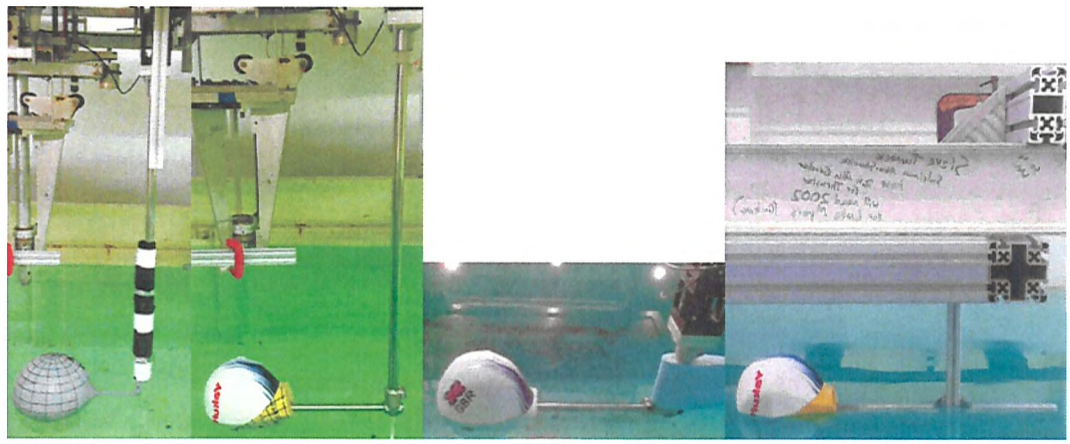

FIGURE 5.11: Overview of the different mounting rig for the head. From left to right: sphere (Test # 3), Tests # 3 & 7, Test # 6 and Test # 2.

Finally, a custom rig was built by the team of post-doc students (Dr. Webb, Dr. Philipps and Dr. Banks) to study the flow past a mannequin. The rig is based on a similar design as previously shown for the 'tow rig' in the pool with three force blocks measuring the drag. Figure 5.12 highlights the key features and the calibration frame based on the same principle as the sphere rig.

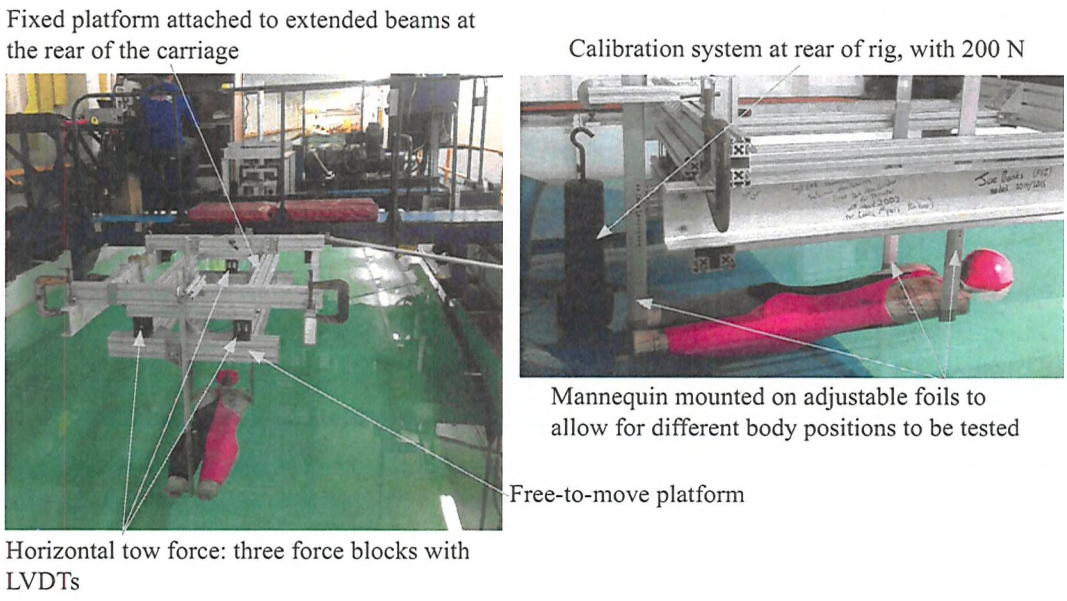

FIGURE 5.12: Bespoke mannequin rig set-up in the Solent tank.

Uncertainty analysis An uncertainty analysis based on the recommended ITTC Procedure 7.5-02-02-02 for towing tank resistance tests (ITTC, 2014) is presented in Appendix D, Section D.2 for the case of the sphere during Test #6. This analysis considers

the following factors :

- Model installation
- Towing speed
- Water temperature
- Dynamometer for the drag force
- Repeatability

The two main types of uncertainty are coming from the model installation (1.4 %) and the dynamometer (3.1 %). Using the Root-Sum-Square method, the maximum error is 3.4 %. In this uncertainty analysis, the repeatability could not be assessed due to the limited number of repeat runs.

The repeatability of the drag force was initially evaluated in the case of the sphere for Tests # 1 & 3 (Figures 5.13 and 5.14). The drag force was averaged over the steady portion of the drag force trace and non-dimensionalised with $0.5\rho(A_p/2)U^2$, where A_p is the sphere projected area. Test # 1 proved to have an excellent repeatability, with on average just over 1 % discrepancy between sets. A larger error of around 3 % was observed at the transitional speed. On average, runs were separated by a 10-minute break to allow for the tank free surface to settle. During Test # 3, no repeats were performed on the same day so the repeatability cannot be assessed there. However, four speeds tested on Day 1 were repeated on Day 2. The experimental data points are on average 5% away from the mean drag curve, which is considered as negligible. On average, a 14-minute break between each run was allowed.

The tank Tests # 1-6 were aimed at learning as much as possible about the fluid mechanics of the flow around a sphere, a head and a mannequin located at the free surface. The testing plan was thus set to run more configurations (different sphere diameters and immersion depths, head/body positions, caps, goggles and hair styles), rather than to perform a large amount of repeats for only a few conditions considering the limited amount of time available at the towing tank facilities. The repeatability analysis presented above for Tests # 1 & 3 proved the reliability of both dynamometers used to study the flow characteristics past the sphere and the head.

Therefore, during the other tests, only a few data points were repeated. The drag data presented through Chapters 6, 7 and 8 thus correspond to either a single data point or the mean of the repeat runs. When evaluating small drag differences between different caps, goggles and hair style on the head only or on the mannequin, the standard deviation between the repeat runs is highlighed on the bar charts (e.g. Figure 7.11).

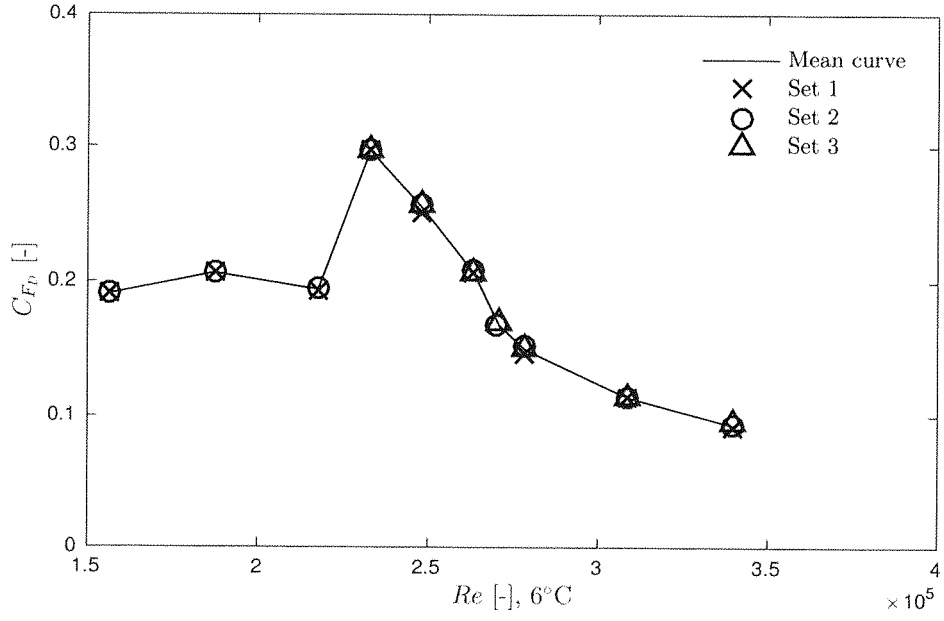

FIGURE 5.13: Test # 1 - Drag coefficient versus Reynolds number showing an excellent repeatability within one day of testing.

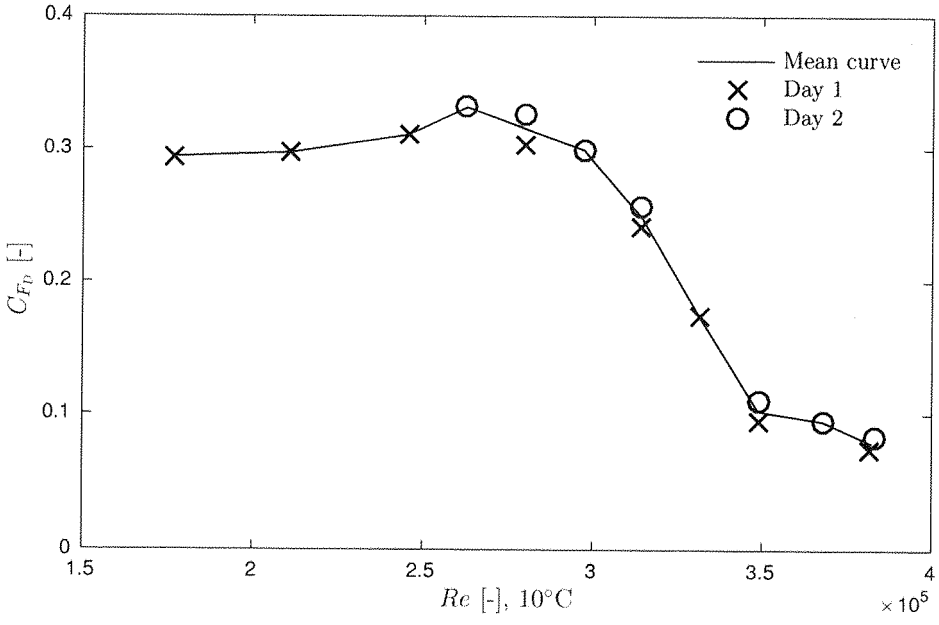

FIGURE 5.14: Test # 3 - Drag coefficient versus Reynolds number showing a good repeatability between Day 1 and Day 2 of testing.

It is important to note that the repeatability of the system is still partially included in the standard uncertainty of the dynamometer since several calibration tests were performed throughout the testing days. Indeed, the calibration process is typically undertaken at the start and end of each testing day to allow for potential changes in the system. This end-to-end calibration includes the uncertainty relating to both electrical

and mechanical components, and therefore provides the user with the total uncertainty in the data acquisition process.

5.3.3 Visualisation tools

In addition to the force measurements, visualisation tools can provide meaningful information to classify different flow regimes. An above water camera was positioned directly above the tested model at all times to observe the development of the bow wave onto the model (sphere, head and mannequin). An additional camera was positioned either in front of the model or by the side to provide further insight into the development of this bow wave. Typical photographs were extracted from all video footage over the steady-speed run portion of the tank. From these photographs, the free surface deformation features could be observed and matrices for each tested configuration have been generated over the speed range and corresponding Re-Fr numbers tested.

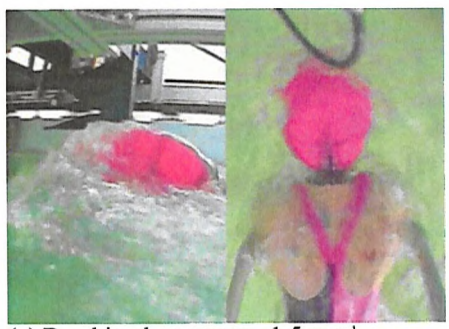

(a) Breaking bow wave - 1.5 m.s^{-1}

(b) Smooth bow wave - 2.0 m.s^{-1}

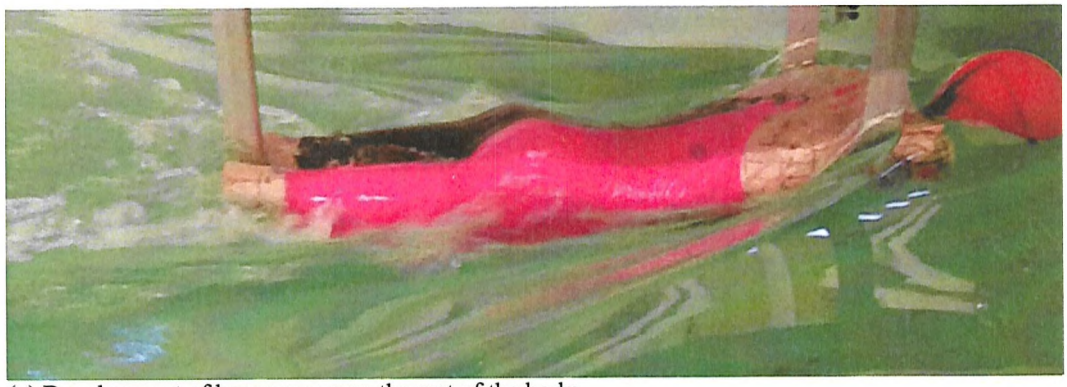

(c) Development of bow wave over the rest of the body

FIGURE 5.15: Flow visualisation in the towing tank with zoomed-in side- and top-views of the head to observe the formation of the bow wave (a)-(b), as well as a side-view camera positioned further away from the model to capture the development of the bow wave on the body (c).

5.4 Method to relate drag differences measured on the head only to a swimmer's performance

Test #7 was specifically organised for British Swimming to rank cap C3 against caps C1 and C2. The tests were performed on the head only. A percentage drag difference between the different caps was obtained when tested under the free surface (study presented in Chapter 7). However, coaches are interested in knowing a time difference for a swimmer wearing different caps. A method using Webb (2013)'s race simulator was thus developed to relate the drag difference measured between two caps on the head to what it would be like on a real swimmer, alllowing a time difference to be evaluated.

Let us consider the following example :

1. Check the actual drag difference between configuration A and configuration B in Newton.
   E.g. At 2.2 $m.s^{-1}$, the drag difference between caps C3 and C2 is:
   $\Delta Drag = 25.8 - 21.8 = 4.0$ N.

2. Check the underwater total body drag for a male swimmer (height = 1.95 m, weight = 98 kg) over a 100-m freestyle race at the tested speeds (Figure 5.16).
   E.g. At 2.2 $m.s^{-1}$, the total underwater body drag is: 117.7 N.

3. Establish the percentage drag change due to cap on underwater total body drag.
   E.g. % Drag change = $\frac{4.0}{117.7} = 3.4\%$.

4. Use Webb (2013) method to relate percentage change to time change.
   From Figure 5.17, over a 100-m freestyle race:

   - On free surface: 1% change in drag $\equiv$ 0.15 s change
   - Underwater: 1% change in drag $\equiv$ 0.10 s change

   E.g. 3.4% underwater drag reduction is estimated to save 0.34 s.
   $\Delta Time = -3.4\% * 0.10 = -0.34$ s.

5. Should percentage drag change on the surface be of significance as well, the simulator would be used as follow:
   E.g. Configuration A shows a 4% decrease in drag compared to configuration B on the surface, but 2% increase in drag underwater. Consequently, swimmer with configuration A will swim 0.4 s faster than swimmer with configuration B.
   $\Delta Time = -4\% * 0.15 + 2\% * 0.10 = -0.6 + 0.2 = -0.4$ s.

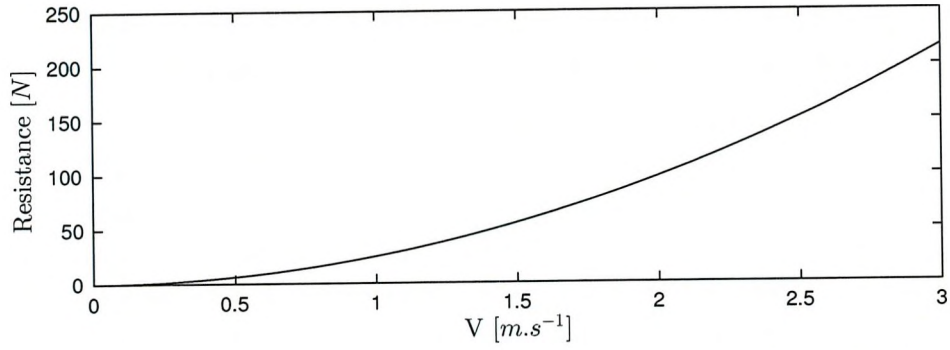

FIGURE 5.16: Simulated underwater resistance curve for a male swimmer (height = 1.95 m, weight = 98 kg). Adapted from Webb (2013).

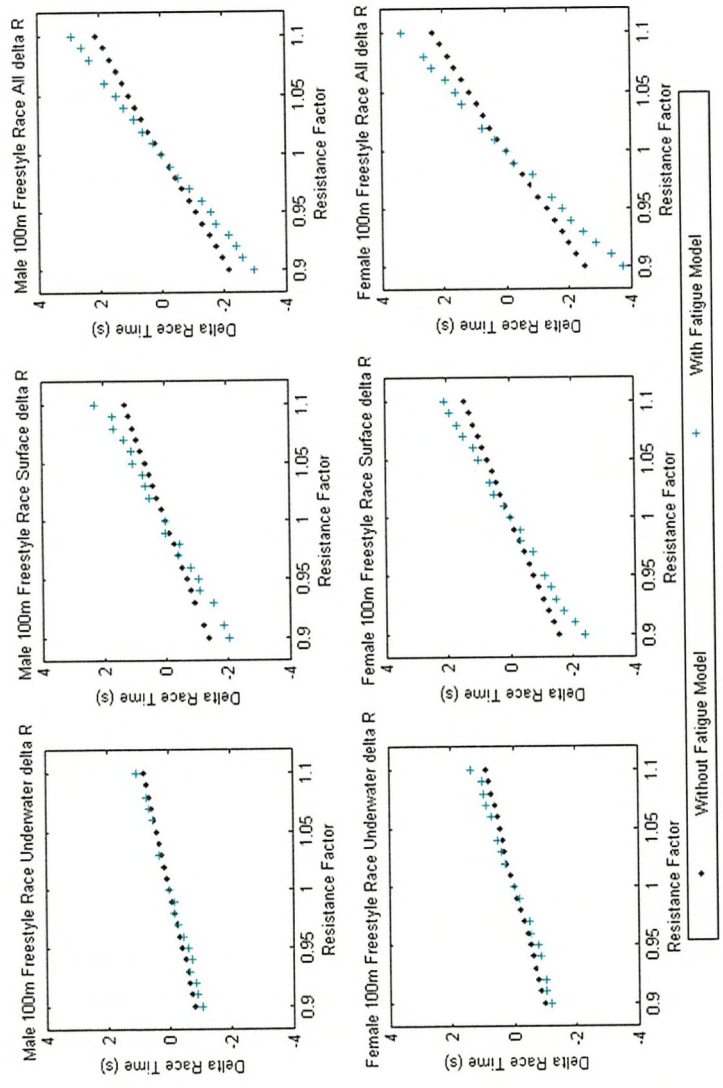

FIGURE 5.17: Male (height = 1.95 m, weight = 98 kg) and female (height = 1.95 m, weight = 98 kg) simulated 100-m freestyle race for a range of resistance changes. These changes have been applied to only underwater resistance (left column), only surface resistance (centre column) and both (right column). All conditions are simulated with and without fatigue modelling (Webb, 2013).

5.5 Chapter summary

In this chapter, the different models tested in a towing tank environment were introduced. The main types of models are a sphere, a head and a mannequin, showing an increase in complexity and reality. Models started with prototypes and eventually evolved as the research path progressed.

Goggles and caps tested on the head only, and/or on the mannequin have been displayed with key features highlighted. In the rest of the report, they will be referred to by their ID (e.g. Goggles 1, G1 - Cap 1, C1).

The main characteristics of the two towing tanks used over the course of this PhD project have been presented. The Lamont tank at the University of Southampton can accomodate the sphere and head models, whereas the mannequin can only be tested at the larger Solent University towing tank.

In order to gain a better understanding of the flow regime experienced by the tested models at the free surface, drag force measurements based on the electrical force transducer are combined with top- and side-view photographs extracted from videos. The different dynamometers and mounting rigs have been illustrated for all models.

Eventually, a method to relate drag differences between different caps on the head only to an actual swimmer's performance in terms of time saved is described. Using Webb (2013)'s race simulator, individual drag curves (underwater and on the free surface) could be simulated for each British Swimming athlete, allowing an estimate of time saved to be given to an athlete simply based on towing tank tests.

To the author's knowledge, the use of a towing tank with models allowing a progressive understanding of the flow around a swimmer has not been undertaken before. The results and discussion of each individual study for the sphere, the head and the mannequin will be presented in Chapters 6, 7 and 8 respectively.

Part C

STUDIES
Increasing reality and complexity:
Sphere
Head
Mannequin
Swimmer

6

Flow past a sphere

As explained in the literature review, a swimmer's head can be modelled by a sphere in order to get a better understanding of the various flow regimes encountered across the elite swimmer speed range before moving back to the more challenging case of a swimmer. Consequently, the flow past a 225mm-diameter sphere, located at the free surface, was studied over the critical range of Reynolds number, $8 \times 10^4 \leq Re \leq 6 \times 10^5$, and Froude number $0.4 \leq Fr \leq 2.9$.

The problem overview and terminology when studying the drag of surface-piercing bluff bodies are first introduced. Initial tests with a prototype sphere model were carried out to establish a first flow taxonomy. Three key studies were then undertaken. First, using two geosim models, the effect of the free surface deformation on the drag crisis is partially decoupled from the laminar-to-turbulent boundary layer transition. Then, the influence of small variation in immersion depths and water temperature on the drag crisis are investigated. From these three studies, a revised flow taxonomy is offered to further enhance the fluid mechanics knowledge of the flow past a surface-piercing sphere over the transitional Fr-Re range.

6.1 Problem overview and terminology

In order to study the mechanics of the flow past a sphere and in particular the drag force F_D, the principal variables must be defined (Figure 6.1). The free-stream velocity, U,

the reference length being the diameter for a bluff-body, D, and the dynamic viscosity, μ, all have an impact on the development of the boundary layer on the sphere surface. The fluid density, ρ, must also be included since it characterises the flow accelerations. With the inclusion of a free surface, the sphere generates gravity waves, and thus the gravitational constant, g, and the immersion depth, d, must be taken into account. The drag force can thus be expressed as follows: $F_D = f(U, D, \rho, \mu, g, d)$.

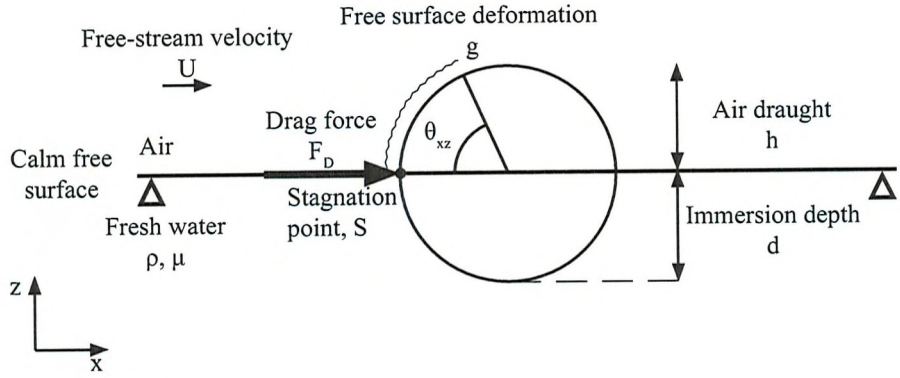

FIGURE 6.1: 2-D schematic of the experiment highlighting the principal variables to describe the drag force coefficient C_{F_D}.

As the immersion depth of the sphere is varied, the spray angle in the x-z plane (side view) remains defined from the centre of the sphere as shown in the 2-D schematic in Figure 6.2. This angle θ_{xz} characterises the development of the breaking wave on top of the sphere.

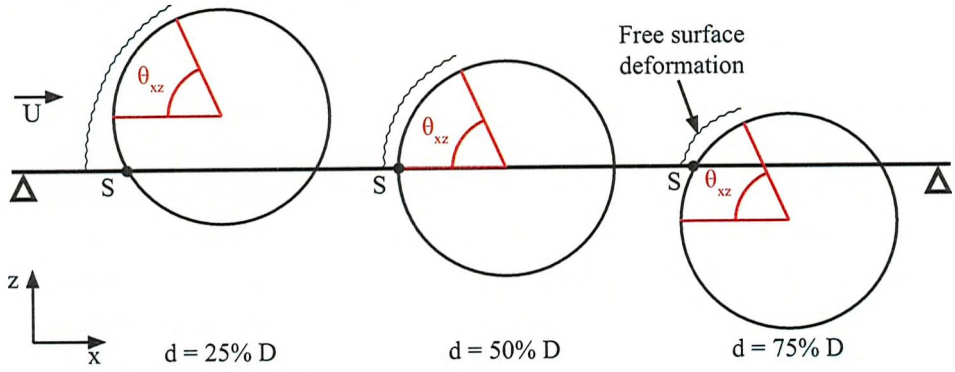

FIGURE 6.2: Schematics of observed spray separation angle from side view.

In order to better characterise the drag force, a dimensionless form is required. Using Buckingham (1914) dimensional analysis, the non-dimensional drag force can be re-written as:

$$C_{F_D} = \frac{F_D}{1/2\rho A_p U^2} = f(Re, Fr, \frac{d}{D}) \tag{6.1}$$

Where:

- $A_p = \frac{\pi D^2}{4}$ is the total sphere projected area, typically chosen as the distance-squared term in the drag coefficient expression for bluff bodies.
- $Re = \frac{\rho U D}{\mu} = \frac{U D}{\nu}$ is Reynolds number, representing the ratio between the inertial forces to viscous forces, thus describing the development of the boundary layer flow.
- $Fr = \frac{U}{\sqrt{Dg}}$ is Froude number, where the square represents the ratio between inertial and gravity forces, thus describing the development of the free surface deformation.
- $\frac{d}{D}$ is the ratio between the immersion depth of the sphere taken as a ship's draught (distance from the calm free surface to the bottom of the sphere).

Although these non-dimensional parameters are inter-related in the physics of the flow past a sphere at the free surface, the investigation of the drag force coefficient with regards to these individual variables allows us to better understand the impact of both phenomena: laminar-to-turbulent boundary layer transition and free surface deformation.

6.2 Initial tests with a prototype model

A first set of towing tank tests was undertaken with the prototype sphere model S1 described in Chapter 5. A full description of this test is presented in James et al. (2015).

Although the existence of the drag crisis for bluff bodies such as spheres or cylinders has long been known to happen between Reynolds number of 10^5 - 10^6, it remains difficult to predict where exactly it occurs. Hoerner (1965) gathered data for a sphere tested in various wind tunnels, with different attachment rigs, surface roughnesses and background turbulences (Figure 6.3). The drag data obtained in Test # 1 are non-dimensionalised by $0.5\rho A_p V^2$ and plotted in log scale against Hoerner (1965) data. The drag crisis occurs over a similar range of Reynolds number as in a single phase case, albeit this study was in a two-phase flow. The surface-piercing sphere presents a drag coefficient which is half the drag coefficient of a sphere in a single phase flow before the drag crisis.

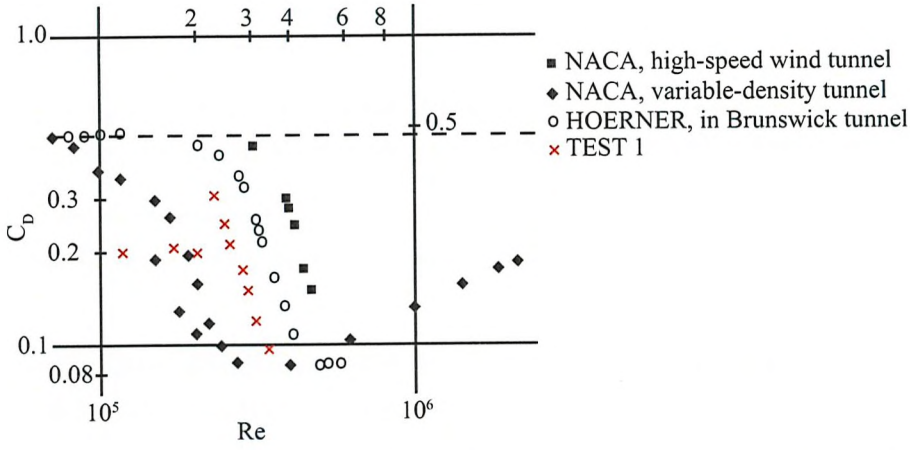

FIGURE 6.3: Initial drag coefficient data for a surface-piercing sphere (James et al., 2015) compared to typical values of the drag coefficient of a sphere in a single phase flow gathered by Hoerner (1965).

From these initial drag-tests, a flow taxonomy was established over the critical Reynolds number range $2.0 \times 10^5 \leq Re \leq 4.4 \times 10^5$, and the Froude number range, $0.7 \leq Fr \leq 1.5$, for a 225-mm diameter sphere located at the free surface with 50%D immersion depth. The taxonomy is based on drag coefficient measurements and above-water photographs (Figure 6.4).

The flow mechanisms were classified into four key flow regimes. In the first flow regime, the boundary layer is laminar and thus separates early leading to a constant drag coefficient around 0.2. The breaking wave is small on the front of the sphere and the turbulent wake behind is wide. As speed increases, the breaking wave builds up as it is transforming more kinetic energy into potential energy, and a sharp increase in drag is measured (flow regime II), up to a point where the drag crisis phenomenon observed for bluff bodies in single phase flow takes place (flow regime III). The boundary layer experiences a laminar-to-turbulent transition. In the second-part of the drag crisis, the breaking wave transitions into a smooth running sheet of fluid. This phenomenon is denoted as the Fr-transition. At this point, the sphere wetted surface area is maximum, and as speed increases the flow stays attached to the sphere for longer reducing further the pressure differential between the front and the rear of the sphere, and hence decreasing the pressure drag (flow regime IV). This flow taxonomy indicates that the well-known drag crisis observed in a single-phase flow is influenced by the presence of the free surface. Studies of flow past other bluff bodies, such as surface-piercing cylinder (Yu et al., 2008), have also emphasised that the flow mechanisms were strongly related to both Reynolds number and Froude number.

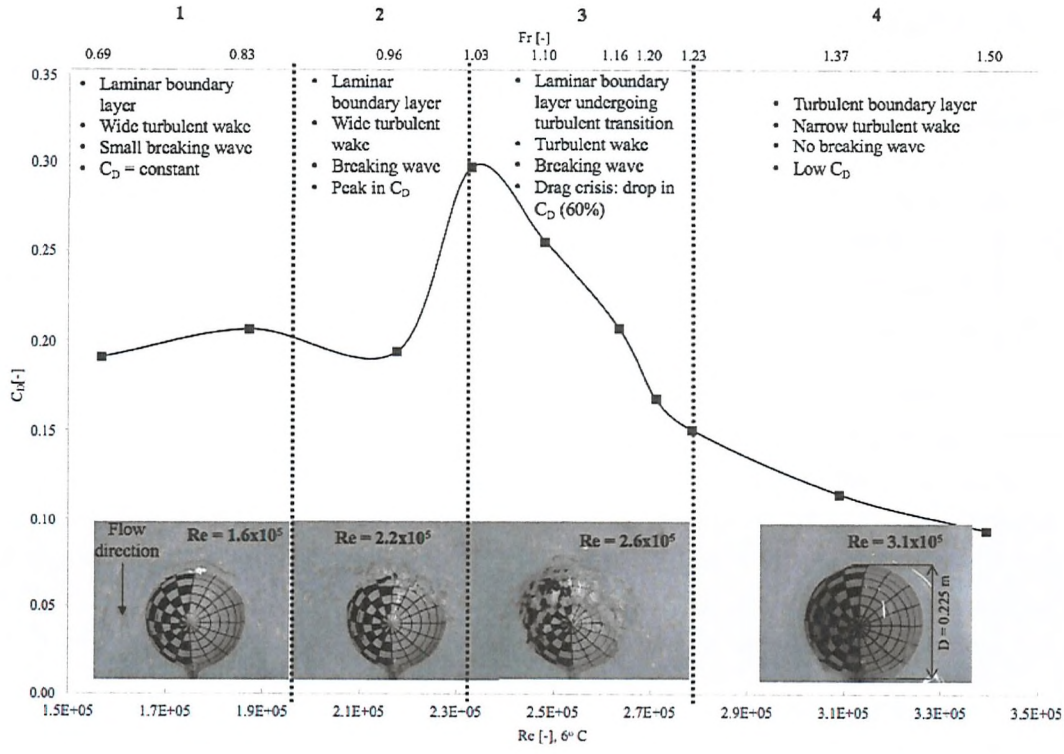

FIGURE 6.4: Flow regime taxonomy for a 225-mm diameter sphere at the free surface with 50%D immersion depth (James et al., 2015).

From this initial study, a more comprehensive tank testing session was devised to enhance the fluid mechanics knowledge of the flow past a surface-piercing sphere over the critical *Re-Fr* range. A methodology to test a sphere in a towing tank environment was developed and three objectives were set:

1. Drag-test two geosim models (different diameters) to better understand the drag crisis phenomena with the inclusion of a free surface over the transitional *Re-Fr* range;

2. Assess the effects of small variations in immersion depth on the flow, and compare it with basic numerical models;

3. Perform an initial investigation on the influence of temperature over the transitional *Re-Fr* range.

6.3 Final tests methodology

6.3.1 Testing plan

A large number of configurations were tested in the Solent towing tank (60 x 3.7 x 1.8 $[m^3]$). Both sphere models (S2), with diameter $D_1 = 225$ mm and $D_2 = 125$ mm, were towed at speeds covering the transitional *Re-Fr* range at different immersion depths (25%, 50%, and 75% of the sphere diameter).

The tank water temperature was measured with a calibrated digital thermometer at three equally-spaced locations along the tank. It was recorded every day as a constant value of 18° Celsius. Reynolds number and other non-dimensional quantities are thus defined based on a density of fresh water for 18° Celcius taken as 998.6 $kg.m^{-3}$ and a kinematic viscosity value of 1.06 $\times 10^{-6}$ $m^2.s^{-1}$ (ITTC, 2011). The range of tested speeds, Froude numbers and Reynolds numbers for each sphere configuration are presented in Table 6.1 for both spheres D_1 and D_2 respectively.

TABLE 6.1: Tests performed on spheres D_1 and D_2.

Configurations	Speed U $[m.s^{-1}]$	Fr [–]	Re [–]	Immersion depth d $[m]$
25%D_1	1.00 - 2.60	0.7 - 1.8	2.1 $\times 10^5$ - 5.5 $\times 10^5$	0.06
40%D_1	1.20 - 2.20	0.8 - 1.5	2.6 $\times 10^5$ - 4.7 $\times 10^5$	0.09
50%D_1	0.60 - 2.80	0.4 - 1.9	1.3 $\times 10^5$ - 6.0 $\times 10^5$	0.11
75%D_1	0.60 - 2.20	0.4 - 1.5	1.3 $\times 10^5$ - 4.7 $\times 10^5$	0.17
25%D_2	0.80 - 2.80	0.7 - 2.5	9.5 $\times 10^4$ - 3.3 $\times 10^5$	0.03
50%D_2	0.70 - 3.20	0.6 - 2.9	8.3 $\times 10^4$ - 3.8 $\times 10^5$	0.06
75%D_2	0.60 - 3.70	0.5 - 3.3	7.1 $\times 10^4$ - 4.4 $\times 10^5$	0.09

6.3.2 Data acquisition

The sphere L-bracket was directly mounted onto a dynamometer attached to the carriage. Both drag and side forces were recorded, as well as wave elevations. Two cameras were positioned on the carriage to get top- and side-view video footage.

Media The top-view videos are available online at James (2017), or can be readily watched by scanning individual QR codes in Appendix D. Photographs were extracted from both top- and side-view video footage over the steady-run portion of the tank (as defined in Section 6.4.1). From these photographs, the free surface deformation features can be observed. Matrices for each configuration (different diameters / different

immersion depths - Table 6.1) have been generated over the range of *Re-Fr* numbers tested and are all presented in Appendix D.

Dynamometry The dynamometer shown in Figure 5.9 was used. The tare drag of the L-bracket was evaluated by removing the sphere from the bracket, rotating it by 90° in the x-z plane with the rear strut pointing up and by placing the sphere 10 mm ahead of the bracket to replicate the on-coming flow onto the bracket when the sphere has an immersion depth of 50%D. Figure 6.5 shows that a similar wave system is exhibited during the standard run and the tare run. The drag curve displayed in Figure 6.6 emphasises that the tare drag represents a small amount of the total drag (13% on average across the speed-range tested). Considering the small tare drag and the fact that the studies presented in this chapter are based on relative comparison (different diameters/different immersion depths), it was decided to not take into account the tare drag. All data presented are derived from the forces obtained from the entire assembly: sphere attached to L-bracket.

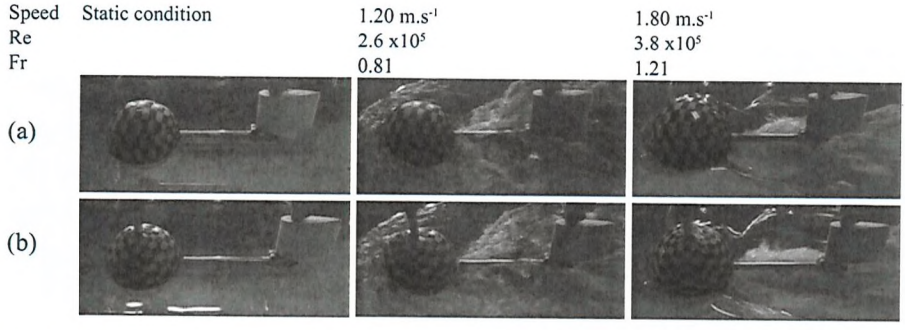

FIGURE 6.5: Observation of similar free surface deformation features between the standard run (a) and tare run (b) at speeds before and after the *Fr*-transition.

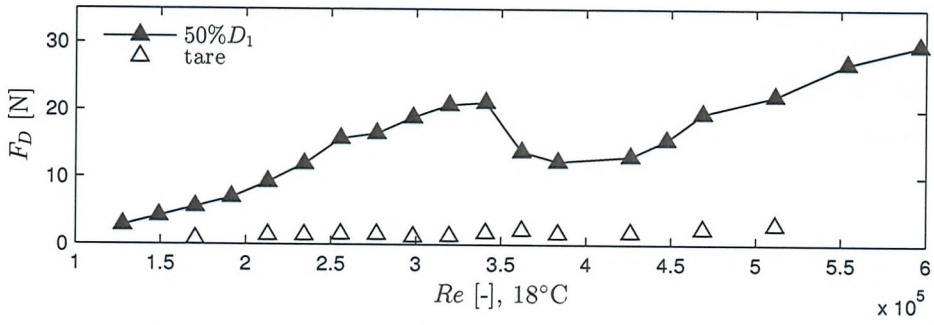

FIGURE 6.6: Drag curve of sphere D1 versus Reynolds number and tare drag of attachment bracket.

Wave elevations An array of four wave probes was set on the side of the tank, at about $\frac{3}{4}$ down the length of the constant-speed section. The probes were located at distances y equal to 645, 795, 945 and 1095 mm from the tank centreline as shown in Figure 6.7.

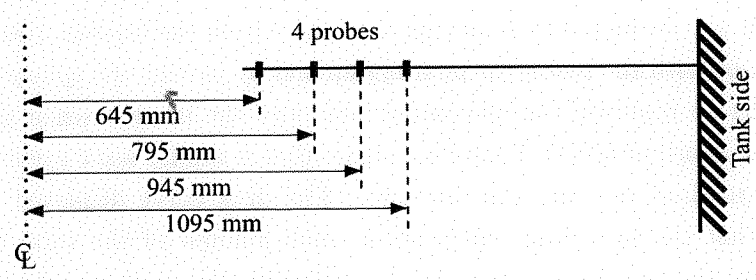

FIGURE 6.7: Plan view of the wave probes set-up.

6.4 Results and discussion

This section is divided into four sub-sections. First, an analysis on how to consider the average drag force of a bluff body in each of the four previously identified key flow regimes is detailed. Using this method, three studies will then be presented to gain further insight on the influence of the non-dimensional Re and Fr numbers on the drag crisis, the influence of small immersion depths and the influence of water temperature.

6.4.1 Drag force analysis

The time history of the drag force over the four characteristic flow regimes previously identified in James et al. (2015) (Figure 6.4) are presented in Figures 6.8 - 6.11. An uncertainty analysis based on the recommended ITTC Procedure 7.5-02-02-02 for towing tank resistance tests (ITTC, 2014) is presented in Appendix D. Repeat runs are plotted all together for the different flow regimes to highlight the good repeatability in the acquisition of the drag force (Section D.2.5).

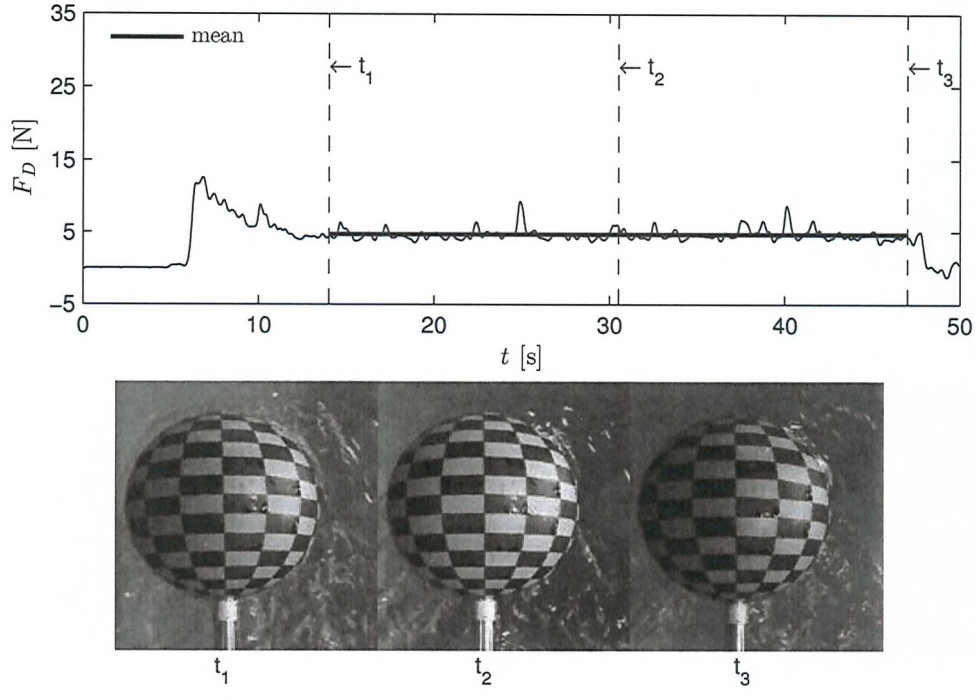

FIGURE 6.8: Flow regime I, $Fr = 0.5$.

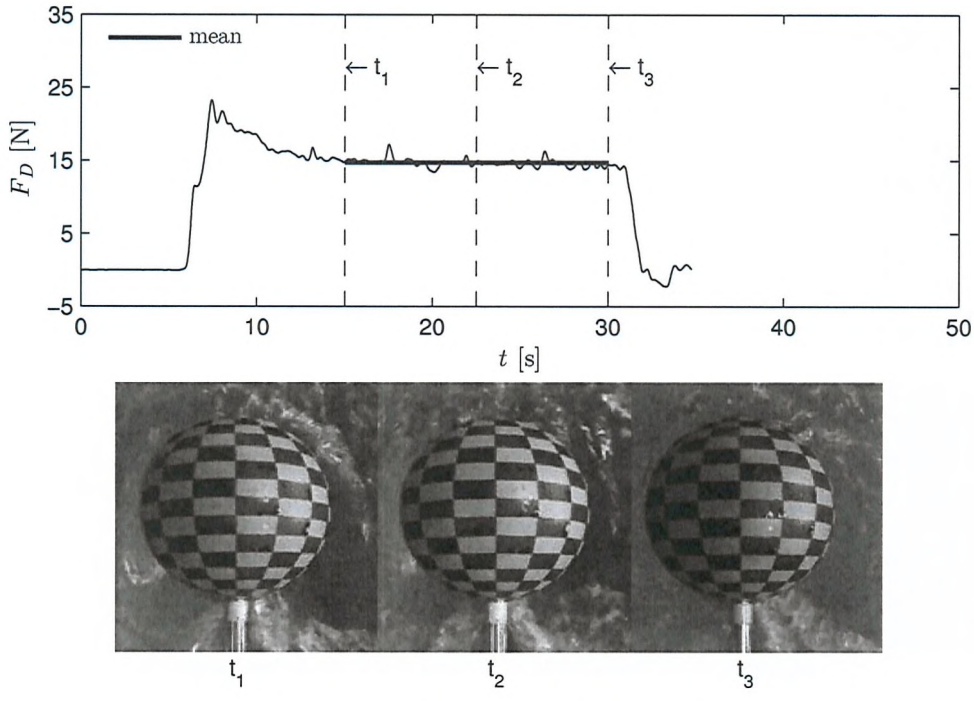

FIGURE 6.9: Flow regime II, $Fr = 0.7$.

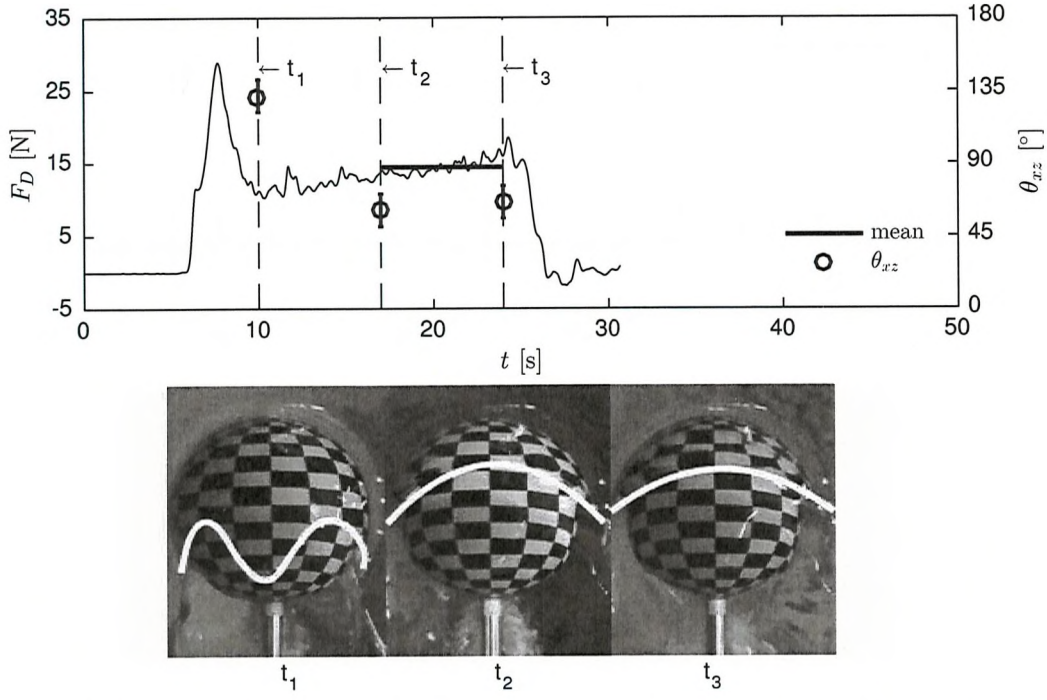

FIGURE 6.10: Flow regime III, $Fr = 1.1$. The white line indicates the end of the breaking wave.

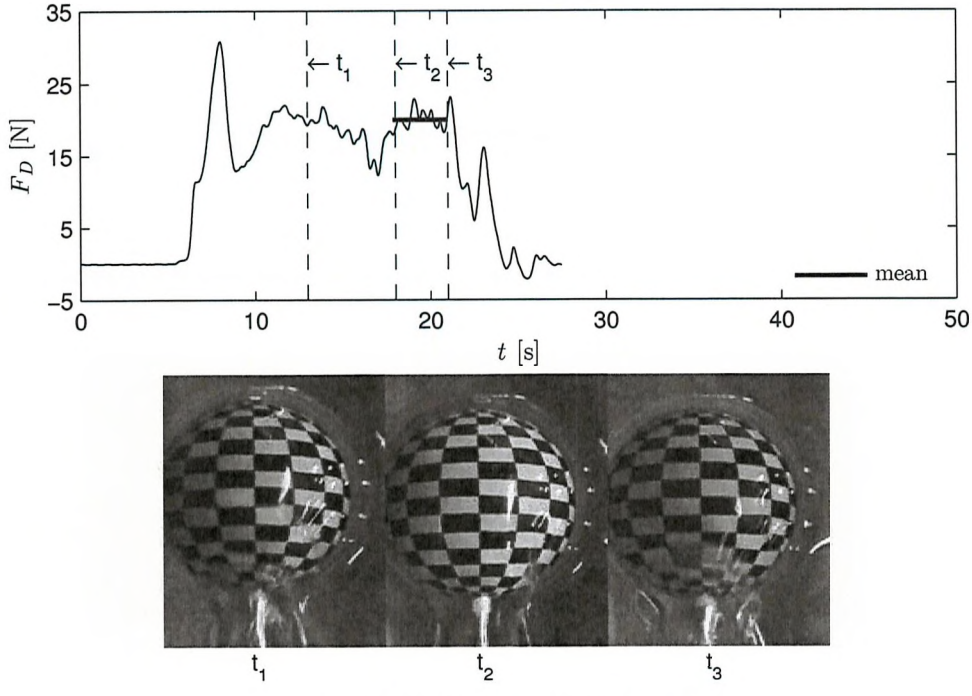

FIGURE 6.11: Flow regime IV, $Fr = 1.5$.

TABLE 6.2: Statistics about different portions of the constant-speed section of the drag trace selected, including mean and COV/run, and mean and COV of all three portions.

Flow regime		Resistance trace selection $t_1 \rightarrow t_2$	$t_2 \rightarrow t_3$	$t_1 \rightarrow t_3$	Mean	COV
I	Mean	4.6	4.7	4.7	4.7	1%
	COV/run	-17%	-18%	-17%		
II	Mean	15.0	14.6	14.8	14.8	2%
	COV/run	-4%	-3%	-4%		
III	Mean	12.6	14.8	13.7	13.7	8%
	COV/run	-8%	-8%	-11%		
IV	Mean	20.0	18.5	19.2	19.2	4%
	COV/run	-6%	-13%	-11%		

Figures 6.8 - 6.11 highlight that there are two phenomena to take into account when discussing the unsteadiness of the flow. Over the constant-speed section of the run, the drag trace presents high-frequency fluctuations due to the unsteadiness of the breaking wave. On the other hand, more significant variations in drag over time are noticed as a result of the large unsteadiness of the flow induced by the interaction between the boundary layer separation point and the free surface deformation. Through the statistical analysis of the drag trace (Table 6.2) and the photographs extracted from the top-view camera at different instants, a procedure for recording the mean drag for each condition can be established.

In flow regime I (Figure 6.8), the drag trace presents small variations of the mean drag over the constant-speed section of the run. As a result, the mean drag can be selected based on the entire constant-speed section of the run. However, there are high-frequency fluctuations around the mean (highest coefficient of variance (COV) within one run $\sim$ 17% F_D), likely arising from the carriage vibrations at the lowest speed.

In flow regime II (Figure 6.9), there is a small variation in mean drag over the constant-speed section of the run, thus the drag is averaged over this entire portion. Smaller unsteadiness in the flow is noticed compared to flow regime I, with the lowest COV within one run $\sim$ 4% F_D.

In flow regime III (Figure 6.10), the drag trace is not constant over time, but presents a positive slope over the constant-speed section of the run. The flow mechanisms are complex at this Fr-transition speed, with the bow wave transitioning to a smooth sheet of fluid. With the acceleration phase, the spray angle of this bow wave in the x-z plane is large at the beginning of the constant-speed section of the drag trace ($\theta_{xz} \sim 132°$). This will likely influence the position of the boundary layer separation point. The delay in separation point results in a lower pressure differential between the front and the rear of

the sphere. Then, the boundary layer slowly loses momentum, and the bow wave comes back forward of the sphere's equator, reducing the boundary layer separation point too; hence the increase in drag. Over the second part of the constant-speed section, the bow wave angle is reduced and oscillates around a mean value of $\theta_{xz} \sim 64°$. The mean drag is thus selected over this second half of the trace only. Ideally, a longer tank would be required to capture the inherent instability of the drag trace in this transitional flow regime.

In flow regime IV (Figure 6.11), a variation in drag between the first-half and second-half of the constant-speed section of the run is noticed, although not as significant as during flow regime III. For this flow regime, the second-half of the drag trace is selected for averaging the drag since the flow is more likely to be steadier then. Very large fluctuations in drag around the mean are measured (COV within one run $\sim$ 13% F_D), likely due to the strong vortex sheddings at high speed.

Power spectral distribution Digital signal processing of the drag and side force traces was performed in order to determine the shedding frequency, F_S, of the vortex features formed at the rear of the sphere at high Reynolds numbers. This frequency represents the number of vortices formed at one side of the 'street' in the unit of time (Hoerner, 1965). The non-dimensionalised form is commonly called Strouhal number, St, and may be expressed as:

$$St = \frac{F_S D}{U} \tag{6.2}$$

The power spectral distribution (PSD) was evaluated using the 'PWELCH' function in Matlab. This function is based on the Goertzel algorithm which efficiently solves the coefficients from the discrete Fourier transform in order to get the sampling data from the time domain into the frequency domain (Roth, 2008). The PSD in N^2/Hz for the drag and side forces are plotted against frequency side-by-side for the four key flow regimes in Figure 6.12.

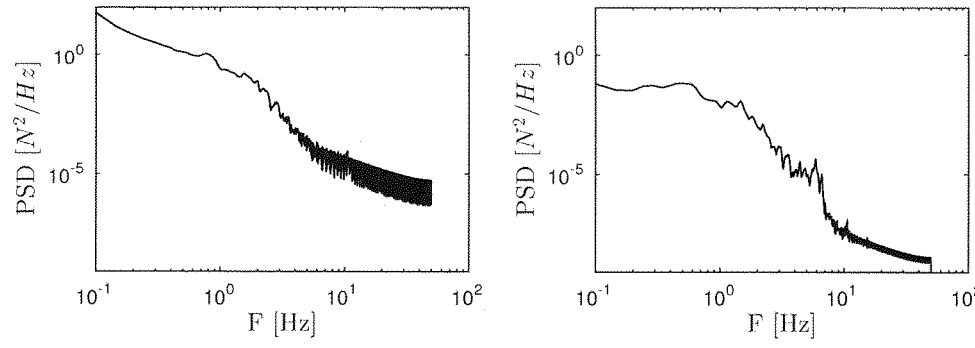

(a) Flow regime I - Drag force

(b) Side force

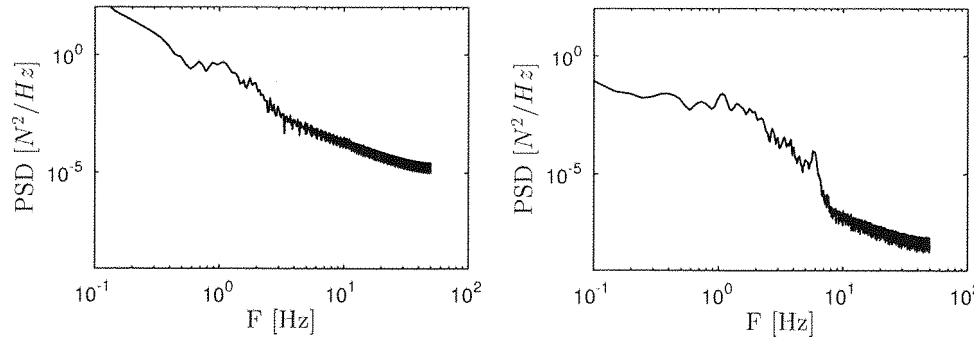

(c) Flow regime II - Drag force

(d) Side force

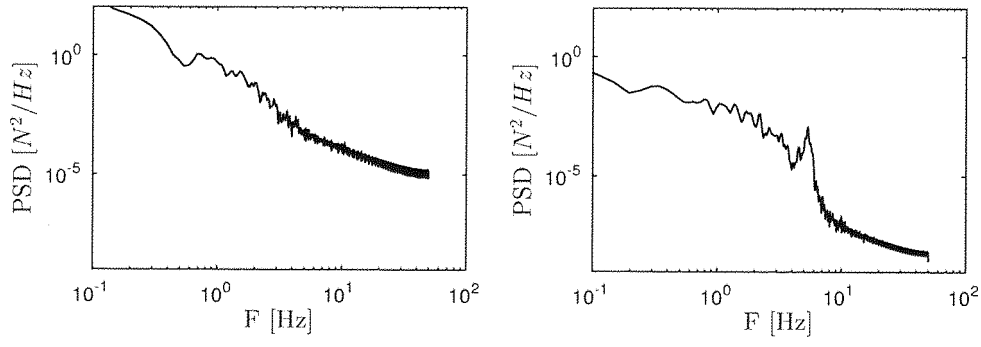

(e) Flow regime III - Drag force

(f) Side force

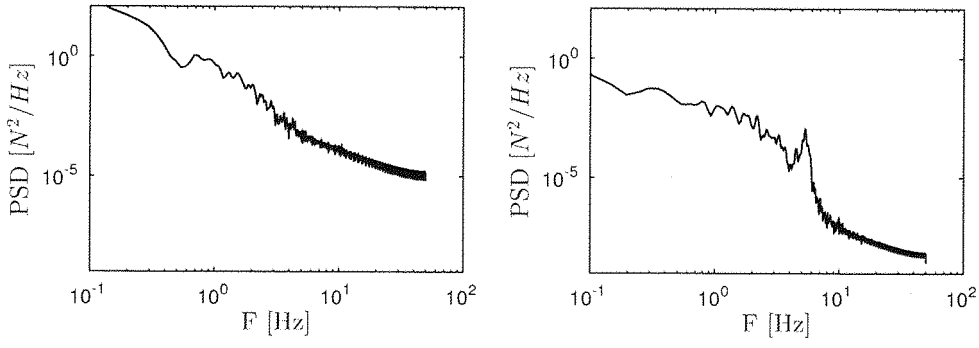

(g) Flow regime IV - Drag force

(h) Side force

FIGURE 6.12: Power spectral distribution of drag and side force traces across all four key flow regimes.

The dominant frequency from the PSD of the side force has a constant value around 5.6 Hz at all speeds, whereas no frequency appear to be dominating in the PSD of the drag force (Figure 6.12). The side force should oscillate at the vortex shedding frequency, while the oscillatory component of the drag force oscillates at twice the vortex shedding frequency (Blevins (2001)).

For a fully submerged sphere, Achenbach (1974*b*) measured a fairly constant Strouhal number of 0.2 at $Re \geq 10^4$. Assuming Strouhal number remains 0.2 despite the presence of the free surface, the shedding frequency should lie between 1 and 2 Hz.

This dominant frequency of 5.6 Hz is thus not the vortex shedding frequency but rather a structural vibration frequency or an electrical noise. The absence of a vortex shedding frequency across all flow regimes indicates that the free surface has a strong effect on the vortex street as previously identified by Ozgoren et al. (2013).

6.4.2 Study 1 - Drag crisis influenced by both Re and Fr numbers

An initial flow taxonomy was established for a 225mm-diameter sphere located at the free surface with its waterline at the equator (James et al., 2015). The Fr-transition occured towards the end of the drag crisis. The free surface deformation therefore has an influence on this drag crisis. The question raised is: how much does the free surface influence the typical drag crisis observed in a single phase flow due to the laminar-to-turbulent boundary layer transition? Two geosim models with different diameters ($D_1 =$ 225 mm and $D_2 = 125$ mm) were drag-tested over a large range of Reynolds number ($8 \times 10^4 \leq Re \leq 6 \times 10^5$) and Froude number ($0.4 \leq Fr \leq 2.9$), in an attempt to separate the different flow phenomena.

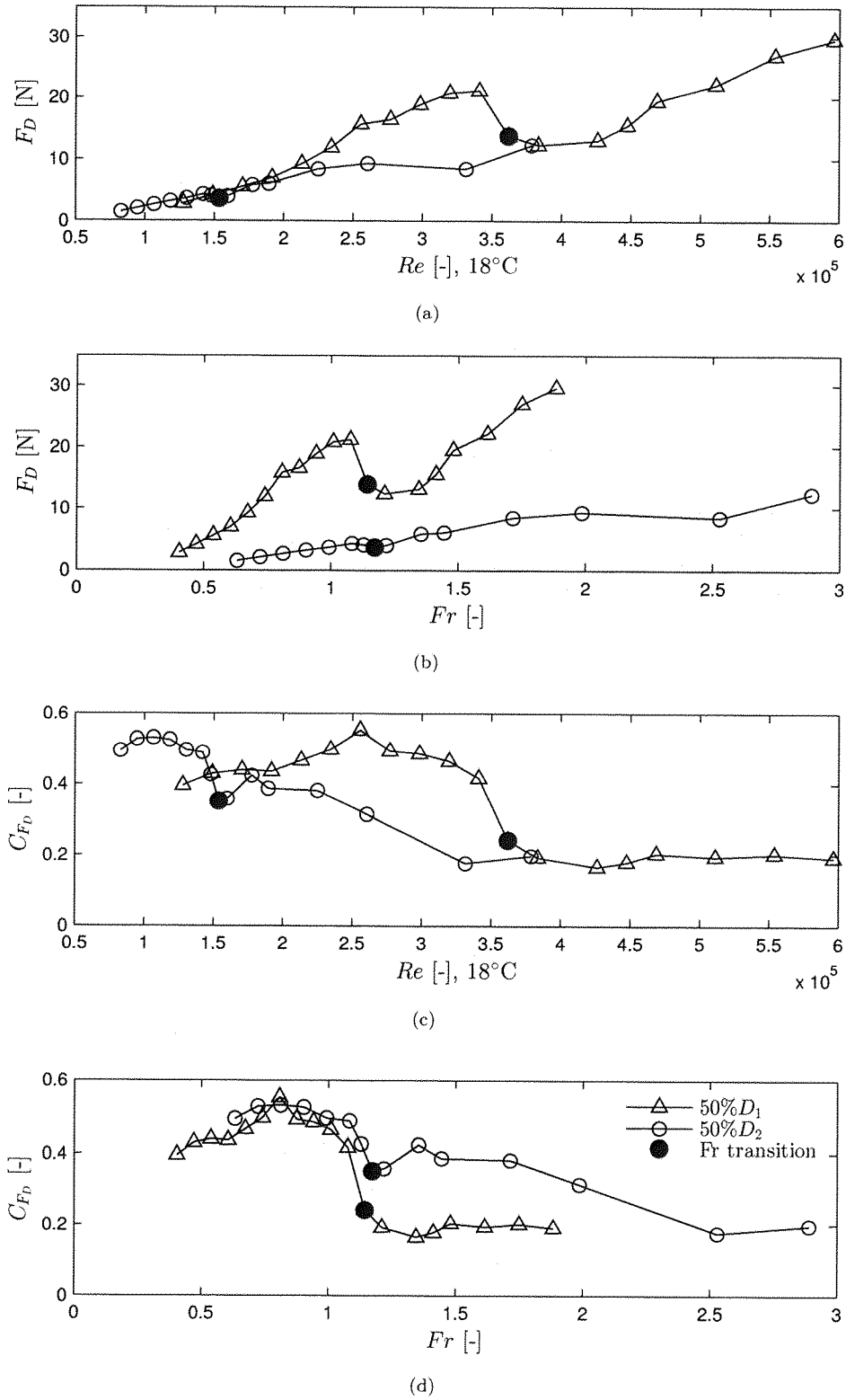

FIGURE 6.13: Drag force and associated coefficient versus Reynolds number and Froude number for both sphere diameters $D_1 = 225$ mm and $D_2 = 125$ mm at 50% immersion depth.

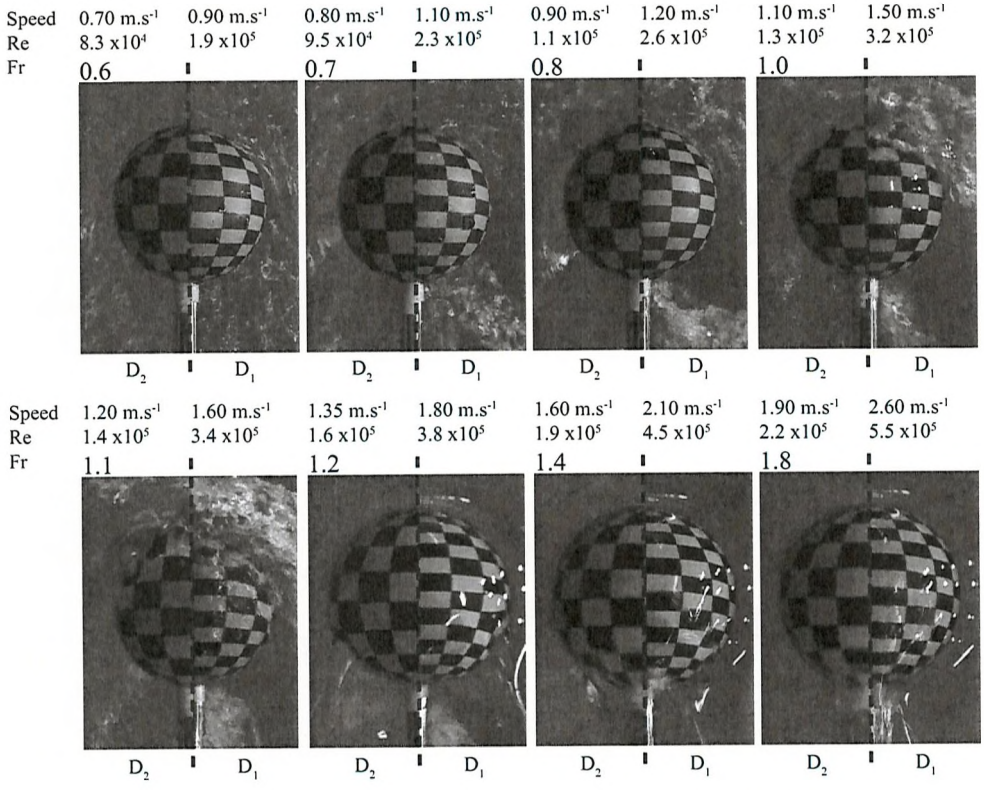

FIGURE 6.14: Free surface deformation comparison between D_2 (left - close-up to match D_1) and D_1 (right) from the top view.

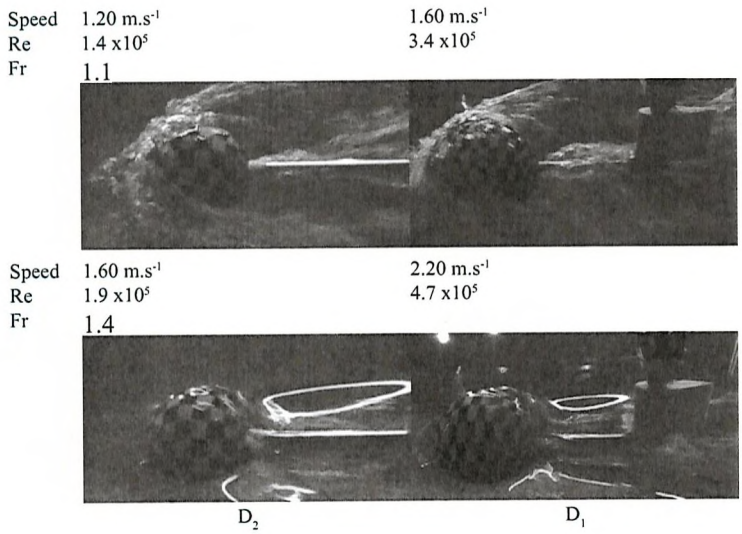

FIGURE 6.15: Free surface deformation comparison between D_2 (left - close-up to match D_1) and D_1 (right) from the side view.

Both drag and associated drag coefficient curves (Figure 6.13) are plotted versus the two non-dimensional parameters of interest Re and Fr. The Fr-transition, occuring when the breaking wave transitions to a thin sheet of fluid running on top of the sphere, is

indicated by a large dot. Both spheres, D_1 and D_2, present a similar drag coefficient in the laminar (FR I - $C_{F_D} \sim 0.5$) and turbulent (FR IV - $C_{F_D} \sim 0.2$) flow regimes. Before the initiation of the drag crisis, the smallest sphere, D_2, also exhibits a peak in drag coefficient at $Fr \sim 0.8$, although smaller than for sphere D_1. Figure 6.13(d) highlights the strong influence of the free surface deformation on the drag crisis. Indeed, the initiation of the drag crisis takes place at $Fr \sim 1.0$ and the Fr-transition occurs at $Fr \sim 1.2$ for both sphere diameters. Similarities in the free surface deformation between the two spheres can be directly observed in Figures 6.14 and 6.15. Top- and side- view photographs of the two spheres are positioned side-by-side at matching Fr, with a close-up on the small sphere, D_2, to match the diameter of sphere D_1.

In the case of the small sphere, D_2, the drag crisis is a two-step process. First, the drag coefficient drops down by 33% with a similar sharp slope as for the bigger sphere D_1, until the Fr-transition occurs.Then, a small rise in drag coefficient happens, followed by a similar drop in drag coefficient (33% C_{F_D}), but with a more gentle slope for ($2.0 \times 10^5 \leq Re \leq 3.3 \times 10^5$), as a result of the boundary layer transition from laminar to turbulent. With an early Fr-transition for sphere D_2 ($Re = 1.5 \times 10^5$), the smooth running sheet of fluid provides extra momentum to the boundary layer, and thus allows the laminar-to-turbulent transition to occur at an earlier Reynolds number. Overall, the drag coefficient drops by about 65% over the total drag crisis in both cases. This re-iterates the great potential for engineering applications.

6.4.3 Study 2 - Influence of small immersion depths on a surface-piercing sphere

Both spheres, D_1 and D_2, were drag-tested at different immersion depths. Figure 6.16 shows the drag coefficient curve versus Reynolds number for sphere D_1 at immersion depths of 25%, 40%, 50% and 75% of D_1. The increase in draught results in a larger projected area under the free surface. Consequently, as the immersion depth increases, the pressure differential between the front and rear of the sphere significantly rises before the drag crisis. This phenomenon (flow regime II) was not previously observed in the case of a single-phase sphere (Figure 6.3). Moreover, as indicated in Figure 6.17, the height of the first wave increases. The first wave height has a hump for Froude number between 1.1 and 1.3. The peak in drag, previously observed before the drag crisis, appears to be much larger as the immersion depth increases.

The Fr-transition occurs at an earlier Reynolds number as the immersion depth increases since there is less potential energy to overcome. Figure 6.18 better explains the effect of the transfer in kinetic energy to potential energy in the breaking wave. The transitional speed (i.e. speed at which the breaking wave transforms into a thin sheet of fluid running on top of the sphere) is plotted against the air draught for all conditions tested. The Fr-transition appears to be independent of the waterplane area, but strongly depends

on the air draught. Indeed, the transitional speeds follow a similar trend to Bernoulli prediction, taken between the front stagnation point and the undisturbed free surface. In order to match the experimental data, a factor of 1.13 was applied to Bernoulli prediction to compensate for the additional kinetic energy required due to the presence of viscous effects (Equation 6.3).

$$U_{transition} = 1.13 \times \sqrt{2hg} \tag{6.3}$$

Finally, in the fully-turbulent boundary layer flow regime (flow regime IV), the drag coefficients of the sphere at different immersion depths do not vary as much, since the sphere is covered with a thin sheet of fluid in all conditions.

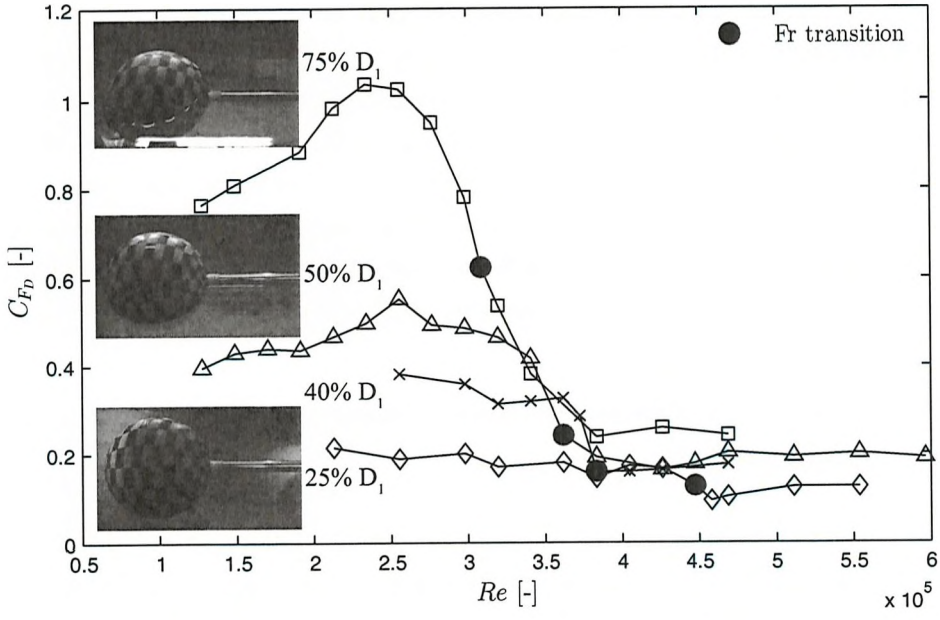

FIGURE 6.16: Drag force coefficient versus Reynolds number for sphere D_1 at different immersion depths.

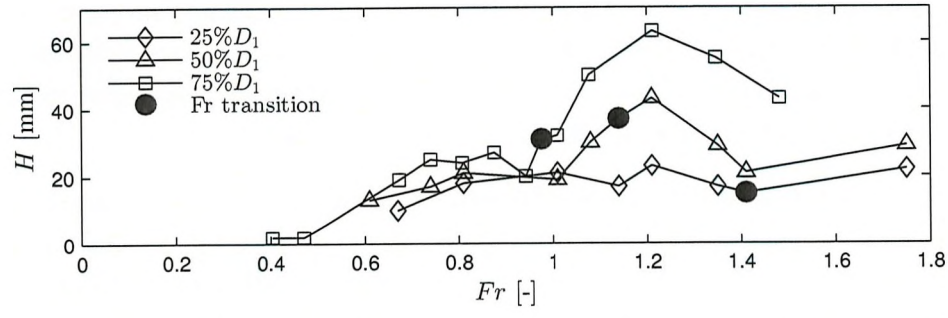

FIGURE 6.17: H, height of the 1^{st} wave recorded by the wave probe closest to the model ($3D_1$ from the centreline) versus Froude number, for a range of immersion depths.

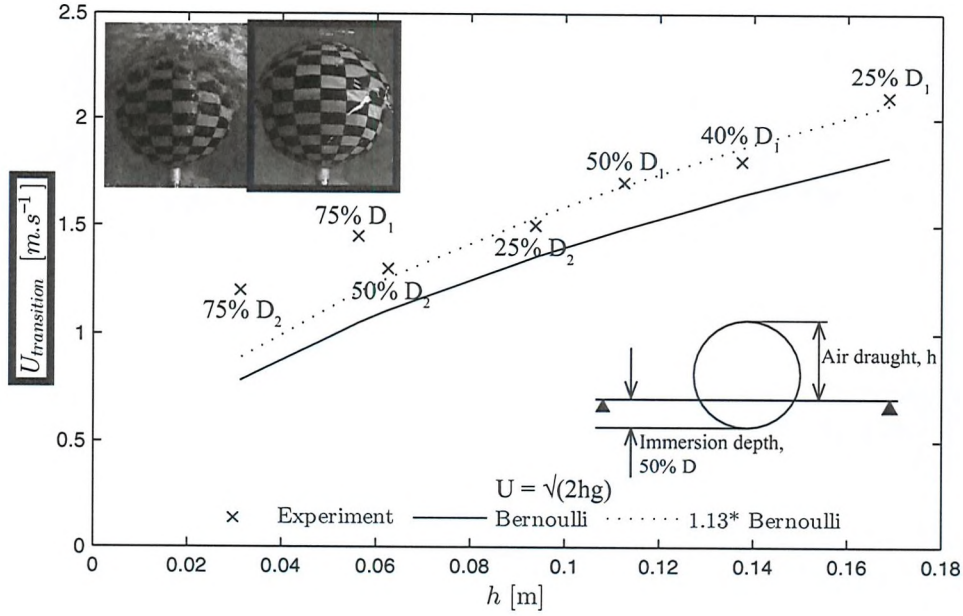

FIGURE 6.18: Fr-transition speed versus air draught for all configurations tested, compared with the prediction from Bernoulli equation.

6.4.4 Study 3 - Influence of water temperature

The drag curve for a 225mm-diameter sphere towed at an immersion depth of 50% D was obtained four times in different fresh water temperatures: 6°C (Test # 1) and 10°C (Test #3), 15°C (Test # 7) and 18°C (Test # 6). In Figure 6.19, the drag coefficient is plotted for all the temperatures against Re at the test temperature (denoted Test T°C) and Re at the standard temperature of 15°C, as recommended by the ITTC procedure 7.5-02-02-02 (ITTC, 2014). It can be noticed that as temperature decreases, the drag coefficient decreases significantly. In particular, in the laminar flow regime, with a ΔT of 12°C between Tests # 1 & 6, the drag coefficient drops down by 60%.

The ITTC skin friction correction was applied to the total resistance coefficient using Equation 6.4. For this study, the drag force was first non-dimensionalised with respect to the wetted surface area defined at the static waterline and the ITTC temperature correction was applied. The corrected total resistance coefficient was then dimensionalised, before being non-dimensionalised with regard to the projected area for consistency with the overal study of the flow past a sphere. With a maximum ΔT of 9°C for Test # 1, the effect on the drag coefficient is under 1%, and thus judged to be negligible. This temperature correction based on the skin friction coefficient is typically used by naval architects who consider ships as slender bodies, but it has a marginal effect on bluff bodies with a high drag coefficient and a low wetted surface area.

$$C_{T,15°C} = C_{T,TEST} - C_{f,TEST} + C_{f,15°C} \tag{6.4}$$

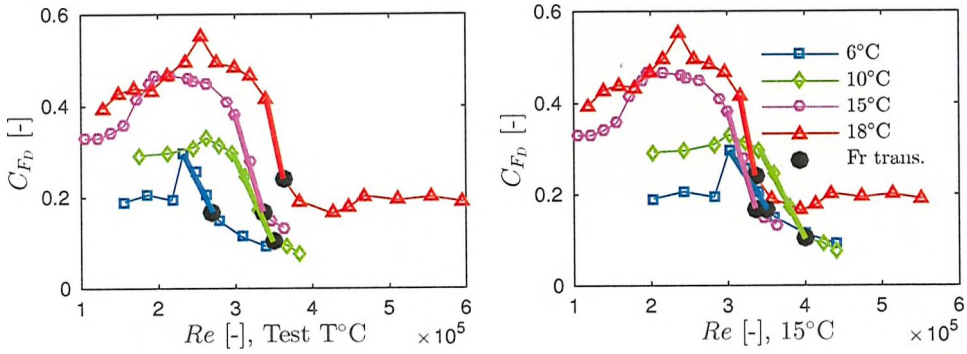

FIGURE 6.19: Sphere with 50% D_1 immersion depth, tested at different water temperatures, 6°, 10° and 18° Celsius. Drag coefficient versus Re at the Test temperature and at 15°.

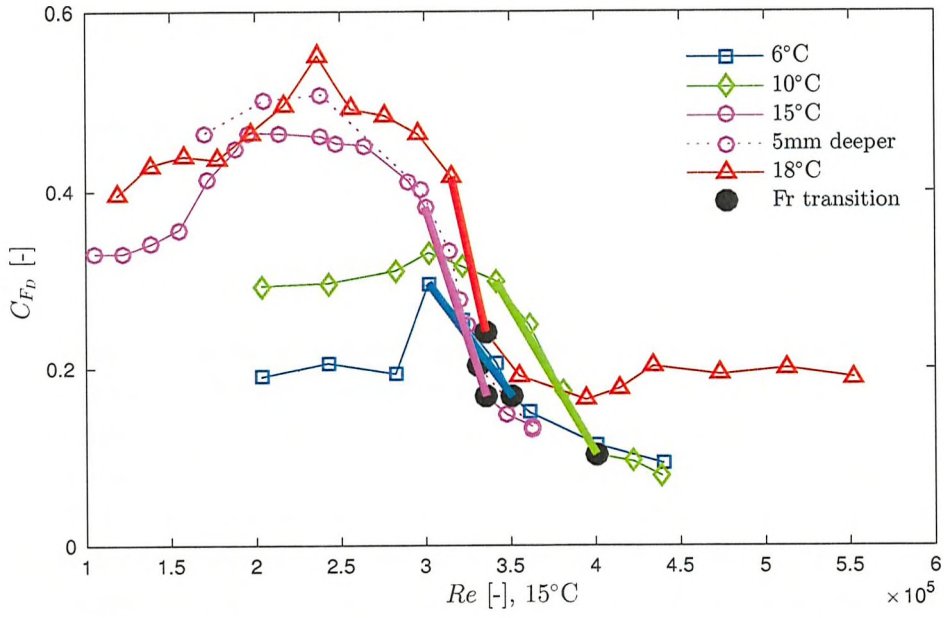

FIGURE 6.20: Drag force coefficient versus Reynolds number for sphere 50% D_1, tested at different water temperatures, 6°, 10° and 18° Celsius. Tank 1 - 30 x 2.4 x 1.2 [m^3] and Tank 2 - 60 x 3.7 x 1.8 [m^3].

Tests # 1, 3 and 7 were carried out in the Lamont tank, whereas Test # 6 was performed in the Solent tank, all using the same dynamometry. The prototype sphere model (S1) was used for Tests # 1 & 3, while the professionally-made sphere model (S2) was tested in Tests # 6 & 7. Although the sphere models, S1 and S2, do not have the same accuracy in terms of diameter and surface finish, the effect of water temperature on the drag force is significant enough to be thought to be a real physical effect, especially in the laminar flow regime. The sphere position was varied by a small vertical amount of 5 mm during Test # 7. Although a noticeable change in drag coefficient is noticed in Figure 6.20, the effect of water temperature still dominates any small variations in immersion depth which may have occured during the model installation.

The water viscosity varies with temperature as a polynomial function of degree 2, with negative gradient. As temperature increases, the water viscosity decreases, as opposed to air (Figure 6.21), and as a consequence Reynolds number increases. This reduction in viscosity lowers the wall shear stress leading to an earlier boundary layer separation. In the case of a flat plate, the drag would be reduced since friction drag dominates the total drag. However, in the case of a bluff body, the pressure drag increase due to the early separation of the boundary layer is much larger than the drop in skin friction. Consequently, as water temperature increases, the sphere experiences a larger resistance, especially in the laminar flow regime where there is less momentum in the boundary layer to keep the flow attached.

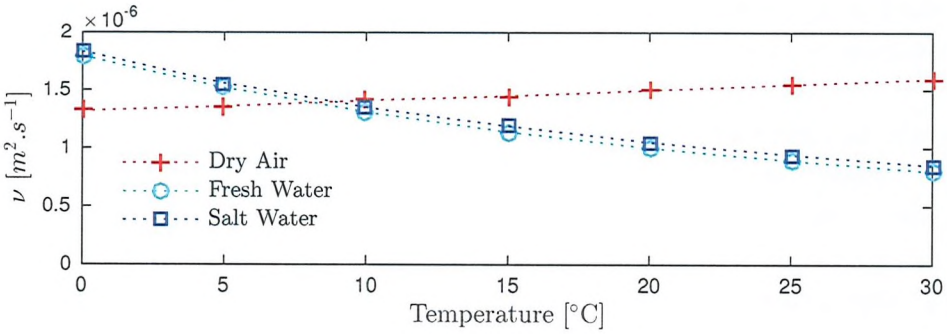

FIGURE 6.21: Kinematic viscosity of air and water exhibiting opposite trends. As water temperature increases, the kinematic viscosity decreases.

Furthermore, the change in water viscosity is also affecting the timing of the drag crisis. As temperature rises, a delay in the initiation of the drag crisis from the peak in drag coefficient is observed. Another noticeable trend is the increase of the drag coefficient gradient over the drag crisis region as temperature rises. On the other hand, there does not seem to be any trend as to when the Fr-transition occurs.

To explain the impact of water temperature on the drag crisis of a surface-piercing sphere, the effects of Froude and Reynolds numbers should be studied. The wave elevations were recorded to measure the wave resistance. However, in the case of a bluff body generating large breaking waves and strong vortex shedding, the evaluation of wave resistance remains difficult with the current method (Taunton, 2013). To assess the impact of temperature on the boundary layer separation, pressure sensors could be used although unsteady pressures with breaking waves are difficult to measure. This is left as further work.

6.5 Revised flow regime taxonomy for a surface-piercing sphere

From the three additional studies considering geosim models, immersion depths and water temperature, further knowledge have been gained to better describe the flow taxonomy of a surface-piercing sphere over the criticial Re-Fr range. The key findings are summarised in Figure 6.22.

It is important to comment on the drag crisis flow regime (III). In Figure 6.22, the drag crisis is presented as a two-step process: with first a transition from breaking wave to a thin sheet of fluid running on top of the sphere, followed by a boundary layer transition from laminar-to-turbulent flow. Depending on the sphere diameter, the phenomena can be more or less coupled. For the tested 225-mm diameter sphere, both phenomena were fully coupled with a single drag crisis. In the case of a smaller sphere ($D_2 = 125$ mm), the drag crisis was extended to a two-step process as shown in the revised flow taxonomy. Two additional geosim models could be tested to further separate the Fr and Re transitions. A smaller sphere diameter would ensure that only the Fr-transition occurs, while a larger sphere diameter would ensure that only the Re-transition occurs.

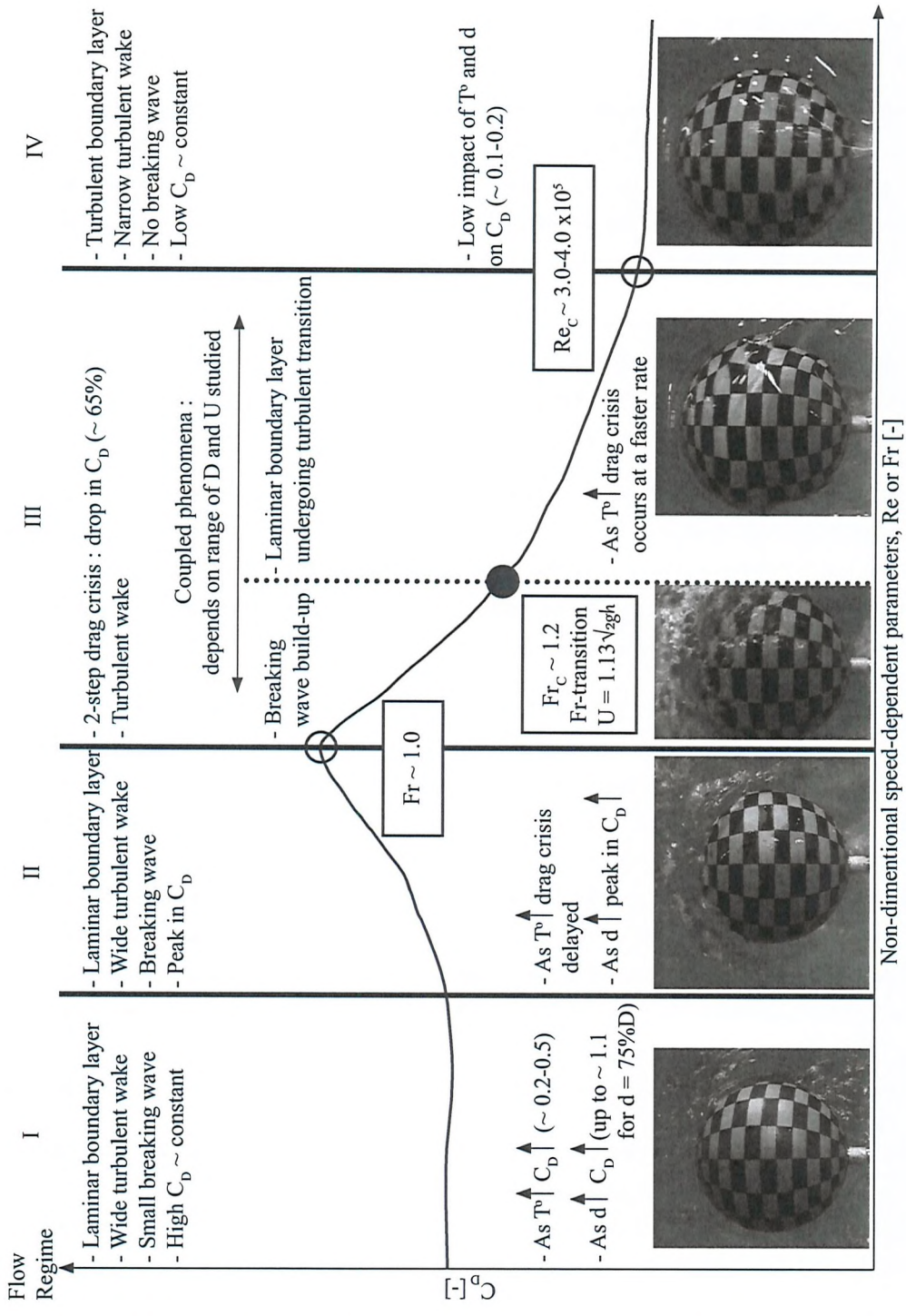

FIGURE 6.22: Revised flow regime taxonomy for a surface-piercing sphere over the critical *Re-Fr* range, $8 \times 10^4 \leq Re \leq 6 \times 10^5$ and Froude number $0.4 \leq Fr \leq 2.9$. Note: T° = temperature, d = immersion depth.

6.6 Chapter summary

Initial tank tests with a sphere prototype over the critical *Re*-*Fr* range ($2.0 \times 10^5 \leq Re \leq 4.4 \times 10^5$ and $0.7 \leq Fr \leq 1.5$) showed that a surface-piercing sphere encounters a more complex version of the drag crisis observed in single phase flow (Hoerner, 1965). This confirms a potential for swimmers to use the drag crisis occuring on their head while swimming at the free surface to swim in a lower drag flow regime.

The drag crisis usually refers to the Reynolds number phase when the laminar-to-turbulent boundary layer transition occurs. With the inclusion of a free surface, another phenomenon occurs during the drag crisis: the breaking wave transitions to a thin sheet of fluid running on top of the sphere. This is denoted the *Fr*-transition.

This chapter presented a large number of drag-tests, supported with photographs extracted from top- and side-views video footage, undertaken in a towing tank to better understand the factors affecting the drag crisis of a surface-piercing sphere. These experimental data provide support for the validation of CFD test-cases for those interested in bluff body flows with the involvement of a free surface.

First, two geosim models revealed the existence of a two-step drag crisis due to both *Re* and *Fr*, initiated at $Fr \sim 1.0$ by a change of free surface deformation and followed by the boundary layer transition until the critical $Re_c \sim 3.0$ to 4.0×10^5 is reached. In the case of a swimmer's head with a diameter close to 200 mm and at typical swimming speeds between 1.4 and 2.0 $m.s^{-1}$, the *Fr*- and *Re*-transitions occur simultaneously, leading to a one-step drag crisis. Although this is not of interest to a swimmer, two other geosim models could be tested to further separate the *Fr*- and *Re*-transitions. A smaller sphere diameter would ensure that only the *Fr*-transition occurs, while a larger sphere diameter would ensure that only the *Re*-transition occurs. In addition, with the use of surface-pressure sensors, the boundary layer separation could be investigated. These data would provide additional information to validate numerical simulations.

In a second part, the influence of immersion depth was investigated, and a key result showed that the *Fr*-transition depends on the air draught and thus occurs at a speed predicted by the Bernoulli equation with a factor of 1.13 (irrespective of the underwater volume and waterplane area).

Eventually, due to repeat tests performed at various times of the year in two different towing tanks, the effect of water temperature could be investigated. As temperature rises, a large increase in laminar drag is noticed and the drag crisis appears to be more sudden. This large effect of temperature on bluff body drag indicates there may be a need to take carefully into account the temperature when testing swimming equipment on a swimmer's head. These initial results suggest that the impact of the drag crisis encountered on a swimmer's head in a heated pool environment may be even larger.

To conclude, the drag crisis for the sphere at the free surface occurs around the elite swimmer's speed range (1.5 - 2.0 $m.s^{-1}$). It is therefore an important range of speed to study as there is potential to use flow control techniques on the swimmer's head to get the drag crisis to start at a lower speed. The swimmer could thus always swim with minimum drag once his or her surface speed is attained. However, does a swimmer's head follow a similar flow regime taxonomy as the sphere (Chapter 7)? Flow control techniques on the head could include goggles design, cap surface roughness, hair management under a cap. All these aspects have been tested on a head model only or on a mannequin and will be discussed in Chapters 7 and 8.

7

Flow past a head

A 3-D printed swimmer's head was tested in two different towing tanks over the same speed range, but in different water temperatures. First, the drag generated by the head when towed at the free surface is compared with the sphere data. The effect of head position on the flow regime is then presented, followed by studies on the influence of goggles and cap designs.

7.1 Initial analogies and dissimilarities between a sphere and a head

The head volume is 0.004 m^3 which is equivalent to the volume of a 0.2m-diameter sphere (Section 5.1.2). The drag data for the head are all non-dimensionalised with $0.5\rho A_p U^2$ so that the drag curves can be compared with the case of a sphere. Reynolds number is defined with the diameter of the equivalent volume sphere.

The sphere and the head were tested during the same set of tests twice but in different water temperatures. The first tests (Test # 3) were undertaken in the Lamont Tank with a water temperature of 10° C; while the second set of tests (Test # 6) was in the Solent tank with a water temperature 8° C greater. The head is positioned in the aligned condition (Figure 7.2) and the sphere is located at the free surface with a 50% immersion depth.

The drag force and associated drag coefficient for the head and the sphere during both tests are plotted in Figure 7.1 against speed, Fr and Re. A sphere and a head present some similarities and differences. They are both bluff bodies. A head has one plane-symmetry going between the eyes, nose and chin centreline, whereas a sphere presents a multi-plane symmetry. As expected, the development of the flow around the head as speed increases presents similarities with the flow regime taxonomy previously established for the sphere. After $Fr \sim 1.0$, the head undergoes a transition from breaking wave to a thin sheet of fluid running on top of the head and this is coupled with a decrease in drag (Figures 7.3 and 7.4).

It was previously observed in Chapter 6 that, as temperature increases, the drag coefficient also rises before the initiation of the drag crisis. The same trend can be observed for the case of the head. However, at low temperature (10° C), the decrease in drag is not as important as at greater temperature (18° C). With a water temperature of 10° C, the drag differential between the laminar and fully-turbulent boundary layer flow regimes is much lower than in the case of the sphere, 40% drop in drag for the head versus 75% for the sphere. Differences in drag coefficients between the sphere and the head were to be expected as the head is narrower than a sphere and presents curved features promoting flow separation and re-attachment.

On the other hand, at higher temperature, the drag coefficient curve for the head follows closely the sphere where similar flow regimes are observed except in the laminar flow regime where data points are lacking in the case of the head. No data points were recorded in this laminar flow regime since speeds below 1.2 $m.s^{-1}$ are not of much importance for elite swimmers.

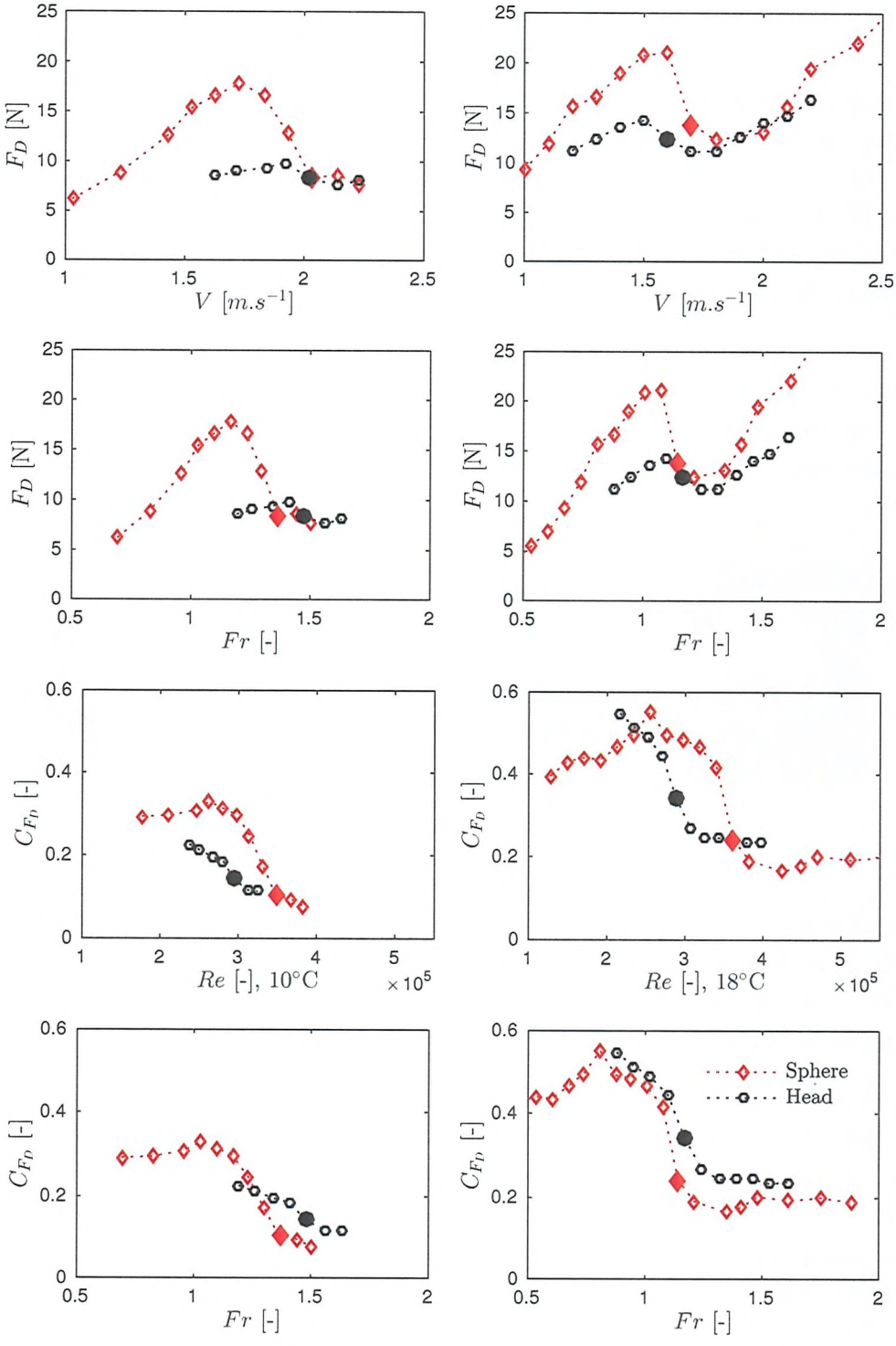

(g) Temperature = 10° C.

(h) Temperature = 18° C.

FIGURE 7.1: Drag force and associated drag coefficient for the head aligned case compared with the sphere tested at 50% D_1 immersion depth, at two different water temperatures, 10° and 18° Celsius. Fr-transition indicated by the filled marker.

7.2 Influence of head position

During Tests # 3 and # 6 , the influence of the head position on the Fr-transition and drag crisis was investigated over the typical swimming speed range. The three head positions tested on the front are illustrated in Figure 7.2. During Test # 3, the flow past the head in the backstroke position was also assessed. The backstroke position is the direct opposite of the head down position, i.e. looking directly up instead of directly down at the pool bottom.

As the head position changes from down to aligned to up, the waterline length varies from 218 mm, to 212 mm and 191 mm. Despite this change in waterline length, the characteristic length remains defined as the diameter of the equivalent volume sphere, i.e. 200 mm.

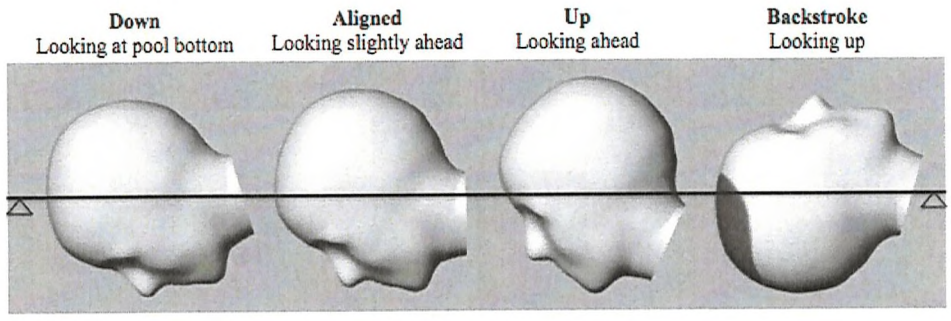

FIGURE 7.2: Different head positions tested.

The influence of the head position is investigated in a similar manner to the sphere, with a combination of above-water photographs and drag coefficient data. Since it was shown that the temperature has an important effect on the drag crisis of the head as well, both tests are presented.

From the above-water cameras, matrices of screenshots taken over the steady-speed portion of each run are extracted. For the initial tests in 10° C water temperature, only a top-view camera was set up (Figures 7.3), whereas during the next set of tests (18° C), both top-view and side-view cameras were positioned (Figures 7.4 and 7.5). The change in free surface deformation from a breaking wave to a thin sheet of fluid running over the top of the head occurs at 2.0 $m.s^{-1}$ for the head in down and aligned conditions in 10° C, whereas it occurs ealier in higher temperature, at a speed of 1.6 $m.s^{-1}$. Irrespective of the water temperature, the Fr-transition is delayed in the head up condition. It occurs just after the head down and aligned cases, at 2.1 $m.s^{-1}$ and 1.7 $m.s^{-1}$ for the respective low and high temperature conditions. In the backstroke position, the flow transitions much earlier, at 1.5 $m.s^{-1}$ since the air draught at the forehead is much smaller than for the other head positions on the front.

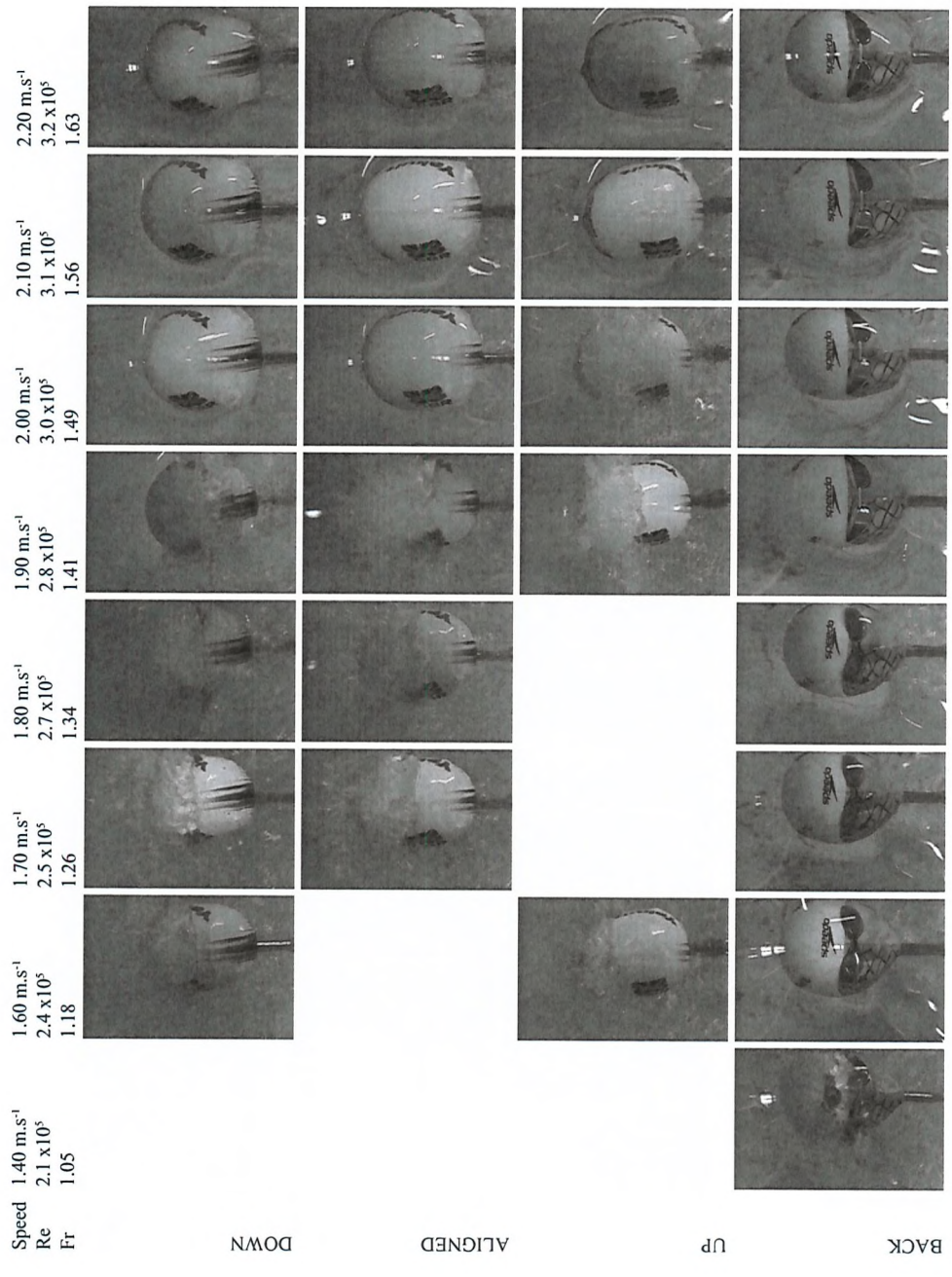

FIGURE 7.3: Top-view flow visualisation around the head in freestyle and backstroke position, at a temperature of 10° Celsius.

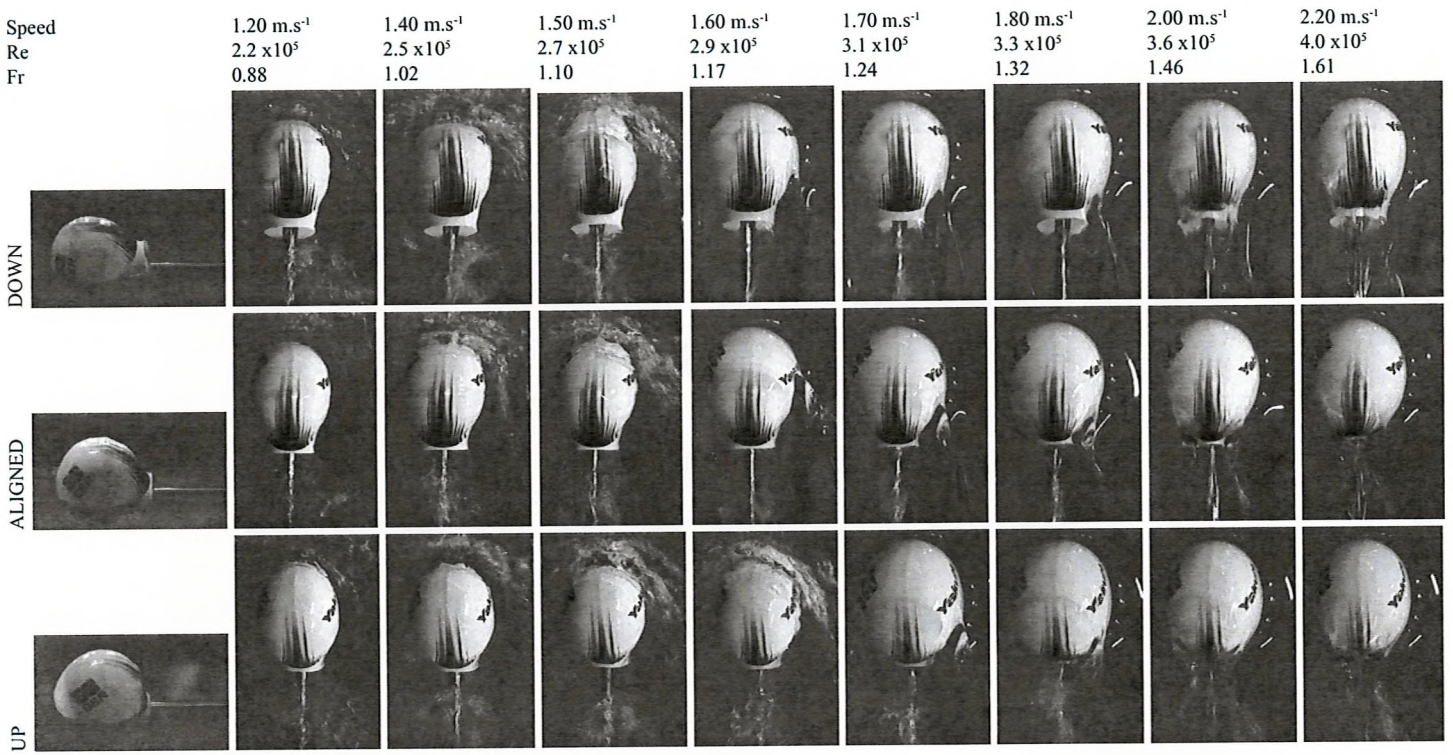

FIGURE 7.4: Top-view flow visualisation around the head in freestyle position, at a temperature of 18° Celsius.

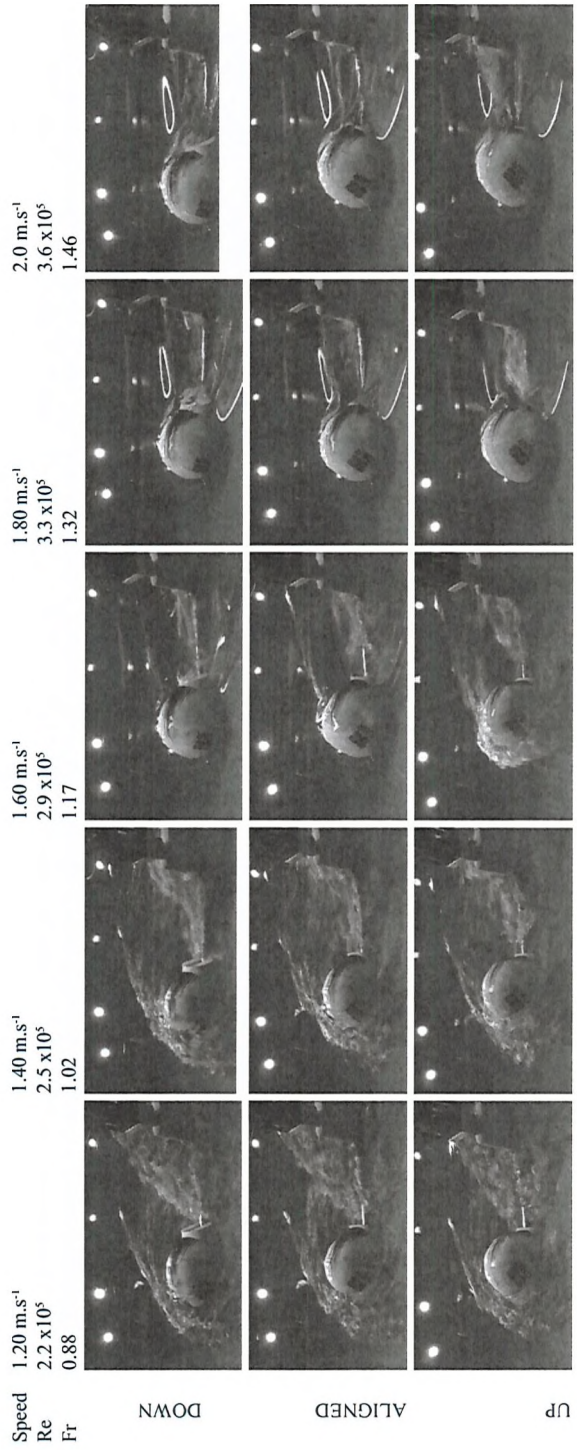

FIGURE 7.5: Side-view flow visualisation around the head in freestyle position, at a temperature of 18° Celsius.

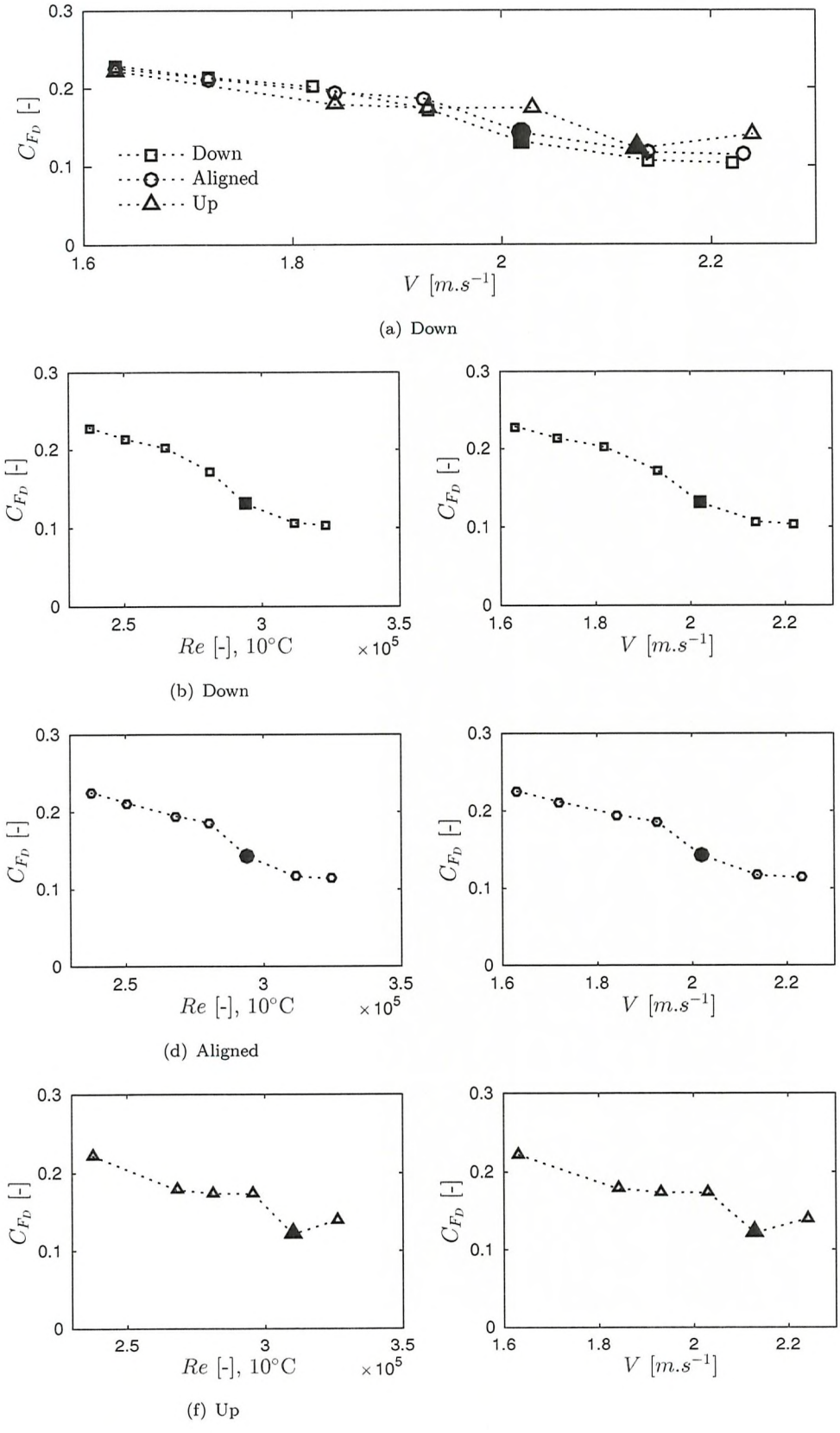

FIGURE 7.6: Drag coefficient versus Reynolds number and speed for the different head positions tested: down, aligned and up at a temperature of 10° Celsius.

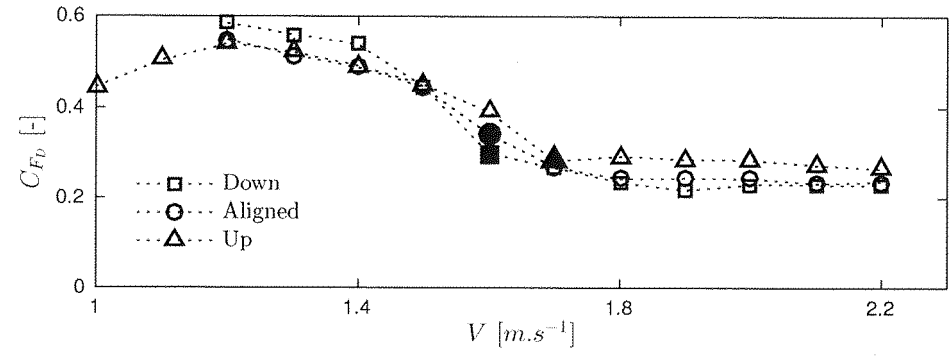

(a) Down

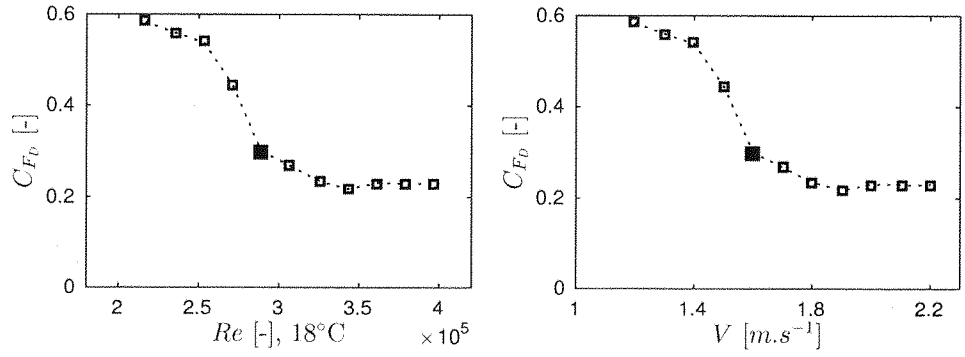

(b) Down

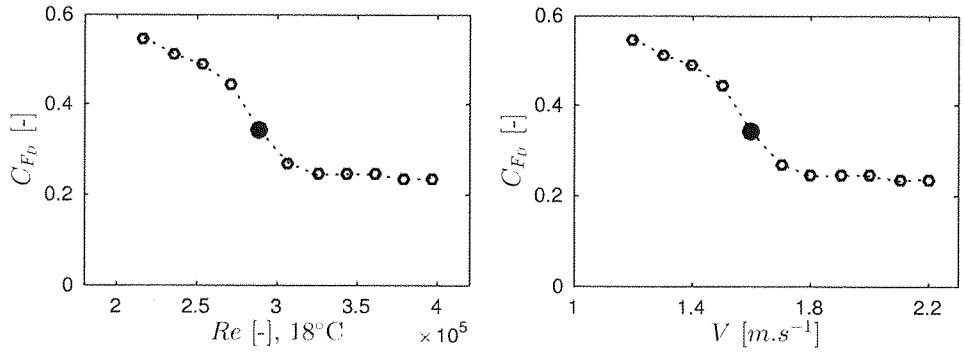

(d) Aligned

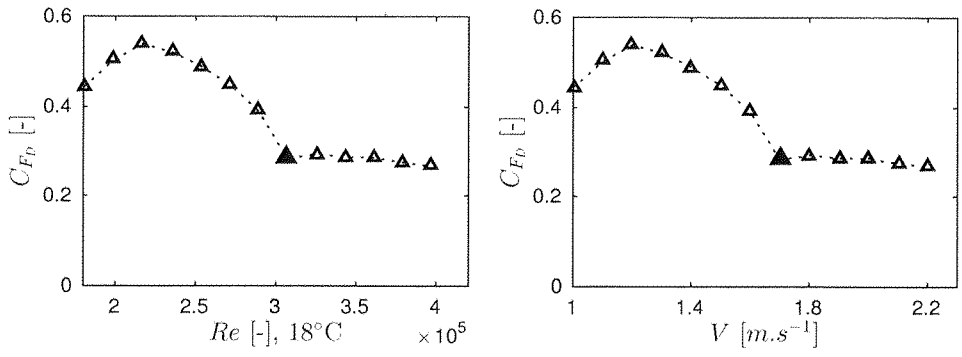

(f) Up

FIGURE 7.7: Drag coefficient versus Reynolds number and speed for the different head positions tested: down, aligned and up at a temperature of 18° Celsius.

Figure 7.6 shows the drag coefficient curves for all conditions together first and then for each head position separately to better analyse each flow regime change in 10° C water temperature. The same plots are presented in Figure 7.7 for Test # 6 with the increased temperature. The head down and aligned cases follow a similar drag curve. In the laminar flow regime, the head down case shows slightly higher drag than the aligned case due to the increased displaced volume. The Fr-transition occurs at the same speed. However, for the head down case, the drag coefficient appears to drop even lower than the aligned case once the boundary layer is fully turbulent. This is likely due to its reduced total projected area.

The head up condition presents a similar drag coefficient to the head aligned case in the laminar flow regime. In the low temperature case, the head up condition encounters a two-step drag crisis, with a plateau just before the Fr-transition. This phenomenon was not observed at high temperature. However, at both water temperatures, in contrary to the head down and aligned cases, the drag coefficient does not carry on decreasing past the Fr-transition. This high drag condition is a consequence of the large amount of potential energy required for the flow to go over the top of the head. The head up condition thus results in the lowest drop in drag coefficient during the transition flow regime. At 2.0 $m.s^{-1}$, a maximum of 30% and 20% drag coefficient difference are observed at respective water temperatures of 10° C and 18° C between the head up and down positions, emphasising the importance of head position on the free surface.

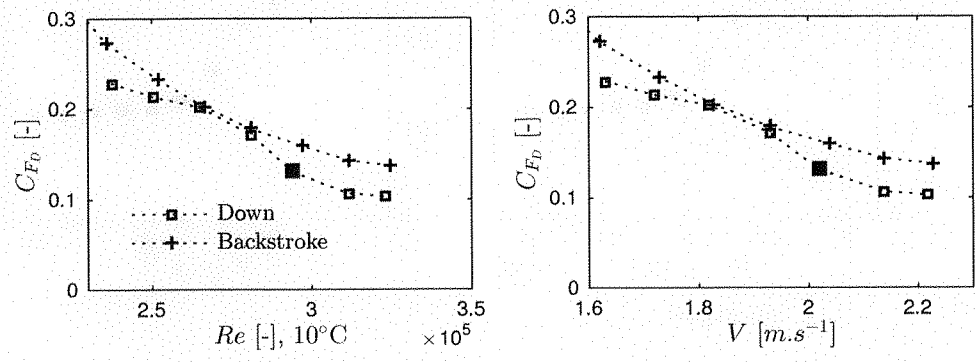

(a) Down (b) Down

FIGURE 7.8: Drag coefficient comparison between head on front (head down) and head on back, at a temperature of 10° Celsius.

Figure 7.8 shows the drag coefficient curve for backstroke in comparison to the head down position since they have the same position, just rotated by 180° around the x-axis. In the backstroke position, more energy is required for the free surface to deform past the nose of the swimmer, resulting in a high drag coefficient at all speeds. Further data points should be obtained at lower speeds for the backstroke in order to see if there is a speed under which the flow regime would follow a constant drag coefficient.

This would be interesting to better understand the flow physics, but it would not be necessarily relevant to an elite level swimmer.

7.3 Influence of goggles design

A preliminary study with bottom range (G4), mid-range (G5) and elite (G2) level goggles was performed (Test # 2). Another study investigated the performance of elite goggles (Test # 3 - G1, G2 and G3). All goggles designs are displayed in Figure 5.2. The head was equipped with cap C1 at all times and no under cap was used. Based on the cap size guide (Figure 5.1), a cap size M was selected.

7.3.1 Initial tests

These tests were the first tests done with the head only and there were initial problems with locking the head in a set position. The head angle was set to a position in-between the head down and aligned cases and was checked at the beginning of every run in case the head angle had moved. After this first test session, the head position locking system was modified to be set to three distinct angles (Figure 7.2) as previously presented.

The head was tested in bare condition (no cap/no goggles). This condition is used as a benchmark to assess the performance of various goggles and cap types. The performances of three goggles designs from the Speedo range (leisure (G4), training (G5), racing (G2)) were assessed and compared against each other.

Above-water footage were not recorded at all times for these tests, however direct observations were noted down. At 1.6 $m.s^{-1}$, the head in both the bare head condition and with the racing goggles (G2) had already encountered the Fr-transition with a thin sheet of water running on top of the head, whereas the head with goggles G4 and G5 was still overcoming the breaking wave.

Visual observations at 2.0 $m.s^{-1}$ were recorded and are presented in Figure 7.9. It can be clearly observed that the wake generated from the head fitted with the bottom-range goggles (G4) is much wider than for the other two more streamlined goggle designs. Consequently, goggles G4 is expected to have more drag than goggles G5 and G2.

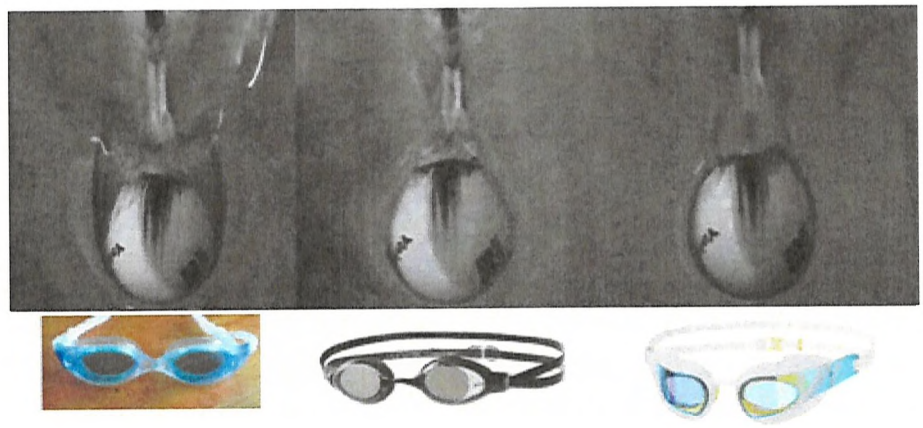

FIGURE 7.9: Top view flow visualisation at 2 $m.s^{-1}$. Head equipped with the leisure (G4),training (G5), racing (G2) goggles (from left to right).

The drag coefficient curves of all goggles designs tested are compared against the bare head benchmark condition in Figure 7.10 and confirm the previous visual observations. All goggles tested present a higher drag than the bare head showing the added-drag created by a cap and goggles. A similar trend is still observed for all goggles designs. Post Fr-transition, there is a sharp drop in drag coefficient at 1.7 $m.s^{-1}$, and a slight rise again as speed increases in the fully turbulent boundary layer flow regime.

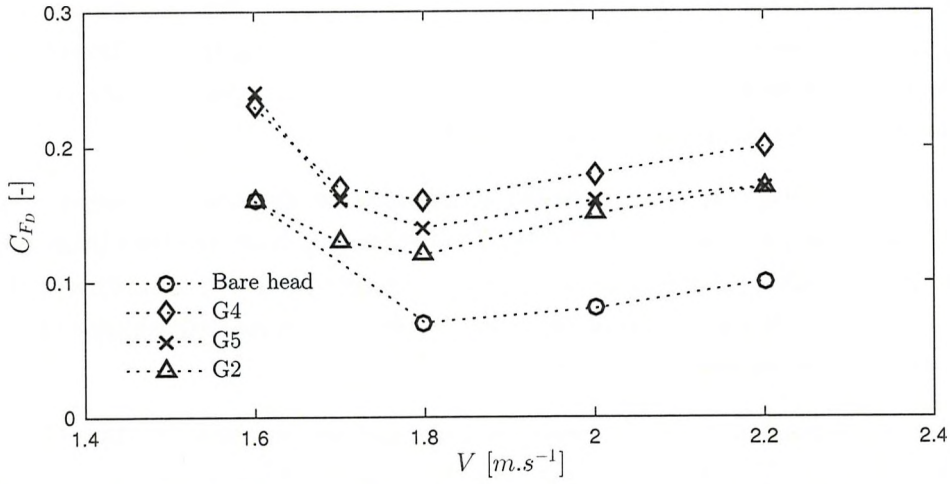

FIGURE 7.10: Drag coefficient comparison of goggles designs - G4: leisure, G5: training, G2: racing.

The drag force is presented for each goggles pre- and post-Fr-transition in Figure 7.11. At 1.6 $m.s^{-1}$, the standard deviation is high, up to 0.8 N (COV = 14%). As for the sphere, drag measurements around the Fr-transition present a larger uncertainty due to the large unsteadiness of the flow when compared to the fully-turbulent flow regime. In addition, the position was not locked for this testing session, the increased unsteadiness of the flow may have triggered the head to move during the acceleration phase. A better

repeatability is noted at 2.0 $m.s^{-1}$, with a standard deviation of 0.2 N (COV = 2%). Overall, the low-range goggles presents the most drag, followed by the mid-range G5 and the top-range G2 as expected. At 1.6 $m.s^{-1}$, a larger drag difference of 2.8 N is observed due to the flow regime difference (pre- and post-Fr-transition), whereas once the flow is fully turbulent a smaller drag difference of 1.9 N is measured. This is still a significant performance improvement with the racing goggles since this represent a drag reduction of -18% on the head.

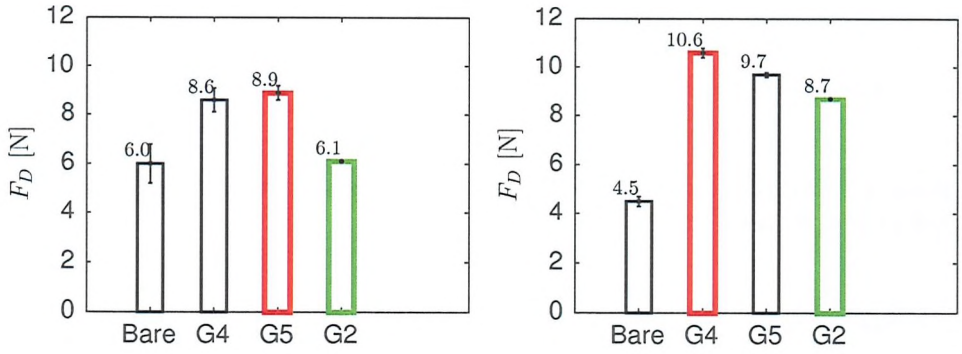

(a) 1.6 $m.s^{-1}$ (b) 2.0 $m.s^{-1}$

FIGURE 7.11: Drag force comparison of goggles designs - G4: leisure, G5: training, G2: racing.

7.3.2 High-performance goggles

On back - A streamline goggles design (G1) and a goggles with extreme sharp edges (G3) were compared in the backstroke position. Figure 7.12 shows that over the entire range of speed tested, the streamline goggles design offers less drag. The sharp-edge goggles presents a 47% additional drag compared to the streamline goggles at the typical backstroke swimming speed of 1.9 $m.s^{-1}$ (Figure 7.13). At the lowest speed, the drag difference is less significant. The difference in resistance between the two goggles designs is due to the high level of vortices shed from the sharp-edge goggles as maybe seen from the side force traces in Figure 7.14. The side force is so high, that the side motion can be visually observed from the above-water video footage.

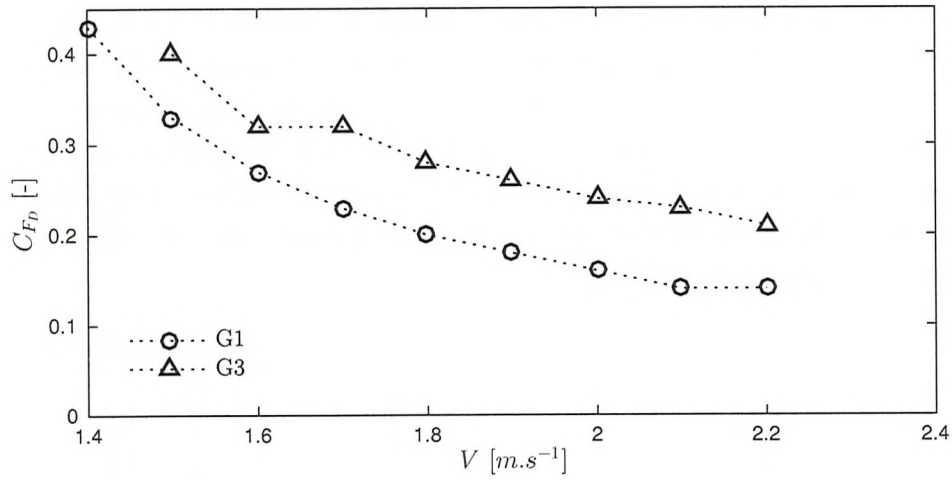

FIGURE 7.12: Drag coefficient versus Reynolds number, comparing a streamline and a sharp-edges goggles design.

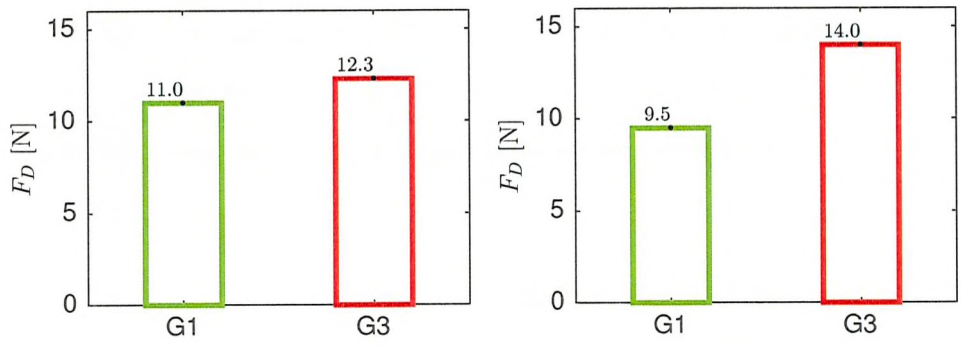

(a) 1.5 $m.s^{-1}$ (b) 1.9 $m.s^{-1}$

FIGURE 7.13: Drag force comparison of goggles designs - G1: streamline, G3: sharp edges.

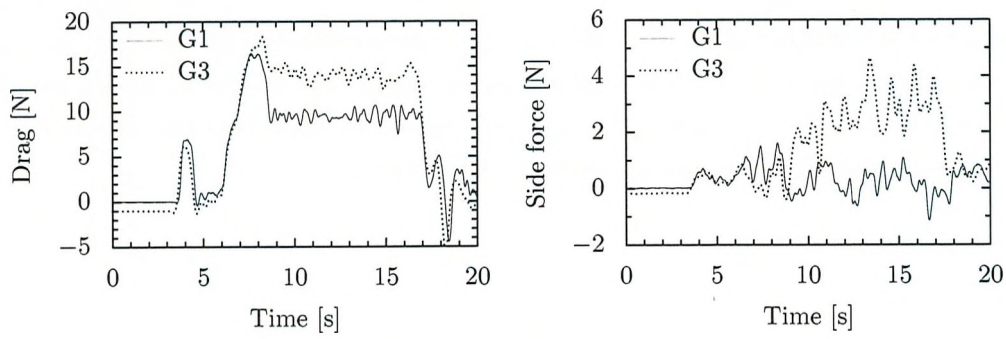

FIGURE 7.14: Comparison of drag and side forces traces for goggles G1 (streamline) and G3 (sharp edges) at 1.9 $m.s^{-1}$, typical elite backstroke speed.

On front - Goggles G2 supposedly benefits from an even more streamline design than goggles G1, and is advertised as a better product. The performance of both goggles were

analysed on the free surface and 250 mm below the free surface with the head aligned in the freestyle position (Figure 7.15).

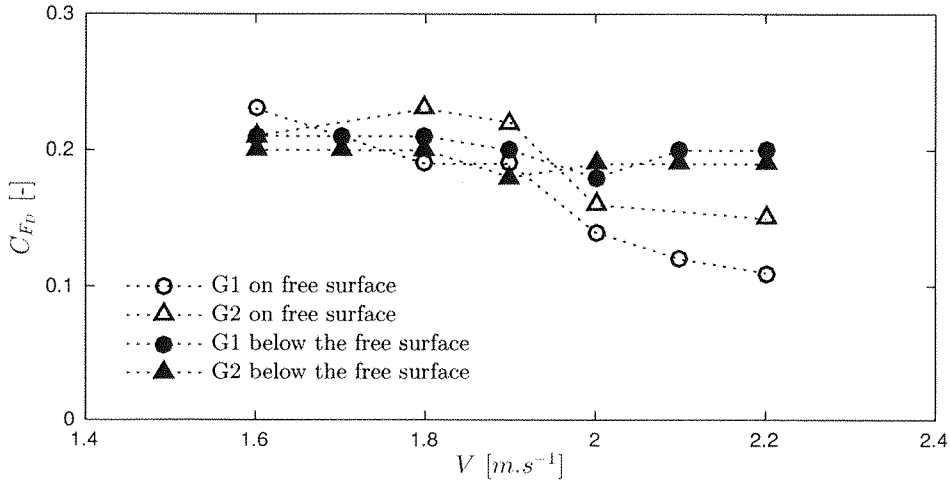

FIGURE 7.15: Drag coefficient versus speed, comparing two different goggles designs G1 and G2 and their respective performance on the free surface and below the free surface.

When studying the influence of immersion depth on goggles design, visual observations cannot be used to determine when the drag crisis occurs. Consequently, one must solely rely on drag measurements. The tare drag of the pole at the rear of the head was subtracted from the submerged data presented. The tare drag was of the same order as the head drag submerged by itself, thus the uncertainty of these data is doubled. The drag crisis below the free surface occurs at the same velocity of 1.9 $m.s^{-1}$ as on the free surface, but is not as significant. Indeed, the drag coefficient drops by only 6% below the free surface, whereas it drops by 50% on the free surface with the goggles G1. This further highlights the importance of the Fr-transition in the drag crisis encountered by a swimmer's head at the free surface.

On the free surface, goggles G2 presented more drag than goggles G1 over most of the speed range, except at 1.6 $m.s^{-1}$. At 2.2 $m.s^{-1}$, goggles G2 displays 34% additional drag (Figure 7.16). Goggles G2 has a large shape which is likely to be sensitive to head position on the free surface, and could result in higher drag than a more conventional smaller streamline design such as goggles G1. Goggles G2 should thus be tested at different head angles on the free surface to confirm this or not.

Below the free surface, goggles G2 offers slightly less drag than G1, with -5% drag before the Fr-transition and -4% drag in the fully turbulent flow regime (Figure 7.17). Goggles G3, with sharp-edges, should be tested below the free surface to draw more conclusions on the impact of goggles design after a dive start or after a turn.

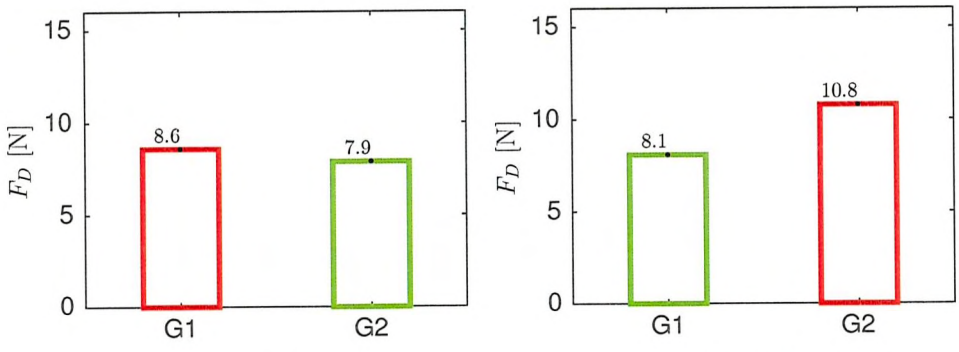

(a) 1.6 $m.s^{-1}$ (b) 2.2 $m.s^{-1}$

FIGURE 7.16: Drag force comparison of goggles designs on the free surface - G1: elite, G2: super-elite.

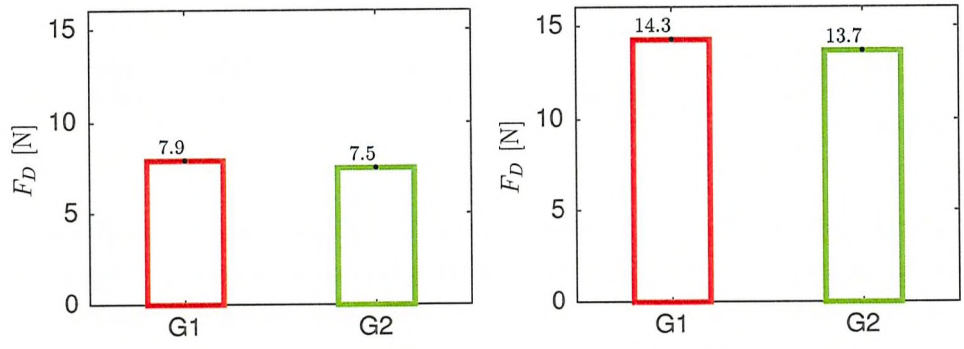

(a) 1.6 $m.s^{-1}$ (b) 2.2 $m.s^{-1}$

FIGURE 7.17: Drag force comparison of goggles designs below the free surface - G1: elite, G2: super-elite.

7.4 Influence of cap design

First the impact of a hydrophobic coating on a cap was investigated as a potential major change on the drag compared to the standard cap coating at the free surface (Test # 2). In a second study, three different elite caps were drag-tested both below and at the free surface (Test # 7).

7.4.1 Cap surface roughness

The effect of cap surface roughness was evaluated with the use of a hydrophobic coating applied on cap C1. Goggles G2 were fitted on the head for this cap study. The drag test for the standard and hydrophobic caps are compared with the bare head condition. The drag coefficient curve presented in Figure 7.18 indicates that the application of a hydrophobic coating can reduce the drag but only once the flow is fully turbulent.

At the transitional speed of 1.6 $m.s^{-1}$, the hydrophobic cap presents a 23% higher drag. However, at 2.2 $m.s^{-1}$, once the flow is fully turbulent, the hydrophobic cap offers a drag reduction of 19%. Further data points at speeds before the drag crisis should be obtained to better understand the influence of a hydrophobic coating on the drag crisis phenomenon.

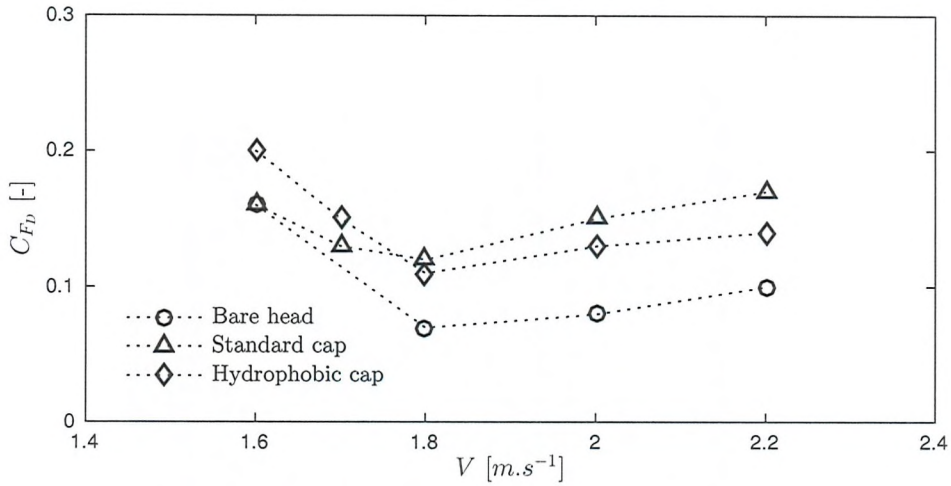

FIGURE 7.18: Influence of cap surface roughness on the drag coefficient.

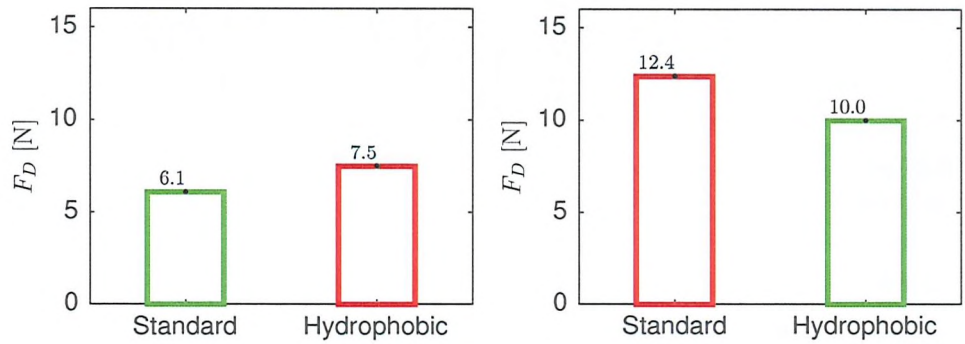

(a) 1.6 $m.s^{-1}$ (b) 2.2 $m.s^{-1}$

FIGURE 7.19: Drag force comparison between a standard cap and one with a hydrophobic coating.

7.4.2 High-performance caps

Three elite caps have been drag-tested, with the prime objective of ranking cap C3 since it is the selected cap for Rio 2016 due to GB Team partnership. Cap C3 was provided in both size M and L. Caps C3 and C1 were compared and it was decided that the cap C3 size M would be the best fit for the head model. The two other caps are cap C2 and C1. Goggles G1 were used with the strap placed underneath the cap.

The caps drag performance were both assessed on the free surface and below the free surface. The speed range was extended down to 1.3 $m.s^{-1}$ for the free surface condition to cover for the para-swimmers speed range. Although elite swimmers can reach underwater speeds around 3.0 $m.s^{-1}$, the maximum carriage speed of the Lamont tank is 2.2 $m.s^{-1}$, hence the selected speed range.

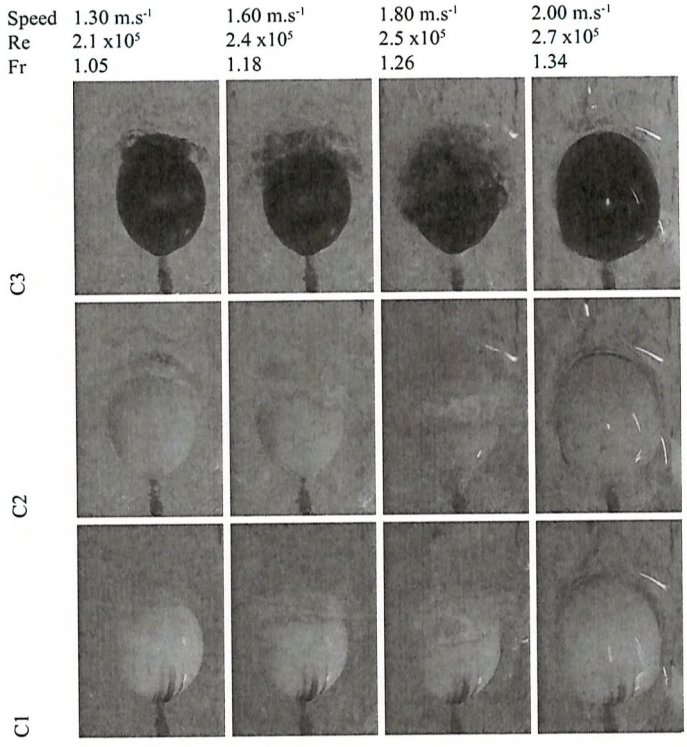

FIGURE 7.20: Top-view flow visualisation around the head for three different elite caps indicates no difference in flow visualisation.

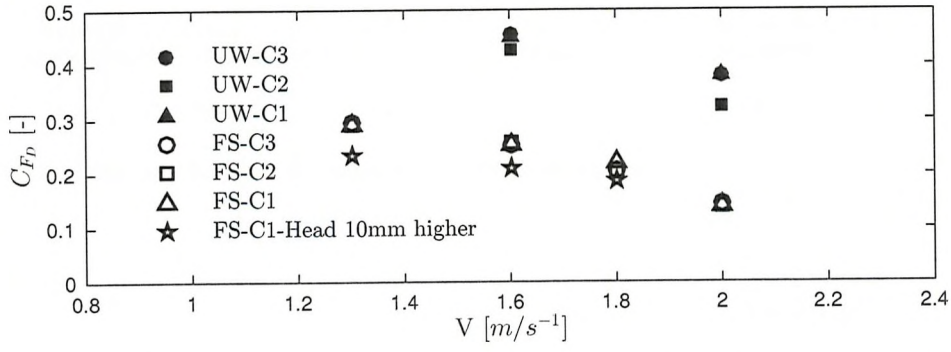

FIGURE 7.21: Drag coefficient curve for the different elite caps tested both on the free surface (FS) and underwater (UW). Note the large influence of a small change in head immersion depth on drag.

Drag variations measured between the different caps tested for the head on the free surface are small, especially when compared to the significant impact that the head position has on the drag. At 1.6 $m.s^{-1}$, raising the head out of the water by 10 mm,

thus reducing the head submerged volume and projected area, decreased the head drag by 19%. Moreover, it was previously shown that varying the head angle (looking at pool bottom, looking slightly ahead and looking ahead) showed drag differences up to 20%. These results emphasise the importance of further studying the complex flow around the head at the free surface.

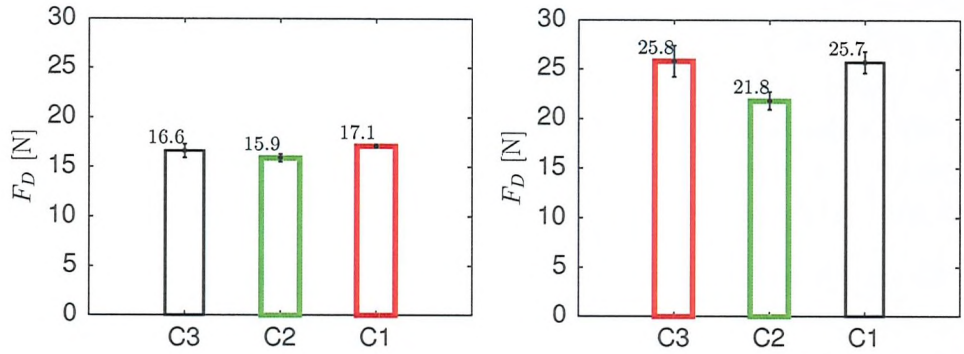

(a) 1.6 $m.s^{-1}$ (b) 2.2 $m.s^{-1}$

FIGURE 7.22: Drag force comparison of elite cap designs below the free surface. Note that C2 presented the smoothest cap surface finish.

TABLE 7.1: Percentage drag difference with cap C3 on the head only.

Speed $[m.s^{-1}]$	1.6	2.2
Cap C2	4%	18%
Cap C1	-3%	0%

TABLE 7.2: Actual drag difference between cap C3 and caps C2 and C1, expressed as a percentage of total body drag for a Male (Height = 1.95 m, Weight = 98 kg).

Speed $[m.s^{-1}]$	1.6		2.2	
Drag	ΔD [N]	% body drag (62.8 N)	ΔD [N]	% body drag (117.7 N)
Cap C2	0.64	1.0 %	4.01	3.4 %
Cap C1	-0.53	-0.8 %	0.09	0.1 %

TABLE 7.3: Time difference with cap C3 in seconds due to underwater phase drag change only, with a 10% uncertainty.

Speed $[m.s^{-1}]$	1.6	2.2
Cap C2	0.10	0.34
Cap C1	-0.08	0.01

Comparing the mean drag of the various caps tested at 1.6 and 2.2 $m.s^{-1}$ below the free surface (Figure 7.22), cap C3 appears to be at mid-range, with a slight increase in performance on cap C1 before the laminar-to-turbulent boundary layer transition. On the other hand, cap C3 shows an increased drag of 4% with cap C2 at 1.6 $m.s^{-1}$, and 18% at 2.2 $m.s^{-1}$, when considering drag changes on the head only. In order to provide an estimate of race time savings, the actual drag difference between the caps on the head only is related to the total underwater swimmer's drag for a male swimmer (Height = 1.95 m, Weight = 98 kg). The estimated time saved would be between 0.10 and 0.34 s, emphasising the superior performance of cap C2. In addition, cap C1 was drag-tested underwater in a larger size (size L) to replicate wrinkles and bubble formed on the top of the head as often seen on swimmers. The effect of this bubble was null.

Cap C3 and C1 looked more alike in terms of shape, material and thickness. On the other hand, cap C2, with the best drag performance, does not present a pre-moulded shape, has a thinner thickness and feels smoother. This last comment on cap surface roughness is only based on a qualitative assessment.

7.5 Chapter summary

In this chapter, it was shown that a surface-piercing swimmer's head also undergoes a similar drag crisis as observed in the case of a sphere. The change to a low-drag flow regime can also be visually identified by the change of a breaking wave to a smooth flow over the top of the head. In the previous chapter, an increase in temperature was associated with an increase in the sphere drag coefficient in the laminar flow regime. The same phenomenon was observed in the case of the head, leading to an amplified drag crisis which occurs over the elite swimming speed range of 1.5 - 2.0 $m.s^{-1}$.

Since the flow past a swimmer's head undergoes a drag crisis, the influence of its angle is of great interest. Three often adopted head angles in freestyle were tested: looking at pool bottom (down), looking slightly ahead (aligned) and looking ahead (up). Before the occurrence of the drag crisis, no real advantage in using a particular head position is noticed. However, more differences may be observed between the different head positions once the flow is fully turbulent. The head down case presents the lowest drag, followed by the head aligned and up cases (up to 30% drag difference between the head down and up cases).

The drag crisis can be directly visualised by observing the flow on top of the head. Pre-transition, a breaking wave is created, indicating a high drag coefficient; whereas post-transition, the flow is running smoothly on top of the head, resulting in a lower drag coefficient (Figure 7.23). A swimmer could simply try different head angles and swim at maximum speed, while being filmed or observed by his/her coach. The earlier

the flow is running smooth over the top of the head, the better the head position will be from a performance and effort point of view.

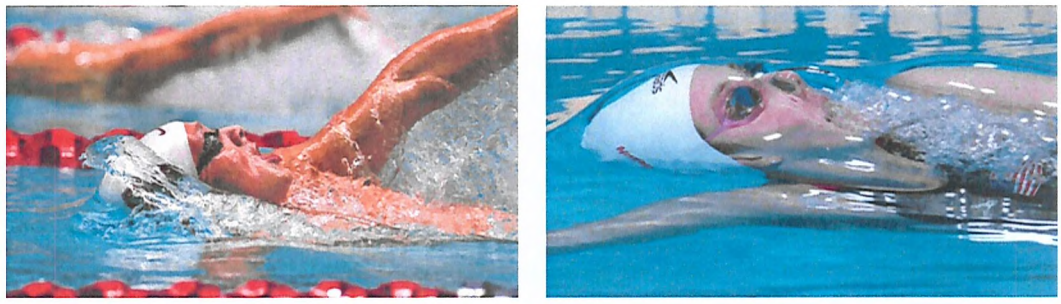

(a) Pre-transition, high drag (b) Post-transition, low drag

FIGURE 7.23: Direct observation of the flow regime transition.

Different goggles and cap designs have been tested both below and on the free surface. These tests have demonstrated that swimming equipment such as a cap or goggles can play a role in reducing a swimmer's drag. When comparing goggles on the free surface, visual observations can be sufficient to distinguish an elite goggles from a bottom range one. Nonetheless, when comparing two similar designs which already have streamline curves, drag measurements are necessary. During the submerged tests, the drag crisis occurs at a similar speed but is not as significant as on the free surface (6% drop in drag coefficient instead of 50% on the free surface). As a result, the drag coefficient difference between two goggles types appears to be greater on the free surface compared to when fully submerged, $\sim$ 35% and 5% respectively.

At the free surface, the application of a hydrophobic coating on a cap can reduce the drag by about 20% once the flow is fully turbulent. Yet, at the transitional speed, the hydrophobic cap presents a higher drag. Further data points at speeds before the drag crisis should be obtained to better understand the influence of a hydrophobic coating on the entire drag crisis phenomenon.

On the other hand, drag testing of different elite caps on the head has shown no impact on the free surface regardless of the flow regime. Below the free surface, a noticeable drag difference was measured in the fully turbulent flow regime, whereas small differences were recorded during the laminar-to-turbulent boundary layer transition. For this last cap study, the percentage drag difference of 18% at 2.2 $m.s^{-1}$ obtained on the head only was converted to the total body resistance. The selection of a specific cap can still save 3.4% in total body drag or 0.34 s over a 100-m freestyle race, which is non-negligeable for elite swimmers.

The cap/goggles study has shown that they could influence the drag of the head at the free surface when they presented a large feature (large goggles shape or hydrophobic coating on cap). This large feature on the head affects the free surface deformation

and thus the boundary layer transition. However, underwater, where only the transition from laminar-to-turbulent flow regime matters, smaller feature changes can still have an effect on the drag (ie. three different elite caps with a difference in surface roughness).

Tests on the head were performed in two different towing tanks over the same elite swimmer speed range of 1.6 - 2.2 $m.s^{-1}$. Nevertheless, the water temperature differed by 8° Celsius which influenced the water viscosity and therefore the drag at a set speed. Both tests proved that the drag crisis for the head occurred around Reynolds number of 3 $\times 10^5$, but the different flow regimes around this critical Reynolds number were not all captured. During a race, an elite swimmer will always experience the drag crisis phenomenon, hence the importance of comparing different caps/goggles performances over the entire Reynolds number range where the flow regimes undergo significant changes ($1.5 \times 10^5 \leq Re \leq 4.5 \times 10^5$). Consequently, the test speed range should be based on the tank water temperature to cover all the flow regimes (pre-transition, drag crisis and post-transition). As shown in Table 7.4, if the water temperature is too cold, testing at higher speeds is required to capture the post-transition flow regime and not all tanks may allow such high speeds.

TABLE 7.4: Test speed range based on water temperature, in $m.s^{-1}$.

	Temperature [° Celsius]		
Re [-]	10° C	18° C	28° C
1.5 $\times 10^5$	0.98	0.80	0.63
3.0 $\times 10^5$	1.97	1.60	1.25
4.5 $\times 10^5$	2.95	2.40	1.88

With all these tests performed on a swimmer's head, the question of how should the performance of new goggles/cap designs be evaluated experimentally is raised. Since differences in drag are more noticeable between two originally thought-to-be similar designs on the free surface, should goggles only be tested in this condition? The goggles shape has a definite influence on the free surface deformation but it may change depending on the head angle. Would it therefore not be better to test goggles in a fully-submerged case as well to remove the effect of free surface deformation? Also, one may question if goggles/cap performance can really be evaluated on a head only or is the rest of the body required for the flow to develop in what could be a more realistic manner?

8

Flow past a mannequin

A female mannequin was drag-tested in the Solent towing tank. The effect of different body positions was studied across a wide range of speeds, 0.50 to 2.25 $m.s^{-1}$, to get a full drag curve for the mannequin. The influence of goggles, caps and other flow control devices on the mannequin's head was then assessed on the free surface over the typical elite swimmer top speed range (1.6 - 2.0 $m.s^{-1}$).

8.1 Influence of body position

The influence of the body position on drag force has been researched on the mannequin in a frontal position. In addition, the mannequin was also positioned in a backstroke position but only one position was considered. In Figures 8.1 and 8.2, side-view photographs of the different body positions tested are presented. A baseline position (A) was first selected to replicate the typical body position of a swimmer during front-crawl swimming. The legs are below the water with the bottom and upper-back slightly out of the water. This initial position was based on the static condition only. In the dynamic condition, the mannequin ended up being too high on the water with the back of the legs being dry. Consequently, successive changes have been tested based on visual observations to replicate the best body position in the dynamic condition. From the baseline position (A), the upper-body was first raised (B), the legs were then lowered (C) and finally the entire body was positioned 40 mm deeper (D).

FIGURE 8.1: Side-view photographs of different body positions (1/2).

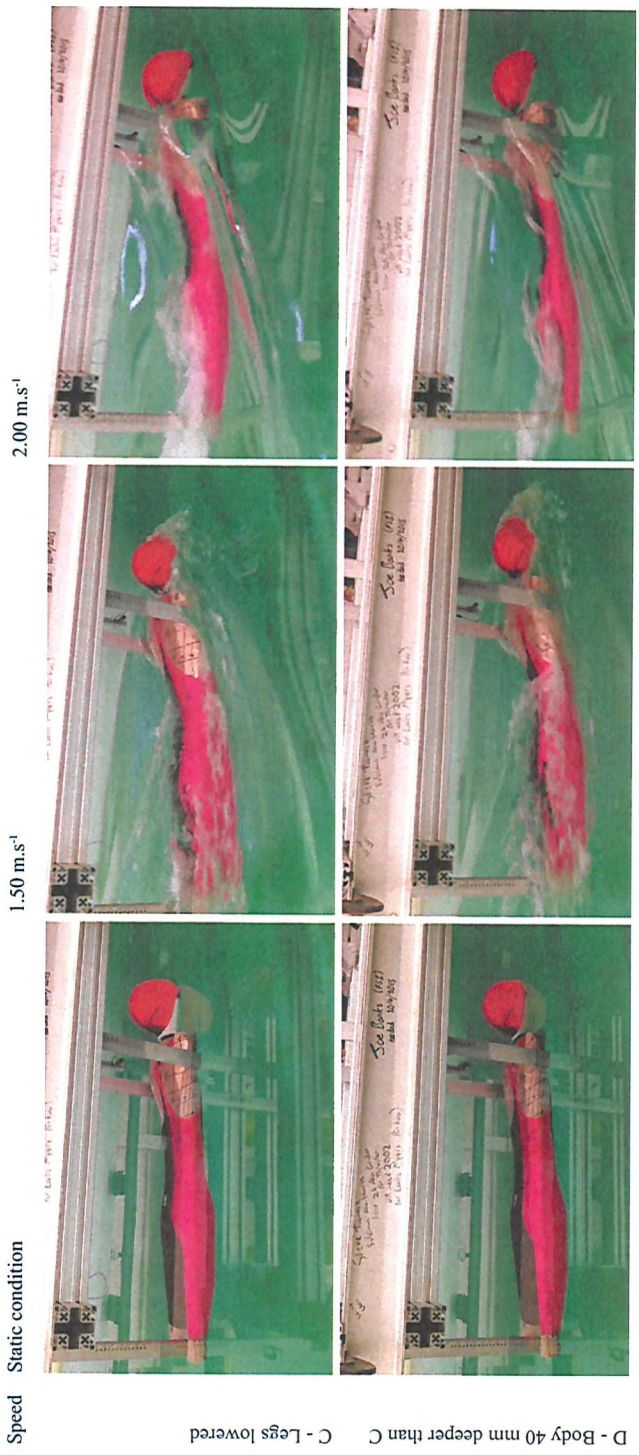

FIGURE 8.2: Side-view photographs of different body positions (2/2).

Similarly to the head only, the head on the mannequin overcomes a change of breaking wave to a thin sheet of fluid running on top of the head (Fr-transition). Overall two wave systems from the mannequin's body can be observed. One is originated from the head and shoulders, and another one starts from the hips at 1.5 $m.s^{-1}$ or further down

the body after the bottom at 2.0 $m.s^{-1}$ since the fluid flowing over the upper-back of the mannequin has more kinetic energy to go around the bottom before separating from the body.

Figure 8.3 presents the drag force for the different body positions across a large speed range extending from 0.50 to 2.25 $m.s^{-1}$. Both positions A and B present a lower drag than positions C and D since the back of the legs are running dry in the dynamic condition. The increase in pitch angle (B) results in an increase in drag pre-Fr-transition, but a lower drag post-Fr-transition. The deeper the body is, the larger the drag as expected, since both pressure and skin friction drag increase. The drag trace for the mannequin on the back follows a similar trend to the deepest body position tested on the front (D).

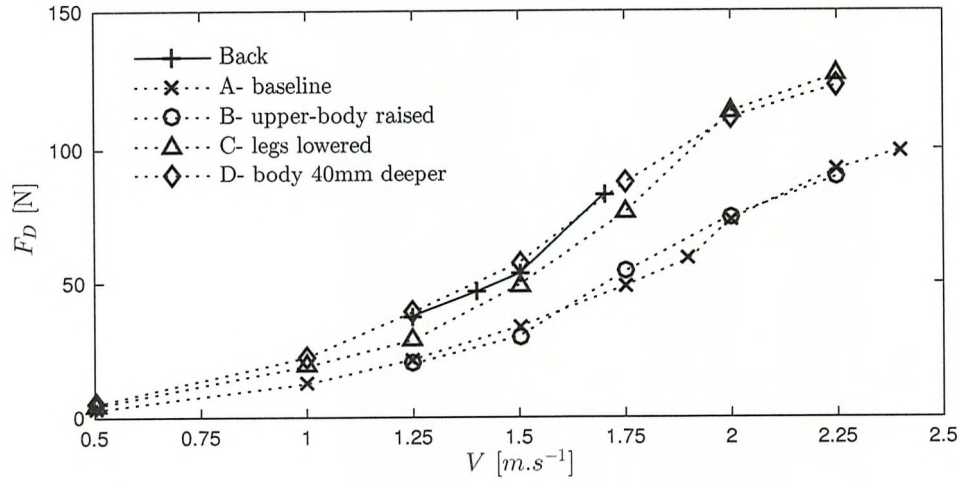

FIGURE 8.3: Influence of body position on drag force. A-D are frontal positions.

The drag force coefficient ($C_{F_D} \times A_p = \frac{F_D}{0.5\rho U^2}$) is plotted versus speed, Fr and Re numbers in Figures 8.4, 8.5(a) and 8.5(b) respectively. Despite the occurence of the Fr-transition on the head, no drag crisis is observed in the case of the mannequin. However, at speeds around 1.7 $m.s^{-1}$ (Fr-transition on the head), a reduction in the rate of drag increase is to be noted. Even if the head experiences a drag crisis, the increased drag over the rest of the body as speed increases remains overall greater than any drop in local drag on the head.

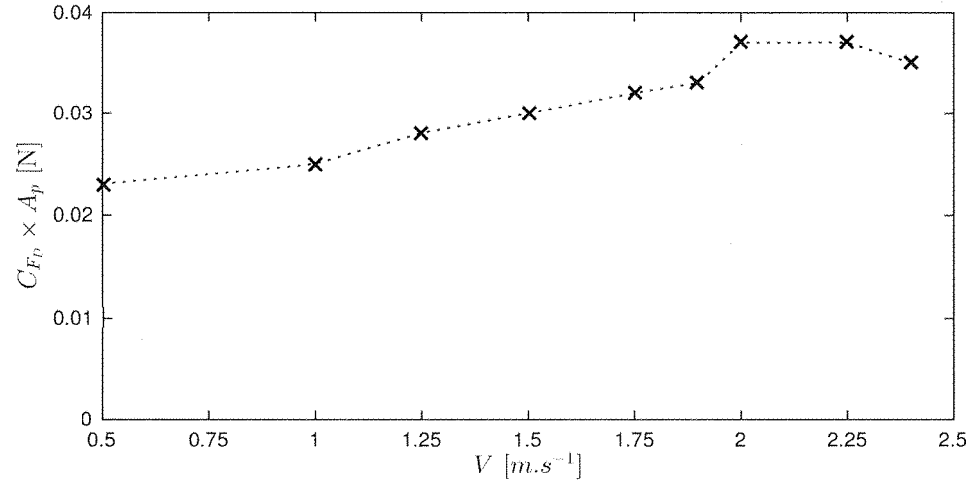

FIGURE 8.4: Drag force coefficient versus speed for the mannequin in the baseline position (A).

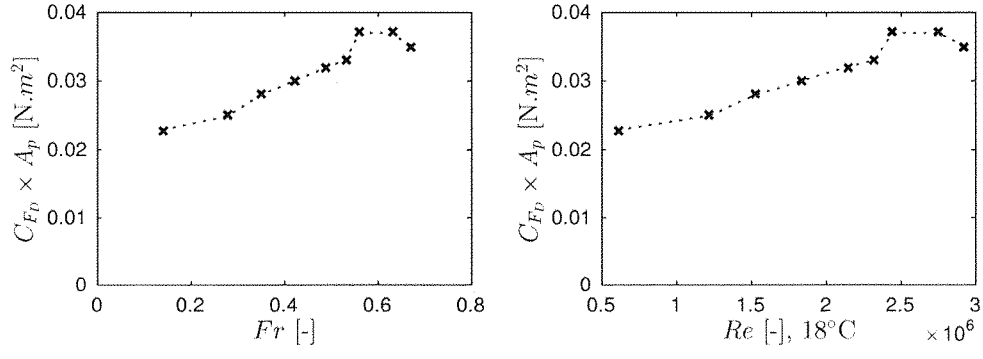

(a) (b)

FIGURE 8.5: Drag force coefficient versus Fr and Re numbers for the mannequin in the baseline position (A). N.B. Fr and Re are based on the length of the mannequin - $L = 1.3$ m.

8.2 Influence of goggles design

Three goggles presenting a streamline design (G1, G2, G5 - Figure 5.2), typically worn during swimming races, were tested on the mannequin's head with the cap C1. The goggles strap were placed underneath the cap. Tests were performed at two speeds only, 1.6 and 1.8 $m.s^{-1}$, corresponding to pre- and post- Fr-transitional speeds.

(a) G1 - Elite (b) G2 - Super-Elite (c) G5 - Aquasocket

FIGURE 8.6: Goggles designs tested.

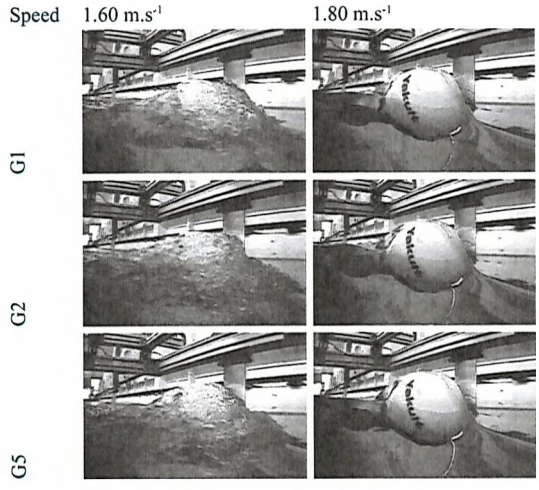

FIGURE 8.7: Front view photographs taken at both 1.6 and 1.8 $m.s^{-1}$ for all goggles tested. No visual indications to rank goggles.

There were no visual indications of which goggles may offer less resistance through the water (Figure 8.7). The drag of each goggles tested is presented in Figure 8.8. At 1.6 $m.s^{-1}$, the maximum drag discrepancy observed is 0.7 N. The measurement error between the only two repeat runs done at this speed is 0.5 N, hence the reliability of these results is questionable. At 1.8 $m.s^{-1}$, goggles G1 offers a 2.4 N drag decrease compared to goggles G2, which equates to a 3% drag reduction over the entire body. Despite goggles G2 being advertised to be the best goggles, this drag difference is significant enough so that goggles G1 could be stated to have better performance than goggles G2. Although a much larger drag difference was noticed on the head, the same trend was observed confirming that goggles could be tested on the head only, reducing testing time and cost.

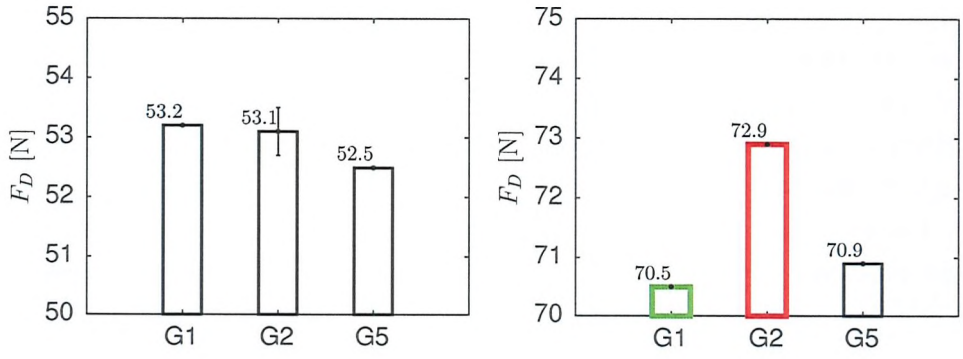

(a) 1.6 $m.s^{-1}$ (b) 1.8 $m.s^{-1}$

FIGURE 8.8: Drag force comparison of streamline goggles designs G1, G2 and G3.

8.3 Influence of cap design

Five caps (C1, C4, C5, C6 and C7 - Figure 5.3) presenting significant differences in terms of surface finish, thickness and shape were tested at typical elite swimmer speeds: 1.6, 1.7, 1.8 and 2.0 $m.s^{-1}$. Goggles G5 were fitted on the head at all times.

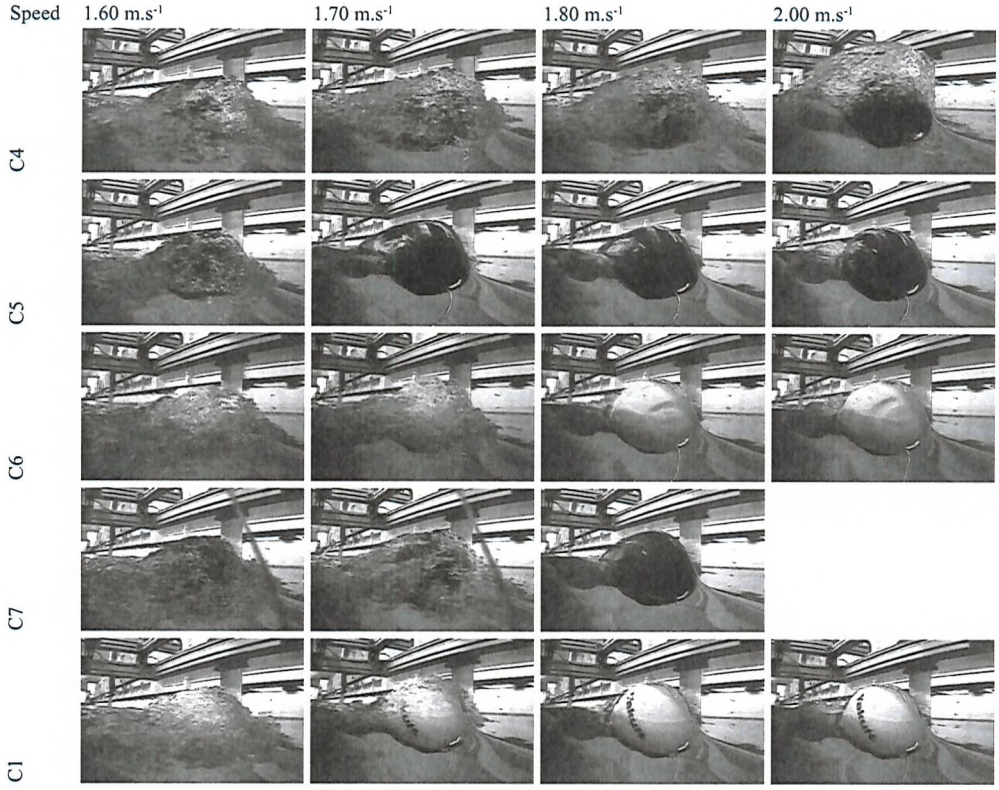

FIGURE 8.9: Front view photographs taken across the speed range 1.6 - 2.0 $m.s^{-1}$ for all caps tested on the mannequin.

A matrix of screenshots from the front view camera was generated to compare the free surface deformation around the mannequin's head for the five caps and at all speeds tested (Figure 8.9). Cap C4 with studs generates a large breaking wave, even at the highest speed and thus will result in a high drag cap. At 1.6 $m.s^{-1}$, the head is encountering a breaking wave with all caps, it is thus difficult to determine which cap offers less drag. However, once the Fr-transition occurs on the head, more distinct flow features appear which allows one to estimate a ranking for the different caps in terms of their drag performance.

- At 1.7 $m.s^{-1}$: Cap C5 is the only one for which the flow is smooth over the top of the head, indicating least drag. Cap C1 is undergoing transition and will thus result in lower drag than caps C4, C6 and C7 which are all still pre-Fr-transition. In order to evaluate a performance ranking for those caps, drag measurements are required.

- At 1.8 $m.s^{-1}$: The turbulent boundary layer appears to stay attached further along the head on cap C1. Both caps C5 and C7 present an earlier separation point at the location of the material change and at the riblets positions respectively. It remains difficult to rank cap C6 from flow visualisation only.

- At 2.0 $m.s^{-1}$: The flow stays attached even further at the rear of the head for cap C6 and C1. Cap C5 is still presenting an air bubble due to the material change, likely resulting in an increase in drag.

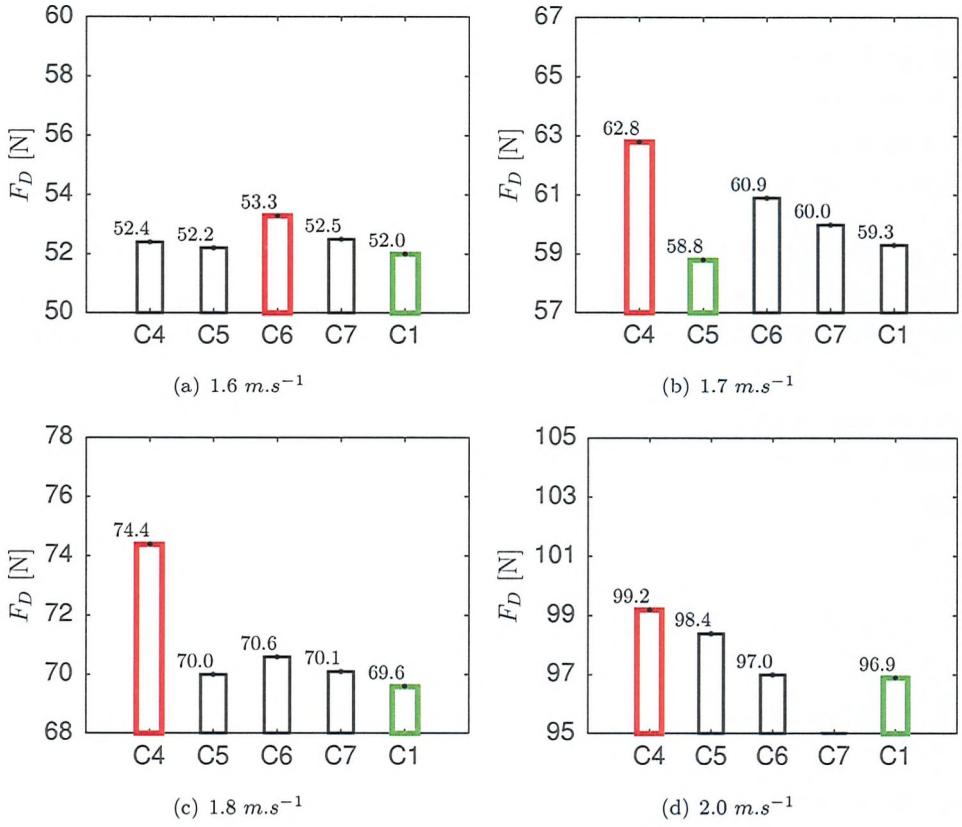

FIGURE 8.10: Drag force comparison of different caps.

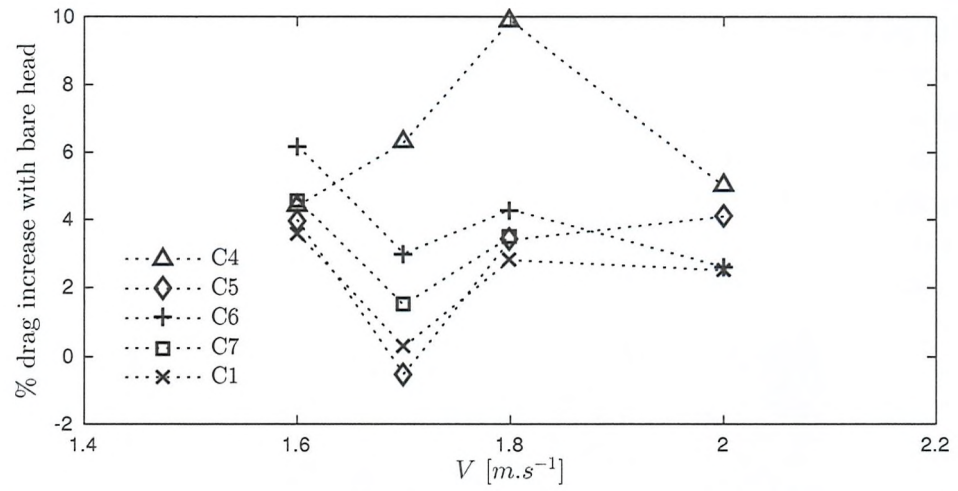

FIGURE 8.11: Percentage drag increase of different caps tested compared to bare head.

The five caps drag data are compared against each other at each speed (Figure 8.10) and benchmarked against the bare head (Figure 8.11). The drag measurements confirm the cap ranking estimated from the front-view screenshots. Caps, which could not be ranked from visual observations since they were in a similar flow regime, either pre- or post-Fr-transition, present a low drag percentage difference (below 2%).

Although there is no drag crisis in the case of the mannequin, the flow regime experienced by the head has a large impact on the total body drag. At a set speed, the total body drag is much lower when the Fr-transition occured. At both 1.7 and 1.8 $m.s^{-1}$, there is a 7% drag reduction between the best cap amongst those which are post-Fr-transition, compared to cap C4 which is still in a pre-Fr-transition flow regime.

The type of caps used can help this Fr-transition to occur earlier for the swimmer to swim in a lower drag flow regime. The caps tested on the mannequin present very different features. Elite caps typically used in racing now present a smooth surface finish (no studs, no riblets). The Fr-transition is unlikely to be changed by the presence of the mannequin body behind the head and it was previously shown in Chapter 7 that no set conclusions could be drawn between different elite caps at the free surface despite having various levels of smoothness.

8.4 Influence of hair management

8.4.1 Initial tests

As an alternative to changing equipment on a swimmer's head to trip the flow to a low-drag flow regime at an earlier speed (i.e. no breaking wave), different hair arrangements could be used. To explore the performance potential of hair management, various flow control devices (trip studs, spray rails, long-hair management - Figure 8.12) were fitted on the mannequin's head and tested at speeds of 1.6 and 1.8 $m.s^{-1}$. The flow control devices are all prototypes made out of basic available materials like hair bands, rulers, plasticine and a fake hair bun. They were tested at a large scale on purpose so that any flow feature changes could be easily identified. The head was fitted with cap C1 and goggles G5 at all times, which constitutes the baseline for the devices tested. The devices are presented alongside protographs extracted from the top-view videos. The flow past each device is discussed in each figure's caption.

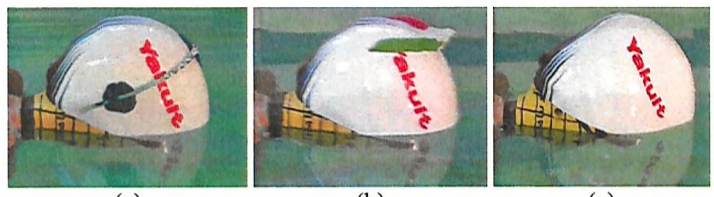

(a) (b) (c)

FIGURE 8.12: Three types of flow control devices fitted on the head: (a) trip studs, (b) spray rails, (c) long-hair management.

Flow visualisation Figure 8.13 provides a top view of the flow past the head for the baseline at both tested speeds. Two wave systems are generated from the head

stagnation point and from the neck. The wave generated from the head is breaking on the shoulders resulting in added drag for the entire mannequin.

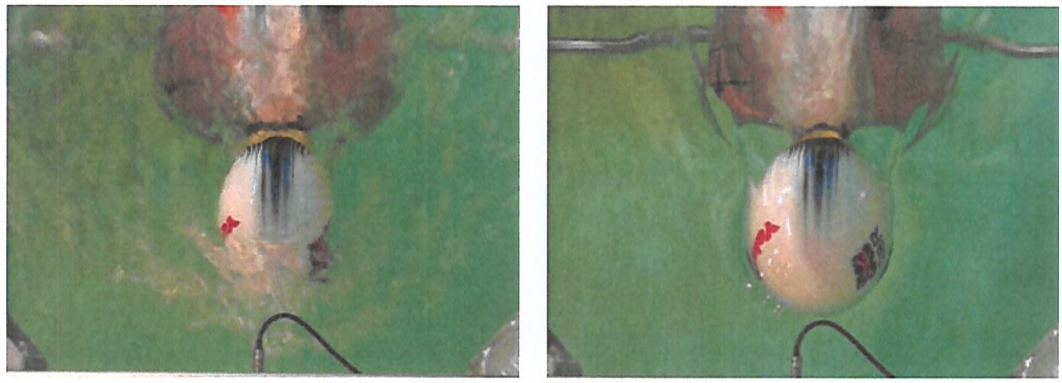

(a) 1.6 $m.s^{-1}$ - large amount of turbulent flow breaking on shoulders

(b) 1.8 $m.s^{-1}$ - smooth flow over the top of the head, but still breaking wave on upper back

FIGURE 8.13: Flow visualisation of baseline.

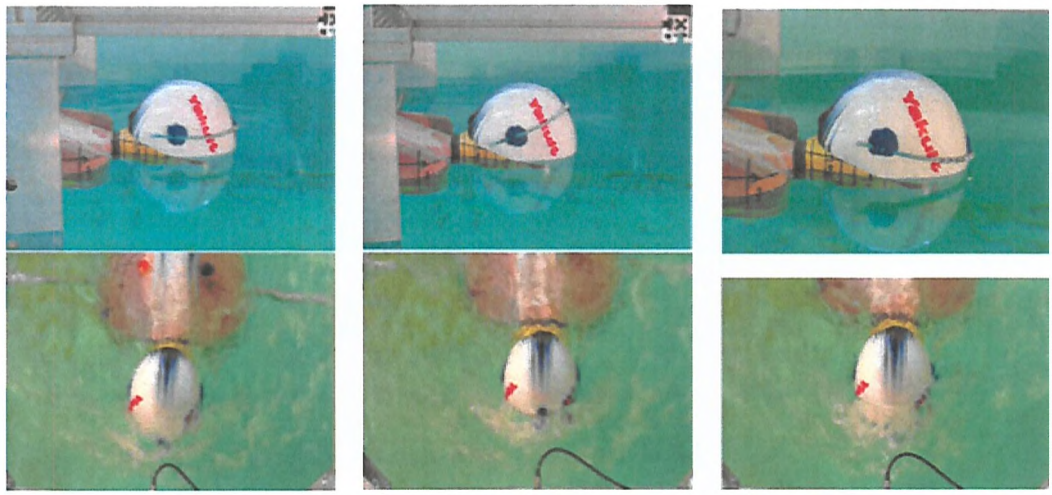

(a) D1 - less breaking wave than baseline

(b) D2 - flow prevented from running smoothly on cap during acceleration phase due to trips positionned further up, increased drag from D1 but less than baseline

(c) D3 - similar to baseline

FIGURE 8.14: D1-3: Row of trip studs stuck on head with different angles - Flow visualisation at 1.6 $m.s^{-1}$.

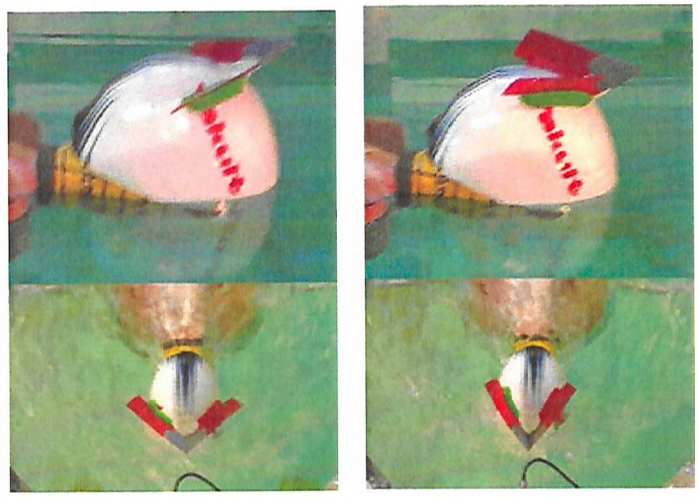

(a) D4 - spray rail prevents water from running on top of the head, but projects water forward of the head

(b) D5 - higher spray rail/sharper angle still prevents water from running on top of the head, with less water projected ahead

FIGURE 8.15: D4-5: Spray rail with different orientations and heights - Flow visualisation at 1.6 $m.s^{-1}$.

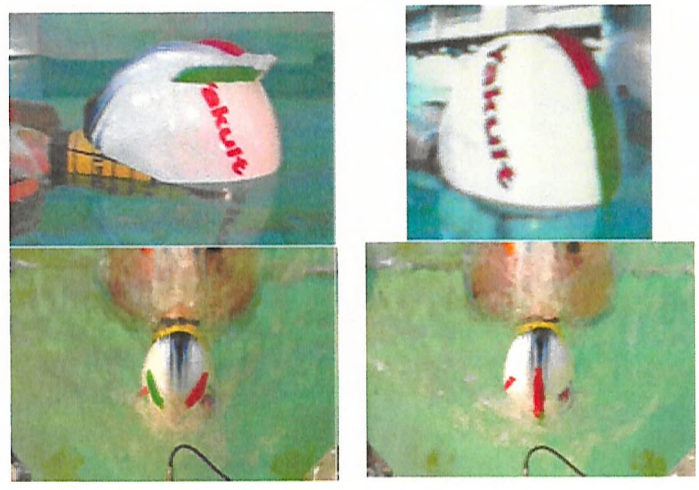

(a) D6 - smaller rail still diverts flow away from shoulders

(b) D7 - wave system created by the head not interfering as much with neck

FIGURE 8.16: D6-7: Spray rail with different orientations and heights - Flow visualisation at 1.6 $m.s^{-1}$.

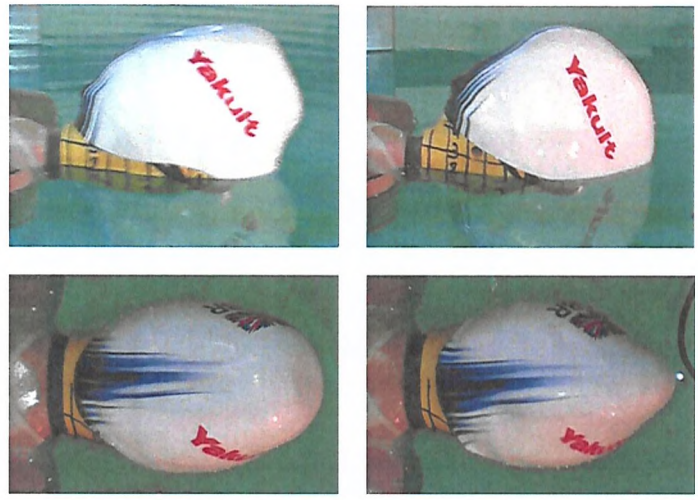

(c) D8 (d) D9

FIGURE 8.17: Side and top view of hair management.

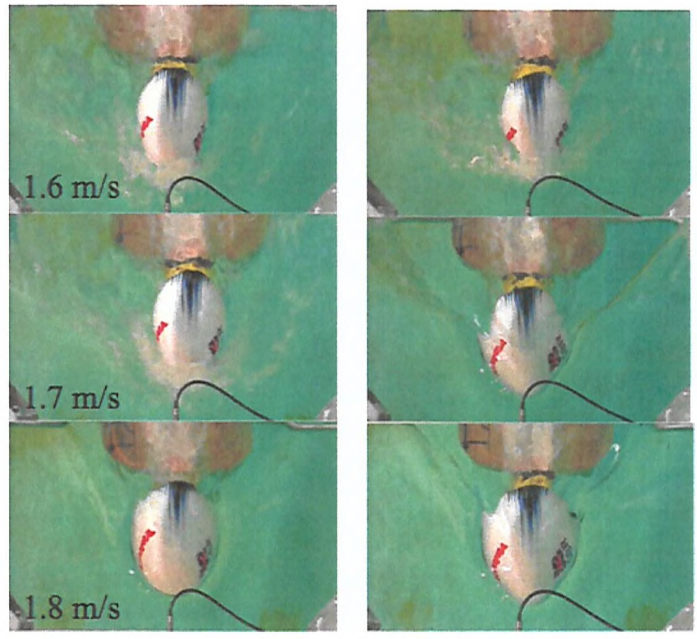

(a) D8 - reduced flow breaking on shoulders

(b) D9 - reduced flow breaking on shoulders, but large wave created from the head side, likely to result in higher drag than D8

FIGURE 8.18: D8 and D9 flow visualisation.

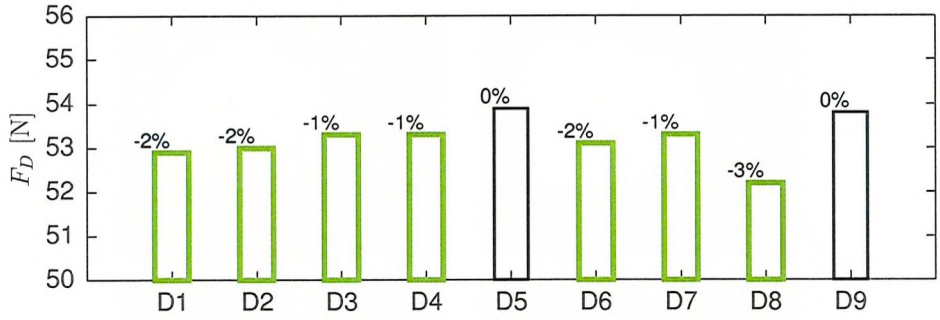

FIGURE 8.19: Drag comparison of devices tested at 1.6 $m.s^{-1}$, percentage difference with averaged drag for the baseline.

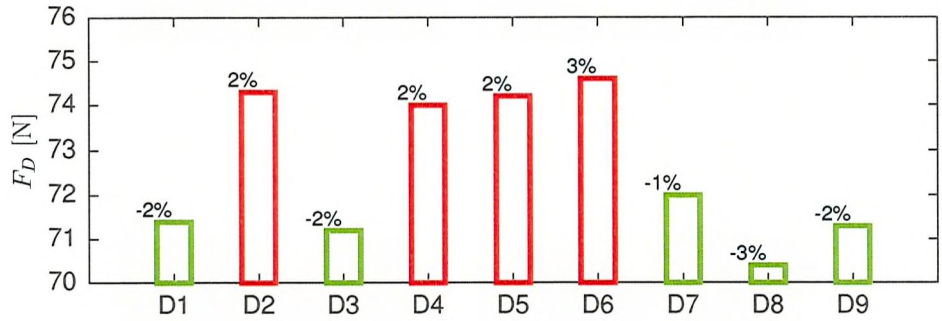

FIGURE 8.20: Drag comparison of devices tested at 1.8 $m.s^{-1}$, percentage difference with averaged drag for the baseline.

Drag measurements Considering the flow observations previously made and the drag measurements (Figures 8.19 and 8.20), the following conclusions can be made for each class of devices tested:

- **Trip studs** - At 1.6 $m.s^{-1}$, all positions of trip studs showed a reduction in drag (1 - 2%) compared to the baseline. However at 1.8 $m.s^{-1}$, only the lower position of trip studs reduced the drag.
- **Spray rails** - At 1.6 $m.s^{-1}$, all devices show reduced drag or no change compared to the baseline. Yet, at 1.8 $m.s^{-1}$, a drag increase is observed for all devices apart from D7 (rail placed on top of head in the same direction of flow). Indeed, it was observed that the wave system generated from this device did not interfere with the neck wave as much and did not break on the shoulder.
- **Hair management** - Both hair styles reduced drag significantly (2 - 3%) at 1.8 $m.s^{-1}$ since the head wave did not break on the shoulder. The mow-hawk style generated a larger wave system, resulting in higher drag than the bun placed close to the head front. This last device (D8) appeared to be the most effective device since the flow was forced to follow the shape of the bun, generating its own wave system which reduced the wave system developed by the head (similar to a ship bulbous bow).

8.4.2 Selection tests before pool testing

From the initial flow control tests, the hair management styles (bun and mow-hawk) were selected to be re-tested on the mannequin in both front and back positions and while on the free surface and underwater. Instead of using the previous hair styles, 3-D printed shapes were attached on the removable scalp of the head. A bun, a mow-hawk and a neck bridge were printed. To increase the effect of the bun on drag, additional material (a bun styler) was placed underneath the cap to create larger buns tested in frontal position (bun 2) and on the back (bun 3). The tested hair styles on the head in its static testing position are presented in Figures 8.21 and 8.23 for the frontal and back positions respectively.

Cap C1 size L was worn to accomodate for the larger hair volume compared to the standard head, and goggles G1 were fitted at all times.

Mannequin on front The different hair styles were tested on the free surface at typical swimming speeds of 1.5 $m.s^{-1}$ and 2.0 $m.s^{-1}$, corresponding to flow regimes before and after the Fr-transition. Visual observations were not sufficient to rank the hair styles in terms of least-drag. The drag force for all hair styles tested on the front are thus reported in Figure 8.22. Both buns appear to offer reduced resistance before and after the Fr-transition. The larger bun has a stronger impact with -3% and -2% drag reduction compared with the baseline at 1.5 and 2.0 $m.s^{-1}$ respectively. This is likely due to the elongation of the head, making it a more streamline body. Similarly, the neck bridge has a 2% drag reduction on the surface.

In the submerged condition, only the bun and neck bridge were compared to the baseline at a single speed of 3.25 $m.s^{-1}$ to replicate the higher speeds attained after a dive start or a turn. Limited change is noticed between the different hair styles, except for the neck bridge which exhibits a small reduction in drag of 1%. This reduction in drag may be explained by the fact that the flow stays attached for longer.

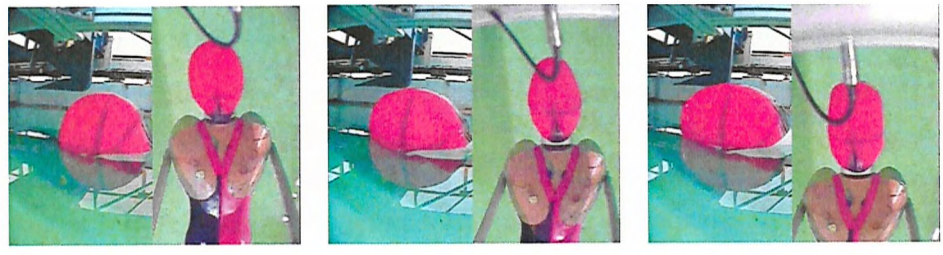

(a) Baseline (b) Bun (3-D printed) (c) Bun 2 (larger)

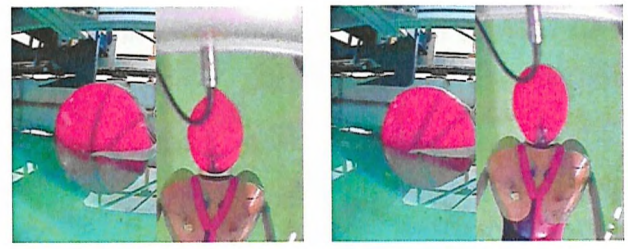

(d) Mow-hawk (e) Neck bridge

FIGURE 8.21: Hair styles tested on the mannequin in the frontal position.

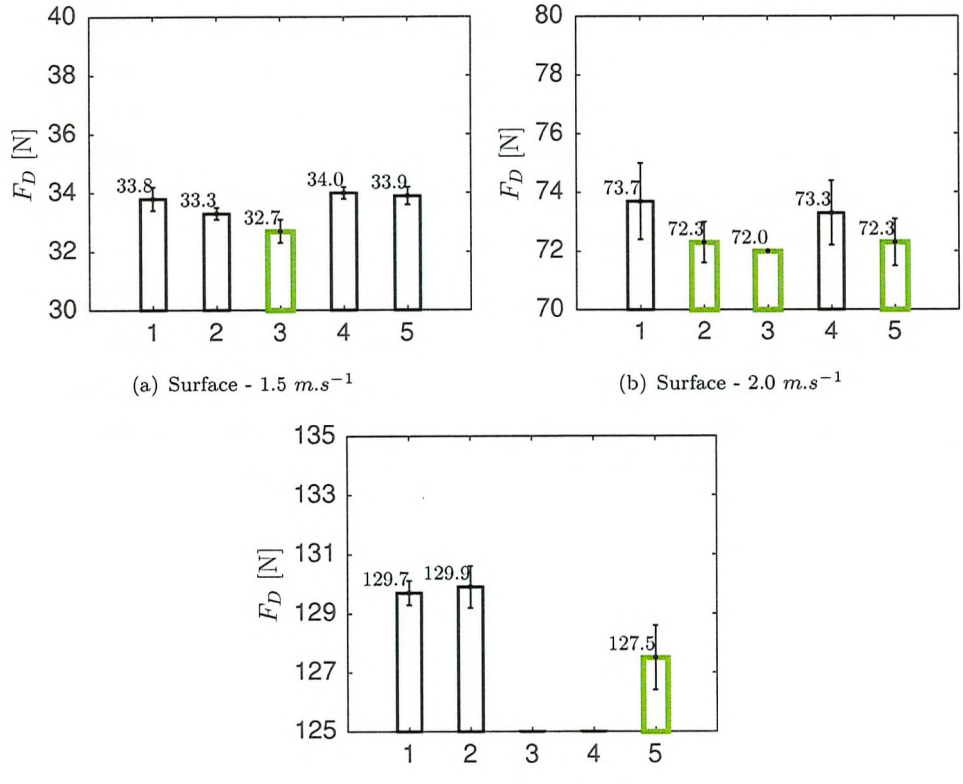

(a) Surface - 1.5 $m.s^{-1}$

(b) Surface - 2.0 $m.s^{-1}$

(c) Submerged - 3.25 $m.s^{-1}$

FIGURE 8.22: Drag force comparison of different hair styles on front. 1: Baseline, 2: Bun, 3: Bun 2 (larger), 4: Mow-hawk, 5: Neck-bridge.

Mannequin on back The effect of the different hair styles in the backstroke position was only assessed on the free surface since the cap was balooning underwater. Three speeds of 1.4, 1.5 and 1.7 $m.s^{-1}$ were selected across the backstroke speed range and repeated between two and five times.

Flow visualisation for the baseline and the large bun (bun 3) are presented at all speeds in Figure 8.24). At 1.4 $m.s^{-1}$, a large breaking wave is exhibited. At 1.5 $m.s^{-1}$, the breaking wave transforms to a thin sheet of fluid which still separates before the googles, whereas at 1.7 $m.s^{-1}$, this thin sheet of fluid has enough.

Now analysing the drag force results shown in Figure 8.25, it is worth noting that the relative standard deviation is small enough (under 1 % during the pre- and post-Fr-transition flow regime) and thus allows a comparison between the different hair management style to be made with confidence. However, during the transitional speed, the relative standard deviation doubles (RSD = 2 %), emphasising the unstability of this transitional flow regime.

The large bun displays a significant drag reduction of 4% both pre- and post-Fr-transition. Though, at the transitional speed of 1.5 $m.s^{-1}$, the bun exhibits a higher drag (2% greater than for the baseline). These results confirm the potential of elongating the head with a bun to reduce swimmers' resistance through the water.

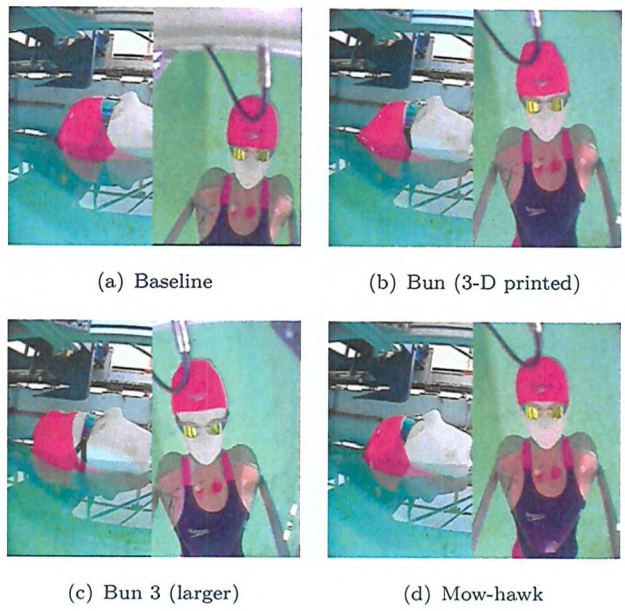

(a) Baseline (b) Bun (3-D printed)

(c) Bun 3 (larger) (d) Mow-hawk

FIGURE 8.23: Hair styles tested on the mannequin on back.

(a) 1.4 $m.s^{-1}$ (b)

(c) 1.5 $m.s^{-1}$ (d)

(e) 1.7 $m.s^{-1}$, Baseline (f) Larger bun (bun 3)

FIGURE 8.24: Flow visualisation of baseline versus large bun (bun 3) on the mannequin on back.

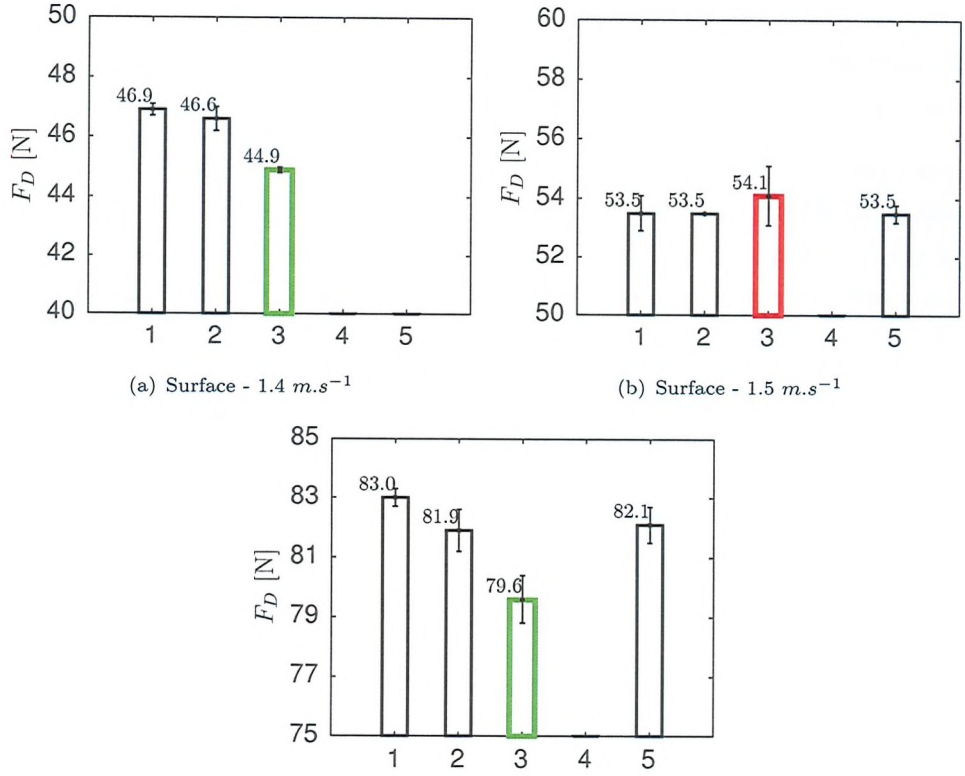

(a) Surface - 1.4 $m.s^{-1}$

(b) Surface - 1.5 $m.s^{-1}$

(c) Surface - 1.7 $m.s^{-1}$

FIGURE 8.25: Drag force comparison of different hair styles on back. 1: Baseline, 2: Bun, 3: Bun 3 (larger), 5: Neck-bridge.

8.5 Chapter summary

In this chapter, it was shown that the body position has a large influence on the drag. When selecting a body position for the mannequin, the dynamic condition should be considered in order to ensure a realistic flow over the rest of the body is replicated.

The same flow feature is noticed on the head only and on the mannequin's head with the Fr-transition occuring over the same range of speed. However, a decrease in drag on the total body drag curve was not observed. Only a reduction in the rate of drag increase is to be noted around the elite swimmer speed (Fr-transition on the head).

Although there is no drag crisis for the mannequin, caps and goggles can still influence the flow regime on the mannequin's head. When comparing different caps at a set speed, the total body drag is much lower once the Fr-transition occured. This would suggest that the same phenomenon would apply to a real swimmer.

Going a step further, flow control devices were applied on the head. Hair management devices such as a bun showed a drag-reduction advantage on the free surface and especially in the backstroke position (-4% pre- and post- Fr-transition). The neck bridge

also showed positive results, emphasing the need to use swimmer's hair to shape their head into a more streamlined body. Elongating the head with hair remains within the rules set by FINA since the hair is part of the head and non-rigid.

From the previous chapters considering the flow past a sphere, a head and a mannequin, the influence of both the head position and hair management on a swimmer's head at the free surface appear to be promising to reduce a swimmer's resistance. These effects will be studied on a real swimmer in a swimming pool environment in the next chapter.

9

Flow past a swimmer

In the previous chapters, knowledge on the flow past a swimmer's head have been gained in a towing tank environment. In this chapter, the complex case of a real swimmer is considered again. The influence of the head position and hair management on a swimmer's resistance are evaluated.

9.1 Influence of head/body position

An amateur male swimmer was towed passively along a 25-m pool, with his arms by his sides, with a tow-belt fixed around his waist.

The swimmer's total resistance and the elevation of the generated waves were measured using the tow rig and wave probes systems described in the methods for pool testing in Chapter 3. The schematic of the pool experimental set-up is provided in Figure 4.1.

The swimmer was instructed to adopt three different head positions: up (looking forward), aligned (looking slightly ahead) and down (looking at pool bottom). The swimmer was towed in each position at three speeds: 1.2 $m.s^{-1}$ (Fr = 0.3), 1.7 $m.s^{-1}$ (Fr = 0.4) and 2.1 $m.s^{-1}$ (Fr = 0.5). Three runs were performed for each configuration (i.e. one head position/one speed), apart from the lowest speed where only one run was done.

Qualitatively, it may be noticed that the wave system behind the swimmer becomes wider as speed increases due to the rise in turbulence intensity (Figure 9.1). A close-up on the head of this wave system shows that the wave system is initiated at a different location along the body depending on the head orientation (Figure 9.2). In the head up position, the wave system is created just in front of the head, whereas with the head aligned it is initiated more at the top of the head. With the head down position, the wave system starts from the shoulders. This difference in wave pattern can be readily identified from the wave elevation measurements presented in Figure 9.3.

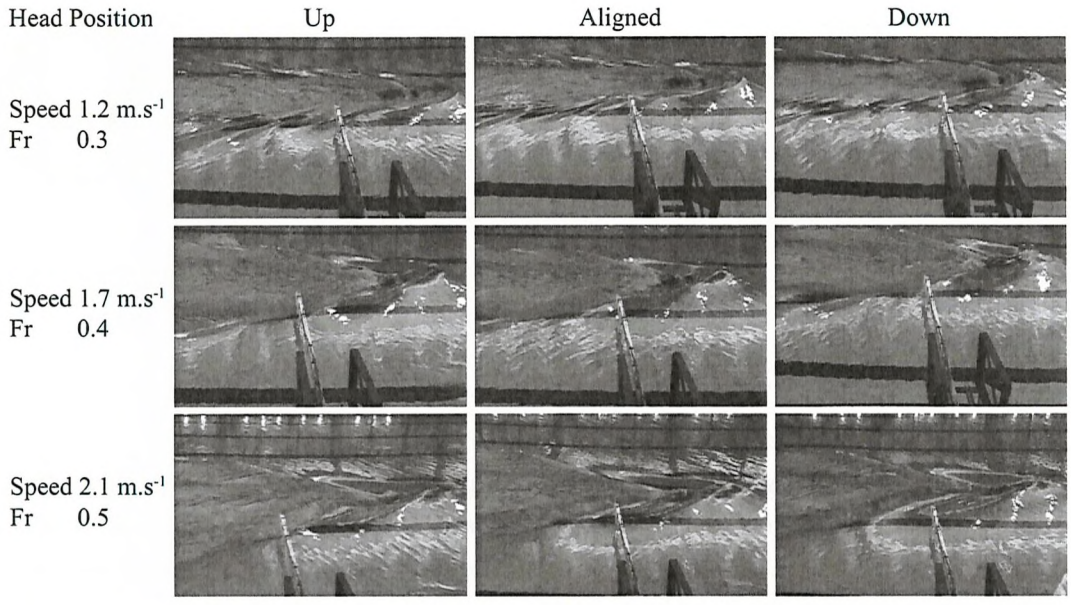

FIGURE 9.1: Observations of wave pattern for a range of head positions and Froude numbers.

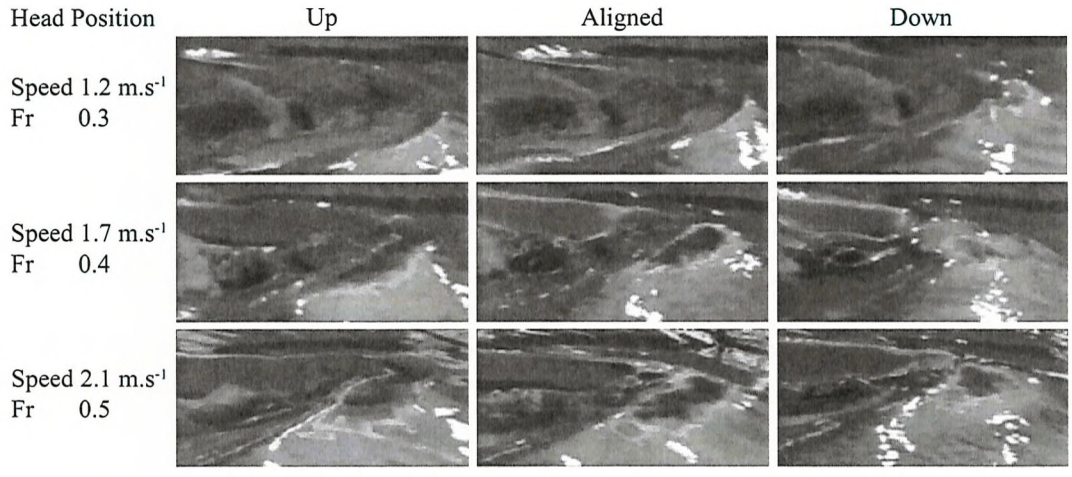

FIGURE 9.2: Close-up on the head from Figure 9.1.

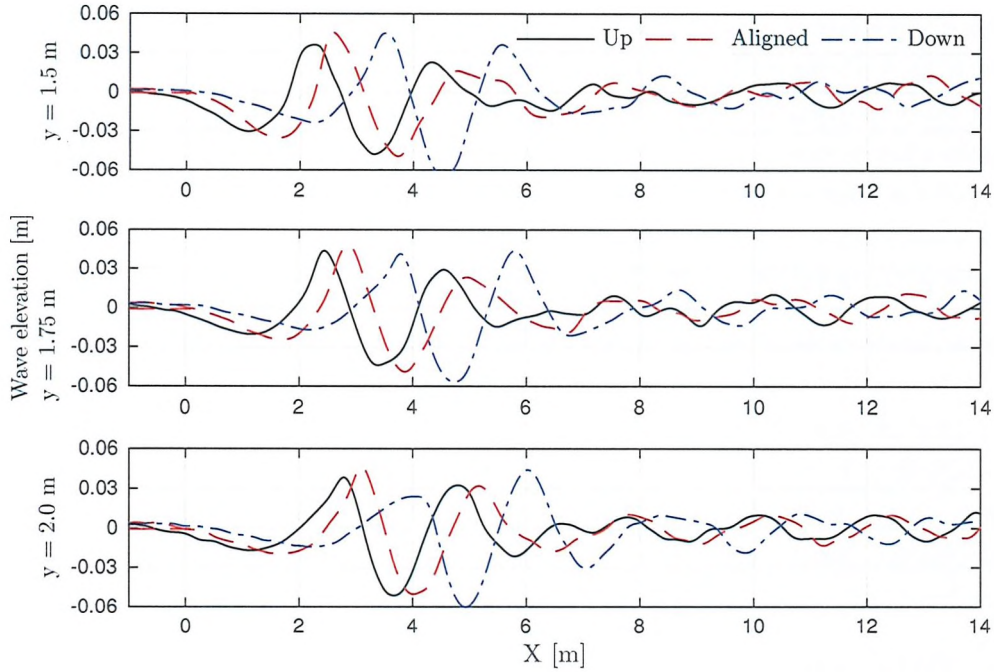

FIGURE 9.3: Measured wave cuts of different head positions at 2.1 $m.s^{-1}$.

TABLE 9.1: Resistance data in the head down position. NB: RSD = Relative standard deviation; drag % difference with head aligned position expressed in brackets.

Speed $[m.s^{-1}]$	R_T [N]	RSD (R_T)	R_W [N]	RSD (R_W)	R_W (% R_t)
1.2	67 (12%)		10 (27%)		15%
1.7	121 (1%)	1%	11 (-31%)	14%	9%
2.1	190 (0%)	2%	28 (28%)	18%	15%

TABLE 9.2: Resistance data in the head aligned position. NB: RSD = Relative standard deviation.

Speed $[m.s^{-1}]$	R_T [N]	RSD (R_T)	R_W [N]	RSD (R_W)	R_W (% R_t)
1.2	60		8		13%
1.7	119	1%	16	19%	13%
2.1	191	3%	22	19%	11%

TABLE 9.3: Resistance data in the head up position. NB: RSD = Relative standard deviation; drag % difference with head aligned position expressed in brackets.

Speed $[m.s^{-1}]$	R_T [N]	RSD (R_T)	R_W [N]	RSD (R_W)	R_W (% R_t)
1.2	67 (12%)		7 (-12%)		10%
1.7	127 (6%)	4%	11 (-32%)	30%	8%
2.1	200 (5%)	3%	26 (18%)	24%	13%

Comparing the total resistance of the swimmer with the different head positions (Tables 9.1 - 9.3), it is observed that the head aligned position offers less total resistance than the other two configurations. The head up position presents the highest total resistance despite a lower wave resistance at the lower speeds. With the head up, the projected area of the head itself is increased, combined with a rise of the body angle of attack resulting in a further increase of the body projected area. The same trend was previously noticed on the study of the flow past a head only.

The accuracy of the measurements is important to comment upon. The relative standard deviation of the wave resistance is determined over three runs at the two highest speeds (1.7 and 2.1 $m.s^{-1}$) and is significant (up to 30%). This uncertainty is partly due to the fact that, in the pool, there is only a partial wall reflection and it is thus difficult to select which portion of the wave cut to take into consideration for the wave resistance calculations. Further analyses on the evaluation of wave resistance in the pool should be carried out.

The relative standard deviation of the total resistance within a run is on average 6% across all the runs performed during this testing session. This variation is due to the difficulty of the swimmer to keep the same body position throughout a run, as illustrated in Figures 9.4 and 9.5. His vertical position is governed by balancing the buoyancy, weight and hydrodynamic forces. His attitude in the water is dictated by the moments generated by these forces. For instance, the distance between the centres of buoyancy and gravity generates a moment which tends to pitch the feet down. Increase in a swimmer's angle of attack leads to a larger frontal area, resulting in a higher drag as previously shown on the mannequin (Chapter 8). As the fluid forces and moments acting on a swimmer's body are unsteady, the athlete naturally controls his position in the water with small movements of his body (Figure 9.5). The ITTC (1967) resistance committee reported a study from Maruo and Ishii, which considered different underwater hull forms in the near free surface to reduce wave resistance. These results emphasise the substantial impact of a body volume and position near the free surface on the wave resistance, and thus on the total resistance.

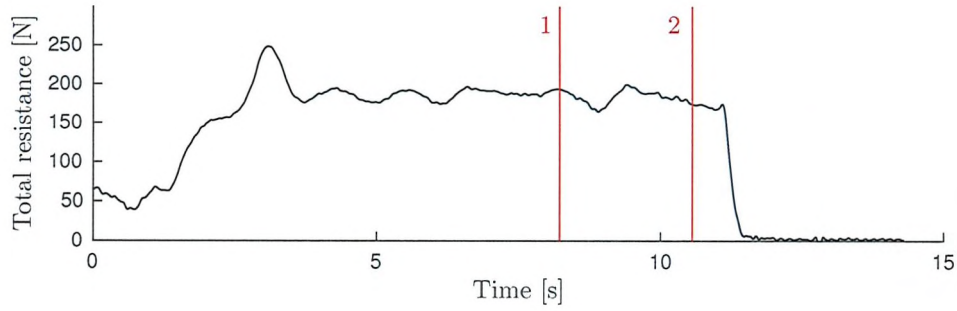

FIGURE 9.4: Total resistance time trace at 2.1 $m.s^{-1}$.

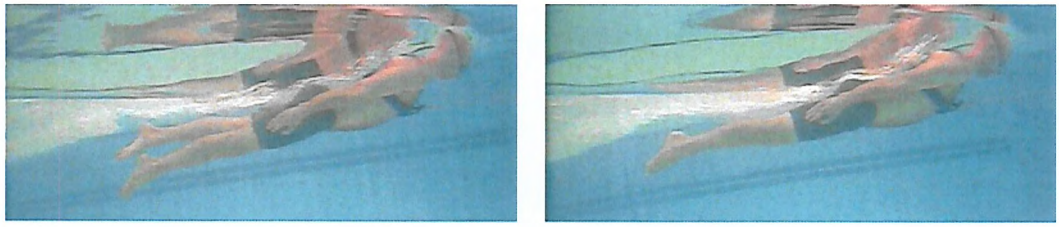

(a) Position 1 - legs apart, high drag

(b) Position 2 - legs together, low drag

FIGURE 9.5: Variation in body attitude at two different time instants.

9.2 Hair management

Potential gains of styling hair into a bun located on top of the head were observed on the mannequin in the towing tank. Drag reduction of 3% with the mannequin on the front and 4% on the back were measured. It was thus decided to take the study a step further and implement the bun on a real swimmer.

The bun was shaped using the natural hair of the swimmer with a bun styler to create additional volume. The aim was to replicate as much as possible the 3-D printed shape produced on the mannequin's head, while assessing feasible options to create a bun for a swimmer. Ultimately, hair extension would remain the only option to create a bun shape under the cap and to comply with the FINA rules (Section 1.3.2).

The drag difference between a traditional cap (baseline) and with a bun on top of the head was assessed over three testing sessions with different objectives:

- Session # 24 - Initially, an amateur swimmer was used to assess the passive swimming performance of the bun during both underwater tows and push-off glides.
- Session # 29 - Testing of the bun on four para-swimmers was then undertaken in both passive mode with push-off glides and active mode for all strokes.

- Session # 31 - A validation testing session of the effect of the bun with different para-swimmers for freestyle and backstroke and the same swimmer for butterfly was organised.

First, the initial results, with the amateur swimmer investigating the passive swimming mode only, will be presented. Results from both testing sessions with elite para-swimmers will be combined and reported in a second part.

Initial passive swimming tests with amateur swimmer The bun shape tested is presented in Figure 9.6. The amateur swimmer performed five under-water tow on the tow rig and 10 push-off glides on the speed reel.

(a) Baseline (b) Bun

FIGURE 9.6: Different views of head shapes tested - Baseline versus Bun.

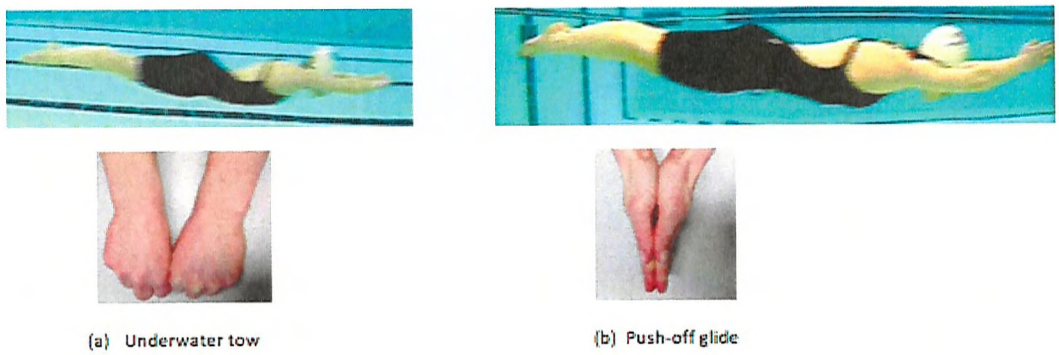

FIGURE 9.7: Body and hand positions during underwater tow and push-off glide.

TABLE 9.4: Underwater passive tows at 2.0 $m.s^{-1}$ - % drag difference given with respect to baseline.

	F_D [N]	STDEV [N]	COV	% diff.
Baseline	83.1	1.98	2%	
Bun	86.6	3.52	4%	4%

TABLE 9.5: Push-off glides - % drag difference given with respect to baseline.

	C_D	COV	% diff.
Baseline	0.025	5%	
Bun	0.024	3%	-4%

Data are collected in Tables 9.4 and 9.5. Underwater, the bun showed opposite trends depending on the hand and body positions. During the passive tow, the bun increased drag by 4%. Figure 9.7 confirms that in this particular body position, the bun increases the frontal area. However, during a push-off glide, the bun is aligned with the streamlined hand position. The bun thus covers a larger area of the turbulent wake which could explain the reduction in drag compared to the baseline. This last point is of great interest for elite swimmers and should be further investigated in both the dive-start and turns phases.

Tests with elite para-swimmers Swimmers' information (height and weight) can be found in Appendix A for each pool testing sessions # 29 & 31. Drag was measured for freestyle and backstroke on the tow-rig. On the other hand, only speed was recorded for breaststroke and butterfly on the speed reel. A velocity-dependent drag coefficient was obtained from the speed reel for the push-off glides. For the active mode, three repeat runs only were performed to minimise the effect of fatigue. For the push-off glides, the athletes did 10 repeat runs. Each athlete was asked to perform 100 m at race pace in their specific stroke, including a start, free-swim and tumble-turn phases. All athletes were then interviewed and feedback was recorded.

On the dive start, no real difference was noticed amongst all athletes, except some mentioning a better body position as a result of the bun making it easier to surface.

During the tumble-turn and push-off, this same feedback of improving the body position underwater was made by some athletes. The added buoyancy generated by the bun allows the swimmer to adopt a more streamlined positioned during the glide as highlighted in Figure 9.8.

FIGURE 9.8: Effect of bun on body position. The added buoyancy generated by the bun helps the swimmer to reach a more streamlined position during the glide.

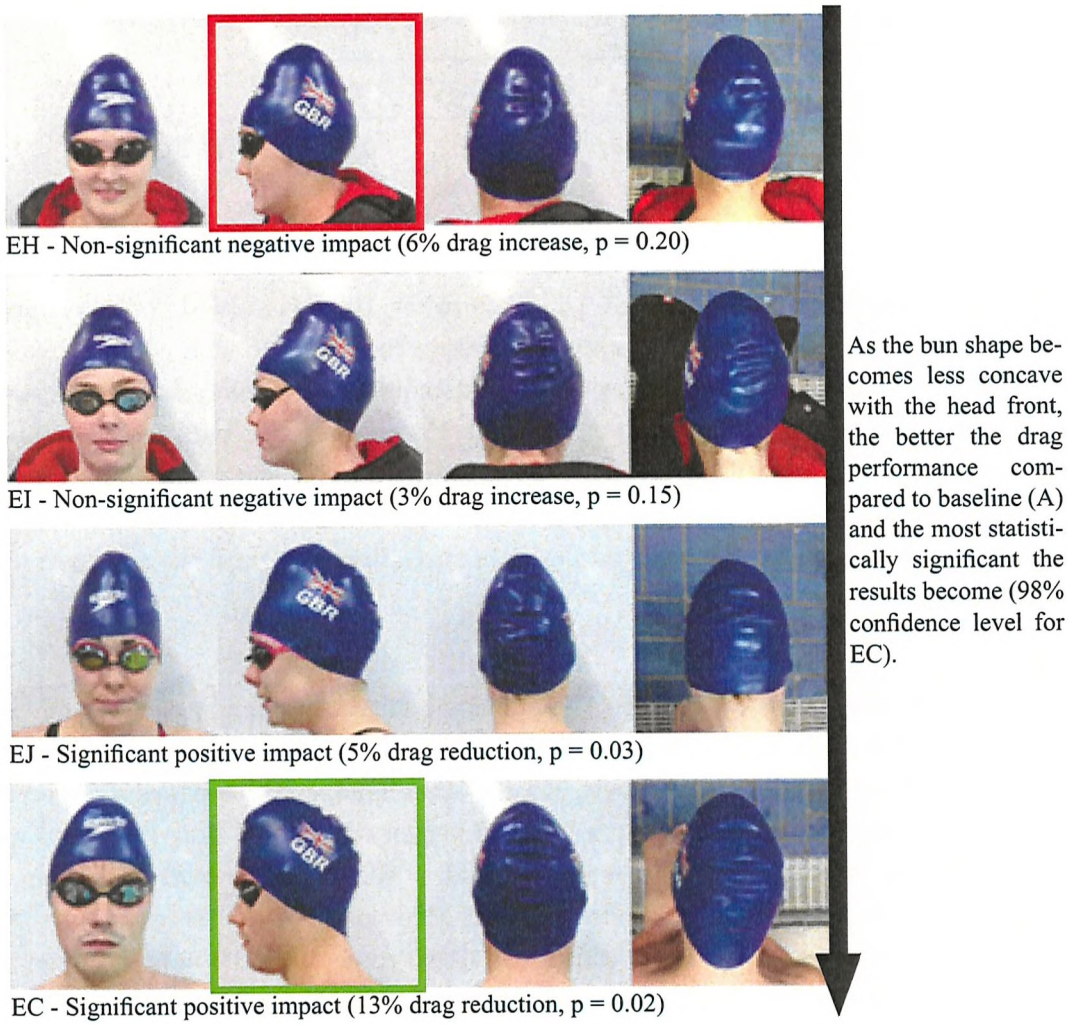

FIGURE 9.9: Summary of effect of bun during the push-off gliding phase. As the bun shape becomes less concave with the head front, the better the drag performance compared to the baseline and the more statistically significant the results become.

Figure 9.9 presents the different bun shapes tested alongside the percentage difference in drag coefficient between the bun and the baseline as obtained for each athlete. The effect of the bun during the underwater phase could be thought to be the same for all athletes since the same push-off glide test was performed. However, the outcome is different depending on the athlete due to 'un-planned' differences in body position and in the bun shape. It was indeed difficult to replicate the same bun shape considering this was a first attempt and swimmers had different hair length and volume. Swimmers also have different head shapes. It can be observed that in the case of the two significantly positive results (EJ and EC), the junction between the bun and the head is better established. In fact, as the bun shape becomes less concave (side view of the head), the impact of the bun becomes better and more statistically significant. The same trend was obtained during the second set of tests. Figure 9.10 shows the same athlete wearing buns shaped

differently. This would suggest that an optimum bun shape would be one that does not present any concave shape and that is streamline between the bun and the forehead.

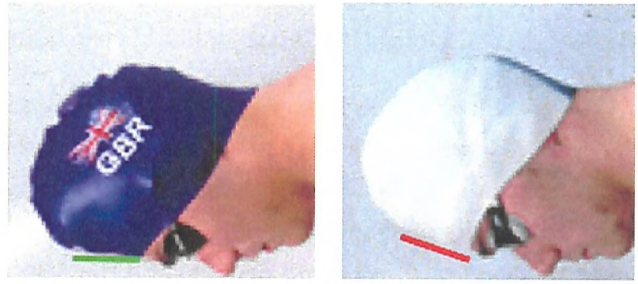

(a) 13% drag reduction, p = 0.02 (b) 3% drag reduction, p = 0.33

FIGURE 9.10: Two different bun shapes highlighting an elongated forehead feature to reduce drag.

General conclusions on the influence of the bun during the active swimming phase remain difficult to establish due to the swimmers' variability (COV across three runs up to 17%). The p-value associated with the percentage drag difference is cited to ensure a fair representation of the data.

In freestyle, although both athletes mentioned an improved body position during the feedback, one athlete showed a reduction in drag of 8% ($p = 0.07$), while the other freestyler showed an increase in drag of 2% ($p = 0.27$).

In backstroke, one swimmer provided a positive feedback as she reported feeling more streamline and as if she was swimming more on top of the water. However, over the average of three runs, the bun increased the drag by 6% ($p = 0.25$) and 10% ($p = 0.16$) in each test. The p-value is high for those tests, emphasising the difficulty for the swimmer to keep a consistent swimming technique during the tests. In addition, although the average showed a negative impact of the bun on the total resistance, the least-drag run in both tests was still the one with the bun on.

Only one breaststroker was tested and a speed reduction of 2% ($p = 0.02$) was observed with the bun on. The swimmer's feedback was in opposition with the measured data as she reported that she was pushing through the water faster.

As for butterfly, the same swimmer was tested in both tests. He indicated that his stroke technique still felt natural with the addition of the bun. The impact on the speed was small ($\pm$ 1%, $p = 0.22$). However, the stroke rate was reduced and the stroke length increased, leading to a better stroke efficiency.

9.3 Chapter summary

Two techniques to reduce a real swimmer's resistance were tested in a pool environment: changing the head position and elongating the swimmer's head using hair.

The head aligned case presented the least total resistance, followed by the head down and head up cases. A similar trend was observed for the case of the head only, except that at the higher speed, the head down case showed reduced drag. To further study the influence of head position, tests should be performed with a real swimmer so that the effect of changing the head position could also include the resulting change in total body position.

Testing a bun shape to elongate the swimmer's head in reality proved to be challenging due to the difficulty in replicating the same bun shape for all athletes. Insight into what could be a more favourable bun shape for the underwater phases was found: no concave surfaces and a bun that ensures a flat connection with the forehead. During a push-off glide, the bun provides additional buoyancy to the head, lifting the upper body, and thus reducing the projected area. Nevertheless, it remains difficult to draw conclusions from the active swimming phase due to the high variability of the swimmer across the three repeat runs. Only the butterfly stroke showed an interesting feature with an increase in stroke efficiency.

Additional time should be spent to improve the creation of the bun shape prior to further tests. These tests could take the form of time-trials with video-recording to do a stroke analysis.

Part D

EPILOGUE

10

Conclusions

During a race, an elite athlete swims at speeds ranging from 0.5 $m.s^{-1}$ to 2.0 $m.s^{-1}$ on the free surface and up to 3.1 $m.s^{-1}$ underwater. In a pool temperature of about 28°C, the swimmer's head operates in the critical Reynolds number ($1 \times 10^5 \leq Re \leq 7 \times 10^5$) and Froude number ($0.4 \leq Fr \leq 1.5$) flow regime. When actively swimming, the swimmer deforms the calm free surface and generates a wave pattern, which is thought to account for a significant portion of the swimmer's total resistance. Hence, the performance evaluation of swimming technique and equipment under such changes in flow regimes offers great challenges, but also a potential to reduce a swimmer's resistance. Several methods with various levels of difficulty and accuracy were applied. After an attempt to perform numerical simulations (linear potential flow and URANS CFD), experimental testing (tank testing and pool testing) was undertaken to tackle these challenges.

This chapter summarises the chosen methodology to study the flow regimes encountered by a swimmer, followed by the key research outcome in the areas of: flow past bluff bodies, head position, goggles/cap design and hair management. Recommendations for further research are presented alongside each study.

10.1 Methodology: from the pool, via the computer to the tank

With the aim of reducing a swimmer's resistance through the water, the first investigations were done in a pool environment. The systems used to assess swimmers' performance were introduced (Chapter 3). Swimmers can either be towed underwater or on the free surface while the resistance is recorded. Alternatively, they can push-off the wall and either just glide or free swim while their velocity is measured. From the deceleration of the push-off glide, a drag coefficient can be obtained. A first study on equipment testing with 12 elite swimmers allowed the researcher to better understand the challenges of testing swimmers in a pool environment. A swimmer is not a solid body, but a human who cannot exactly repeat the same test. The coefficient of variation across the five to ten runs performed is on average 3%. Although this could be considered as small, the percentage difference in drag or drag coefficient between two configurations is sometimes less than the relative standard deviation, which makes it difficult to establish a judgement on the reliability of the data. Consequently, the permutation test statistical method was used to determine if the difference in mean was statistically significant.

Although the pool testing systems allow swimmers to select their best equipment in some cases, there still exist some issues with the swimmers' variability. In addition, it remains difficult to take elite swimmers out of their training environment. They already are reluctant to participate into product development testing sessions, and thus will be even less likely to take part in pool testing sessions aimed at better understanding the flow mechanisms encountered by a swimmer. To remedy to both the swimmers' variability and their lack of availability, it was thought that a numerical pool could be implemented (Chapter 4).

A male swimmer was thus passively towed at the free surface at two typical elite swimmer's speed of 1.7 and 2.1 $m.s^{-1}$, and both total and wave resistance were measured. This experimental test case was modelled in a 3-D CFD domain using URANS. These simulations underestimated the total resistance by about 25%. Although differences in the wave pattern could be pointed out, another source of error comes from the variability of the swimmer's position during the experimental run. Due to a short domain length, the wave resistance could not be obtained from the CFD wave cuts. Increasing the domain length would dramatically raise the number of cells in the mesh which already counts eight million cells. The computational time required to run 3-D URANS simulations of a swimmer would thus be too large to lead to key conclusions on swimming over less than three years. A much faster simulation considering 2-D linear potential flow (thinship) was used to investigate the wave resistance component. By extending the domain width from the original experimental case and by lowering the static body vertical position to a more dynamic position, the simulated wave pattern became closer to the 3-D simulations and the experimental case. This led to a good comparison of

the wave resistance obtained in the pool. Since this last method cannot model the large amount of breaking flow developed by a swimmer, the total resistance cannot be evaluated. It was thus decided to not pursue simulation techniques and to instead move to a more controlled experimental environment that is a towing tank with solid models.

Tank testing studies were conducted with the prime aim of first reducing the level of complexity of the fluid mechanics encountered by a swimmer. A sphere model was thus built to replicate a simplified swimmer's head (Chapter 6). Once the flow physics over the typical elite swimmer speed range was better understood, the flow past a head and a mannequin were then considered (Chapters 7 and 8). The influence of the head position and shape, as well as cap and googgles designs was researched. The experimental methodologies were described in Chapter 5. Several dynamometer rigs relying on the electrical force transducer principle were built to accommodate all the tested models in two different towing tanks.

Eventually, after a build up of complexity towards reality performed in the towing tank, the study was taken back to the pool with real swimmers. Two key studies investigating the influence of head position and hair management under the cap were undertaken.

10.2 Flow past bluff bodies

Drag-tests of surface-piercing spheres, combined with above-water footage, allowed a flow taxonomy to be derived across the Re-Fr range encountered by an elite swimmer's head. Four key flow regimes were observed as highlighted in Figure 10.1. A key result is that a sphere at the free surface undergoes a more complex version of the drag crisis phenomenon as typically observed in single phase flow. Swimmers could thus take advantage of this drag crisis to swim in a lower drag flow regime at an earlier speed. The drag crisis is initiated at $Fr \sim 1.0$ and ends at the critical Reynolds number ($\sim$ 3.0-4.0 $\times 10^5$), once both the breaking wave has transitioned to a thin sheet of fluid running on top of the sphere (denoted Fr-transition) and when the laminar boundary layer becomes fully turbulent (Re-transition).

Using a geosim model (D_2 = 125 mm, i.e. 56%D_1) has emphasised the fact that the free surface plays a key role in the drag crisis since a sharp drop in drag coefficient is observed between $Fr \sim 1.0$ and the Fr-transition. This first drag crisis due to a change in the free surface deformation happens before the critical Reynolds number range is reached, after which a second drag-crisis with a lower gradient takes place.

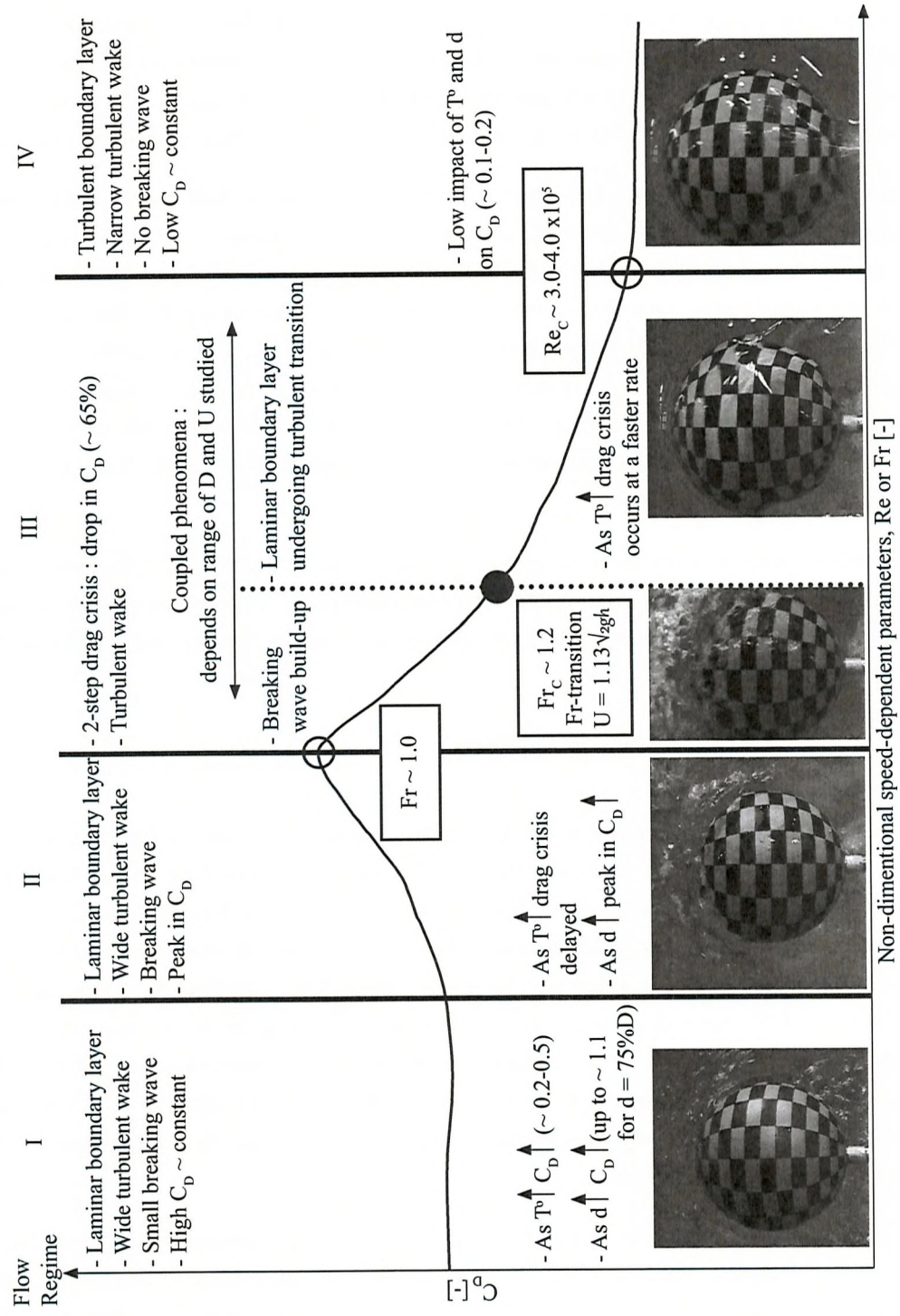

FIGURE 10.1: Revised flow regime taxonomy for a surface-piercing sphere over the critical *Re-Fr* range, $8 \times 10^4 \leq Re \leq 6 \times 10^5$ and Froude number $0.4 \leq Fr \leq 2.9$. Note: T° = temperature, d = immersion depth.

The tested 3-D printed head follows a similar flow taxonomy as defined for the sphere. In the case of a swimmer's head, a single drag crisis takes place as both the Fr- and Re-transitions occur over the same speed range.

The Fr-transition, the change from a breaking wave to a smooth flow over the top of the head, becomes a visual marker indicating a low-drag flow regime. With the addition of the rest of the body, the mannequin's head still encounters this free surface deformation, as well as a real swimmer (Figure 10.2). This emphasises that equipment such as cap and goggles may be tested on a head model only to reduce testing time and cost.

The drag force coefficient for the mannequin ($C_{F_D} \times A_p = \frac{F_D}{0.5\rho U^2}$) is plotted versus speed, Fr and Re numbers in Figures 8.4, 8.5(a) and 8.5(b) respectively. Despite the occurence of the Fr-transition on the head, no drag crisis is observed in the case of the mannequin. Only a reduction in the rate of drag increase is to be noted around the elite swimmer speed (Fr-transition on the head, $\simeq 1.7\ m.s^{-1}$). Even if the head experiences a drag crisis, the increased drag over the rest of the body, as speed increases, remains overall greater than any drop in local drag on the head. Although there is not a sharp drag crisis, there is still potential to use flow control devices on the head to decrease the overall resistance of a swimmer.

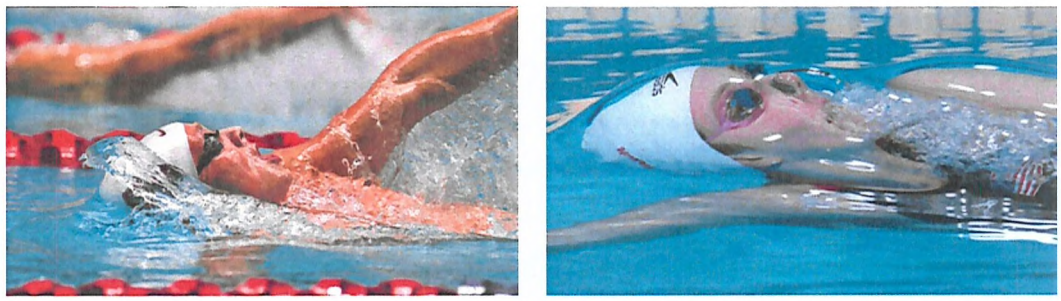

(a) Pre-transition, high drag

(b) Post-transition, low drag

FIGURE 10.2: Direct observation of the Fr-transition, change from a breaking wave to a smooth flow over the top of the head.

Small variation of the immersion depth (while still keeping a portion of the sphere or head in the air) has a large impact on the drag coefficient, especially in the laminar flow regime. A higher immersion depth implies a greater projected area which results in a large peak in drag coefficient just before the initiation of the drag crisis (flow regime II). Follows the Fr-transition which was shown to not be dependent on the waterplane area of the bluff body but primarily on the air draught as the kinematic energy has to overcome the potential energy. The speed at which this Fr-transition occurs can thus be determined by Bernoulli equation using a coefficient to compensate for the additional kinetic energy required due to the presence of viscous effects (Equation 10.1).

$$U_{transition} = 1.13 \times \sqrt{2hg} \tag{10.1}$$

Through the use of two towing tanks at different times of the year, an initial investigation into the effect of water temperature on bluff body drag could be undertaken. As temperature rises, the drag coefficient increases before the drag crisis; whereas post-drag crisis, the drag coefficient remains low around 0.1 or 0.2. This would imply that the impact of the drag crisis would be stronger in pool water temperature of 28°C. Also, due to the high dependence of the kinematic viscosity on water temperature, Reynolds number shift will be taking place. If the water temperature is too cold, testing at higher speeds is required to capture the post-transition flow regime and not all tanks may allow such high speeds.

Recommendations for further research

- Drag-testing a sphere in a longer towing tank to further learn about the unsteadiness of the flow during a run. The use of surface-pressure sensors would allow the researcher to better understand the laminar-to-turbulent boundary layer transition. Dye paint could be used as well to observe where the flow separates.
- Although this is not of interest to a swimmer, two other geosim models could be tested to further separate the Fr- and Re-transitions. A smaller sphere diameter would ensure that only the Fr-transition occurs, while a larger sphere diameter would ensure that only the Re-transition occurs.
- Develop a numerical case for the sphere, which could then be used for the head. Providing that a numerical simulation is validated against the experimental test case offered in this thesis, then a parametric study with different sphere diameters could be run.
- Investigate a methodology to assess the wave resistance of bluff bodies using wave probes.
- Through the assessment of wave resistance and unsteady surface pressures, study the influence of temperature on the drag crisis of bluff body flows.

10.3 Head and body position

Since the flow past a swimmer's head undergoes a drag crisis, the influence of its angle is of great interest. Three often adopted head angles in front crawl were tested: looking at pool bottom (down), looking slightly ahead (aligned) and looking ahead (up). The

influence of the head position was first investigated on a head model only and then on a real swimmer.

Before the occurrence of the drag crisis, no real advantage in using a particular head position is noticed. However, more differences may be observed between the different head positions once the flow is fully turbulent. The head down case presents the lowest drag, followed by the head aligned and up cases (up to 30% drag difference between the head down and up cases). During the pool tests, the swimmer's best head position was in the aligned position, where a decrease in drag of 9 N (5% R_T) was measured at 2.1 $m.s^{-1}$ compared to the head up case. Studying the influence of the head position directly on a swimmer is critical since the head position will influence the total body position. It was shown with the mannequin study that a change of the body angle of attack and immersion depth had a large impact on the total resistance.

Although all studies are representing passive swimming, they emphasise the importance of the head position on the performance of a swimmer. In reality, the head position of a swimmer varies in all strokes due to the stroke technique and the need to breathe. Although there is not an optimum set head position which can be found, there is still potential to reduce drag by adopting a suitable head position during some part of a stroke. In order to find these suitable head positions, a swimmer could simply try different head angles and swim at maximum speed, while being filmed or observed by his/her coach. The earlier the flow is running smooth over the top of the head, the better the head position will be from a performance and effort point of view. A similar method could be used in the backstroke position, although the drag coefficient appeared to keep on decreasing over a longer speed range past the Fr-transition.

Recommendations for further research

- Ask a coach and his/her swimmers to work on their head position and run time-trials before and after to verify the impact.
- Using active tow, assess the influence of the head position for a swimmer during freestyle and while including the breathing phase.
- Test the head model in the backstroke position with other head angles and over a longer Reynolds number range to better characterise the drag crisis observed for this specific stroke.

10.4 Goggles and cap design

The investigation of cap/goggles design undertaken on the head only has shown that they could influence the drag of the head at the free surface when they presented a

large feature (large goggles shape or hydrophobic coating on cap). This large feature on the head affects the free surface deformation and thus the boundary layer transition. However, underwater, where only the transition from laminar-to-turbulent flow regime matters, smaller feature changes can still have an effect on the drag (ie. three different elite caps with a difference in surface roughness).

Although there is no drag crisis for the mannequin, caps and goggles can still influence the flow regime on the mannequin's head. When comparing different caps at a set speed, the total body drag is much lower once the Fr-transition occurred. This would suggest that the same phenomenon would apply to a real swimmer. These initial tests highlight that there is still scope for product developer to improve their design and that this development could be carried out with a head model only in a towing tank.

Recommendations for further research

- Test further goggles types on the head model only, both on the free surface and underwater.
- Further investigate the use of hydrophobic coating on caps over the different flow regimes encountered by a swimmer.
- Develop a rig to run tests in a larger tank with several 3-D printed head positionned side-by-side to minimise testing time and cost. Several caps and goggles could thus be tested at the same speed in one run. Providing that the towing tank is long enough, the drag of the head could be recorded over multiple speeds.

10.5 Hair management

Goggles and caps are the two technical equipment allowed on a swimmer's head during a swimming race, according to FINA. Nothing in the rules suggests that hair could not be shaped in a way that could reduce the swimmer's resistance through the water.

Various flow control devices (trip studs, spray rails, long-hair management) were fitted on the mannequin's head and tested at speeds pre- and post-Fr-transition. From top-view videos, two wave systems were observed around the upper-body of the mannequin. One is generated from the head stagnation point and another one from the neck. The wave generated from the head is breaking on the shoulders resulting in added drag for the entire mannequin, hence the need for flow control devices. Devices such as a bun showed a drag-reduction advantage on the free surface and especially in the backstroke position (-4% pre- and post- Fr-transition). Indeed, by forcing the flow to follow the hair shape, the total head wave system is reduced and diverted away to not break on

the shoulders. The neck bridge also showed positive results, emphasing the need to use swimmer's hair to shape their head into a more streamlined body.

Testing a bun shape to elongate the swimmer's head in reality proved to be challenging due to difficulty in replicating the same bun shape for all athletes. Insight into what could be a more favourable bun shape for the underwater phases was found: no concave surfaces and a bun that ensures a flat connection with the forehead (Figure 10.3). During a push-off glide, the bun provides additional buoyancy to the head, lifting the upper-body and thus reducing the projected area. Nevertheless, it remains difficult to draw conclusions from the active swimming phase due to the high variability of the swimmer across the repeat runs. Only the butterfly stroke showed a promising feature with an increase in stroke efficiency.

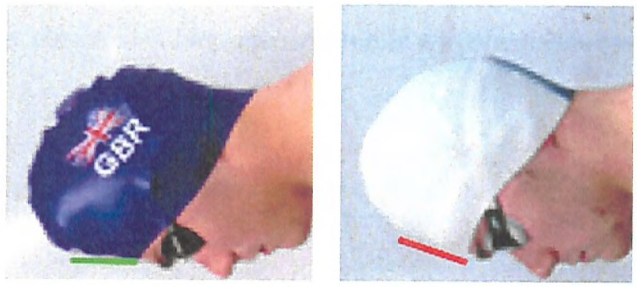

(a) 13% drag reduction, p = 0.02 (b) 3% drag reduction, p = 0.33

FIGURE 10.3: Two different bun shapes highlighting an elongated forehead feature to reduce drag.

Recommendations for further research

- Perform additional pool tests. These tests should be conducted on able-body swimmers instead of paralympic swimmers to reduce the variability in the swimming technique during repeat runs. Several swimmers should be tested for each stroke so that insight on how a bun should be shaped for a specific stroke can be offered. This may even be swimmer specific, as there is not just one way of swimming a stroke. For instance, in breaststroke, there exists a flat-style versus a wave-style. Each technique and swimmer's head geometry will likely require a different bun shape.

10.6 Protocol for equipment selection

Through the research undertaken, equipment selection has been improved and an initial protocol is suggested. Although a pre-selection process can be operated in a towing tank environment to avoid swimmers' variability and reduce swimmers' participation,

pool testing for each individual athlete for the final selection remains essential. Cap and goggles designs will largely depend on a swimmer's head shape and position. In addition, suit selection appears to be morphology- and stroke-dependent.

Protocol:

1. Undertake pre-selection tests for cap and goggles on a head model only in a towing tank. Beware to assess the performance before and after the Fr-transiton. The best two caps and goggles should be selected for further tests in the pool.
2. Assess the effect of skin friction of various suits on the mannequin in the towing tank and eliminate suits which present a large amount of surface roughness.
3. Perform two sets of push-off tests (10 repeats) on the speed reel to select the best goggles for a specific athlete. The same cap and suit should be kept during both sets.
4. While wearing the selected goggles, perform two sets of push-off tests on the speed reel to select the best cap for a specific athlete. The same goggles and suit should be kept during both sets.
5. While wearing the selected goggles and cap, the athlete can try in free swim several best suits from the tank tests results. This free swim pre-selection test is important since each athlete will have a preferred type of suit depending on compression levels and areas. The stroke types will also impact the suit selection.
6. In the case of para-swimming, the best two suits should be fitted to the athlete prior to pool testing.
7. Perform final suit drag tests with the cap and goggles selected on each athlete. Both active and passive swimming tests should be performed. The active swimming tests are run on the tow rig (freestyle, backstroke) or speed reel (breaststroke, butterfly) depending on the stroke with three repeat runs per configuration. Passive drag tests can be either done on the tow rig (five repeats) or speed reel (ten repeats) depending on the available equipment at hand.

When performing the pool tests, it is important to do the selection from goggles, cap and then suit to ensure equipment is selected with the correct incoming flow. It could be the case that the percentage drag difference between two configurations is non-statistically significant. In this grey area, the equipment with the least drag should still be favoured, providing that the athlete feels confortable wearing it.

10.7 Overall conclusions

The presented aim and objectives for this Ph.D. thesis have been fulfilled. First, a swimmer's passive resistance at the free surface has been investigated in both a real and numerical pool environment. Equipment proved to have an effect on the resistance of a swimmer, however testing human swimmers remains challenging due to difficulties in keeping a set body position during a tow or a glide. In addition, the lack of availability of elite athletes for swimming research emphasised the need to move towards multi-phase numerical simulations. Nonetheless, the current lack of computational power available limits research progress.

In order to better understand the complex fluid mechanics around a swimmer within the course of one Olympic cycle, an experimental methodology was developed. Three models, a sphere, a head and a mannequin, were tank-tested before returning to the pool with a real swimmer.

The sphere tests, followed by the head tests, allowed a flow taxonomy to be established and emphasised the drag crisis occurring at the typical elite swimmer speed range. A strong influence of the free surface on this drag crisis was highlighted. Although a drag crisis cannot be noticed with the full-body, the same flow features can be observed on the head, reinforcing the idea that the head, as the body's leading edge, plays an important role in the total drag of the swimmer. Gaining a better understanding of when and why this drag crisis phenomenon occurs on a swimmer or a mannequin's head presents a great benefit to assess technique (head position) and swimming equipment performances.

Cap and goggles design can influence the drag crisis and can be developed on a head model only. In addition, complex natural flow control techniques such as head position or hair management were introduced. However, these natural flow control techniques still require the involvement of a swimmer since they both influence the overall body position.

Finally, the undertaken research highlighted that, although a pre-selection process in a towing tank environment proved to be useful for manufacturers, an elite athlete should still be drag-tested to determine the best equipment for his/her head shape and body morphology. An initial protocol to select the best equipment (goggles, cap and suit) for each individual athlete is therefore suggested.

10.8 Beyond swimming...

Looking beyond the world of swimming, this research project on surface-piercing bluff bodies over the critical *Re-Fr* range has a great potential to benefit many other engineering fields.

In particular, further research could be undertaken to apply the novel flow taxonomy defined for a sphere to a bulbous bow on a ship. By reducing ship resistance with a better tailored bulbous bow based on the ship's hull form and its operating trim, fuel consumption could be reduced, therefore decreasing greenhouse gas emisions for a cleaner and brighter future.

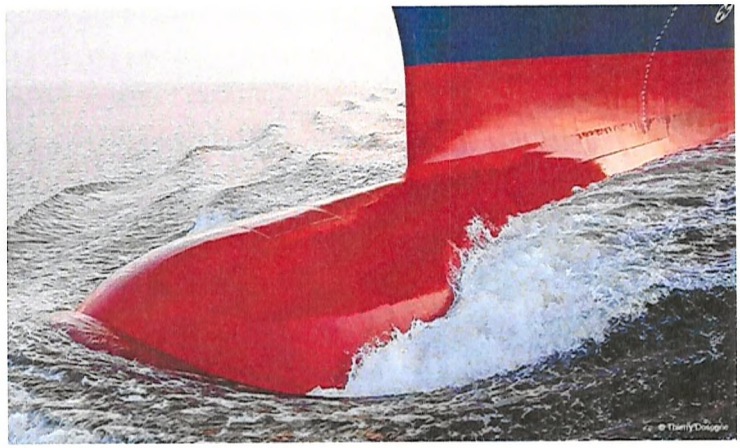

FIGURE 10.4: A bulbous bow of a large container ship: an example of engineering application for the sphere flow taxonomy beyond the world of swimming. Credit: CMA CGM.

A

2012-2016 Olympics Cycle
List of pool testing sessions

Over the 2012 - 2016 Olympic Games cycle, several pool testing sessions have been undertaken. They are chronologically listed in Tables A.1 - A.5. Each session is approved by an ethics ID. The symbol $\star$ indicates that the swimmer was a member of the SwimSIM team and thus did not require an ethics approval. All data are stored anonymously through the use of a letter code for each swimmer. The same code is maintained for each swimmer to allow for longitudinal comparisons of performance. The swimmer's details is given as ID (gender - height / weight), where the gender is F for female or M for male.

TABLE A.1: 2012 - Pool testing sessions.

Session #	Date	Ethics #	Pool	Swimmer	Aim
1	28/06/2012	7207	Loughborough ITC	AN (F - 1.73 m / 60 kg) C (M - 1.78 m / 76 kg) CO (M - 1.83 m / 76 kg) F (M - 1.82 m / 84 kg)	Media Media Media Push-off glide - suit selection
2	24/09/2012	7207	Jubilee	CU (F - 1.68 m / 57 kg) CB (M - 1.75 m / 81 kg)	Push-off glide, UW tow - drag short tests
3	08/10/2012	7207	Jubilee	CV (F - 1.68 m / 52 kg) CW (M - 1.93 m / 84 kg)	Push-off glide, UW tow - drag short tests
4	22/10/2012	7207	Jubilee	CX (F - 1.57 m / 50 kg) CY (M - 1.88 m / 77 kg)	Push-off glide, UW tow - drag short tests
5	05/11/2012	7207	Jubilee	C (M - 1.78 m / 76 kg) CZ (M - 1.83 m / 75 kg) DA (F - 1.73 m / 62 kg)	FS passive tow - Wave study
6	19/11/2012	*	Jubilee	C (M - 1.78 m / 76 kg) CP (M - 1.77 m / 80 kg)	UW speed reel - Fly-kick with sensors

TABLE A.2: 2013 - Pool testing sessions.

Session #	Date	Ethics #	Pool	Swimmer	Aim
7	28/01/2013	*	Jubilee	C (M - 1.78 m / 76 kg)	FS passive tow - Head position, wave study
8	11/02/2013	*	Jubilee	CP (M - 1.77 m / 80 kg)	UW tow - Drag curve
9	11/03/2013	*	Jubilee	EN (M - XX m / XX kg)	UW tow - Shoulder position
10	15/03/2013	7207	Loughborough ITC	AL (F - 1.70 m / 61 kg)	FS tow, speed reel - Baseline for all strokes
				F (M - 1.82 m / 84 kg)	UW tow, speed reel - Underwater fly-kick
				K (M - 1.78 m / 76 kg)	FS tow - Freestyle
				BK (M - 1.83 m / 80 kg)	Speed reel - Underwater fly-kick
11	22/03/2013	7207	Bath ITC	G (F - 1.72 m / 63 kg)	Speed reel - Underwater fly-kick
				W (M - 1.89 m / 83 kg)	Speed reel - Breaststroke pull-down
12	22/04/2013	7207	Jubilee	CB (M - 1.75 m / 79 kg)	FS passive tow - Added propulsion with paddles
13	07/10/2013	7773	Jubilee	DZ (M - 1.82 m / 78 kg)	Speed reel - Breaststroke pull-down
14	19/10/2013	7878	Moulton College	DQ (M - 1.91 m / 86 kg)	Speed reel - Breaststroke pull-down
15	21/10/2013	*	Jubilee	C (M - 1.78 m / 76 kg)	Speed reel - Dive start and turns
16	18/11/2013	8312	Jubilee	DD (M - 1.76 m / 72 kg)	FS passive tow - Dragtini
17	02/12/2013	8307	Jubilee	CO (M - 1.83 m / 81 kg)	Speed reel - Breaststroke pull-down
				DC (M - 1.91 m / 84 kg)	Speed reel - Backstroke underwater fly-kick

TABLE A.3: 2014 - Pool testing sessions.

Session #	Date	Ethics #	Pool	Swimmer	Aim
18	17/02/2014	*	Jubilee	C (M - 1.78 m / 76 kg)	General systems tests
				G (F - 1.72 m / 61 kg)	FS tow - Backstroke
	24/02/2014			BH (M - 1.97 m / 83 kg)	Speed reel - Breaststroke
				BG (F - 1.73 m / 65 kg)	FS tow, speed reel - All strokes
19		9218	St Mary's College	BJ (M - 1.88 m / 88 kg)	Speed reel - Breaststroke
				DE (M - 1.93 m / 91 kg)	FS tow - Freestyle and Backstroke
	25/02/2014			BK (M - 1.83 m / 84 kg)	FS tow, speed reel - Backstroke
				CH (F - 1.71 m / 70 kg)	FS tow, speed reel - Backstroke and Breaststroke
				W (M - 1.89 m / 88 kg)	
				BJ (M - 1.89 m / 83 kg)	
20	05/03/2014	9218	Bath ITC	AH (F - 1.72 m / 62 kg)	
				G (F - 1.72 m / 61 kg)	
				BG (F - 1.72 m / 64 kg)	
				BO (M - 1.79 m / 76 kg)	Push-off glide - Equipment selection
				DO (M - 1.84 m / 74 kg)	
				DL (M - 1.89 m / 88 kg)	
21	13/03/2014	9218	Loughborough ITC	BE (F - 1.73 m / 68 kg)	
				AL (F - 1.70 m / 61 kg)	
				AJ (F - 1.75 m / 64 kg)	
				DM (F - 1.69 m / 72 kg)	
				DT (M - 1.96 m / 90 kg)	
22	18/03/2014	9321	St Mary's College	DU (M - 1.84 m / 78 kg)	UW tow - Suit selection
				DR (F - 1.70 m / 63 kg)	
				DS (F - 1.75 m / 62 kg)	
23	24/03/2014	9219	Jubilee	DW (M - 1.82 m / 76 kg)	Speed reel - Underwater fly-kick
				DX (M - 2.05 m / 90 kg)	Speed reel - Breaststroke pull-down

TABLE A.4: 2015 - Pool testing sessions.

Session #	Date	Ethics #	Pool	Swimmer	Aim
24	16/03/2015	*	Jubilee	EA (F - 1.69 m / 58 kg) EB (M - 1.85 m / 76 kg)	Push-off glide, UW tow - Hair management
25	08/04/2015	14067	Manchester	EC (M - 1.72 m / 68 kg) ED (F - 1.23 m / 43 kg) EE (F - 1.63 m / 58 kg)	UW tow - Suit selection
26	06/05/2015	14067	Manchester	EB (M - 1.85 m / 76 kg) EC (M - 1.72 m / 68 kg) ED (F - 1.23 m / 43 kg) EE (F - 1.63 m / 58 kg)	UW tow, FS freestyle tow - Suit selection
27	10/08/2015	14066	Jubilee	EF (M - 1.84 m / 75 kg)	FS tow and speed reel - Freestyle
28	11/08/2015	*	Jubilee	EG (M - 1.77 m / 74 kg) EC (M - 1.72 m / 68 kg)	Push-off glide, UW tow - Hydrophobic body scrub
29	23/09/2015	17239	Manchester	EH (F - 1.71 m / 61 kg) EI (F - 1.73 m / 61 kg) EJ (F - 1.67 m / 58 kg)	Push-off glide, FS tow, speed reel - Hair management
30	13/10/2015	17240	St Mary's College	AX (M - 1.85 m / 81 kg) AT (M - 1.82 m / 80 kg) AV (F - 1.78 m / 71 kg) EM (F - 1.68 m / 60 kg)	Push-off glide, UW tow, FS tow - Suit selection
31	10/11/2015	17239	Manchester	EC (M - 1.72 m / 68 kg) EK (M - 1.81 m / 73 kg) EL (F - 1.67 m / 66 kg)	Push-off glide, FS tow, speed reel - Hair management

TABLE A.5: 2016 - Pool testing sessions.

Session #	Date	Ethics #	Pool	Swimmer	Aim
32	18/01/2016	*	Jubilee	EA (F - 1.69 m / 58 kg) EO (M - 1.91 m / 86 kg)	Push-off glide - Cap/Goggles selection

B

Wave Resistance Background theory

B.1 Wave resistance

In this appendix, the main steps towards the wave resistance expression will be explained. Further details on the derivation can be found in Molland et al. (2011) and Newman (1977).

B.1.1 Momentum flow analysis

A momentum flow analysis is carried out in a control volume defined by the tank width, b, and depth, h (Figure B.1). The ship advances at a free-stream speed U and creates a propagating wave field which is fixed relative to the ship. Behind the ship, the flow is disturbed and has a velocity vector q = (U+u, v, w). The fluid is assumed to be incompressible and inviscid, and the flow is irrotational.

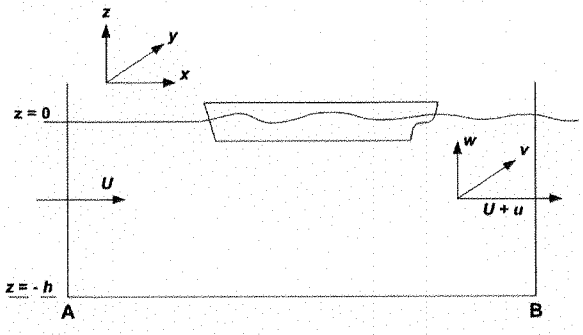

FIGURE B.1: Control volume of width b and depth h to carry out momentum flow analysis (Molland et al., 2011).

The total resistance of the ship can be derived as:

$$R_T = \left\{ \frac{1}{2}\rho g \int_{-\frac{b}{2}}^{\frac{b}{2}} \zeta_B^2 \mathrm{d}y + \frac{1}{2}\rho \int_{-\frac{b}{2}}^{\frac{b}{2}} \int_{-h}^{\zeta_B} (v^2 + w^2 - u^2) \mathrm{d}z\mathrm{d}y \right\} + \left\{ \int_{-\frac{b}{2}}^{\frac{b}{2}} \int_{-h}^{\zeta_B} \Delta p \mathrm{d}z\mathrm{d}y \right\} \quad \text{(B.1)}$$

The first term is mainly due to wave drag, although the perturbation velocities u, v, w are partly due to viscous shear in the boundary layer. The second term is due to viscous drag. In order to evaluate the wave resistance, expressions for the wave elevation and the perturbation velocities need to be determined.

B.1.2 Numerical wave pattern - Eggers series

A theoretical wave pattern can be derived by combining a set of 2-D waves, with elevation $\zeta_n = A_n cos(\gamma_n y' + \epsilon_n)$, as shown in Figure B.2.

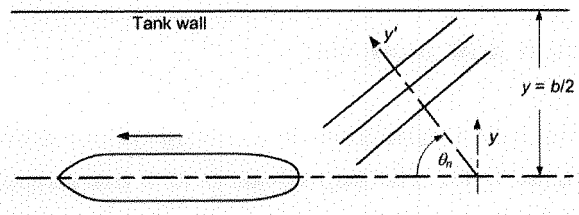

FIGURE B.2: Schematic view of a ship moving with a wave system (Molland et al., 2011).

The wave pattern is assumed:

- to be symmetric and stationary,
- to move with the model speed (wave speed condition - Equation B.3),

- to reflect on the tank wall; no flow through (wall reflection condition - Equation B.4).

This numerical wave pattern is commonly known as 'Eggers series' (Equation B.2).

$$\zeta(x,y) = \sum_n \xi_n cos(x\gamma_n cos\theta_n) + \eta_n sin(x\gamma_n cos\theta_n) cos\left(\frac{2\pi n}{b}y\right) \tag{B.2}$$

$$\gamma_n cos\theta_n = \frac{g}{c^2} tanh(\gamma_n h) \tag{B.3}$$

$$\gamma_n sin\theta_n = \frac{2\pi m}{b} \qquad where\, m \in \mathbb{N} \tag{B.4}$$

From the wave speed and wall reflection conditions ($B.3^2 + B.4^2$), the following condition for Eggers series to be valid is:

$$\gamma_n^2 = \frac{g\gamma_n}{c^2} tanh(\gamma_n h) + \left(\frac{2\pi m}{b}\right)^2 \tag{B.5}$$

The Eggers coefficient ξ_n and η_n can be found experimentally using a transverse or longitudinal wave cut. Details will be given in Section B.2.

B.1.3 Perturbation velocities and final wave resistance expression

The perturbation velocities are difficult to measure in a towing tank. Consequently, the linearised potential flow theory for small waves is used with the measured wave pattern ζ. From the linearised dynamic free surface boundary condition, at z = 0, is $-c\frac{\partial\phi}{\partial x} + g\zeta = 0$, the velocity potential for the measured wave pattern can be deduced as:

$$\phi = \frac{g}{c}\sum_{n=0}^{\infty} \frac{cosh\left[\gamma_n(z+h)\right]}{\omega_n cosh(\gamma_n h)} \left[\eta_n cos\left(\omega_n x\right) - \xi_n sin\left(\omega_n x\right)\right] cos\left(\frac{2\pi n}{b}y\right) \tag{B.6}$$

where $\omega_n = \gamma_n cos\theta_n$.

The perturbation velocities can then be derived as: $u = \frac{\partial\phi}{\partial x}$, $v = \frac{\partial\phi}{\partial y}$, $w = \frac{\partial\phi}{\partial z}$. Substituting the perturbation velocities and the Eggers wave pattern (Equation B.2) in the first term of the total drag (Equation B.1) leads to the final expression of the wave resistance:

$$R_w = \frac{1}{4}\rho g b \left\{ \left(\xi_0^2 + \eta_0^2\right)\left(1 - \frac{2\gamma_0 h}{sinh(2\gamma_0 h)}\right) + \sum_{n=1}^{M}\left(\xi_n^2 + \eta_n^2\right)\left[1 - \frac{1}{2}cos^2\theta_n\left(1 + \frac{2\gamma_n h}{sinh(2\gamma_n h)}\right)\right]\right\} \tag{B.7}$$

In deep water (if $\frac{h}{\lambda} \leq 1.2$), since $\lim_{h\to+\infty} sinh(h) = \infty$, the wave resistance expression reduces to:

$$R_w = \frac{1}{4}\rho g b \left[\left(\xi_0^2 + \eta_0^2\right) + \sum_{n=1}^{M} \left(\xi_n^2 + \eta_n^2\right) \left(1 - \frac{1}{2} cos^2\theta_n\right) \right] \tag{B.8}$$

B.2 Wave resistance from experimental wave cuts

Equation B.7 for the wave resistance can be solved once the Eggers coefficients ξ_n and η_n, the wave number, γ_n, and the wave angle θ_n are found. They can all be found from a wave cut method. The elevation of the wave pattern is measured with wave probes made of two stainless wires. The conductivity between air and water is significant enough that a change in voltage output can be measured as the water surface deforms. A numerical wave profile is fitted through each experimental wave cut and the matrix method developed by Insel (1990) can be used to determine the Eggers coefficient ξ_n and η_n. The wave number γ_n, and the wave angle θ_n are obtained by solving Equations B.4 and B.5. The full wave pattern is now defined and the wave resistance of the model can be evaluated.

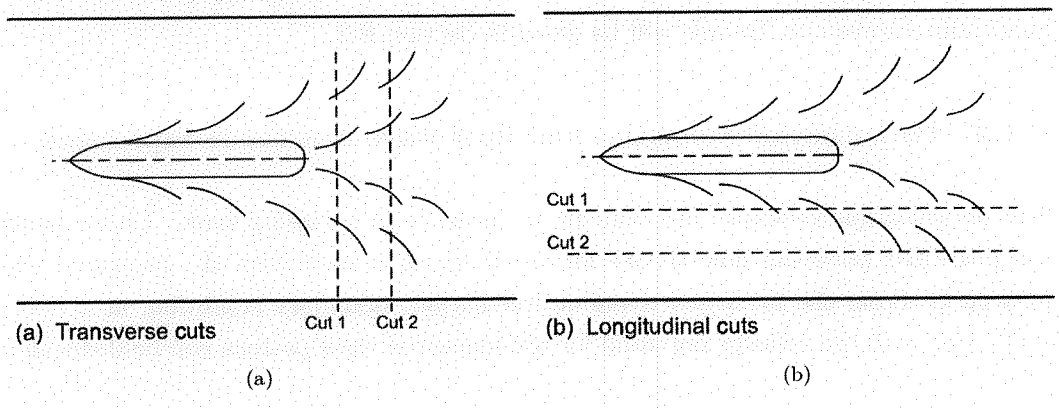

FIGURE B.3: Experimental methods to get wave resistance for a ship (Molland et al., 2011).

There exists two different experimental wave cut methods, transverse and longitudinal, as shown in Figure B.3. Although the transverse cut method is theoretically more efficient since it is a finite cut, it is not a practical method. During towing tank tests, a gap needs to be left at the centre of the tank for the model to pass through. Alternatively, probes have been fixed to the moving carriage, but non-linear velocity effects caused problems.

On the other hand, the longitudinal wave cut method has long been used in towing tank testing. Theoretically, only one cut is required; but, in practice, up to four cuts are used

in order to eliminate the possible case of the term $cos\left(\frac{2\pi ny}{b}\right) \rightarrow 0$ for that n. Eggers et al. (1967) noted that the measurements must be made in the region where the effects of boundary layer and wake are negligibly small, since the derivation the wave resistance equation is based on the assumption that the fluid is inviscid and the flow is irrotational.

A major problem with the longitudinal wave cut is to decide the start and end points of the wave cut to fit a numerical wave through. Degiuli et al. (2005) amongst others has emphasised the importance of the record length. If it is too short, the results dissipate; whereas if it is too long, the wave resistance decreases which has no physical sense.

The longitudinal wave cut method used was defined by Eggers (1955), developed by Insel (1990) and refined by Taunton (2013). In 'waveSis' (Taunton, 2013), the in-house software used to determine wave resistance, a specific methodology has been used. Several window traces are selected and the same number of harmonics is chosen for them all. The number of harmonics is set to a high enough value to reach convergence and kept low to achieve a minimum wave angle of 75°. The Fourier fit tolerance is first set high and then decreased until the wave resistance converges and a realistic wave energy distribution is obtained. As shown in Figure B.4, a typical wave pattern has most of its energy when the wave angle is lower than 35.3° and almost no energy past 75°. The process of adjusting the tolerance is repeated for each window trace. The wave resistance value kept is the one presenting the best Fourier fit.

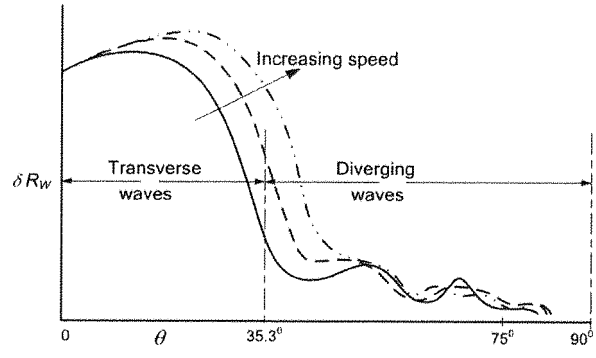

FIGURE B.4: Typical wave energy distribution (Molland et al., 2011).

C

Equipment Testing Results

This appendix includes the statistical analyses performed for each athlete tested during the British Swimming equipment tests (Testing sessions # 20 and # 21) and the Speedo equipment tests (Testing session # 22). A statistical analysis comprises a bootstrap distribution with a 95% level of confidence interval and a permutation test.

C.1 British Swimming tests

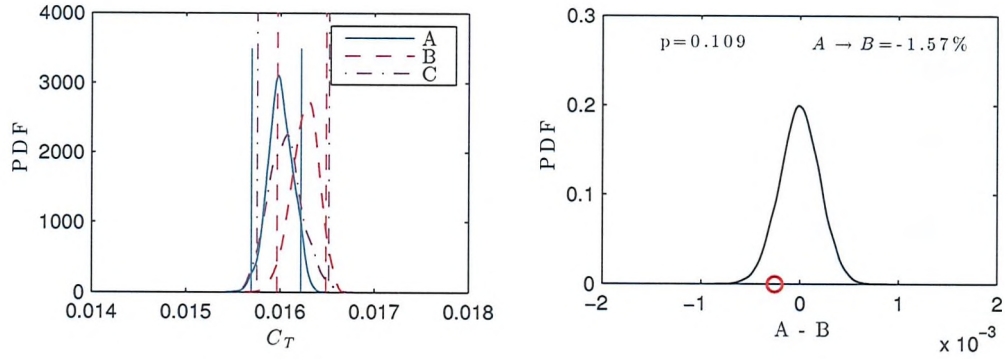

(a) Athlete BO

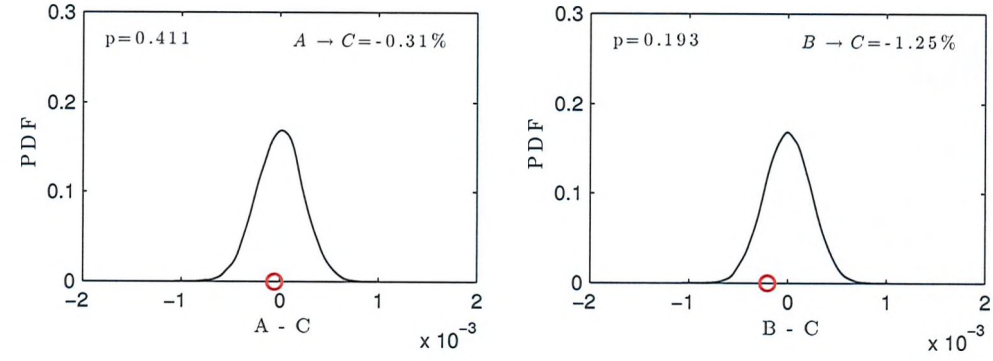

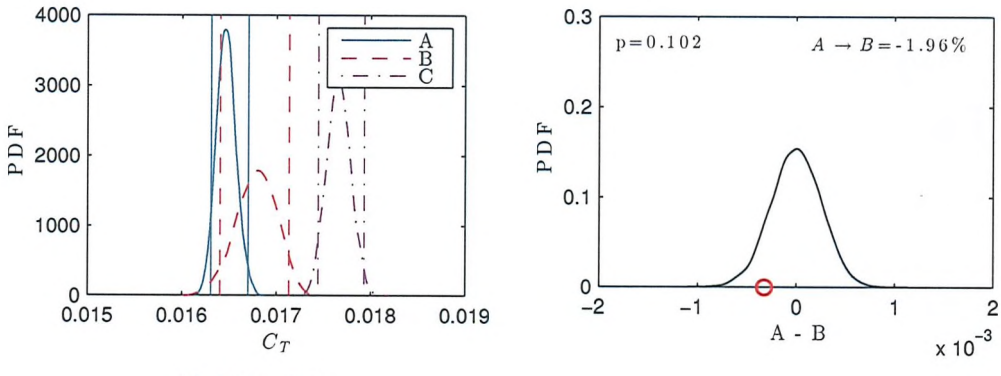

(e) Athlete DO

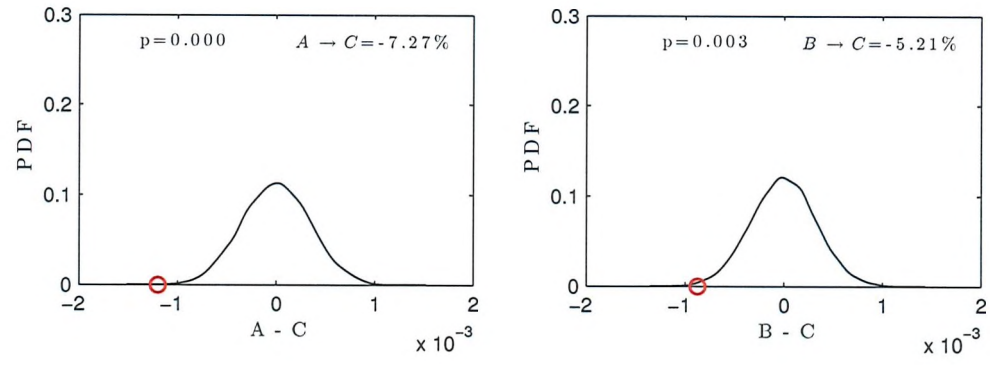

FIGURE C.1: British Swimming - Male open-water swimmers. o: True mean.

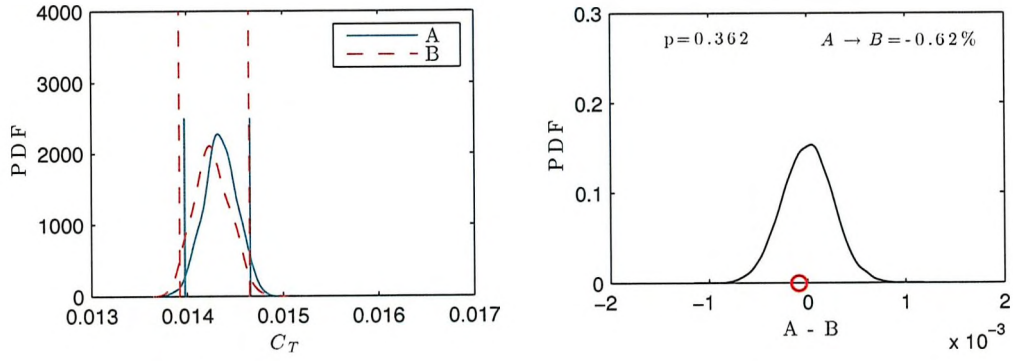

(a) Athlete DL

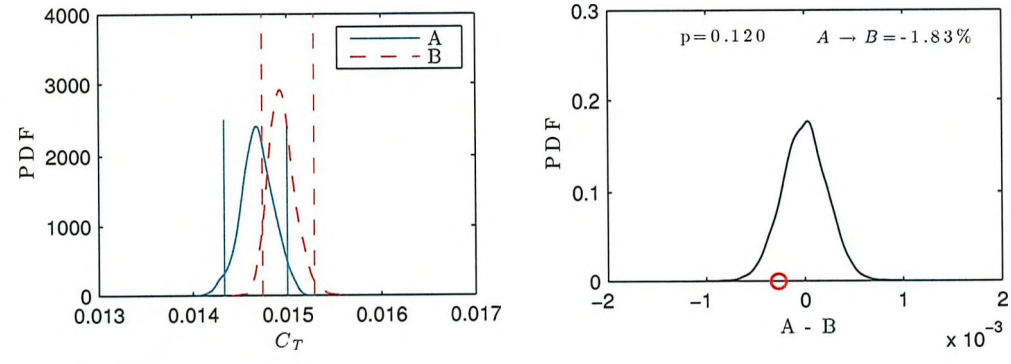

(c) Athlete W

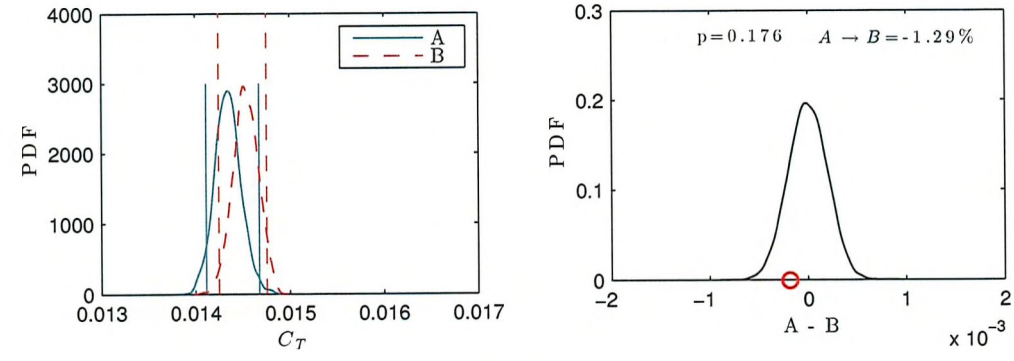

(e) Athlete BJ

FIGURE C.2: British Swimming - Male swimmers. o: True mean.

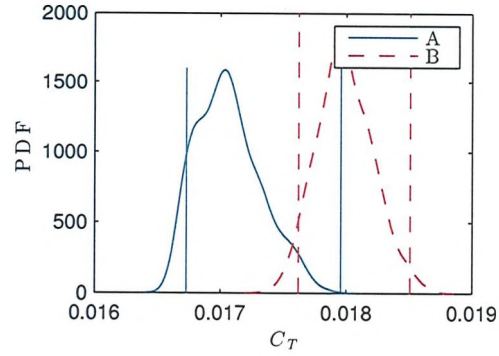

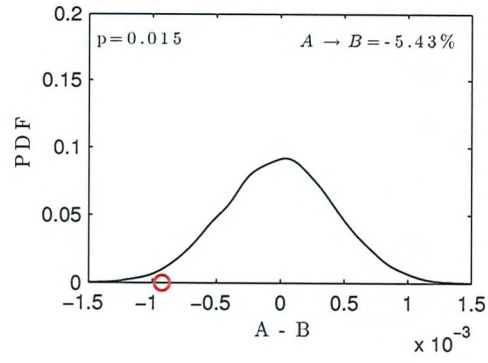

(a) Athlete BE

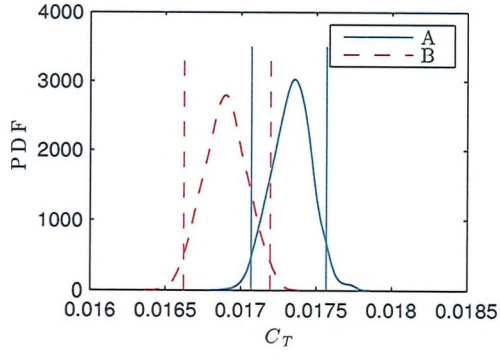

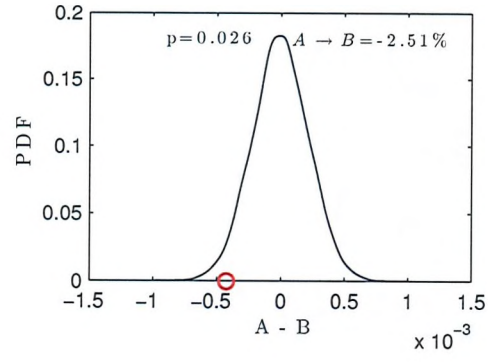

(c) Athlete AL

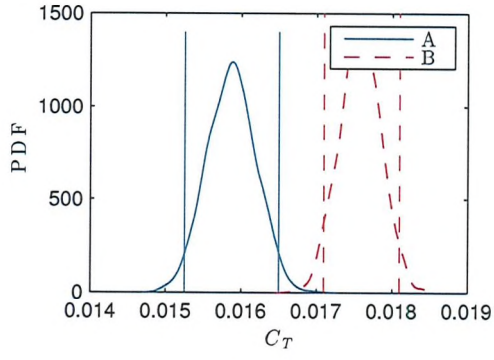

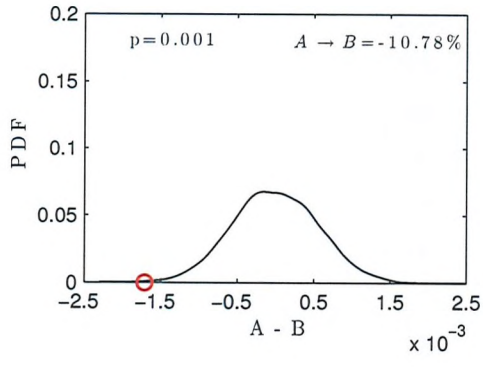

(e) Athlete AJ

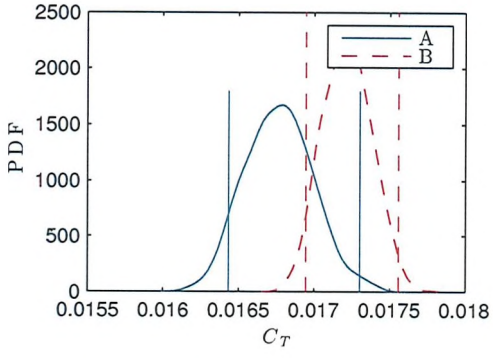

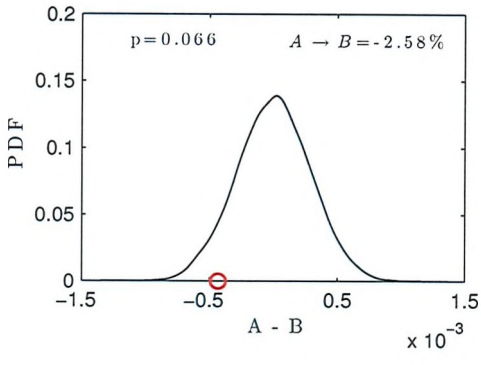

(g) Athlete DM

FIGURE C.3: British Swimming - Female swimmers (1). o: True mean.

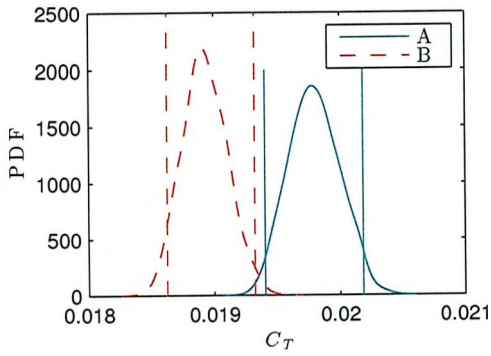

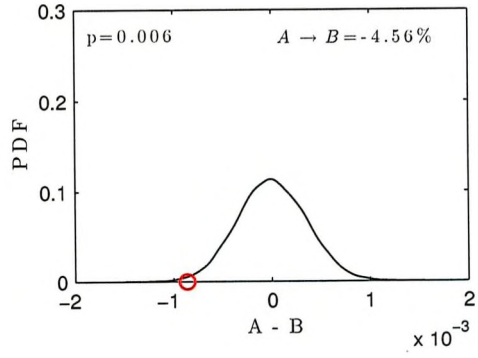

(a) Athlete AH

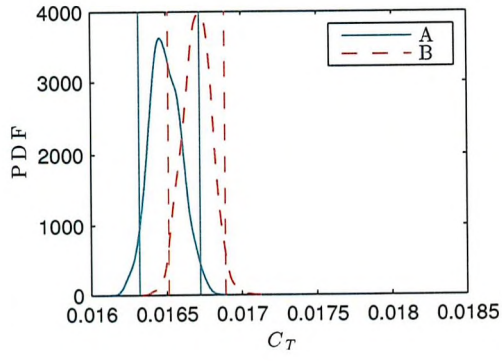

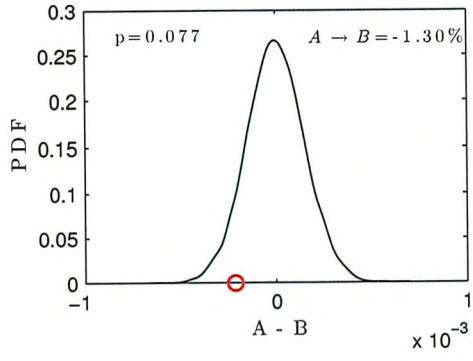

(c) Athlete G

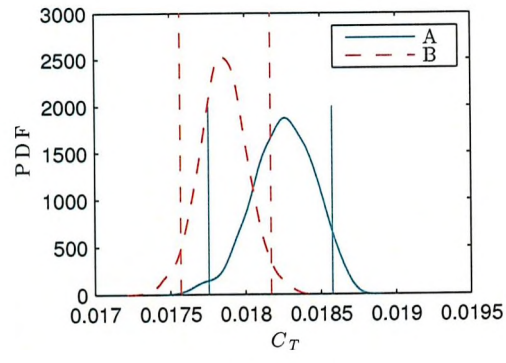

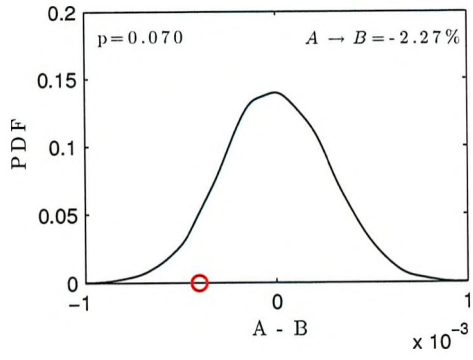

(e) Athlete BG

FIGURE C.4: British Swimming - Female swimmers (2). o: True mean.

C.2 Speedo tests

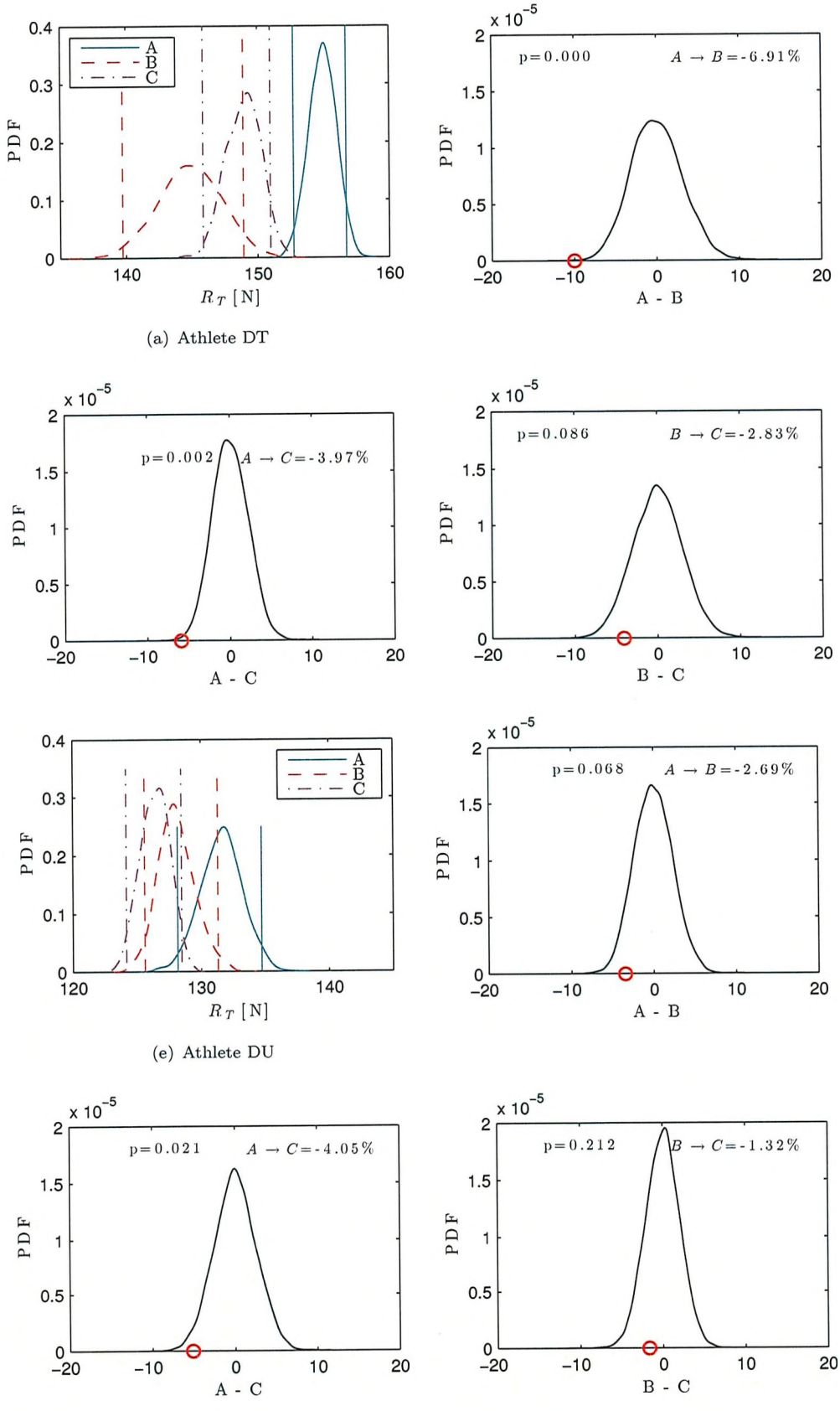

(a) Athlete DT

(e) Athlete DU

FIGURE C.5: Speedo - Male swimmers. o: True mean.

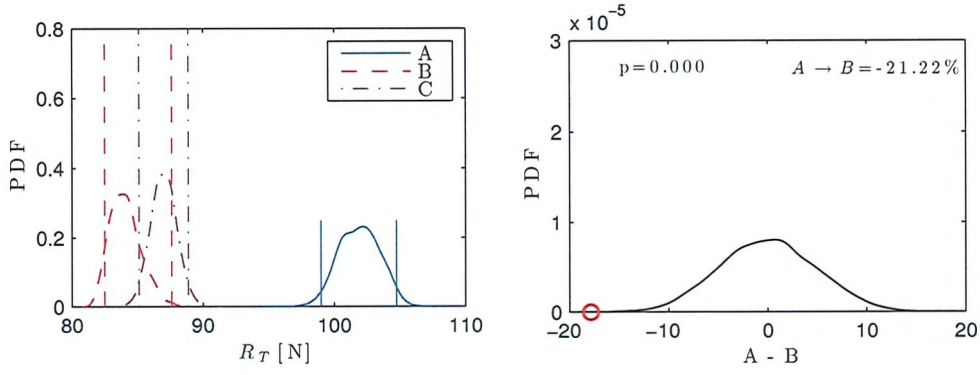

(a) Athlete DR

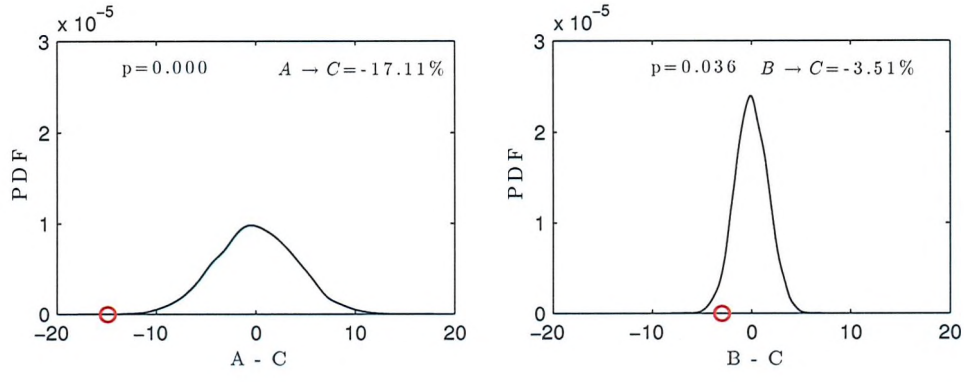

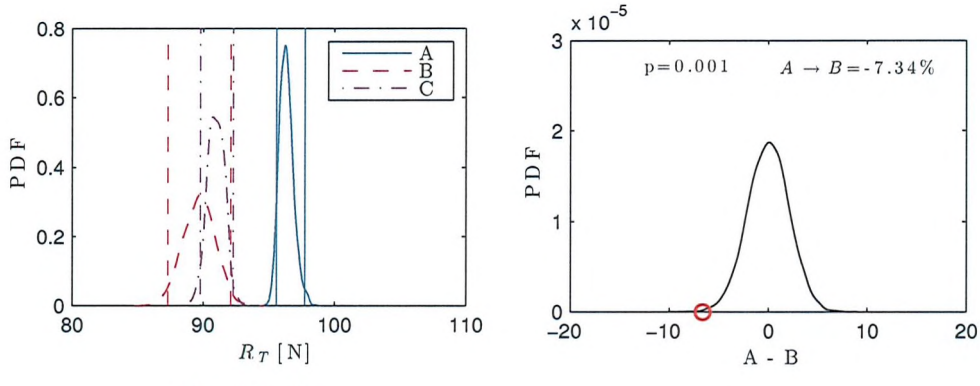

(e) Athlete DS

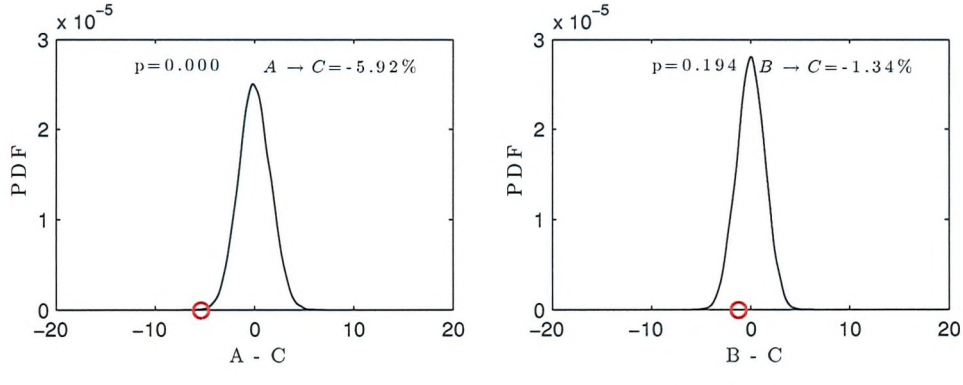

FIGURE C.6: Speedo - Female swimmers. o: True mean.

D

Sphere
Supplementary materials

In the first section of this appendix (Section D.1), photographs taken from both an above- and a side-water camera are included. Matrices of these photographs are generated for each configuration tested. Videos from which the top-view photographs are extracted from are available via individual QR codes.

In the second second of this appendix (Section D.2), an uncertainty analysis based on the recommended ITTC Procedure 7.5-02-02-02 for towing tank resistance tests (ITTC, 2014) is presented for Test #6.

D.1 Media

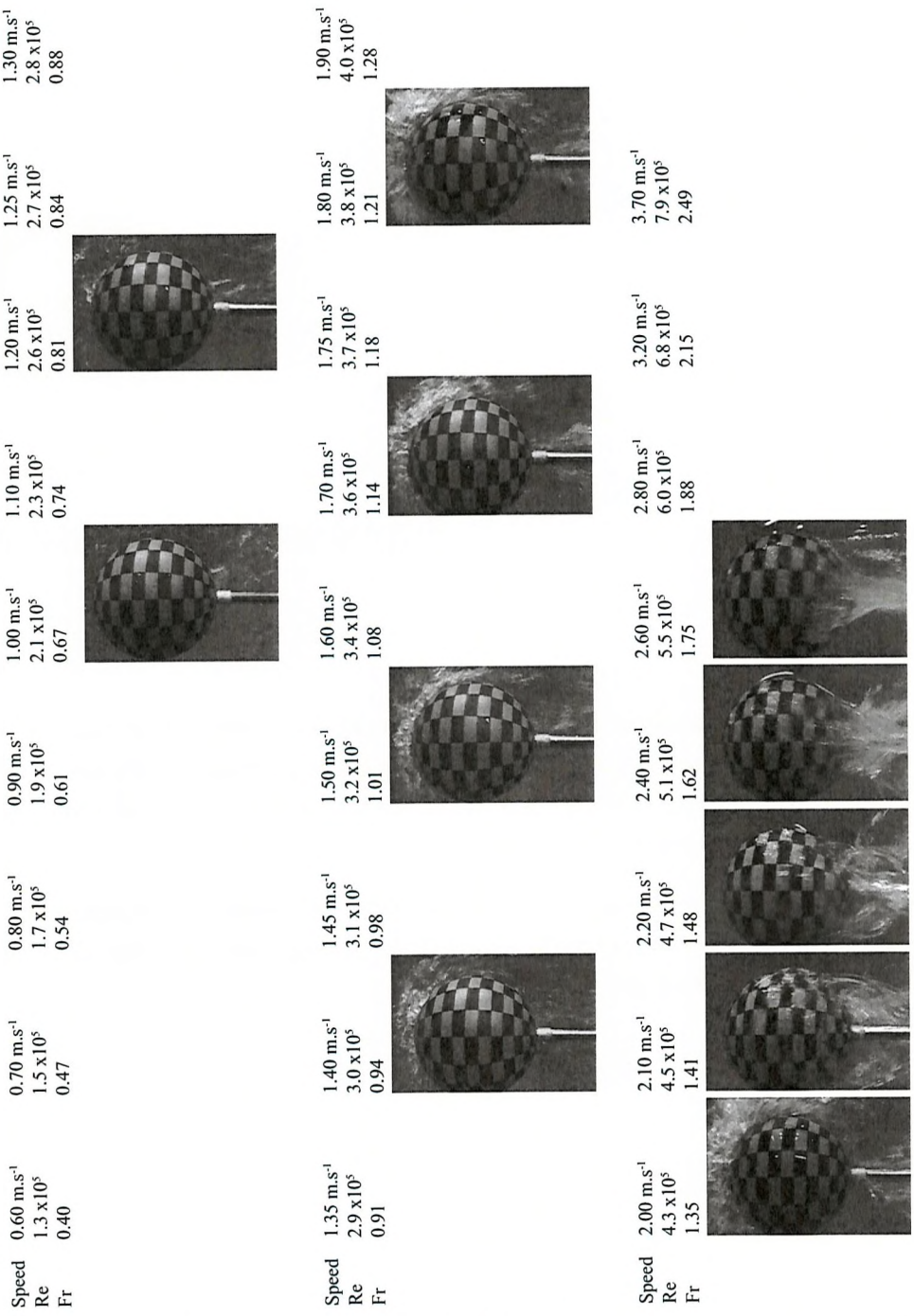

FIGURE D.1: Configuration 25% D_1 - Matrix of photographs taken from an above-water camera.

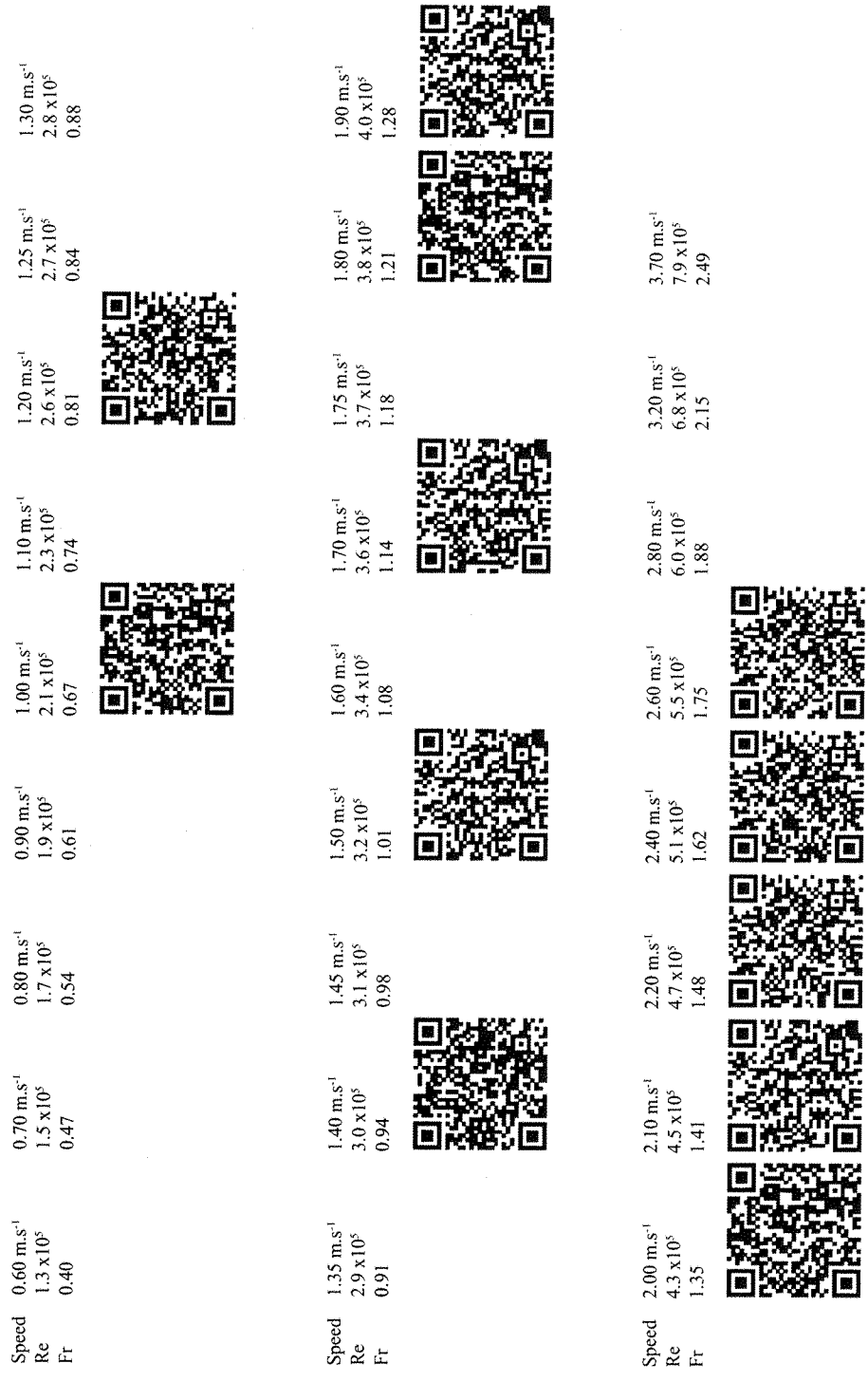

FIGURE D.2: Configuration 25% D_1 - Matrix of QR codes linked to videos of photographs displayed on Figure D.1 (James, 2017).

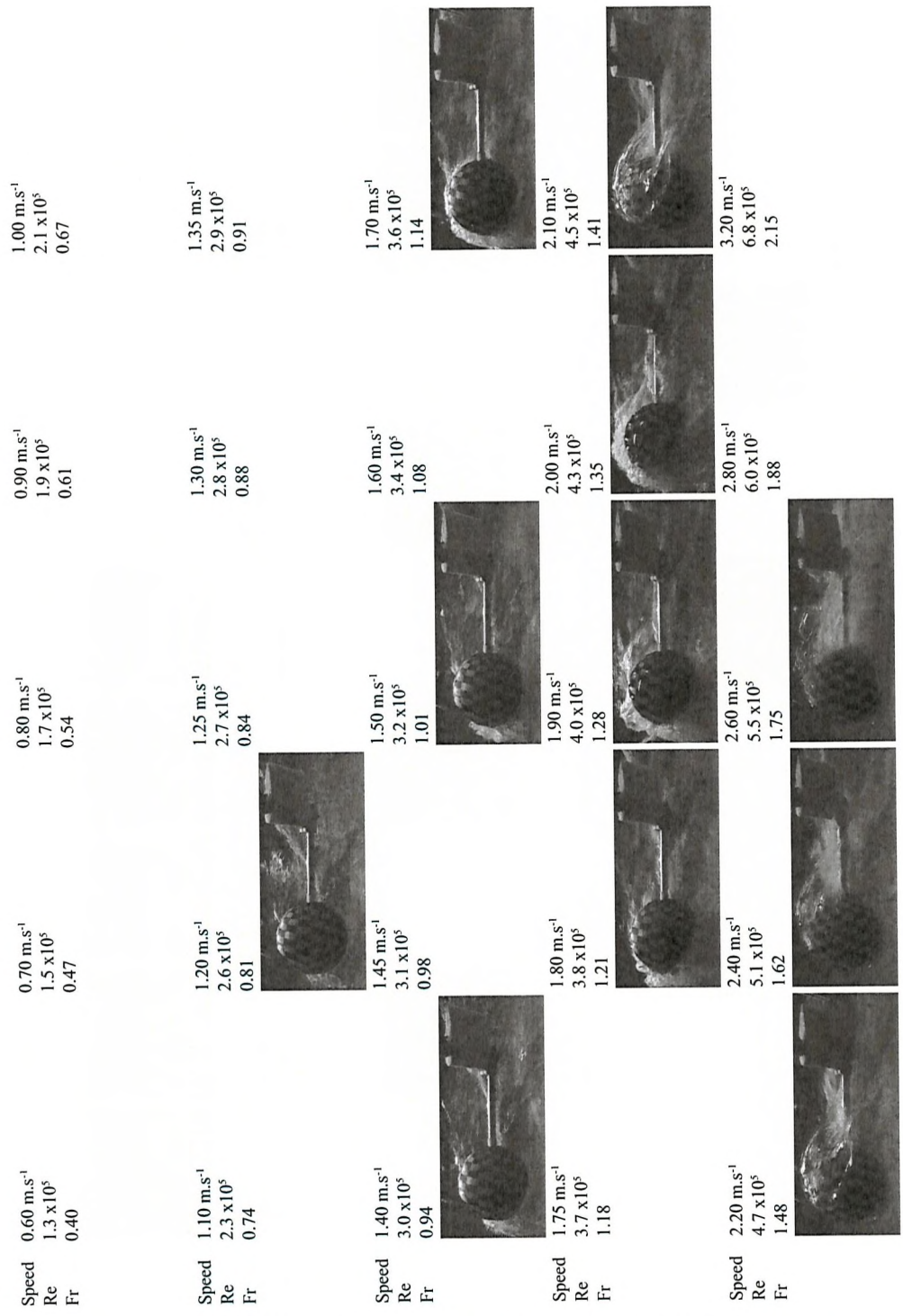

FIGURE D.3: Configuration 25% D_1 - Matrix of photographs taken from a side camera.

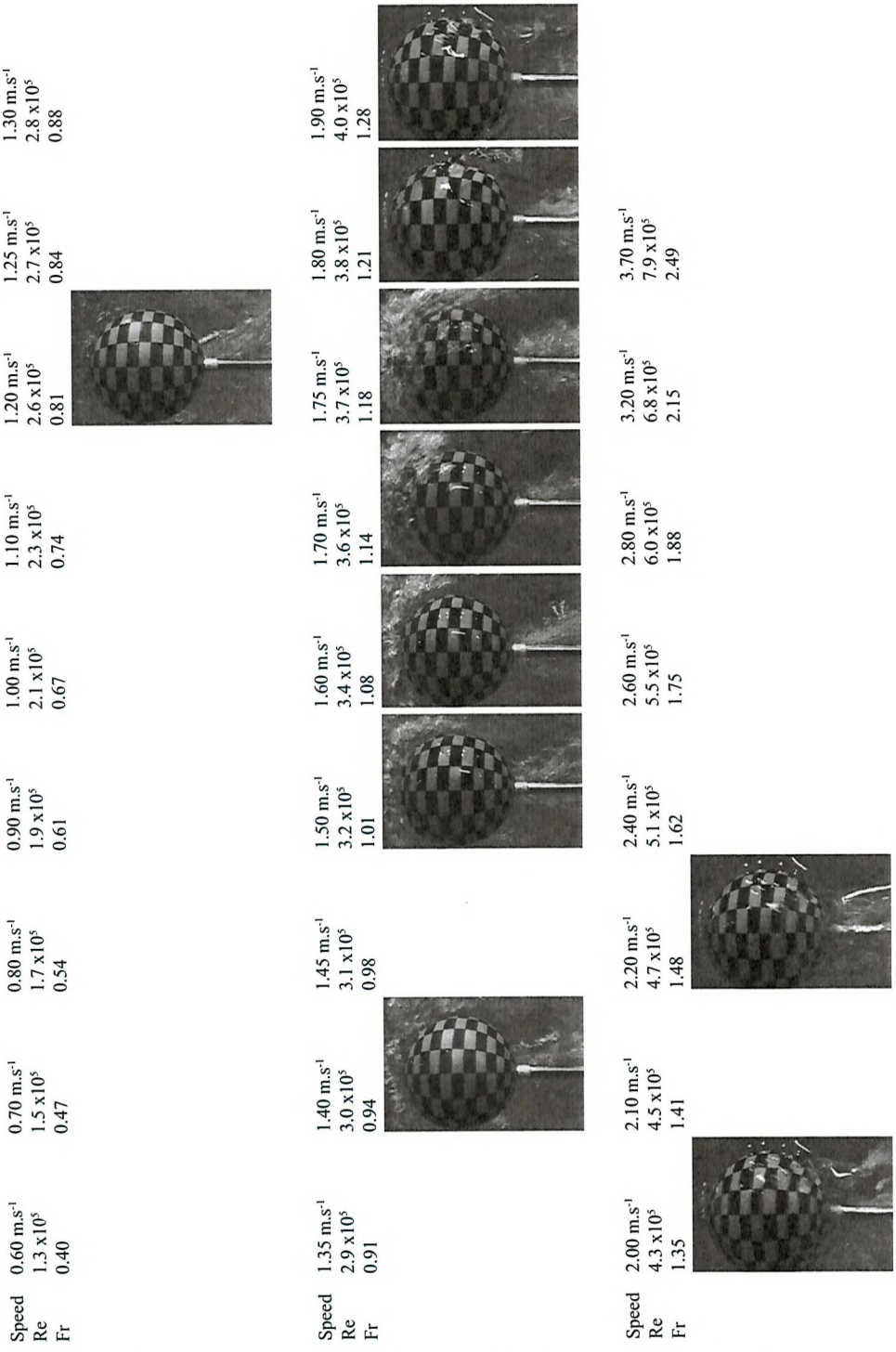

FIGURE D.4: Configuration 40% D_1 - Matrix of photographs taken from an above-water camera.

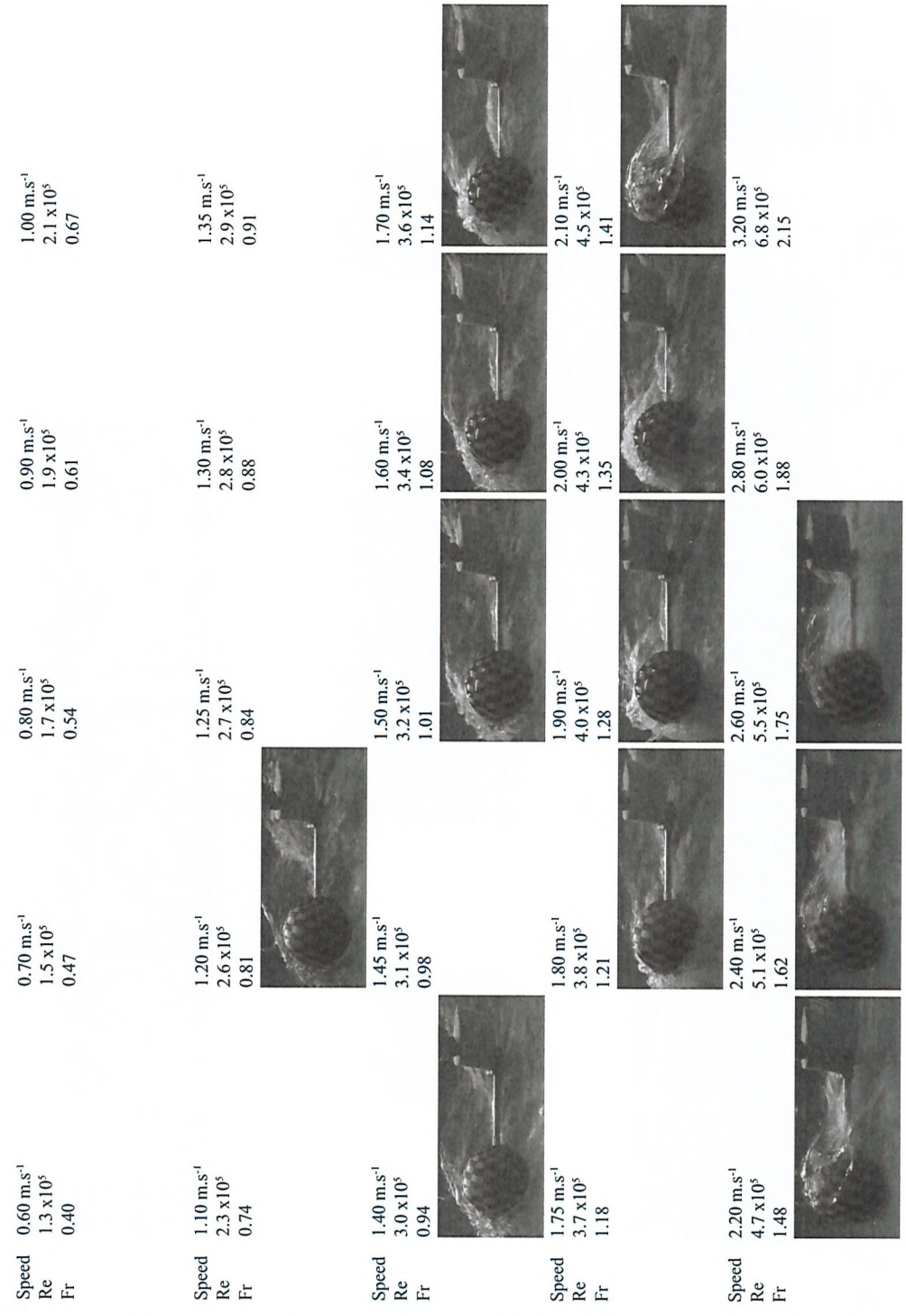

FIGURE D.5: Configuration 40% D_1 - Matrix of photographs taken from a side camera.

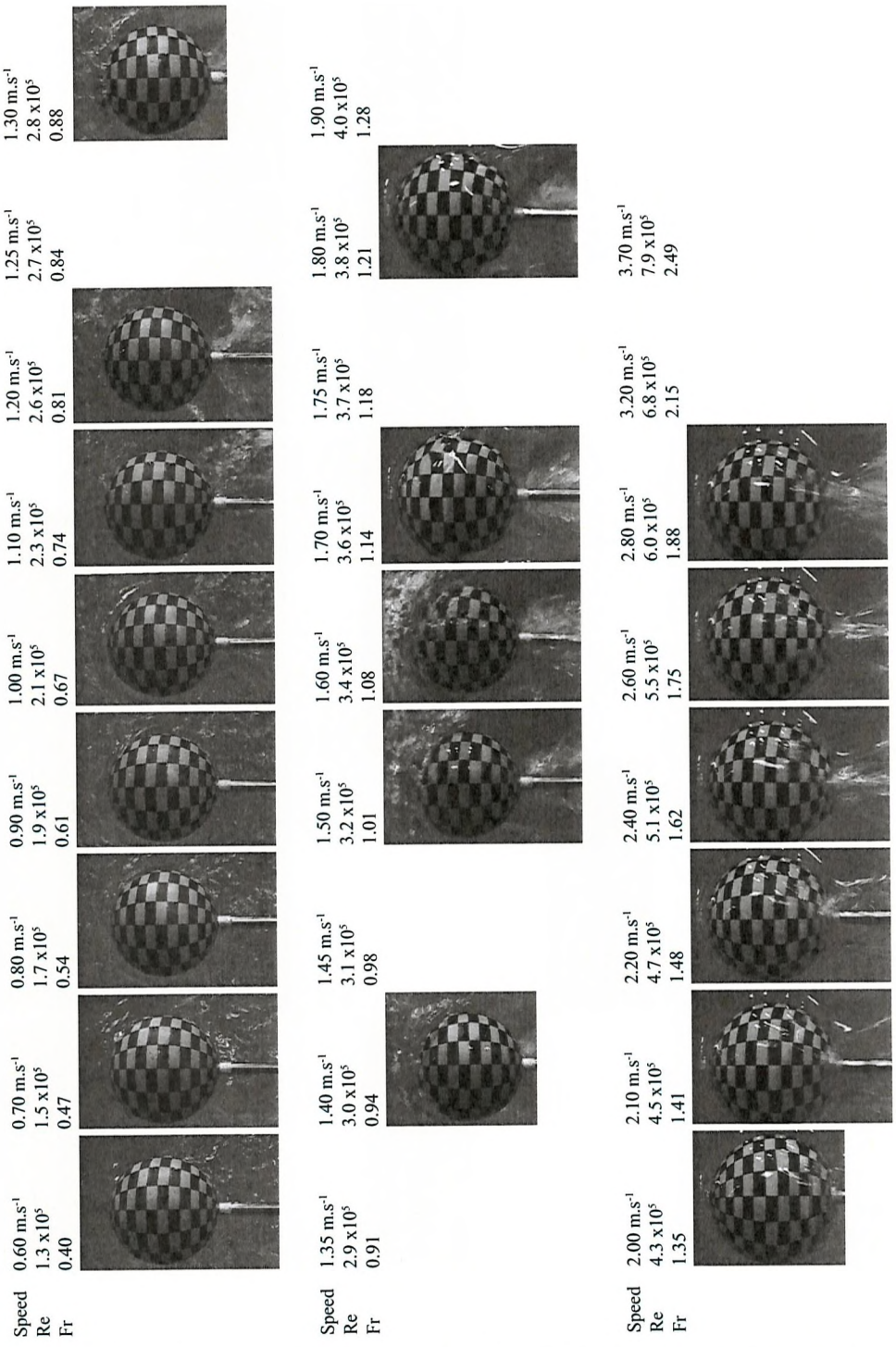

FIGURE D.6: Configuration 50% D_1 - Matrix of photographs taken from an above-water camera.

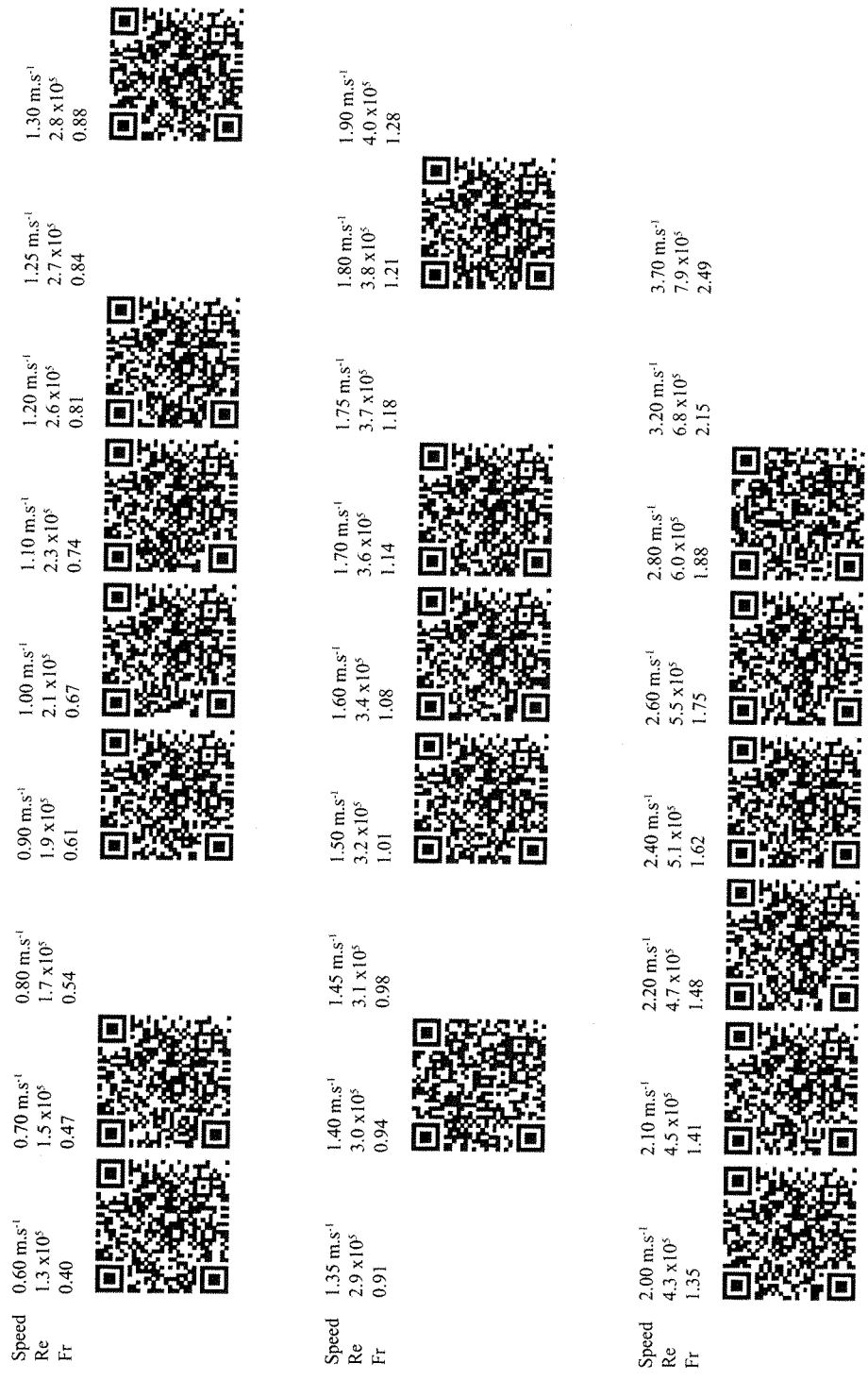

FIGURE D.7: Configuration 50% D_1 - Matrix of QR codes linked to videos of photographs displayed on Figure D.6 (James, 2017).

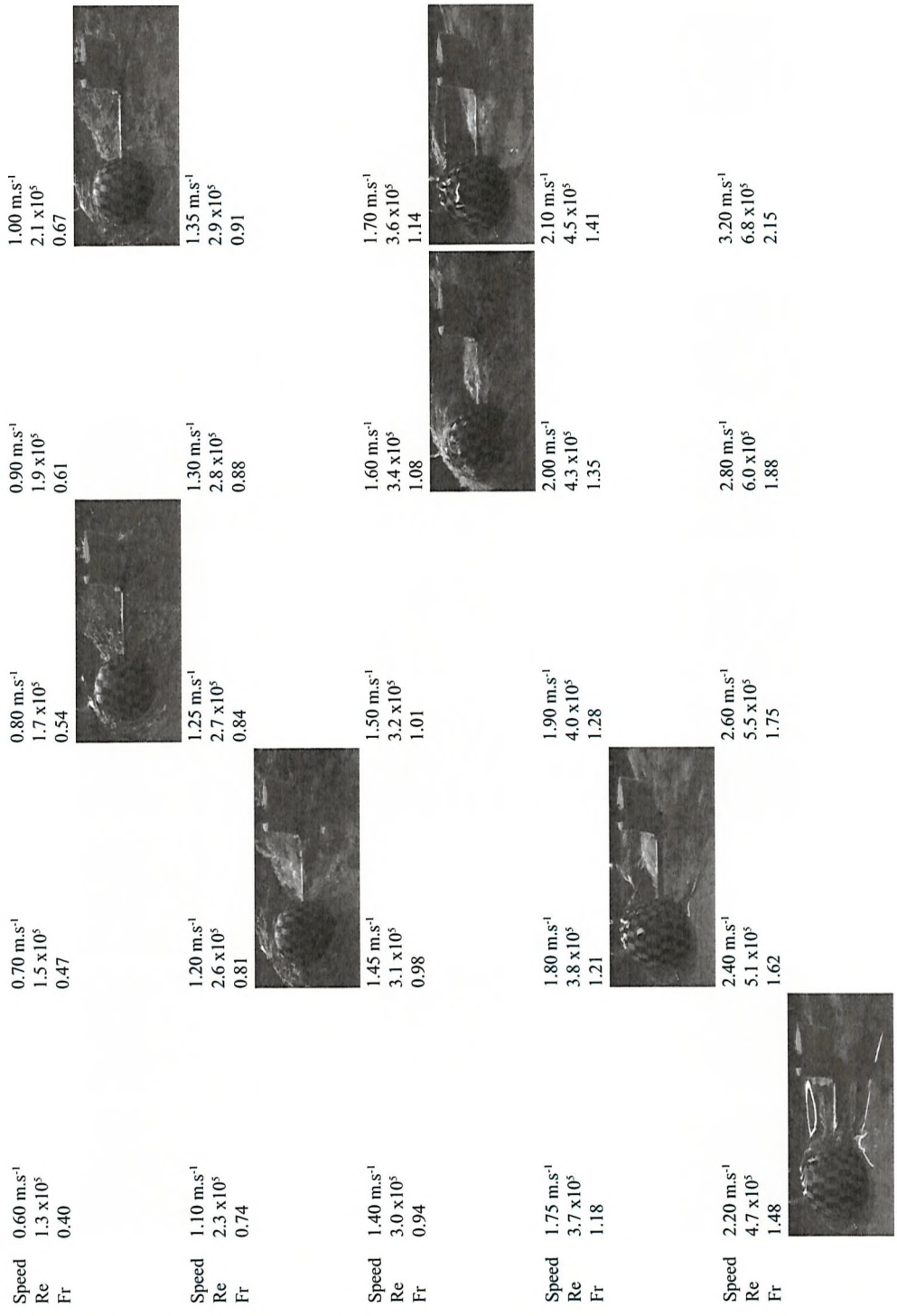

FIGURE D.8: Configuration 50% D_1 - Matrix of photographs taken from a side camera.

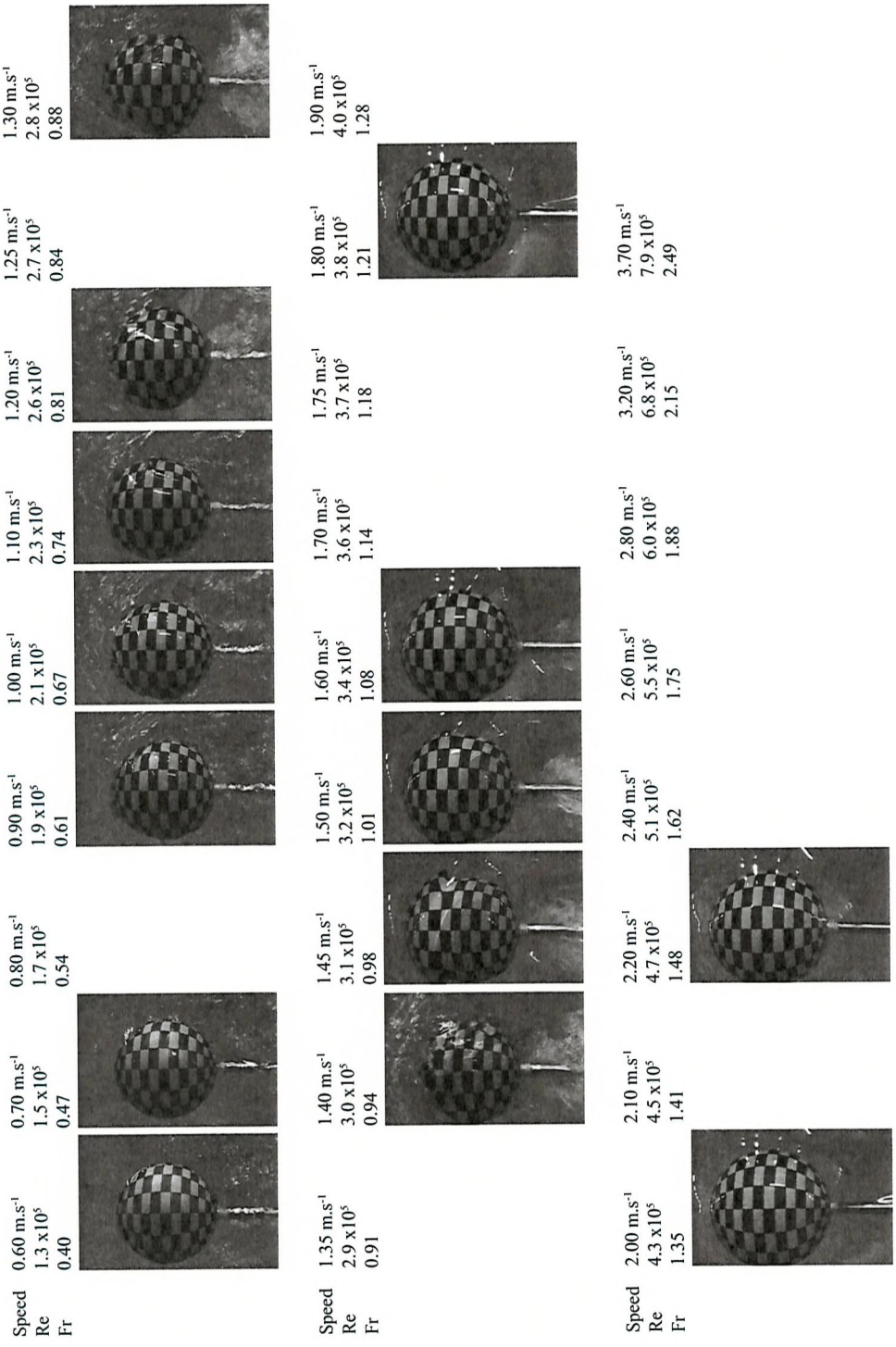

FIGURE D.9: Configuration 75% D_1 - Matrix of photographs taken from an above-water camera.

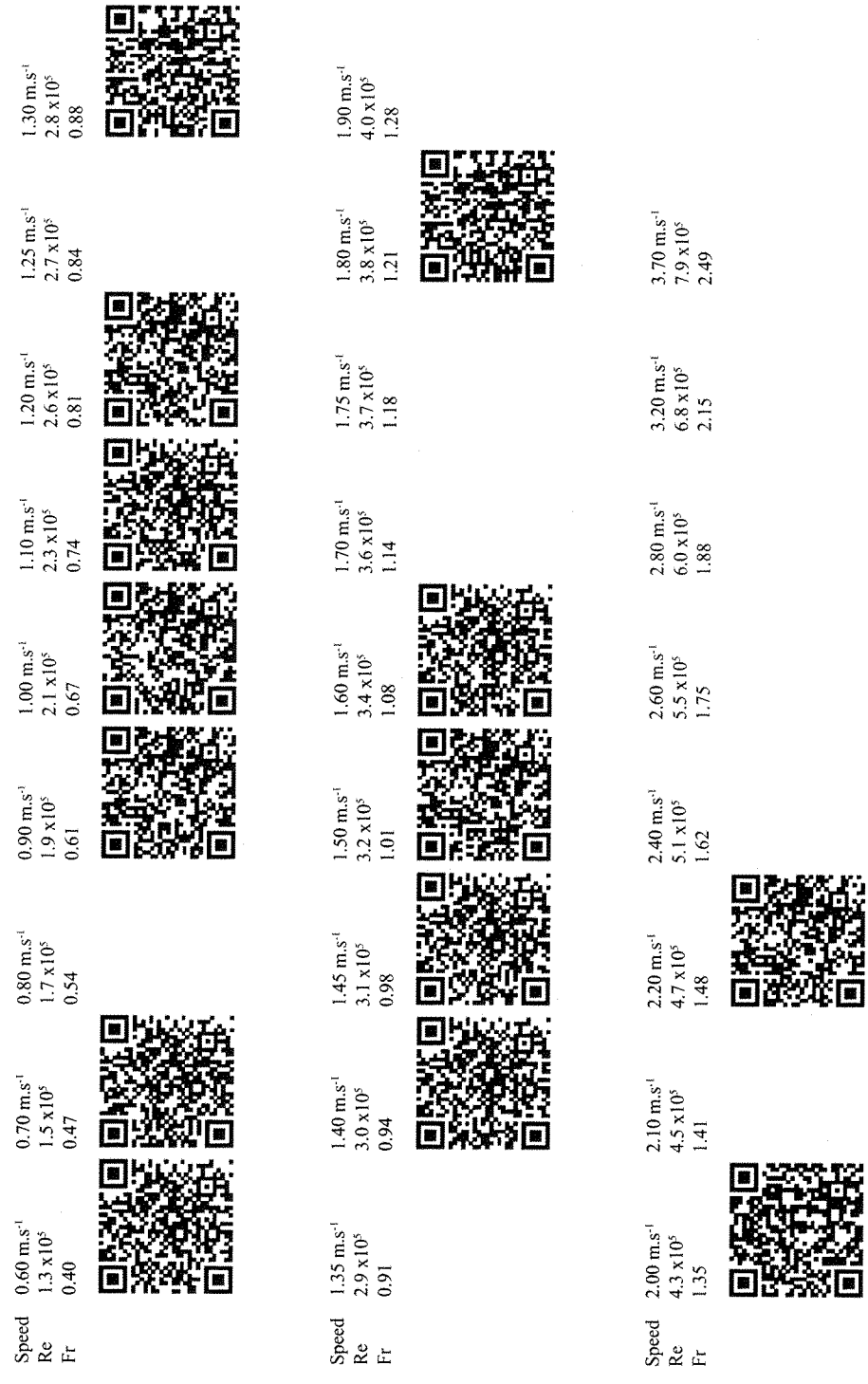

FIGURE D.10: Configuration75% D_1 - Matrix of QR codes linked to videos of photographs displayed on Figure D.9 (James, 2017).

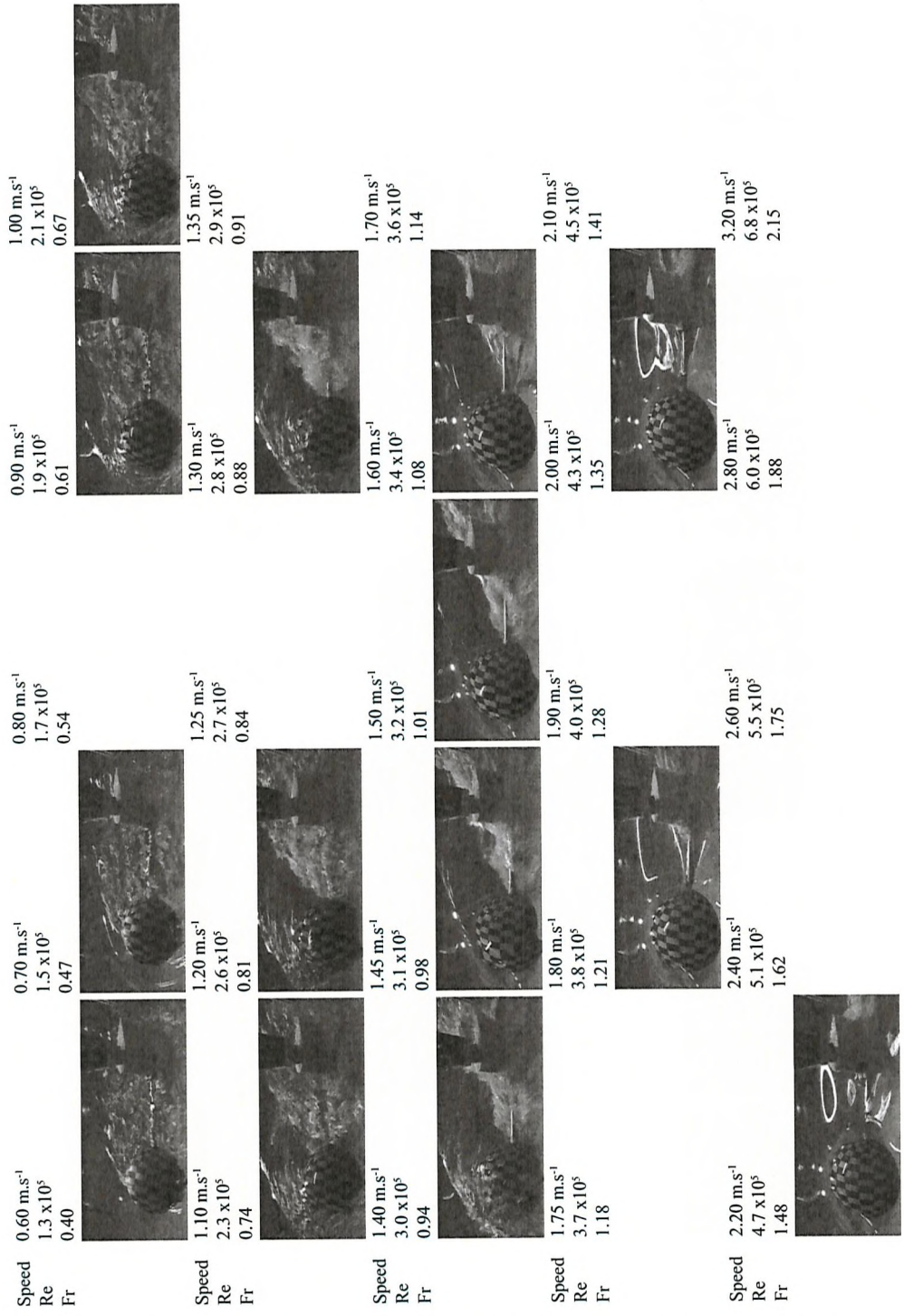

FIGURE D.11: Configuration 75% D_1 - Matrix of photographs taken from a side camera.

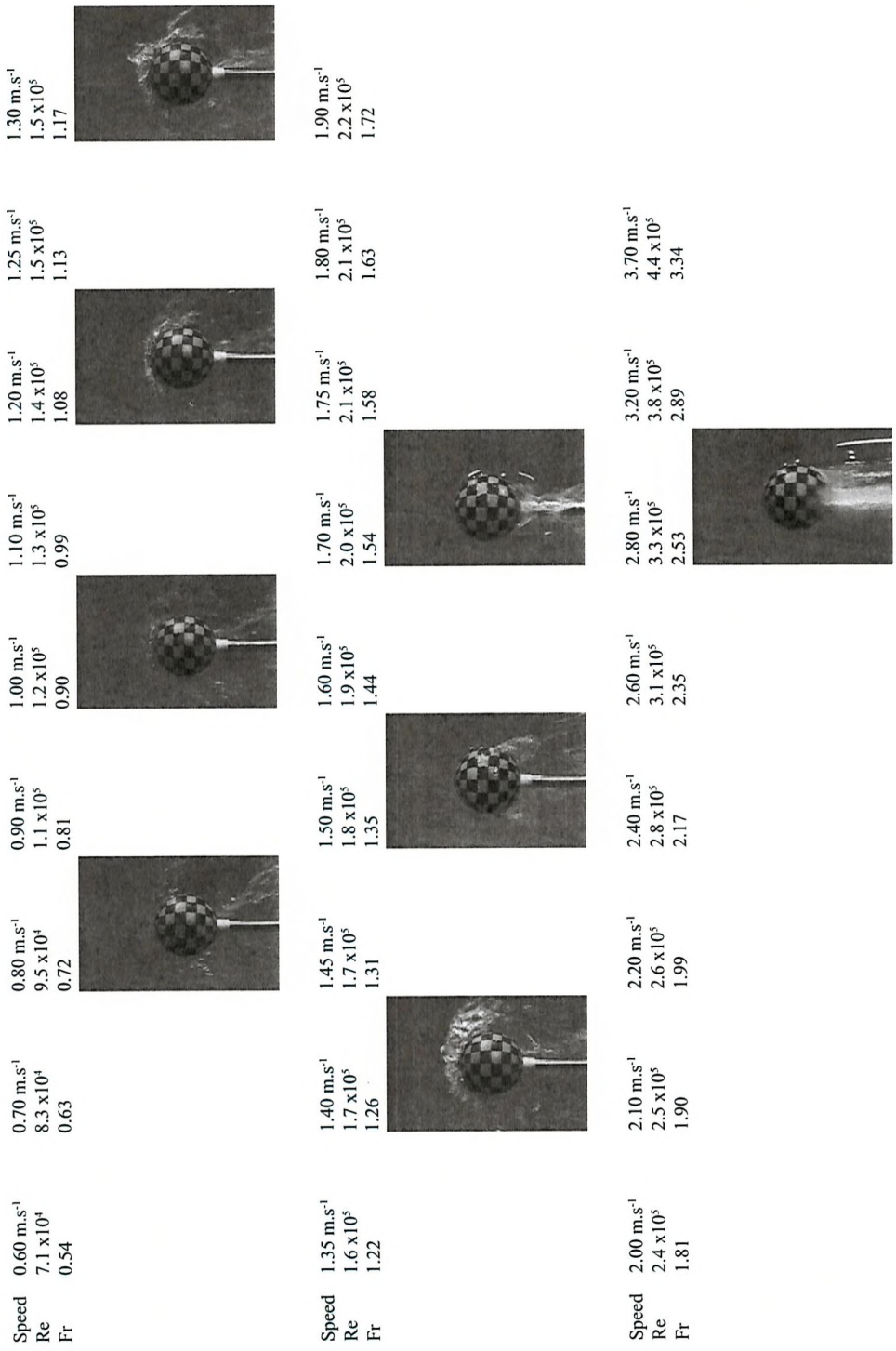

FIGURE D.12: Configuration 25% D_2 - Matrix of photographs taken from an above-water camera.

FIGURE D.13: Configuration 25% D_2 - Matrix of QR codes linked to videos of photographs displayed on Figure D.12 (James, 2017).

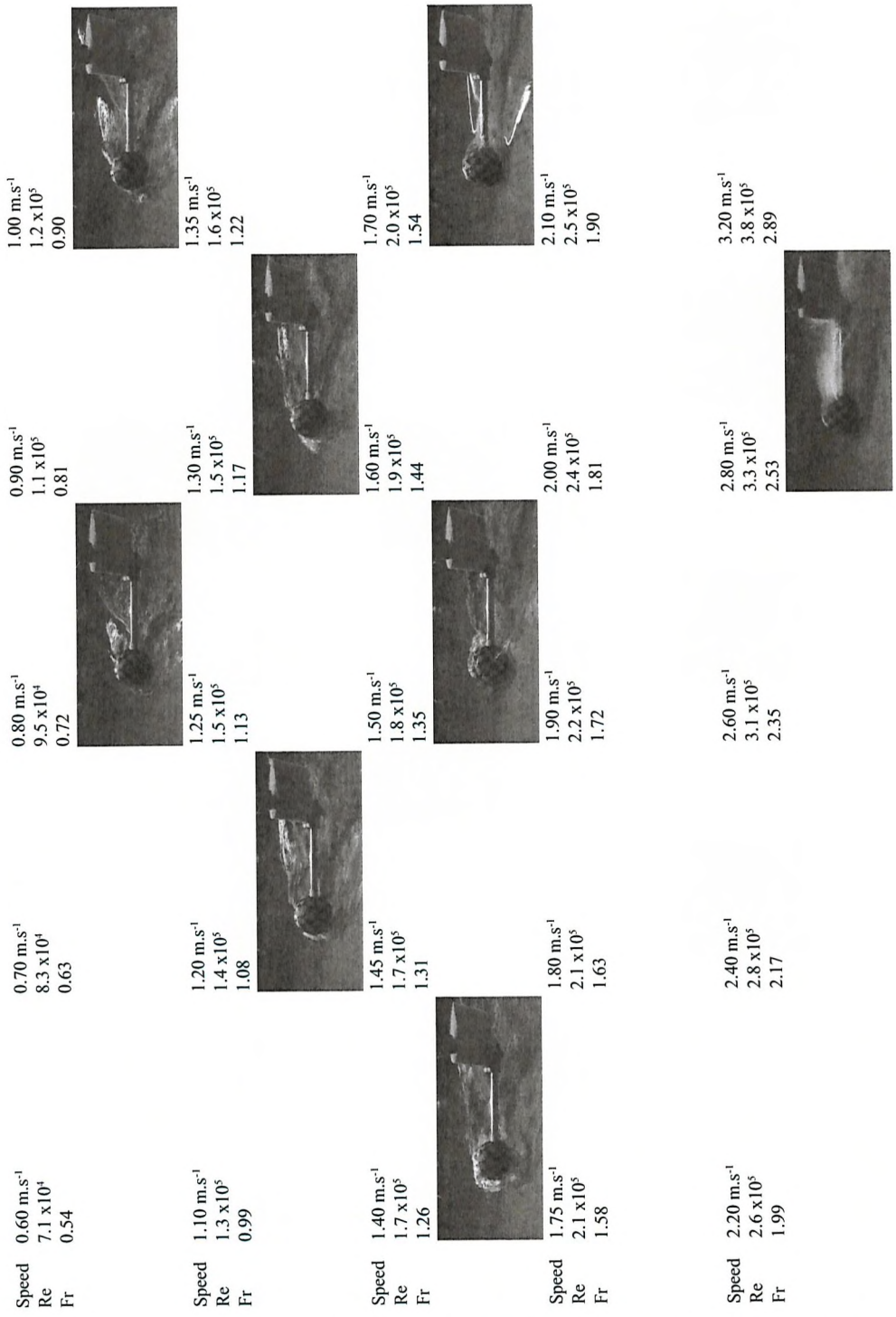

FIGURE D.14: Configuration 25% D_2 - Matrix of photographs taken from a side camera.

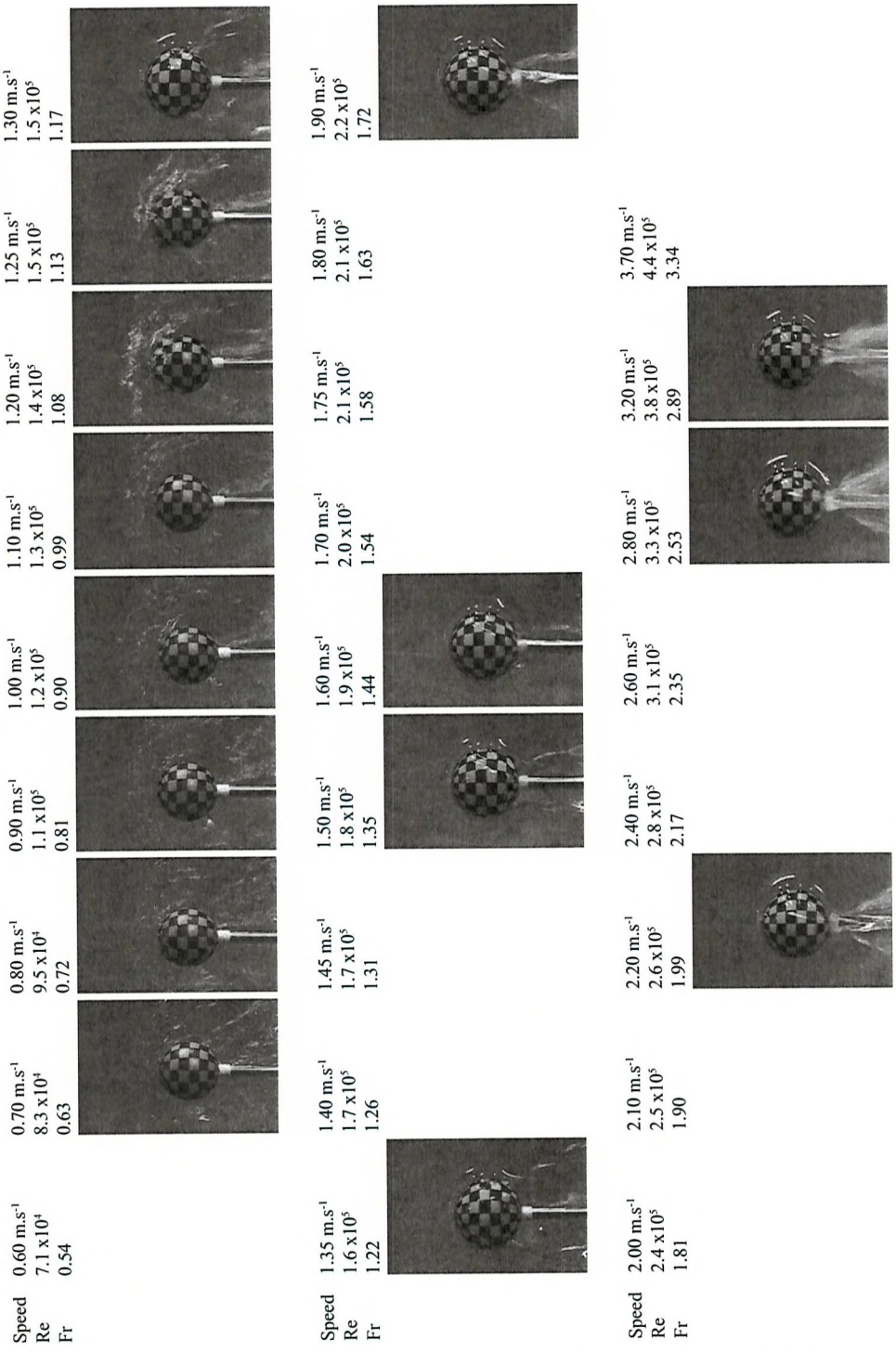

FIGURE D.15: Configuration 50% D_2 - Matrix of photographs taken from an above-water camera.

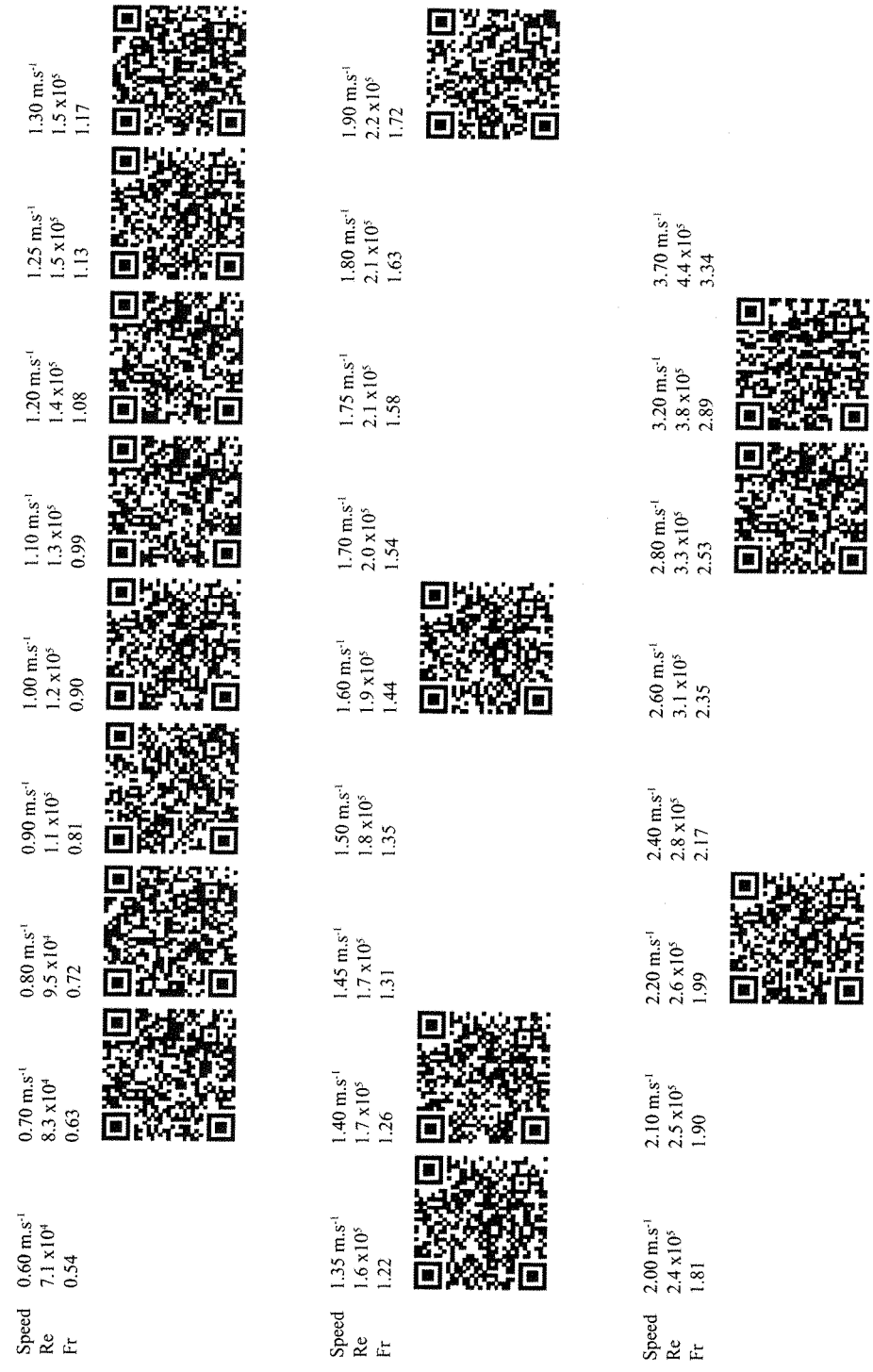

FIGURE D.16: Configuration 50% D_2 - Matrix of QR codes linked to videos of photographs displayed on Figure D.15 (James, 2017).

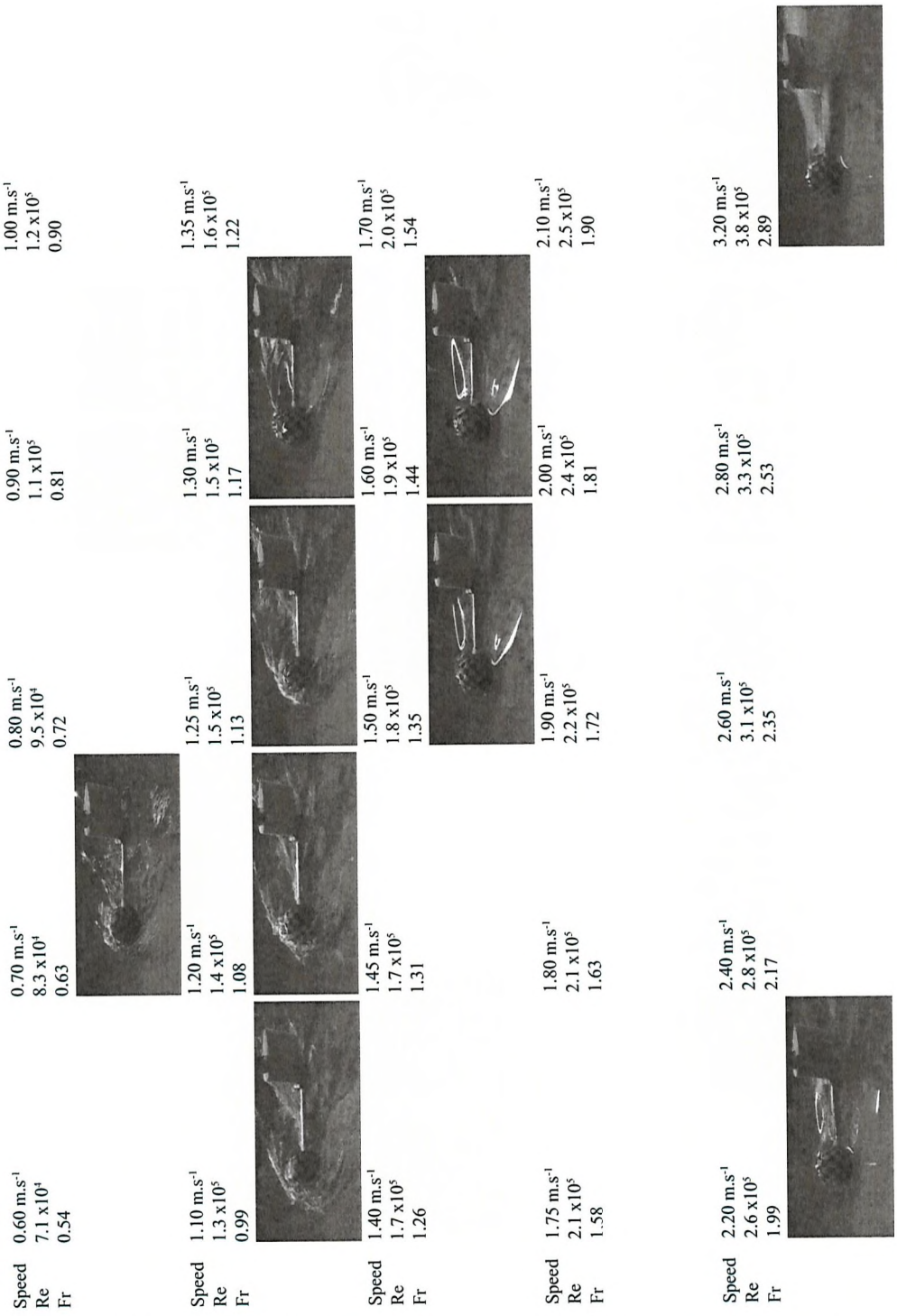

FIGURE D.17: Configuration 50% D_2 - Matrix of photographs taken from a side camera.

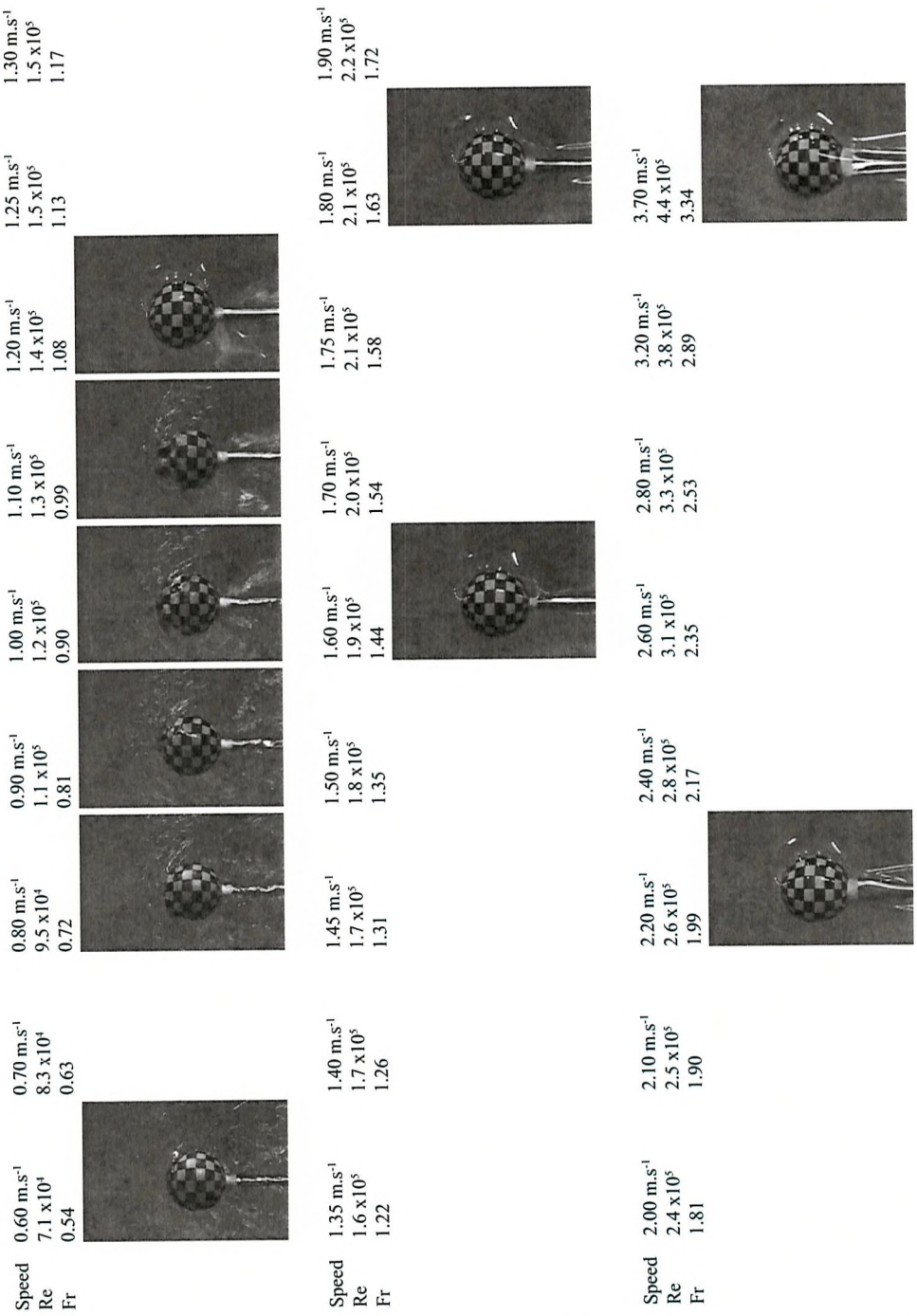

FIGURE D.18: Configuration 75% D_2 - Matrix of photographs taken from an above-water camera.

FIGURE D.19: Configuration 75% D_2 - Matrix of QR codes linked to videos of photographs displayed on Figure D.18 (James, 2017).

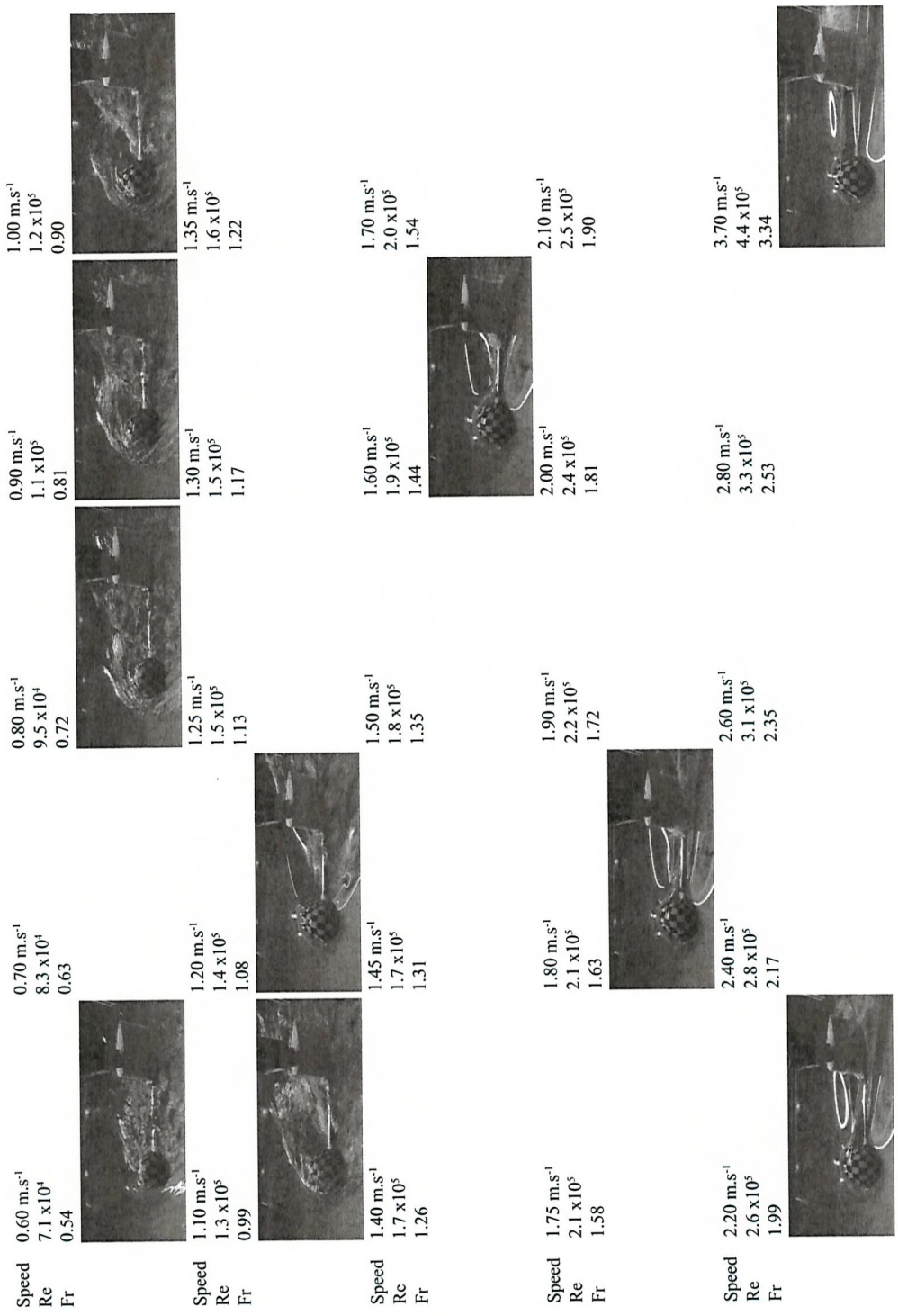

FIGURE D.20: Configuration 75% D_2 - Matrix of photographs taken from a side camera.

D.2 Uncertainty analysis for the towing tank Test # 6

An uncertainty analysis on the main reported data, the drag coefficient C_{F_D}, is undertaken as recommended in the ITTC Procedure 7.5-02-02-02 for towing tank resistance tests (ITTC, 2014). Sources of error may come from the model manufacturing, the model installation, the carriage speed, the tank water temperature and errors in the data acquisition system. The analysis based on a conservative approach is broken down in the following sections.

D.2.1 Model installation

The uncertainties on the total resistance associated with the installation procedure are due to the uncertainty in the wetted surface area and the alignment of the sphere with the centreline of the tank.

The uncertainty associated with the wetted surface area is due to the installation of the sphere, based on the draught mark (25%, 50% or 75% of the diameter). The sphere was marked at a reference draught of 50%D, with a pen having a 0.8 mm nib. The alignment on this mark was established by eye with an estimated bias of ± 0.5 mm, resulting in a total bias of ± 1.3 mm on the draught. Using the spherical cap formula for the wetted surface area, $S = \pi D * T$, the bias on the wetted surface area can be established for both sphere diameters D_1 and D_2. Assuming a normal distribution, the relative standard uncertainty on the wetted surface area, and thus on the total resistance can be derived and is summarised in table D.1 for each configuration.

TABLE D.1: Relative standard uncertainties on the total resistance due to model installation.

Immersion depth (%D)	D1	D2
25%	0.8%	1.4%
40%	0.5%	0.9%
50%	0.4%	0.7%
75%	0.3%	0.5%
100%	0.2%	0.3%

The alignment of the sphere model with respect to the centreline of tank was done by eye and is estimated to have a bias of ± 5°. This misalignment leads to an uncertainty of ± 0.4% R_T.

The maximum combined standard uncertainty associated with the model installation is:

$$u_1'(R_T) = \sqrt{1.4^2 + 0.4^2} = 1.4 \tag{D.1}$$

D.2.2 Towing speed

The speed of the Solent carriage is set on a speed controller with a display resolution of 0.01 $m.s^{-1}$ (uniform distribution). The speed is calculated from the distance (50 feet = 15.24 m) over the time spent on a defined constant-speed portion. Assuming that a tape measurer and a clock have bias of ± 0.5 mm and ± 0.5 s, the resulting bias limit on the speed controller is 0.001 $m.s^{-1}$. The standard uncertainty on the speed controller will thus be:

$$u(U) = \sqrt{\left(\frac{\frac{0.01}{2}}{\sqrt{3}}\right)^2 + \left(\frac{0.001}{3}\right)^2} = 0.003 \quad m.s^{-1} \tag{D.2}$$

$$u_2'(R_T) = 2u_U' \tag{D.3}$$

- At 0.6 $m.s^{-1}$, $u_2'(R_T) = 1.0$
- At 3.6 $m.s^{-1}$, $u_2'(R_T) = 0.2$

D.2.3 Water temperature

The digital thermometer has a display resolution of 0.5° C (uniform distribution). According to its technical specification, the bias limit is quoted as 0.2° C (normal distribution). The readings of thermometer for water temperature will thus have a standard uncertainty of:

$$u(T) = \sqrt{\left(\frac{\frac{0.5}{2}}{\sqrt{3}}\right)^2 + \left(\frac{0.2}{3}\right)^2} = 0.159°C \tag{D.4}$$

With a recorded fresh water temperature of 18° C, the temperature deviation of 0.159° C will lead to a relative standard deviation, $u'(\nu)$, of 0.42% in the water kinematic viscosity. The corresponding component of uncertainty in resistance for each tow speed will be estimated by:

$$u_3'(R_T) = \frac{\frac{C_F}{C_T} * 0.87}{\log_{10} Re - 2} * u'(\nu) \tag{D.5}$$

With a maximum uncertainty associated with the water viscosity of $0.003\%R_T$ across all configurations tested, it is judged negligible.

D.2.4 Dynamometer for the drag force

The maximum drag force was measured as 32 N. According to the ITTC procedure 7.5-01-03-01, the dynamometer was calibrated over a range covering 1.5 times the maximum measured force. The calibration process involved weights ranging from 5 N up to 50 N, with an increment of 5 N. The calibration weights used are certified with a limit bias of 0.005%. The resulting standard uncertainty of 0.003% (normal distribution) in the drag measurement is negligible. The sphere models were tested over a period of six days. Several calibration procedure were undertaken. For each calibration procedure, a linear curve was fitted through the data points with a least-square method and the rate in [N/V] was obtained. The mean of the six rates obtained is taken as the reference rate for all runs. The coefficient of variation is 3.1%, and this will be used as the relative standard uncertainty on the resistance measurement due to the dynamometry. This uncertainty covers all the sources of error associated with the dynamometry: wiring, electrical noise, A/D bias errors, filtering, etc.

D.2.5 Repeatability

This set of tow-tank tests was aimed at learning as much as possible about the fluid mechanics of the flow around a sphere located at the free surface. The testing plan was thus set to run more configurations (different sphere diameters and immersion depths), rather than to perform a large amount of repeats for only a few conditions considering the limited amount of time available at the towing tank facility. Although repeatability is usually part of the dominating uncertainties in resistance, it cannot be evaluated for this set of tests. Only a few data points were repeated.

It is important to note that the repeatability of the system is still partially included in the standard uncertainty of the dynamometer since several calibration tests were performed throughout the testing week.

In addition, the repeat drag traces are presented in Figure D.21 to emphasise the good repeatability of the drag force acquisition during the four key flow regimes.

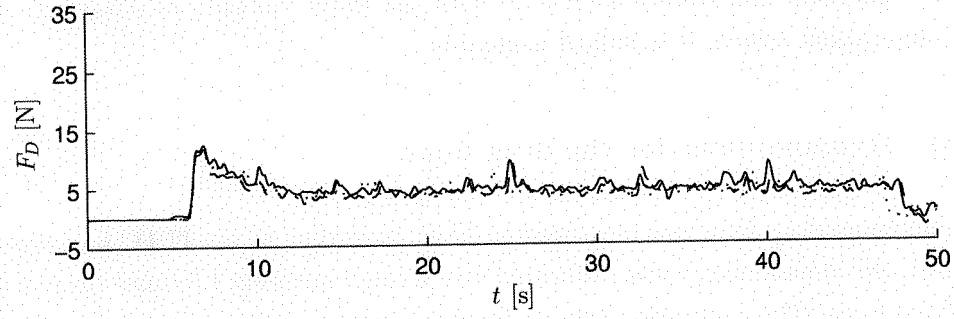

(a) Flow regime I, $Fr = 0.5$.

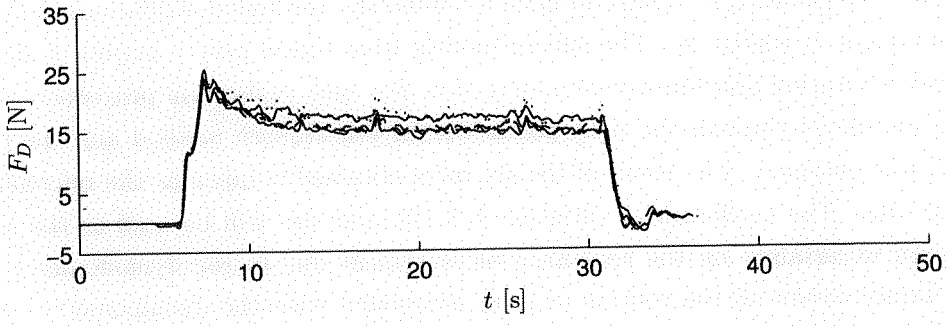

(b) Flow regime II, $Fr = 0.7$.

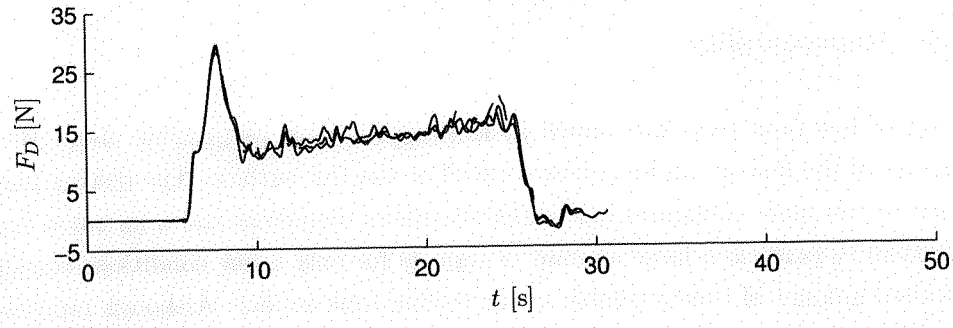

(c) Flow regime III, $Fr = 1.1$.

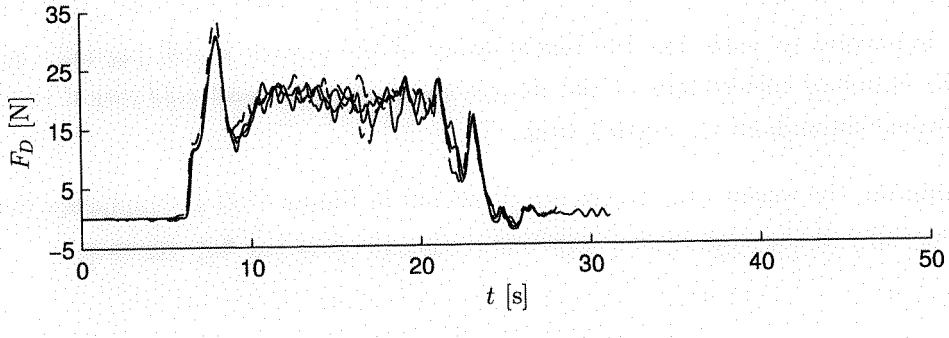

(d) Flow regime IV, $Fr = 1.5$.

FIGURE D.21: Drag traces of all the repeat runs for the four flow regimes studied.

D.2.6 Combination of uncertainty components

The two main types of uncertainty are coming from the model installation (1.4 %) and the dynamometer (3.1%). Using the Root-Sum-Square method, the maximum error is 3.4%.

References

Achenbach, E. (1972), 'Experiments on the flow past spheres at very high Reynolds numbers', *Journal of Fluid Mechanics* **54**(03), 565.

Achenbach, E. (1974*a*), 'The effects of surface roughness and tunnel blockage on the flow past spheres', *Journal of Fluid Mechanics* **65**(01), 113–125.

Achenbach, E. (1974*b*), 'Vortex shedding from spheres', *Journal of Fluid Mechanics* **62**(02), 209–221.

Aljallis, E., Sarshar, M. A., Datla, R., Sikka, V., Jones, A. and Choi, C. H. (2013), 'Experimental study of skin friction drag reduction on superhydrophobic flat plates in high Reynolds number boundary layer flow', *Physics of Fluids* **25**(2), 025103.

Bakic, V. and Peric, M. (2005), 'Visualisation of flow around sphere for Reynolds numbers between 22000 and 400000', *Thermophysics ad Aeromechanics* **12**(3), 307–315.

Bakic, V., Schmid, M. and Stankovi, B. (2006), 'Experimental investigations of turbulent structures', pp. 97–112.

Banks, J. (2013), Modelling the propelled resistance of a freestyle swimmer using Computational Fluid Dynamics, Ph.d. thesis, University of Southampton.

Behm, H. (2014), 'Review on swimming goggles'.
URL: *http://www.swimmingscience.net/review-on-swimming-goggles/*

Bergen, P. (2001), 'Coach Paul Bergen's tests of bodsuits'.
URL: *http://coachsci.sdsu.edu/swim/bodysuit/bergen.htm*

Berger, M., de Groot, G. and Hollander, A. (1995), 'Hydrodynamic drag and lift forces on human hand and arm models', *Journal of Biomechanics* **2**, 125–133.

Bixler, B., Pease, D. and Fairhurst, F. (2007), 'The accuracy of computational fluid dynamics analysis of the passive drag of a male swimmer', pp. 37–41.

Bixler, B. and Riewald, S. (2002), 'Analysis of a swimmer's hand and arm in steady flow conditions using computational fluid dynamics.', *Journal of biomechanics* **35**(5), 713–717.

Bixler, B. and Schloder, M. (1996), 'Computational fluid dynamics: An analytical tool for the 21st century swimming scientist', *Journal of Swimming Research* **11**, 4–22.

Blevins, R. (2001), *Flow-induced vibrations*, reprint ed edn, Krieger Publishing Company.

Boussinesq, J. (1877), 'Essai sur la theorie des eaux courantes', *23* **1**, 1–680.

Buckingham, E. (1914), 'On physically similar systems; illustrations of the use of dimensional equations', *Physical Review* **2-IV**(4), 345–376.

Bushby, K. M. D., Cole, T., Matthews, J. N. S. and Goodship, J. A. (1992), 'Centiles for adult head circumference', *Achives of Disease in Childhood* **67**(1), 1286–1287.

Chatard, J. C., Bourgoin, B. and Lacour, J. R. (1990), 'Passive drag is still a good evaluator of swimming aptitude', *European Journal of Applied Physiology and Occupational Physiology* **59**(6), 399–404.

Chung, C. and Nakashima, M. (2013), 'Development of a Swimming Humanoid robot for Research of Human Swimming', *Journal of Aero Aqua Bio-mechanisms* **3**(1), 109–117.

Clarys, J. P. (1979), 'Human morphology and hydrodynamics', *International Series on Sports Science - Swimming III* **8**, 3–41.

Clothier, P. (2004), Underwater kicking following the freestyle tumble turn, PhD thesis, University of Ballarat, Australia.

Cohen, R. C. Z., Cleary, P. W. and Mason, B. (2009), Simulation of human swimming using smoothed particle, *in* 'Seventh International Conference on CFD in the Minerals and Process Industries', number December, Melbourne, pp. 1–6.

Cohen, R. C. Z., Cleary, P. W. and Mason, B. R. (2011), 'Simulations of dolphin kick swimming using smoothed particle hydrodynamics.', *Human movement science* **31**(3), 604–19.

Cortesi, M. and Gatta, G. (2015), 'Effect of the swimmer's head position on passive drag.', *Journal of human kinetics* **49**(December), 37–45.

Couser, P. R., Wellicome, J. F. and Molland, A. F. (1998), 'An improved method for the theoretical prediction of the wave resistance of transom-stern hulls using a slender body approach', *International Shipbuilding Progress* **45**(444), 1–18.

Degiuli, N., Werner, A. and Stasic, T. (2005), Some parameters influencing the accuracy of the wave patterm resistance determination, *in* '11th International Congress of the International Maritime Association of the Mediterranean', Taylor & Francis, Lisbon, Portugal, pp. 121–127.

DuBois, D. and DuBois, D. (1916), 'A formula to estimate the approximate surface area if height and weight be known', *Arch Int Med* **17**, 863–871.

Eggers, K. (1955), 'Resistance components of two-body ships', *Jahrbuch der Schiffbautechnischen Gesellschaft,* **49**.

Eggers, K., Sharma, S. and Ward, L. (1967), 'An assessment of some experimental methods for determining the wavemaking characteristics of a ship form', *Transactions of the institution of naval architects and marine engineers* **75**, 112–144.

Epic Sports Swimming (2016), 'History of Swim Caps'.
URL: *http://swimming.epicsports.com/swim-cap-history.html*

FINA (2014), FINA requirements for swimwear approval, Technical report.

Gatta, G., Cortesi, M. and Zamparo, P. (2015), 'Effect of Swim Cap Surface Roughness on Passive Drag.', *Journal of strength and conditioning research / National Strength & Conditioning Association* **29**(11), 3253–3259.

Gatta, G., Zamparo, P. and Cortesi, M. (2013), 'Effect of swim-cap model on passive drag', *Journal of strength and conditioning research* **27**, 2904–2908.

Hassanzadeh, R., Sahin, B. and Ozgoren, M. (2012), 'Large eddy simulation of free-surface effects on the wake structures downstream of a spherical body', *Ocean Engineering* **54**, 213–222.

Hertel, H. (1966), *Structure, Form, Movement*, New York: Reinhold Publishing Corporation.

Hervouet, J.-M. (2007), *Hydrodynamics of free surface flows: modelling with the finite element method*, John Wiley & Sons.

Hesterberg, T., Monaghan, S., Moore, D. S., Epstein, R., College, R. and Rucker, J. (2003), Bootstrap methods and permutation tests, *in* 'The practice of business statistics', W. H. Freeman and Company, chapter 18, pp. 4–73.

Hoerner, S. F. (1965), *Fluid Dynamic Drag*, Hoerner Fluid Dynamics.

Hollander, A., de Groot, G., Van Ingen Schenau, G., Toussaint, H., de Best, H., Peeters, W., Meulemans, A. and Schreurs, A. (1986), 'Measurement of active drag during crawl arm stroke swimming', *Journal of Sports Sciences* **4**, 21–30.

Insel, M. (1990), An investigation into the resistance components of high speed displacement catamarans, PhD thesis, University of Southampton.

ITTC (1967), Report of resistance committee, Technical report, ITTC.

ITTC (2011), Density and viscosity of water, ITTC Procedure 7.5-02-01-03, Technical report.

ITTC (2014), Final report and recommendations, *in* '27th ITTC Ocean Engineering Committee', number February, Copenhagen, pp. 1–86.

James, M. C. (2017), 'Dataset for 'Flow taxonomy of a surface-piercing sphere over the transitional Fr-Re range''.
URL: *http://doi.org/10.5258/SOTON/D0078*

James, M. C., Forester, A., Hudson, D. A., Taunton, D. J. and Stephen, R. (2015), Experimental study of the transitional flow of a sphere located at the free surface, *in* 'Proceedings of the 9th International Workshop on Ship and Marine Hydrodynamics', Glasgow, pp. 1–7.

Jones, J. (2011), 'Space age swimsuit reduces drag, breaks records'.
URL: *https://spinoff.nasa.gov/Spinoff2008/ch_4.html*

Karpovich, P. (1933), 'Water resistance in swimming', *Res. Quart.* (4), 21–28.

Keys, M. (2010), Establishing computational fluid dynamics models for swimming technique assessment, Phd thesis, The University of Western Australia.

Kim, K. J. and Durbin, P. A. (1988), 'Observation of the frequencies in a sphere wake and drag increase by accoustic excitation', *Phys. Fluids* **31**(11), 3260–3265.

Kiya, M., Mochizuki, O. and Ishikawa, H. (2000), Challenging issues in separated and complex turbulent flows, *in* '10th International Symposium on Applications of Laser Techniques to Fluid Mechanics', Lisbon, Portugal, pp. 1–13.

Kjendlie, P.-l. and Stallman, R. K. (2008), 'Drag characteristics of competitive swimming children and adults', *Journal of Applied Biomechanics* (24), 35–42.

Larsen, O. W. (1981), 'Boat design and swimming performance', *Swimming Technique* **18**, 38–44.

Larsson, L. and Eliasson, R. E. (1994), *Principles of yacht design*, Adlard Coles Nautical, London.

Launder, B. and Sharma, B. (1974), 'Application of the energy dissipation model of turbulence to the calculation of flow near a spinning disc', *Letters in Heat and Mass Transfer* **1**(2), 131–138.

Lloyd, T. P. and James, M. (2015), 'Large eddy simulations of a circular cylinder at Reynolds numbers surrounding the drag crisis', *Applied Ocean Research* (November).

Lowry, R. (1998), 'Concepts & applications of inferential statistics'.
URL: *http://vassarstats.net/textbook/index.html*

Lyttle, A. D., Blanksby, B. A., Elliott, B. C. and Lloyd, D. G. (1998), 'The effect of depth and velocity on drag during the streamlined glide', *Journal of Swimming Research* **13**, 15–22.

Maglischo, E. (2003), *Swimming Faster*, human kine edn.

Marinho, D. A. (2009), 'The study of swimming propulsion using computational fluid dynamics: A three-dimensional analysis of the swimmer 's hand and forearm'.

Marinho, D. A., Barbosa, T. M., Reis, V. M., Kjendlie, P. L., Alves, F. B., Vilas-boas, J. P., Machado, L., Silva, A. J. and Rouboa, A. I. (2010), 'Swimming propulsion forces are enhanced by a small finger spread', (1979), 87–92.

Marinho, D. A., Mantha, V. R., Rouboa, A. I., Vilas, J. P., Machado, L., Barbosa, T. M. and Silva, A. J. (2011), 'The effect of wearing a cap on a the swimmer passive drag', *Portuguese Journal of Sport Sciences* (11), 319–322.

Marinho, D. A., Mantha, V. R., Vilas-boas, J. P., Ramos, R. J., Machado, L., Rouboa, A. I. and Silva, A. J. (2012), 'Effect of wearing a swimsuit on hydrodynamic drag of swimmer', *Brazilian Archives of Biology and Technology* **55**(6), 851–856.

MedCalc (1993), 'Values of the t-distribution (two-tailed)'.
URL: *https://www.medcalc.org/manual/t-distribution.php*

Menter, F. (1994), 'Two-equation eddy-viscosity turbulence models for engineering applications', *AIAA Journal* **32**(8), 269–289.

Menter, F. R., Kuntz, M. and Langtry, R. (2003), 'Ten Years of Industrial Experience with the SST Turbulence Model', *Turbulence, Heat and Mass Transfer* .

Meyer, D. (2013), 'The need for speed: how high-technology swimsuits changed the sport of swimming'.
URL: *http://swimswam.com/wp-content/uploads/2013/06/The-Need-for-Speed-How-High-Technology-Swimsuits-Changed-the-Sport-of-Swimming.pdf*

Michell, J. H. (1898), 'The wave-resistance of a ship', *Phil. Mag.* **45**(5), 106–123.

Miller, D. (1975), 'Biomechanics of swimming', *Exercise and Sport Sciences Reviews* **2**, 219–248.

Miyashita, M. (1999), 'Biomechanics of swimming: past, present and future studies', *Biomechanics and Medicine in Swimming VIII* pp. 1–8.

Molland, A. F., Turnock, S. R. and Hudson, D. A. (2011), *Ship resistance and propulsion: practical estimation of propulsive power*, Cambridge University Press.

Molland, A. F., Turnock, S. R., Taunton, D. J. and Chandraprabha, S. (2002), Theoretical prediction of the characteristics of ship generated near-field wash waves, Technical Report November, University of Southampton, Southampton.

Mollendorf, J. C., Termin, A. C., Oppenheim, E. and Pendergast, D. R. (2004), 'Effect of swim suit design on passive drag', *Medicine & Science in Sports & Exercise* **36**(6), 1029–1035.

Monaghan, J. J. (1994), 'Simulating free surface flows with SPH', *Journal of Computational Physics* **110**, 399–406.

Nakashima M. (2007), 'Mechanical study of standard six beat front crawl swimming by using swimming human simulation model', *Journal of Fluid Science and Technology* **2**(1), 290–301.
URL: *http://joi.jlc.jst.go.jp/JST.JSTAGE/jfst/2.290?from=CrossRef*

Nakashima M. (2009), 'Simulation analysis of the effect of trunk undulation on swimming performance in underwater dolphin kick of human', *Journal of Biomechanical Science and Engineering* **4**(1), 94–104.

Nakashima, M. and Motegi, Y. (2007), Development of a full-body musculo-skeletal simulator for swimming, Technical report, Tokyo Institute of Technology, Tokyo.
URL: *www.swum.org*

Nakashima, M., Satou, K. and Miura, Y. (2007), 'Development of Swimming Human Simulation Model Considering Rigid Body Dynamics and Unsteady Fluid Force for Whole Body', *Journal of Fluid Science and Technology* **2**(1), 56–67.

Newman, J. N. (1977), *Marine Hydrodynamics*, The Massachussets Institute of Technology.

Oh, Y.-T., Burkett, B., Osborough, C., Formosa, D. and Payton, C. (2013), 'London 2012 Paralympic swimming: passive drag and the classification system.', *British journal of sports medicine* **47**, 838–43.

Olympic Committee (2016), 'Olympic swimming'.
URL: *http://www.rio2016.com/en/swimming*

OpenFOAM (2013), 'OpenFOAM - The Open Source CFD Toolbox - User-guide V.2.2.0'.

Ozgoren, M., Dogan, S., Okbaz, A., Aksoy, M. H., Sahin, B. and Akilli, H. (2013), 'Comparison of flow characteristics of different sphere geometries under the free surface effect', *EPJ* **45**.

Ozgoren, M., Dogan, S., Okbaz, A., Sahin, B. and Akilli, H. (2012), 'Passive control of flow structure interaction between a sphere and free-surface', *EPJ* **25**.

Ozgoren, M., Okbaz, A., Kahraman, A., Hassanzadeh, R., Sahin, B., Akilli, H. and Dogan, S. (2011), Experimental investigation of the flow structure around a sphere and its control with jet flow via PIV, *in* '6th IATS', number 5, pp. 16–18.

Pendergast, D. R., Mollendorf, J. C., Cuviello, R. and Termin, a. C. (2006), 'Application of theoretical principles to swimsuit drag reduction', *Sports Engineering* **9**(2), 65–76.

Pendergast, D. R., Mollendorf, J. C., Zamparo, P., Termin, A., Bushnell, D. and Paschke, D. (2005), 'The influence of drag on human locomotion in water', *Undersea Hyperb Med* **32**(1), 45–57.

Peric, M. and Ferziger, J. H. (2002), *Computational methods for fluid dynamics*, springer edn, Berlin.

Popa, C. V., Arfaoui, A., Fohanno, S., Taïar, R. and Polidori, G. (2012), 'Influence of a postural change of the swimmer's head in hydrodynamic performances using 3D CFD', *Computer methods in biomechanics and biomedical engineering* (August 2012), 37–41.

Reynolds, E., Anderson, B. and Walker, G. (1997), Effects of turbulence and velocity profile variation in a circulating water channel as determined by sphere and ellipsoid tests, Technical report, Australian Maritime Engineering CRC Ltd., Lauceston.

Roth, E. H. (2008), Artic Ocean long-term acoustic monitoring: ambient noise, environmental correlates, and transients North of Barrow, PhD thesis, University of California, San Diego.

Rouboa, A., Silva, A., Leal, L., Rocha, J. and Alves, F. (2006), 'The effect of swimmer's hand/forearm acceleration on propulsive forces generation using Computational Fluid Dynamics', *Journal of Biomechanics* **39**, 1239–1248.

Rushall, B. S., Holt, L. E., Sprigings, E. J. and Cappaert, J. M. (1994), 'A re-evaluation of forces in swimming', *Journal of Swimming Research* (10), 6–30.

Sakamoto, H. and Haniu, H. (1990), 'A Study on Vortex Shedding From Spheres in a Uniform Flow', *ASME* **112**(December), 386–392.

Sanders, R., Rushall, B., Toussaint, H., Stager, J. and Takagi, H. (2001), 'Bodysuit yourself: but first think about it', *American Swimming Magazine* (5), 23–32.

Schleihauf, R. (1979), 'A hydrodynamic analysis of swimming propulsion', *J. Terauds, E.W. Bedingfield* **Swimming I**, 70–109.

Sheehan, D. and Laughrin, D. (1992), 'Device for quantitative measurements of hydrodynamic drag on swimmers', *The Journal of Swimming Research* **8**(Fall), 30.

Silva, A. J., Rouboa, A., Moreira, A., Reis, V. M. and Alves, F. (2008), 'Analysis of drafting effects in swimming using computational fluid dynamics', (September 2007), 60–66.

Silva, A., Rouboa, A., Leal, L., Rocha, J., Alves, F., Moreira, A., Reis, V. and Vilas-Boas, J. (2005), 'Measurement of swimmer's hand/forearm propulsive forces generation using computational fluid dynamics', *Portuguese Journal of Sport Sciences* **5**(3), 288–297.

Silvester, S. (2012), 'Excellence in Engineering Simulation (ANSYS SPORTS)', *Advantage, ANSYS* **VI**(2), 10–14.

Taneda, S. (1956), 'Experimental investigation of the wake behind a sphere at low Reynolds numbers', *Journal of the Physical Society of Japan* **11**(10), 1104 – 1108.

Taneda, S. (1978), 'Visual observations of the flow past a sphere at Reynolds numbers between 10^4 and 10^6', *Journal of Fluid Mechanics* **85**(1), 187–192.

Taunton, D. (2012), 'In-house slender body theory code (wavelstl)'.

Taunton, D. J. (2013), 'In-house slender body theory code to get wave resistance from wave cuts (waveSis)'.

Thurow, R. and Rhoads, C. (2008), 'Fast Times'.
URL: *http://online.wsj.com/article/SB121865005500237497.html*

Toussaint, H. M., Bruinink, L., Coster, R., De Looze, M., Van Rossem, B., Van Veenen, R. and De Groot, G. (1989), 'Effect of a triathlon wet suit on drag during swimming.', *Medicine and science in sports and exercise* **21**(3), 325–8.

Toussaint, H. M., Hollander, A. P., Berg, C. V. D. and Vorontsov, A. (2000), 'Biomechanics of swimming', *Exercise and Sport Science* pp. 639–660.

Toussaint, H. M., Truijens, M., Elzinga, M., van de Ven, A., de Best, H., Snabel, B. and de Groot, G. (2002), 'Effect of a Fast-skin 'body' suit on drag during front crawl swimming.', *Sports biomechanics / International Society of Biomechanics in Sports* **1**(1), 1–10.

Toussaint, H. M., Van den Berg, C. and Beek, W. J. (2002), '"Pumped-up propulsion" during front crawl swimming.', *Medicine and science in sports and exercise* **34**(2), 314–319.

Toussaint, H., Roos, P. and Kolmogorov, S. (2004), 'The determination of drag in front crawl swimming', *Journal of biomechanics* **37**(11), 1655–63.

Toussaint, H. and Truijens, M. (2005), 'Biomechanical aspects of peak performance in human swimming', *Animal Biology* **55**(1), 17–40.

Turnock, S. R. (2004), 'Parametric definition of complex multi-appended bodies for marine and aerospace application: a user guide to Adaptflexi'.

Vennell, R., Pease, D. and Wilson, B. (2006), 'Wave drag on human swimmers.', *Journal of biomechanics* **39**(4), 664–71.

Vogel-Prandtl, J. and Ram, V. V. (2004), *A biographical sketch, remembrances and documents*, The International Centre for Theoretical Physics.

von Loebbecke, A., Mittal, R., Mark, R. and Hahn, J. (2009), 'A computational method for analysis of underwater dolphin kick hydrodynamics in human swimming', *Sports biomechanics* **8**(1), 60–77.

Webb, A. (2013), Identifying race time benefits of best practice in freestyle swimming using simulation, Ph.d. thesis, University of Southampton.

Webb, A. P., Banks, J., Phillips, C. W., Hudson, D. A., Taunton, D. J. and Turnock, S. R. (2011), 'Prediction of passive and active drag in swimming', *Procedia Engineering* **13**, 133–140.

Webb, A. P., Turnock, S. R., Hudson, D. A., Forrester, A. I. and Taunton, D. J. (2014), 'Repeatable techniques for assessing changes in passive swimming resistance', *Journal of Sports Engineering and Technology* **Proc IMech**(Part P), 1–10.

Wilcox, D. (1988), 'Re-assessment of the scale-determining equation for advanced turbulence models', *AIAA Journal* **26**(11), 1299–1310.

Wilson, B. and Thorp, R. (2003), Active drag in swimming, *in* 'Biomechanics and medicine in swimming IX', pp. 15–20.

WS Atkins Consultants (2003), Best practice guidelines fro marine applications of computational fluid dynamics, Technical report.
URL: *https://pronet.atkinsglobal.com/marnet/publications/bpg.pdf*

Wumtia (n.d.), 'Wumtia dynamometry'.
URL: *http://www.wumtia.soton.ac.uk/products/dynamometry*

Yu, G., Avital, E. J. and Williams, J. J. R. (2008), 'Large Eddy Simulation of Flow Past Free Surface Piercing Circular Cylinders', *Journal of Fluids Engineering* **130**(10), 101304.

Zaidi, H. (2008), Contribution a l'etude des ecoulements turbilionnaires en biomecanique du geste sportif, PhD thesis, Universite de Reims, Champagne-Ardenne.

Zaïdi, H., Taïar, R., Fohanno, S. and Polidori, G. (2008), 'Analysis of the effect of swimmer's head position on swimming performance using computational fluid dynamics', *Journal of Biomechanics* **41**(6), 1350–1358.

Zamparo, P., Gatta, G., Pendergast, D. and Capelli, C. (2009), 'Active and passive drag: The role of trunk incline', *European Journal of Applied Physiology* **106**(2), 195–205.